

Spectroscopy and Dissociation Dynamics of Cold, Biomolecular Ions

THÈSE N° 4573 (2010)

PRÉSENTÉE LE 5 FÉVRIER 2010

À LA FACULTÉ SCIENCES DE BASE

LABORATOIRE DE CHIMIE PHYSIQUE MOLÉCULAIRE

PROGRAMME DOCTORAL EN CHIMIE ET GÉNIE CHIMIQUE

ÉCOLE POLYTECHNIQUE FÉDÉRALE DE LAUSANNE

POUR L'OBTENTION DU GRADE DE DOCTEUR ÈS SCIENCES

PAR

Monia GUIDI

acceptée sur proposition du jury:

Prof. L. Helm, président du jury
Prof. T. Rizzo, directeur de thèse
Prof. A.-C. Corminboeuf, rapporteur
Prof. C. Juvet, rapporteur
Prof. J. Simons, rapporteur



ÉCOLE POLYTECHNIQUE
FÉDÉRALE DE LAUSANNE

Suisse
2010

Abstract

The function of a peptide is intimately connected to its structure, which in solution is the result of the balance between non-covalent interactions within the molecule and the molecule-solvent interactions. Theory has the power to predict the properties of a wide variety of molecules, but the accuracy of the theoretical predictions must be verified by experiments. A way to test, and hopefully improve, theory is to study proteins or peptides in the gas-phase.

The combination of mass spectrometry and laser spectroscopy is used to investigate properties of biological ions in the gas-phase. Closed-shell biomolecular ions produced by an electrospray source are cooled down in an RF ion trap to less than 10 K and interrogated spectroscopically.

Electronic and conformer-specific vibrational spectra have been measured for small protonated peptides applying photofragment-based detection schemes. These measurements allow us to investigate the role of the charge and the influence of the nature and the position of the chromophore in the peptide chain on its conformational preferences. Highly-resolved conformer-specific vibrational spectra of such species, as well as those of a double-chromophore molecule, help elucidate the mechanism of the IR-UV double-resonance methods and provide benchmarks for testing the accuracy of theoretical calculations.

This thesis shows also the experimental developments that allow us to use photofragment-based detection scheme to measure highly-resolved electronic spectra of peptides of up to 17 amino acids, containing one or two chromophores, using infrared laser-assisted photofragment spectroscopy (IRLAPS). The fragmentation yield of UV pre-excited molecules increases by as much as two orders of magnitude when they further interact with the CO₂ laser. This approach can be also applied in a IR-UV double resonance scheme, allowing measurements of conformer-specific infrared spectra of protonated peptides. The fragmentation channel, which is always greatly enhanced by IRMPD of UV pre-excited molecules, is the loss of the neutral, aromatic side chain via cleavage of the C_α-C_β bond, independent of the chromophore excited in the peptide. The possible mechanisms, involving the formation of a long-lived intermediate species, that lead to the formation of the observed photofragment are discussed in this thesis work.

Keywords: gas-phase biological molecules; ion traps; mass spectrometry; photodissociation spectroscopy; IR-UV double-resonance spectroscopy.

Riassunto

La funzione di un peptide è intimamente connessa alla sua struttura, che, in soluzione, è il risultato dell'equilibrio tra forze non-covalenti interne alla molecola e interazioni tra la molecola e il solvente. Differenti proprietà molecolari possono essere caratterizzate con metodi teorici, la cui accuratezza deve essere verificata da misure sperimentali, come, ad esempio, lo studio di proteine o peptidi in fase gassosa.

Attraverso la combinazione di spettroscopia di massa e laser è possibile studiare le proprietà di molecole biologiche in forma ionica nella fase gassosa. Tali ioni, prodotti in una sorgente electrospray, sono raffreddati ad una temperatura inferiore ai 10 K e interagiscono con i laser.

La spettroscopia basata sul rilevamento di frammenti ha consentito di misurare spettri elettronici e vibrazionali associati a singole conformazioni di cationi peptidici di modeste dimensioni. In questo modo è possibile studiare il ruolo della carica, l'influenza della natura del cromoforo e della sua posizione nella catena polipeptidica sulle proprietà conformazionali del peptide stesso. Inoltre, gli spettri vibrazionali delle singole conformazioni di queste molecole e di peptidi contenenti due cromofori permettono di comprendere il meccanismo della spettroscopia di doppia-risonanza IR-UV e forniscono un mezzo fondamentale per verificare i metodi teorici utilizzati.

In questa tesi vengono anche illustrati i progressi sperimentali che hanno consentito di misurare spettri elettronici di peptidi di massimo diciassette amminoacidi, contenenti uno o più cromofori, incrementando la dissociazione di una molecola eccitata nell'ultravioletto con un laser infrarosso. Tale tecnica è nota come IRLAPS. La frazione di molecole che, dopo essere state promosse in uno stato eccitato, si dissociano assorbendo la radiazione proveniente da un laser a CO₂ è di due ordini di grandezza maggiore di quella dei cationi che invece non interagiscono con il suddetto laser. La tecnica può essere anche applicata in una configurazione di doppia risonanza IR-UV, consentendo di misurare spettri vibrazionali delle conformazioni di peptidi cationici. L'effetto dell'IRLAPS si manifesta sempre con la rottura del legame C_α-C_β, indipendentemente dal cromoforo eccitato nella catena polipeptidica. In questa tesi vengono proposti possibili meccanismi, basati sull'esistenza di stati intermedi con tempi di vita lunghi, per spiegare la formazione di questo frammento.

Parole chiave: molecole biologiche in fase gassosa; trappole ioniche; spettroscopia di massa; spettroscopia di foto-dissociazione; spettroscopia di doppia risonanza IR-UV.

Contents

Chapter 1: Introduction	1
1.1 Biological molecules in the gas-phase	2
1.2 Spectroscopy of neutrals	4
1.3 Spectroscopy of ions	5
1.4 Low-temperature biomolecules	7
1.5 Interplay with theory	9
1.6 Goals and outline	9
References	12
 Chapter 2: Experimental setup	 19
2.1 The home-built tandem mass spectrometer	19
2.1.1 Electrospray ionization	20
2.1.2 Quadrupole mass filtering	23
2.1.3 Linear multipoles ions traps and guides	25
2.1.4 Machine overview	31
2.2 Description of the laser setup	33
2.2.1 Generation of UV laser light	33
2.2.2 Generation of IR laser light	34
2.2.3 TEA-CO ₂ laser	36
References	37

Chapter 3: Spectroscopic techniques and theoretical approach.....41

3.1 Photofragment Spectroscopy	41
3.1.1 Introduction	41
3.1.2 Timing of the events	45
3.1.3 Measurement of photofragment mass spectra	47
3.1.4 Molecular size and lifetime considerations	48
3.2 Conformer-specific spectra by IR-UV double-resonance spectroscopy	52
3.2.1 Adaptation to the spectroscopy of cold trapped ions	53
3.2.2 Mechanisms and limitations of the IR-UV double-resonance methods	55
3.3 Theoretical methods	58
3.4 Overview of the photophysics of the aromatic amino acids	60
References	65

Chapter 4: Photofragmentation spectroscopy of small charged peptides71

4.1 Tyrosine-based protonated dipeptides: H^+AlaTyr and H^+TyrAla	71
4.1.1 Introduction	71
4.1.2 H^+TyrAla	72
4.1.3 H^+AlaTyr	78
4.1.4 Conclusions	82
4.2 Single- and double-chromophore seven-amino-acid peptides	82
4.2.1 Introduction	82
4.2.2 $\text{Ac-Tyr-(Ala)}_5\text{-LysH}^+$	85
4.2.3 $\text{Ac-(Ala)}_5\text{-Phe-LysH}^+$	95
4.2.4 $\text{Ac-Tyr-(Ala)}_4\text{-Phe-LysH}^+$	100
4.2.5 Discussion and Conclusions	109

4.3 State of comparison with theory	111
References	114
Chapter 5: Toward larger peptides	117
5.1 Introduction	117
5.2 Infrared laser assisted photofragment spectroscopy	120
5.2.1 Measurements of weak overtone transitions of small molecules	120
5.2.2 Adaptation of IRLAPS to measure electronic and vibrational spectra of biomolecular ions	122
5.3 Results	124
5.3.1 Phenylalanine containing peptides	124
5.3.2 Tyrosine containing peptides	129
5.3.3 Tryptophan containing peptide	132
5.3.4 Double-chromophore peptide	132
5.3.5 Fragment mass spectra	133
5.4 Discussion on the IRLAPS mechanism	137
5.4.1 Timing of the lasers in the IRLAPS experiment	138
5.4.2 C α -C β bond cleavage in protonated aromatic amino acids	142
5.4.3 Electron-driven proton-transfer reaction	149
5.5 Conclusions	159
References	161
Chapter 6: Conclusions and Perspectives	165
References	168
List of Figures	169

List of Tables	173
List of Schemes	175
Acknowledgements	177
Curriculum vitae	179

Chapter 1

Introduction

Proteins are biological macromolecules essential for all living organisms; they perform a variety of functions such as enzymatic activity, catalysis, signal transduction and molecular transportation. The primary structure of a protein consists of a sequence of amino acid building blocks linked together by covalent peptide bonds. The additional non-covalent interactions between the amino acids largely determine the three-dimensional structure of the protein, which is related to its biological function. Understanding the forces that drive protein folding into a particular conformation and how these conformers are related to a specific function is necessary for developing a fundamental understanding of “living matter”.

It is extremely difficult to predict the three-dimensional shape of a peptide or protein starting from its primary structure alone, since its final architecture in solution results from a delicate balance between non-covalent interactions within the molecule itself and the molecule-solvent interactions. Protein structures typically measured by X-ray diffraction in crystals may differ substantially from those in their natural environment, where packing forces may influence their conformation. Nuclear magnetic resonance (NMR) can be used for biomolecular structure determination in the solution phase, but its applicability is limited to biomolecules of ~50 kDa [1-3]. On the other hand, theory has the potential to predict the conformations of a wide variety of molecules of virtually any size and to reveal the nature of the counterbalancing forces that control them. However, the accuracy of the theoretical methods needs to be verified by experiments. One way to test, and hopefully improve, theory would be to study proteins or peptides in the gas phase. Indeed, removing these species from their natural environment allows the investigation of their intrinsic properties free from external perturbations. High resolution spectra of gas-phase peptides, for example, would provide an important benchmark for theoretical methods.

1.1 Biological molecules in the gas-phase

Investigation of biomolecules in the gas-phase requires a means to volatilize them in sufficient quantity. Since even relatively small biological molecules have a low vapor pressure, they usually decompose upon heating before vaporizing so that standard thermal methods cannot be employed. One way to circumvent this problem is to deliver the energy to the system quickly so that the molecules desorb before they dissociate. An example of this approach is laser desorption (LD) [4-6], a method based on the ejection of material from a sample-covered surface by using an intense laser light. A related technique, known as matrix-assisted laser desorption/ionization (MALDI), allows generating gas-phase macromolecules of up to several kilodaltons by embedding the sample molecules in a matrix that strongly absorbs the desorbing light [7, 8]. Other techniques, such as thermospray [9, 10] and electrospray (ESI) [11-13], use the nebulization of a sample solution through a capillary to produce charged droplets from which ions can desorb. The latter method, which will be extensively discussed in *Chapter 2*, has allowed intact biomolecules of virtually any size to be put into the gas-phase in the form of closed-shell molecular ions. This is why, together with MALDI, ESI has become widely used in academic research and is a standard option on commercial mass spectrometers.

Information on the primary structure of biological molecules can be inferred by coupling these volatilizing techniques with mass spectrometry, using mass analysis to identify the peptide fragments produced in the gas-phase by photo-, collision-, surface- or electron capture-induced dissociation [14-18]. However, as previously discussed, the amino acid sequence of a protein or peptide does not uniquely determine its three-dimensional structure. Several additional techniques have thus been developed in order to gain insight into the spatial architecture of a biological molecule.

Hydrogen/deuterium (H/D) exchange experiments can provide information on the conformational preferences of a biological molecule. Indeed, when exposing a peptide to a deuterated solvent, the hydrogen atoms located in the core of the molecule or involved into hydrogen-bonds will exchange with deuterium atoms more slowly than those on the biomolecular surface. By detecting how many of the labile hydrogens have been replaced by deuterium, using for example ESI, it is possible to monitor the conformational changes of the

protein in solution [19]. An alternative approach is to first volatilize the polypeptides and then bring them in contact with a deuterated solvent. This allows studying the folding and unfolding of gas-phase molecules, in addition to their conformational preferences [20-22]. For instance, using this method, Freitas and Marshall studied bradykinin, a nonapeptide containing two arginines, and concluded that its protonated form in the gas-phase exists as a zwitterionic structure, with both arginine side chains protonated and the terminal acidic group deprotonated [22].

Another strategy to characterize the three-dimensional shape of a biomolecule is to perform ion mobility studies. The generated gas-phase ions enter into a drift tube containing several millibars of a buffer gas where they move under the influence of a weak electric field. Since the mobility of a gas-phase ion depends on its average cross section, biomolecular ions that differ in their charge states and/or conformation will have distinct mobilities and thus will exit the tube at different times [23-26]. Measured drift times are then converted into cross sections that are in turn compared with those of model structures. As examples, Jarrold and coworkers probed the conformations and folding properties of cytochrome c [27, 28], bovine pancreatic trypsin inhibitor (BPTI) [28] and a series of polyalanine peptides [29-31]. High-field asymmetric waveform ion mobility spectrometry (FAIMS) is a variant of the standard ion mobility method where the ions are separated by the difference in their mobility at high and low electric field [32]. This method seems to be somewhat orthogonal to standard, drift-tube ion mobility in that it allows the separation of distinct conformations of similar collision cross sections [33-36].

Williams and coworkers developed a method to measure the dissociation energies of trapped protonated biomolecular ions. This technique, known as blackbody infrared radiative dissociation (BIRD), consists in measuring the dissociation rate of ions trapped in a Fourier transform ion cyclotron resonance mass spectrometer (FT-ICR) induced by the slow absorption of the blackbody radiation from the vacuum chamber walls [37-42]. Temperature-dependent experiments allow the measurement of the activation energies and frequency factors for the lowest-energy dissociation pathways of mass-selected ions. These parameters are highly sensitive to changes in the biomolecular structures and can thus provide information on the conformational preferences of biomolecules. For instance, the Williams group has shown evidence that the most stable form of singly-protonated bradykinin is a salt-

bridge structure [38] and proven that short strands of oligonucleotides forms Watson-Crick hydrogen-bonds [42].

In addition to the methods just presented, spectroscopic techniques have also been extensively used to explore the conformations of biological molecules in the gas-phase. Some of these methods will be discussed in the following sections.

1.2 Spectroscopy of neutrals

The techniques described above offer a means to infer important properties of biological molecules, but they provide only limited information about their conformational preferences. On the other hand, the spectroscopic properties of a molecule are extremely sensitive to the three-dimensional arrangement of its atoms, and even a small difference in its structure can lead to detectable spectroscopic shifts. A variety of spectroscopic techniques have thus been employed to characterize the three-dimensional structures of gas-phase biomolecules.

Several spectroscopic methods allow measurements of the rotational constants of a biomolecule, which are related to its moments of inertia. In particular, microwave spectroscopy [43], rotational coherence spectroscopy [44, 45] and fully [46-49] or partially [50-54] resolved electronic spectroscopy have been employed to assign a geometry to the different conformations of neutral, jet-cooled analogues of the three aromatic amino acids (tryptophan, tyrosine and phenylalanine). Vibrational spectroscopy, examples of which will be presented below, is a powerful technique employed to probe biomolecular structure, since the vibrational frequency of a given bond is highly dependent on its local environment. Finally, electronic spectroscopy can provide information on the molecular structure by detecting the influence of the environment on the chromophore's photophysics.

Levy and coworkers pioneered the application of gas-phase spectroscopy to biologically relevant molecules, reporting in the mid 1980s the first electronic spectra of jet-cooled, neutral tryptophan [55-57] and some of its derivatives [58]. They demonstrated the existence of several conformers for these species using resonant enhanced two-photon ionization (R2PI) saturation spectroscopy and dispersed fluorescence spectroscopy. Similar

experiments were later carried out in the same group to identify different conformations of tyrosine and phenylalanine [59]. Following this pioneering work, a number of groups began to investigate the conformational preferences of small molecules of biological interest and developed innovative double-resonance spectroscopic schemes (e.g., IR-UV depletion spectroscopy and UV-UV hole-burning spectroscopy) to acquire conformer-specific vibrational and electronic spectra [60-71]. The size of the molecules that is possible to investigate with the mentioned techniques gradually increased with time over the past twenty years. As a consequence, it has been possible to observe secondary structures of the peptide backbone such as β - and γ - turns or 3_{10} helices in capped tripeptides [72-74], and the formation of β -sheet structures in short peptide chains [75-78]. In the last few years, these double-resonance spectroscopic techniques have been applied to investigate larger peptides, such as gramicidin [79, 80], as well as nucleotide bases and their pairing [81-83]. Moreover, they have been used to monitor the influence of solvation on the conformational preferences of small biomolecules by examining their hydrated clusters [75, 83-88].

Zwier and coworkers have developed two innovative spectroscopic schemes, whose application provides complementary information to those obtained by the standard double-resonance techniques. The first one consists in transferring part of the population of a conformer into the potential wells of the others upon absorption of an IR photon or by stimulated emission pumping [89-92]. These techniques enable the study of conformational isomerization in flexible molecules (i.e., those having a large number of minima on the potential energy surface (PES)) measuring the energy barriers between the different conformers and the product quantum yields, following infrared excitation. The second method is a triple-resonance spectroscopic scheme, IR-IR-UV hole-burning, that allows obtaining conformer-specific vibrational spectra when the two conformers have indistinguishable electronic spectra [93].

1.3 Spectroscopy of ions

The spectroscopic studies described in the previous section have been performed on neutral biological molecules in the gas phase. However, these species are often charged in their native environment. It is well known, for instance, that most amino acids in solution at

physiological pH are zwitterions, with a deprotonated carboxylate group and a charged ammonium group. Moreover, some of them have basic (lysine, arginine and histidine) or acidic (aspartic and glutamic acids) side chains so that a protein containing multiple residues of these types possesses an overall charge. The presence of a charge can strongly influence the molecular and spectroscopic properties of a peptide, and thus investigating charged biomolecular ions, in addition to their neutral counterparts, is of fundamental importance.

Because of the difficulty of producing sufficient gas-phase concentration of ions, these species only began to be explored by optical spectroscopy at the beginning of the new millennium [94-96]. As already mentioned, the advent of soft ionization techniques, MALDI and ESI, have made it possible to volatilize biological molecules of virtually any size in the form of closed-shell molecular ions, opening up new avenues of investigation. However, the low density of ions renders the use of direct absorption spectroscopy or fluorescence spectroscopy extremely difficult. Hence, the spectrum of gas-phase molecular ions must be recorded using some sort of *action spectroscopy*, in which a consequence of the photon absorption is measured rather than the absorption itself.

Andersen and coworkers were the first to use action spectroscopy to characterize closed-shell molecular ions produced by electrospray [94, 95]. They measured the electronic excitation spectra of the green fluorescent protein chromophore in its protonated and deprotonated forms in an electrostatic ion storage ring by detecting the neutral products subsequent to photofragmentation or photodetachment respectively. It was not until 2004 that Nolting *et al.* reported the first electronic spectrum of a protonated amino acid in the gas phase (i.e. tryptophan) [97]. Dugourd and coworkers also measured the electronic spectrum of protonated tryptophan but in a wider wavelength range and performed a detailed analysis of its different dissociation patterns [98]. Parks and coworkers probed the conformational dynamics of weakly bound protonated oligonucleotides duplexes, produced in the gas phase by electrospray and stored in a quadrupole ion trap, by fluorescence resonance energy transfer (FRET) spectroscopy. This method allowed them to observe an intermediate state in the dissociation of the oligonucleotides duplexes [99].

In addition to the electronic structure of a biomolecule, electronic spectroscopy also provides information on its excited-state dynamics, which is essential to understanding the photostability of biological chromophores such as the DNA bases or the aromatic amino

acids. Nielsen and coworkers monitored the decay of cationic and anionic mono- and dinucleotides in an ion storage ring after absorption of a UV photon on the microsecond time scale [100, 101]. They could thus identify both statistical and non-statistical photodissociation channels, the latter of which becomes predominant for the protonated species. Other groups have explored the excited-state dynamics of positively charged chromophores on a much shorter time scale, using femtosecond pump-probe laser schemes [102-108] and coincidence experiments [109-111]. With these approaches, they could determine the excited-state lifetimes of protonated aromatic amino acids and of di- and tripeptides containing them. Since some of these experiments are closely related to our work, they will be discussed in detail in later chapters.

Concerning vibrational spectroscopy, McLafferty and coworkers demonstrated that it is possible to acquire infrared spectra of electrosprayed peptides and proteins in a FT-ICR mass spectrometer in the light-atom stretch region by resonant infrared multiphoton dissociation (R-IRMPD), using an optical parametric oscillator (OPO) [96, 112]. Although the ions in the trap were at room temperature, the observed bands were about 30 cm^{-1} wide, which made it possible to distinguish between many light atom stretch bands. Von Helden and coworkers extended IRMPD spectroscopy into the amide I and II regions of the infrared employing a free-electron laser to measure the infrared spectrum of potassiumated cytochrome C formed by electrospray [113]. The analysis of the vibrational spectrum in this region reveals a large degree of α -helical content in cytochrome C. Such measurements have also been used to elucidate the structures of many protonated amino acids, small peptides and other biomolecules [114-123].

1.4 Low-temperature biomolecules

The gas-phase studies presented in the previous sections provide spectroscopic data to help elucidate the conformational preferences of biomolecules. As already mentioned, our main motivation for putting biologically relevant molecules into the gas-phase is to disentangle the contributions of the intermolecular and intramolecular interactions that determine their three-dimensional structure.

A direct consequence of this approach in the case of optical measurements is a simplification of the acquired spectra with respect to those recorded in solution-phase. Indeed, the environment fluctuations in solution influence the optical response of the molecule, thus preventing access to a resolved vibronic spectrum. This solvent-related inhomogeneous broadening is obviously completely suppressed in the gas-phase, where the acquired optical spectrum would be a signature of the molecular intrinsic properties. The other main contribution to inhomogeneous broadening derives from the large number of rotational and low-energy vibrational degrees of freedom populated at room temperature. This gives rise to thermal inhomogeneous broadening of the molecular spectrum that can be significantly reduced at low temperature.

Neutral molecules can be efficiently cooled in seeded supersonic expansions. The typical temperatures achievable with this method for the different degrees of freedom are ~ 1 K for translation, a few degrees Kelvin for rotations and a few tens of degrees Kelvin for vibrations. Examples of applications to the study of biomolecules include all those presented in *Section 1.2*.

Johnson and coworkers developed a method to cool ion-molecule complexes by condensation of solvent molecules onto argon-solvated ions formed in a supersonic expansion [124, 125]. Another strategy is to produce cations in a pulsed high voltage electric discharge source coupled to a pulsed nozzle supersonic expansion. Collisional cooling in the expansion leads the cation with estimated temperatures below 100 K [126, 127].

Ions can also be cooled by confining them in a trap maintained at low temperature, where they collide with a buffer gas for thermalization. In 2004, Weinkauff and coworkers employed a liquid-nitrogen-cooled quadrupole ion trap in order to measure the electronic spectrum of protonated tryptophan [97]. The spectral features they observed were orders of magnitude broader than those of neutral tryptophan cooled in a supersonic expansion, but this was later attributed to the intrinsic lifetime of the protonated aromatic amino acid [102, 103, 105, 109, 110] and not to incomplete cooling. Nevertheless this work served as a major stimulus to study electrosprayed ions in a cold trap. Another approach is to use a linear multipole ion trap cooled with a liquid-helium refrigerator, which makes possible to reach temperatures as low as 10 K [128]. This method will be extensively discussed in *Chapter 2*.

1.5 Interplay with theory

All the experimental work reviewed above relies upon strong support of calculations for structural determination. The applied methods range from simple molecular mechanics to high-level *ab initio* or density functional theory (DFT) calculations depending on the size and the complexity of the system under investigation, as well as on the computational expense to achieve the desired accuracy of the theoretical prediction.

The general approach is to perform low-level calculations to explore the conformational space of a molecule and to identify candidate structures for further analysis. These conformers are then investigated at an increasingly higher level of theory, and some of their properties, such as their vibrational spectra or collision cross sections, are computed and compared with experimental findings. This methodology ideally allows unambiguous geometrical assignments to the species probed experimentally.

However, the agreement between theory and experiment is not always satisfactory, revealing insufficiency of the chosen theoretical procedure. Theory and experiment are intimately connected since the predictions obtained through calculations are necessary to interpret the data acquired in laboratory, which in turn serve as test cases to improve the computational procedures. Examples of this interplay between theory and experiments, as well as a detailed description of the computational methods we employed and their limitations, will be given in later chapters.

1.6 Goals and outline

This introduction has reviewed some of the experimental techniques that have been implemented for characterizing the structures and properties of gas-phase biomolecules. A unique apparatus that combines several of these approaches was realized in our laboratory a few years ago to perform spectroscopic investigations of cold, gas-phase biomolecular ions [129-131]. The machine is a tandem mass spectrometer that employs an ESI source for ion generation and two quadrupole mass filters to select the parent ions and analyze the fragments. A cooled 22-pole ion trap, placed between these two quadrupole mass filters,

serves to accumulate and cool the mass-selected parent ions to $\sim 10\text{K}$. While stored inside the trap, the ions interact with laser light and fragment upon absorption of a resonant ultraviolet photon. Implementation of double-resonance spectroscopic schemes, analogous to those routinely used for jet-cooled molecules, enables the measurement of conformer-specific infrared spectra of cold, protonated biomolecular ions in the gas-phase. The power of this unique approach has been demonstrated by measuring the electronic and vibrational spectra of the three protonated aromatic amino acids in the gas-phase [130-132]. Because of the low-temperature achieved by the protonated molecules in the 22-pole ion trap, the spectra attain an unprecedented resolution for ions that is comparable to that achieved for neutrals in supersonic molecular beams. These results on single aromatic amino acids encouraged us to push further the limit of applicability of our photodissociation technique to larger molecules. Measurements of the electronic and conformer-specific vibrational spectra of a variety of small peptides will be discussed as part of this thesis work.

The primary goals of the work carried out in this thesis have been to understand the intrinsic properties of biological molecules and provide benchmark tests for the current theoretical approaches. In addition, the spectroscopy of gas-phase biomolecular ions is relevant in itself inasmuch as they are the same species found in solution, where most biomolecules carry a net charge. Finally, investigation of the vibrational spectra of larger molecules provides the means to understand the mechanism responsible for the double-resonance spectroscopic schemes to work.

The use of spectroscopic techniques based on photofragmentation methods requires that the ions dissociate on a short enough timescale in order for us to be able to detect the photon absorption and thus record an optical spectrum. However, as a molecule gets larger, its dissociation rate may decrease, making the measurement of electronic or conformer-specific vibrational spectra increasingly difficult if not impossible. Another objective of this thesis work was thus to develop a new experimental procedure that will allow us to apply photofragment-based detection schemes to measure optical spectra of increasingly larger molecules. This method consists in implementing the *Infrared Laser Assisted Photofragment Spectroscopy* (IRLAPS) technique, originally developed to measure the weak vibrational overtone transitions of small neutral molecules [133-137], for the spectroscopy of large biomolecular ions in the gas-phase.

This thesis is organized as follows. *Chapter 2* discusses some of the most important principles of the main components of our experimental apparatus, such as the electrospray source, the quadrupole mass filters and the 22-pole ion trap, followed by a detailed description of the instrument itself. Finally, it describes the laser setups that we use to generate the ultraviolet and infrared laser beams as well as the CO₂ laser employed in the IRLAPS experiment.

After discussing the photophysical processes a molecule undergoes when interacting with laser light, *Chapter 3* illustrates the possible spectroscopic techniques used to reveal this interaction, drawing particular attention to UV *photofragment spectroscopy*. It then presents the timing of events in a typical pulsed experiment and explains in detail the different kind of spectra that it is possible to measure in our apparatus: fragment mass spectra, standard ultraviolet photodissociation spectra and double-resonance infrared and ultraviolet spectra. Different mechanisms that might be responsible for the latter methods to work are discussed in *Chapter 3*, as well as the range of applicability of these photofragment techniques as regards the size of the molecules. *Chapter 3* also describes the theoretical approach we employ to assign a geometry to each molecular conformation, and it finally reviews the photophysics of the three aromatic amino acids used to probe the conformational preferences of the charged peptides.

Chapter 4 presents the measurements of the ultraviolet and conformer-specific infrared spectra of protonated peptides, ranging from dipeptides to seven-amino-acid peptide chains. The role of the charge and the influence of the nature and location of the chromophore on the conformational preferences of the molecule are investigated with the support of theoretical methods. *Chapter 4* also describes work on the electronic and conformer-specific vibrational spectra of a multi-chromophore peptide. Since calculations do not always allow the assignment of a structure to each conformer, the results discussed in this chapter reveal the limits of our present theoretical approach. Moreover, they provide a means to understand the mechanism of double-resonance spectroscopic schemes.

Chapter 5 shows the recent experimental developments we made to apply photofragment-based spectroscopic schemes to large molecules. After discussing the limits of our standard photofragment techniques when applied to large molecules, this chapter describes the IRLAPS method we employed to achieve our goal, first in its original

application and then as adapted for measuring the electronic and vibrational spectra of biomolecular ions. *Chapter 5* demonstrates that the IRLAPS scheme allows the measurements of such spectra for peptide chains containing as many as seventeen amino acids. Surprisingly, this method does not work as initially previewed; several mechanisms are proposed and discussed to explain our experimental observations.

Finally, *Chapter 6* gives a summary of the main results presented in this thesis and suggests future research directions.

References

1. Wuthrich, K., *Acc. Chem. Res.*, **1989**. 22: p. 36-44.
2. Wuthrich, K., *Science*, **1989**. 243: p. 45-50.
3. Cavanagh, J., Fairbrother, W., Palmer III, A.G., and Sketlon, N.J., *Protein NMR spectroscopy: principles and practice*. 1996: Elsevier Science (USA).
4. Posthumus, M.A., Kistemaker, P.G., Meuzelaar, H.L.C., and Ten Noever de Brauw, M.C., *Anal. Chem.*, **1982**. 50: p. 985-991.
5. Cable, J.R., Tubergen, M.J., and Levy, D.H., *J. Am. Chem. Soc.*, **1987**. 109: p. 6198-6199.
6. Levis, R.J., *Ann. Rev. Phys. Chem.*, **1994**. 45: p. 483-518.
7. Karas, M. and Hillenkamp, F., *Anal. Chem.*, **1985**. 60: p. 2299-2301.
8. Karas, M., Bachmann, D., Bahr, U., and Hillenkamp, F., *Int. J. Mass Spectrom. Ion Processes*, **1987**. 78: p. 53-68.
9. Blakley, C.R., Carmody, J.J., and Vestal, M.L., *Anal. Chem.*, **2002**. 52: p. 1636-1641.
10. Blakley, C.R., Carmody, J.J., and Vestal, M.L., *J. Am. Chem. Soc.*, **2002**. 102: p. 5931-5933.
11. Yamashita, M. and Fenn, J.B., *J. Phys. Chem.*, **1984**. 88: p. 4671-4675.
12. Yamashita, M. and Fenn, J.B., *J. Phys. Chem.*, **1984**. 88: p. 4451-4459.
13. Fenn, J.B., Mann, M., Chin, K.M., Wong, S.F., and Whitehouse, C.M., *Science*, **1989**. 246: p. 64-71.
14. Meot-Ner, M., Dongré, A.R., Somogyi, Á., and Wysocki, V.H., *Rapid Commun. Mass Spectrom.*, **1995**. 9: p. 829-836.
15. Horn, D.M., Breuker, K., Frank, A.J., and McLafferty, F.W., *J. Am. Chem. Soc.*, **2001**. 123: p. 9792-9799.
16. Senko, M.W., Speir, J.P., and McLafferty, F.W., *Anal. Chem.*, **2002**. 66: p. 2801-2808.
17. Little, D.P., Speir, J.P., Senko, M.W., O'Connor, P.B., and McLafferty, F.W., *Anal. Chem.*, **2002**. 66: p. 2809-2815.
18. Keller, K.M. and Brodbelt, J.S., *Anal. Biochem.*, **2004**. 326: p. 200-210.
19. Katta, V. and Chait, B.T., *J. Am. Chem. Soc.*, **2002**. 115: p. 6317-6321.
20. Suckau, D., Shi, Y., Beu, S.C., Senko, M.W., Quinn, J.P., Wampler, F.M., and McLafferty, F.W., *Proc. Natl. Acad. Sci. U. S. A.*, **1993**. 90: p. 790-793.

21. Wood, T.D., Chorush, R.A., Wampler, F.M., Little, D.P., Oconnor, P.B., and McLafferty, F.W., *Proc. Natl. Acad. Sci. U. S. A.*, **1995**. 92: p. 2451-2454.
22. Freitas, M.A. and Marshall, A.G., *Int. J. Mass Spectrom.*, **1999**. 183: p. 221-231.
23. Bowers, M.T., Kemper, P.R., Vonhelden, G., and Vankoppen, P.A.M., *Science*, **1993**. 260: p. 1446-1451.
24. von Helden, G., Hsu, M.T., Gotts, N., and Bowers, M.T., *J. Phys. Chem.*, **1993**. 97: p. 8182-8192.
25. von Helden, G., Wytttenbach, T., and Bowers, M.T., *Int. J. Mass Spectrom. Ion Processes*, **1995**. 146-147: p. 349-364.
26. Wytttenbach, T., von Helden, G., and Bowers, M.T., *J. Am. Chem. Soc.*, **1996**. 118: p. 8355-8364.
27. Clemmer, D.E., Hudgins, R.R., and Jarrold, M.F., *J. Am. Chem. Soc.*, **1995**. 117: p. 10141-10142.
28. Shelimov, K.B., Clemmer, D.E., Hudgins, R.R., and Jarrold, M.F., *J. Am. Chem. Soc.*, **1997**. 119: p. 2240-2248.
29. Hudgins, R.R. and Jarrold, M.F., *J. Am. Chem. Soc.*, **1999**. 121: p. 3494-3501.
30. Kaleta, D.T. and Jarrold, M.F., *J. Am. Chem. Soc.*, **2003**. 125: p. 7186-7187.
31. Kohtani, M., Jones, T.C., Schneider, J.E., and Jarrold, M.F., *J. Am. Chem. Soc.*, **2004**. 126: p. 7420-7421.
32. Purves, R.W., Guevremont, R., Day, S., Pipich, C.W., and Matyjaszczyk, M.S., *Review of Scientific Instruments*, **1998**. 69: p. 4094-4105.
33. Purves, R.W., Barnett, D.A., and Guevremont, R., *International Journal of Mass Spectrometry*, **2000**. 197: p. 163-177.
34. Purves, R.W., Barnett, D.A., Ells, B., and Guevremont, R., *Rapid Communications in Mass Spectrometry*, **2001**. 15: p. 1453-1456.
35. Guevremont, R., *Journal of Chromatography A*, **2004**. 1058: p. 3-19.
36. Shvartsburg, A.A., Li, F., Tang, K., and Smith, R.D., *Anal. Chem.*, **2006**. 78: p. 3706-3714.
37. Price, W.D., Schnier, P.D., and Williams, E.R., *Anal. Chem.*, **1996**. 68: p. 859-866.
38. Schnier, P.D., Price, W.D., Jockusch, R.A., and Williams, E.R., *J. Am. Chem. Soc.*, **1996**. 118: p. 7178-7189.
39. Gross, D.S., Zhao, Y.X., and Williams, E.R., *J. Am. Soc. Mass Spectrom.*, **1997**. 8: p. 519-524.
40. Price, W.D. and Williams, E.R., *J. Phys. Chem. A*, **1997**. 101: p. 8844-8852.
41. Schnier, P.D., Price, W.D., Strittmatter, E.F., and Williams, E.R., *J. Am. Soc. Mass Spectrom.*, **1997**. 8: p. 771-780.
42. Strittmatter, E.F., Schnier, P.D., Klassen, J.S., and Williams, E.R., *J. Am. Soc. Mass Spectrom.*, **1999**. 10: p. 1095-1104.
43. Caminati, W., *Phys. Chem. Chem. Phys.*, **2004**. 6: p. 2806-2809.
44. Felker, P.M., *J. Phys. Chem.*, **1992**. 96: p. 7844-7857.
45. Connell, L.L., Corcoran, T.C., Joireman, P.W., and Felker, P.M., *J. Phys. Chem.*, **2002**. 94: p. 1229-1232.
46. Pratt, D.W., *Annual Review of Physical Chemistry*, **1998**. 49: p. 481-530.
47. Nguyen, T.V., Korter, T.M., and Pratt, D.W., *Mol. Phys.*, **2005**. 103: p. 1603-1613.
48. Nguyen, T.V., Korter, T.M., and Pratt, D.W., *Mol. Phys.*, **2005**. 103: p. 2453-2453.
49. Nguyen, T.V. and Pratt, D.W., *J. Chem. Phys.*, **2006**. 124: p.
50. Philips, L.A. and Levy, D.H., *J. Chem. Phys.*, **1986**. 85: p. 1327-1332.
51. Philips, L.A. and Levy, D.H., *J. Chem. Phys.*, **1988**. 89: p. 85-90.
52. Wu, Y.R. and Levy, D.H., *J. Chem. Phys.*, **1989**. 91: p. 5278-5284.

53. Dickinson, J.A., Joireman, P.W., Randall, R.W., Robertson, E.G., and Simons, J.P., *J. Phys. Chem. A*, **1997**. 101: p. 513-521.
54. Lee, Y., Jung, J., Kim, B., Butz, P., Snoek, L.C., Kroemer, R.T., and Simons, J.P., *J. Phys. Chem. A*, **2003**. 108: p. 69-73.
55. Rizzo, T.R., Park, Y.D., Petenau, L.A., and Levy, D.H., *J. Chem. Phys.*, **1985**. 83: p. 4819-4820.
56. Rizzo, T.R., Park, Y.D., Peteanu, L.A., and Levy, D.H., *J. Chem. Phys.*, **1986**. 84: p. 2534-2541.
57. Rizzo, T.R., Park, Y.D., and Levy, D.H., *J. Chem. Phys.*, **1986**. 85: p. 6945-6951.
58. Park, Y.D., Rizzo, T.R., Petenau, L.A., and Levy, D.H., *J. Chem. Phys.*, **1986**. 84: p. 6539-6549.
59. Martinez, S.J., Alfano, J.C., and Levy, D.H., *J. Mol. Spectroscop.*, **1992**. 156: p. 421-430.
60. Page, R.H., Shen, Y.R., and Lee, Y.T., *J. Chem. Phys.*, **1988**. 88: p. 4621-4636.
61. Page, R.H., Shen, Y.R., and Lee, Y.T., *J. Chem. Phys.*, **1988**. 88: p. 5362-5376.
62. Cable, J.R., Tubergen, M.J., and Levy, D.H., *J. Am. Chem. Soc.*, **1988**. 110: p. 7349-7355.
63. Snoeck, L.C., Robertson, E.G., Kroemer, R.T., and Simons, J.P., *Chem. Phys. Lett.*, **2000**. 321: p. 49-56.
64. Carney, J.R. and Zwier, T.S., *J. Phys. Chem. A*, **2000**. 104: p. 8677-8688.
65. Snoeck, L.C., Kroemer, R.T., Hockridge, M.R., and Simons, J.P., *Phys. Chem. Chem. Phys.*, **2001**. 3: p. 1819-1826.
66. Lipert, R.J. and Colson, S.D., *J. Phys. Chem.*, **2002**. 93: p. 3894-3896.
67. Dian, B.C., Longarte, A., Mercier, S., Evans, D.A., Wales, D.J., and Zwier, T.S., *Journal of Chemical Physics*, **2002**. 117: p. 10688-10702.
68. Hunig, I., Seefeld, K.A., and Kleinermanns, K., *Chem. Phys. Lett.*, **2003**. 369: p. 173-179.
69. Bakker, J.M., Aleese, L.M., Meijer, G., and von Helden, G., *Phys. Rev. Lett.*, **2003**. 91: p. 203003.
70. Hunig, I. and Kleinermanns, K., *Phys. Chem. Chem. Phys.*, **2004**. 6: p. 2650-2658.
71. Callahan, M.P., Crews, B., Abo-Riziq, A., Grace, L., de Vries, M.S., Gengeliczki, Z., Holmes, T.M., and Hill, G.A., *Phys. Chem. Chem. Phys.*, **2007**. 9: p. 4587-4591.
72. Chin, W., PiuZZi, F., and Dognon, J.-P., *J. Am. Chem. Soc.*, **2005**. 127: p. 11900-11901.
73. Chin, W., Dognon, J.-P., Canuel, C., PiuZZi, F., Dimicoli, I., Mons, M., Compagnon, I., von Helden, G., and Meijer, G., *J. Chem. Phys.*, **2005**. 122: p. 054317-.
74. Chin, W., Mons, M., Dognon, J.P., Mirasol, R., Chass, G., Dimicoli, I., PiuZZi, F., Butz, P., Tardivel, B., Compagnon, I., vonHelden, G., and Meijer, G., *J. Phys. Chem. A*, **2005**. 109: p. 5281-5288.
75. Fricke, H., Gerlach, A., Unterberg, C., Rzepecki, P., Schrader, T., and Gerhards, M., *Phys. Chem. Chem. Phys.*, **2004**. 6: p. 4636-4641.
76. Gerhards, M., Unterberg, C., and Gerlach, A., *Phys. Chem. Chem. Phys.*, **2002**. 4: p. 5563-5565.
77. Gerhards, M., C. Unterberg, *Phys. Chem. Chem. Phys.*, **2002**. 4: p. 1760-1765.
78. Gerhards, M., Unterberg, C., Gerlach, A., and Jansen, A., *Phys. Chem. Chem. Phys.*, **2004**. 6: p. 2682-2690.
79. Bakker, J.M., Plützer, C., Hünig, I., Häber, T., Compagnon, I., von Helden, G., Meijer, G., and Kleinermanns, K., *Chemphyschem*, **2005**. 6: p. 120-128.

80. Abo-Riziq, A., Crews, B.O., Callahan, M.P., Grace, L., and de Vries, M.S., *Angew. Chem. Int. Ed.*, **2006**. 45: p. 5166-5169.
81. Nir, E., Janzen, C., Imhof, P., Kleinermanns, K., and De Vries, M.S., *Phys. Chem. Chem. Phys.*, **2002**. 4: p. 740-750.
82. Abo-Riziq, A., Grace, L., Nir, E., Kabelac, M., Hobza, P., and de Vries, M.S., *Proc. Natl. Acad. Sci. U. S. A.*, **2005**. 102: p. 20-23.
83. Crews, B., Abo-Riziq, A., Grace, L., Callahan, M., Kabelac, M., Hobza, P., and de Vries, M.S., *Phys. Chem. Chem. Phys.*, **2005**. 7: p. 3015-3020.
84. Unterberg, C., Jansen, A., and Gerhards, M., *J. Chem. Phys.*, **2000**. 113: p. 7945-7954.
85. Robertson, E.G. and Simons, J.P., *Phys. Chem. Chem. Phys.*, **2001**. 3: p. 1-18.
86. Zwier, T.S., *J. Phys. Chem. A*, **2001**. 105: p. 8827-8839.
87. Carcabal, P., Kroemer, R.T., Snoek, L.C., Simons, J.P., Bakker, J.M., Compagnon, I., Meijer, G., and von Helden, G., *Phys. Chem. Chem. Phys.*, **2004**. 6: p. 4546-4552.
88. Carcabal, P., Jockusch, R.A., Hunig, I., Snoek, L.C., Kroemer, R.T., Davis, B.G., Gamblin, D.P., Compagnon, I., Oomens, J., and Simons, J.P., *J. Am. Chem. Soc.*, **2005**. 127: p. 11414-11425.
89. Dian, B.C., Clarkson, J.R., and Zwier, T.S., *Science*, **2004**. 303: p. 1169-1173.
90. Clarkson, J.R., Dian, B.C., Moriggi, L., DeFusco, A., McCarthy, V., Jordan, K.D., and Zwier, T.S., *J. Chem. Phys.*, **2005**. 122: p. 214311.
91. Clarkson, J.R., Baquero, E., and Zwier, T.S., *J. Chem. Phys.*, **2005**. 122: p. 214312.
92. Zwier, T.S., *J. Phys. Chem. A*, **2006**. 110: p. 4133-4150.
93. Shubert, V.A. and Zwier, T.S., *J. Phys. Chem. A*, **2007**. 111: p. 13283-13286.
94. Nielsen, S.B., Lapierre, A., Andersen, J.U., Pedersen, U.V., Tomita, S., and Andersen, L.H., *Physical Review Letters*, **2001**. 87: p.
95. Andersen, L.H., Lapierre, A., Nielsen, S.B., Nielsen, I.B., Pedersen, S.U., Pedersen, U.V., and Tomita, S., *European Physical Journal D*, **2002**. 20: p. 597-600.
96. Oh, H., Breuker, K., Sze, S.K., Ge, Y., Carpenter, B.K., and McLafferty, F.W., *Proc. Natl. Acad. Sci. U. S. A.*, **2002**. 99: p. 15863-15868.
97. Nolting, D., Marian, C., and Weinkauff, R., *Phys. Chem. Chem. Phys.*, **2004**. 6: p. 2633-2640.
98. Talbot, F.O., Tabarin, T., Antoine, R., Broyer, M., and Dugourd, P., *J. Chem. Phys.*, **2005**. 122: p. 074310.
99. Danell, A.S. and Parks, J.H., *Int. J. Mass Spectrom.*, **2003**. 229: p. 35-45.
100. Nielsen, S.B., Andersen, J.U., Forster, J.S., Hvelplund, P., Liu, B., Pedersen, U.V., and Tomita, S., *Phys. Rev. Lett.*, **2003**. 91: p.
101. Worm, E.S., Andersen, I.H., Andersen, J.U., Holm, A.I.S., Hvelplund, P., Kadhane, U., Nielsen, S.B., Pouilly, J.C., and Stochkel, K., *Phys. Rev. A*, **2007**. 75: p.
102. Kang, H., Dedonder-Lardeux, C., Jouvét, C., Martrenchard, S., Gregoire, G., Desfrancois, C., Schermann, J.P., Barat, M., and Fayeton, J.A., *Phys. Chem. Chem. Phys.*, **2004**. 6: p. 2628-2632.
103. Kang, H., Jouvét, C., Dedonder-Lardeux, C., Martrenchard, S., Grègoire, G., Desfrancoise, C., Schermann, J.P., Barat, M., and Fayeton, J.A., *Phys. Chem. Chem. Phys.*, **2005**. 7: p. 394-398.
104. Kang, H., Jouvét, C., Dedonder-Lardeux, C., Martrenchard, S., Charrière, C., Grègoire, G., Desfrancoise, C., Schermann, J.P., Barat, M., and Fayeton, J.A., *J. Chem. Phys.*, **2005**. 122: p. 084307.

105. Kang, H., Dedonder-Lardeux, C., Jouvét, C., Gregoire, G., Desfrancois, C., Schermann, J.P., Barat, M., and Fayeton, A., *J. Phys. Chem. A*, **2005**. 109: p. 2417-2420.
106. Gregoire, G., Kang, H., Dedonder-Lardeux, C., Jouvét, C., Desfrancois, C., Onidas, D., Lepere, V., and Fayeton, J.A., *Phys. Chem. Chem. Phys.*, **2006**. 8: p. 122-128.
107. Gregoire, G., Jouvét, C., Dedonder, C., and Sobolewski, A.L., *J. Am. Chem. Soc.*, **2007**. 129: p. 6223-6231.
108. Gregoire, G., Dedonder-Lardeux, C., Jouvét, C., Desfrancois, C., and Fayeton, J.A., *Phys. Chem. Chem. Phys.*, **2007**. 9: p. 78-82.
109. Lepere, V., Lucas, B., Barat, M., Fayeton, J.A., Picard, V.J., Jouvét, C., Carcabal, P., Nielsen, I., Dedonder-Lardeux, C., Gregoire, G., and Fujii, A., *J. Chem. Phys.*, **2007**. 127: p. 134313.
110. Lucas, B., Barat, M., Fayeton, J.A., Perot, M., Jouvét, C., Gregoire, G., and Nielsen, S.B., *J. Chem. Phys.*, **2008**. 128: p. 7.
111. Lucas, B., Barat, M., Fayeton, J.A., Jouvét, C., Carcabal, P., and Gregoire, G., *Chem. Phys. Lett.*, **2008**. 347: p. 324-330.
112. Oh, H.B., Lin, C., Hwang, H.Y., Zhai, H.L., Breuker, K., Zabrouskov, V., Carpenter, B.K., and McLafferty, F.W., *J. Am. Chem. Soc.*, **2005**. 127: p. 4076-4083.
113. Oomens, J., Polfer, N., Moore, D.T., van der Meer, L., Marshall, A.G., Eyler, J.R., Meijere, G., and von Helden, G., *Phys. Chem. Chem. Phys.*, **2005**. 7: p. 1345-1348.
114. Lucas, B., Gregoire, G., Lemaire, J., Maitre, P., Ortega, J.M., Rupenyán, A., Reimann, B., Schermann, J.P., and Desfrancois, C., *Phys. Chem. Chem. Phys.*, **2004**. 6: p. 2659-2663.
115. Lucas, B., Gregoire, G., Lemaire, J., Maitre, P., Glotin, F., Schermann, J.P., and Desfrancois, C., *Int. J. Mass Spectrom.*, **2005**. 243: p. 105-113.
116. Polfer, N.C., Paizs, B., Snoeck, L.C., Compagnon, I., Suhai, S., Meijer, G., von Helden, G., and Oomens, J., *J. Am. Chem. Soc.*, **2005**. 127: p. 8571-8579.
117. Macleod, N.A. and Simons, J.P., *Mol. Phys.*, **2006**. 104: p. 3317-3328.
118. Polfer, N.C., Oomens, J., and Dunbar, R.C., *Phys. Chem. Chem. Phys.*, **2006**. 8: p. 2744-2751.
119. Macleod, N.A. and Simons, J.P., *Mol. Phys.*, **2007**. 105: p. I-+.
120. Vaden, T.D., de Boer, T., MacLeod, N.A., Marzluff, E.M., Simons, J.P., and Snoek, L.C., *Phys. Chem. Chem. Phys.*, **2007**. 9: p. 2549-2555.
121. Polfer, N.C., Oomens, J., Suhai, S., and Paizs, B., *J. Am. Chem. Soc.*, **2007**. 129: p. 5887-5897.
122. Gregoire, G., Gaigeot, M.P., Marinica, D.C., Lemaire, J., Schermann, J.P., and Desfrancois, C., *Phys. Chem. Chem. Phys.*, **2007**. 9: p. 3082-3097.
123. Vaden, T.D., de Boer, T.S.J.A., Simons, J.P., Snoek, L.C., Suhai, S.n., and Paizs, B.l., *J. Phys. Chem. A*, **2008**. 112: p. 4608-4616.
124. Robertson, W.H., Kelley, J.A., and Johnson, M.A., *Rev. Sci. Instrum.*, **2000**. 71: p. 4431-4434.
125. Diken, E.G., Hammer, N.I., and Johnson, M.A., *J. Chem. Phys.*, **2004**. 120: p. 9899-9902.
126. Douberly, G.E., Ricks, A.M., Ticknor, B.W., and Duncan, M.A., *J. Phys. Chem. A*, **2008**. 112: p. 950-959.
127. Douberly, G.E., Ricks, A.M., Ticknor, B.W., McKee, W.C., Schleyer, P.v.R., and Duncan, M.A., *J. Phys. Chem. A*, **2008**. 112: p. 1897-1906.
128. Gerlich, D., *J. Chem. Soc. Faraday Trans.*, **1993**. 89: p. 2199-2208.

- 129. Kamariotis, A., Boyarkin, O.V., Mercier, S.R., Beck, R.D., Bush, M.F., Williams, E.R., and Rizzo, T.R., *J. Am. Chem. Soc.*, **2006**. *128*: p. 905-916.
- 130. Boyarkin, O.V., Mercier, S.R., Kamariotis, A., and Rizzo, T.R., *J. Am. Chem. Soc.*, **2006**. *128*: p. 2816.
- 131. Mercier, S., *Electronic and Vibrational Spectroscopy of cold protonated amino acids in the gas phase*, in *PhD Thesis, EPFL, Lausanne*. 2008.
- 132. Stearns, J.A., Mercier, S., Seaiby, C., Guidi, M., Boyarkin, O.V., and Rizzo, T.R., *J. Am. Chem. Soc.*, **2007**. *129*: p. 11814-11820.
- 133. Settle, R.D.F. and Rizzo, T.R., *J. Chem. Phys.*, **1992**. *97*: p. 2823-2825.
- 134. Lubich, L., Boyarkin, O.V., Settle, R.D.S., Perry, D.S., and Rizzo, T.R., *Faraday Discuss.*, **1995**. *102*: p. 167-178.
- 135. Boyarkin, O.V. and Rizzo, T.R., *J. Chem. Phys.*, **1996**. *105*: p. 6285-6292.
- 136. Boyarkin, O.V., Lubich, L., Settle, R.D.S., Perry, D.S., and Rizzo, T.R., *J. Chem. Phys.*, **1997**. *107*: p. 8409-8422.
- 137. Boyarkin, O.V., Rizzo, T.R., and Perry, D.S., *J. Chem. Phys.*, **1999**. *110*: p. 11346-11358.

Chapter 2

Experimental setup

This chapter illustrates the home-built tandem mass spectrometer employed to carry out the experiments presented in this thesis. It first explains the basic concepts of the techniques used to produce, select and trap the ions, followed by a detailed description of the machine. Finally, it discusses the UV and IR laser setups used for photodissociation spectroscopy of the cold trapped ions and the CO₂ laser needed for the IRLAPS experiment.

2.1 The home-built tandem mass spectrometer

The scheme in Figure 2.1 gives an overview of the techniques combined together in the home-built mass spectrometer, whose basic principles will be explained in the following paragraphs. It also shows the steps the ions go through along their path in the machine during a typical experiment.

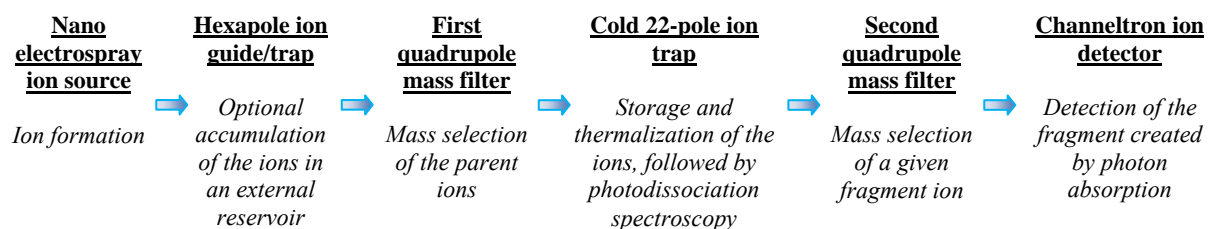


Figure 2.1: Schematic of the techniques combined together in the experiment

2.1.1 Electrospray ionization

The first description of the electrospray phenomenon was made by Zeleny at the beginning of the 20th century [1, 2], but it was only at the end of 1960s that Dole used this conception to generate beams of macroions *in vacuo* [3]. However, it was in the mid 1980s that Fenn and coworkers implemented successfully this ionization method for mass spectrometry [4-6]. Since then, the electrospray ionization has emerged as a powerful technique for producing intact ions *in vacuo* directly from solution (cf. for example [7-20] and references contained therein). J. B. Fenn was rewarded with part of the 2002 Nobel Prize in Chemistry for this development. Figure 2.2 illustrates the electrospray mechanism in the positive ion mode configuration.

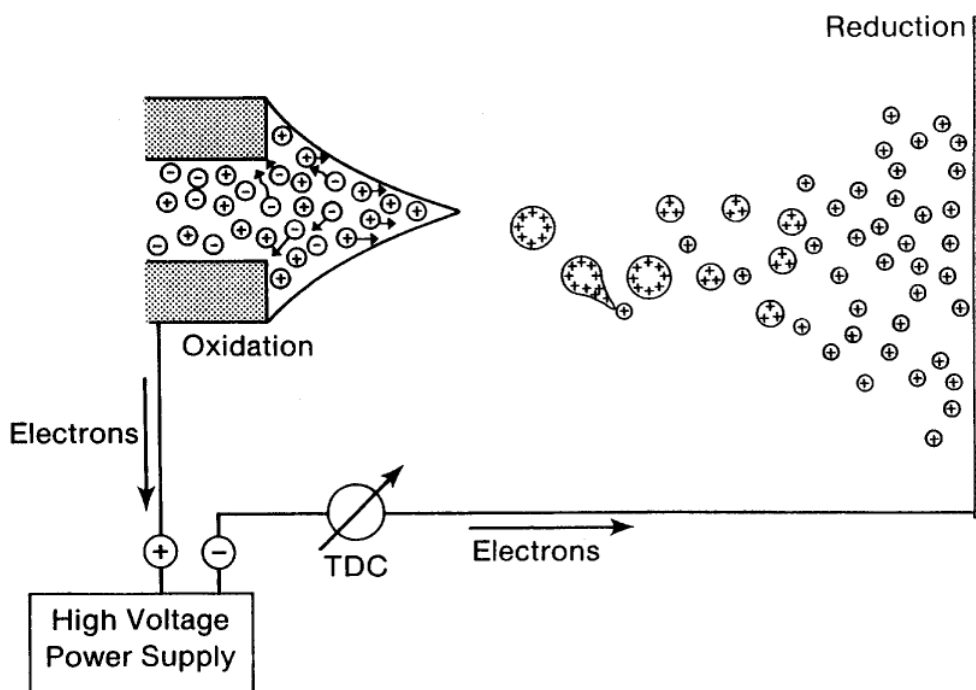


Figure 2.2: Droplets formation in the atmospheric part of an electrospray source. (Adapted from Kebarle and Tang [21])

The sample solution enters in the atmospheric part of the electrospray chamber flowing through a conductive fine capillary (or needle) at sufficiently low flow rates. A high voltage difference applied between the needle and a counter electrode causes a separation of the charges in the liquid and an accumulation of positive ions at the tip of the needle itself [21]. When the charge repulsion overcomes the surface tension, the liquid expands, forming a Taylor cone [22]. Its apex is the least stable point of the cone and it elongates into a filament, which then breaks producing charged droplets. Under the influence of the electric field, the

micro-droplet spray travels towards the counter-electrode in the atmosphere. Collisions with the surrounding gas lead to solvent evaporation in the droplets, which shrink in size, increasing their charge density until the Raylight limit is reached [23]. At this point, the coulombic repulsion between the charges overcomes the cohesive force of the surface tension, leading to Coulomb fissions of the parent droplets into highly charged daughter ions. The iteration of this evaporation/fission process produces droplets with radii in the nanometer range that have only a few elementary charges. There is still debate on the exact mechanism by which a single analyte molecule is finally formed during the electrospray process [24-26]. In the *charge residue model*, it is obtained by a complete solvent evaporation on the smallest droplet emitted by fission [3, 27]. The *ion evaporation model* proposes direct emission of the ions from a droplet surface, when their radius is in the order of 10-20 nm [28, 29]. Although the mechanism of the ion formation is not fully understood, evidence was shown that both of the models mentioned above are valid and one may prevail on the other, depending on the size of the droplet [30, 31].

The liquid sample flows through an electrospray needle with an inner diameter of $\sim 100 \mu\text{m}$ at a flow rate of $1\text{-}2 \mu\text{l min}^{-1}$, producing droplets with an initial diameter of more than $1 \mu\text{m}$. The onset potential $V_{\text{on}}(\text{kV})$ to initiate a stable spray is given by Eq. 2.1 [32], where r (μm) is the inner diameter of the needle, $\gamma(\text{Nm}^{-1})$ is the solvent surface tension and d (mm) is the distance between the needle tip and the counter electrode:

$$V_{\text{on}} \approx 0.2\sqrt{r\gamma} \ln\left(\frac{4000d}{r}\right) \quad \text{Eq. 2.1}$$

This equation suggests that pure water cannot be used as sample solvent for an electrospray source because of its high surface tension. Indeed, the electric field on the needle tip would be higher than the one required to cause electron corona discharge prior to the liquid disruption. This problem has been solved using mixtures of water and other organic liquids, whose surface tension is smaller than that of pure water.

In our apparatus we use a commercial nano-electrospray (a.k.a., nanospray) source, the development of which started in the mid 1990s [33, 34]. The principles of spray formation are the same for both nanospray and electrospray, the difference being in the smaller inner diameter of the spraying orifice for the former ($\sim 1\text{-}2 \mu\text{m}$ instead of $\sim 100 \mu\text{m}$). This leads to

formation of droplets of ~ 200 nm diameter at a reduced flow rates, ~ 1 nL min⁻¹ to 1 μ L min⁻¹. The nanospray setup allows one to reduce the onset potential applied between the needle tip and the capillary and to use solvent which possesses a much higher surface tension than in the normal electrospray configuration (i.e. pure water).

The source used in our apparatus is depicted schematically in Figure 2.3.

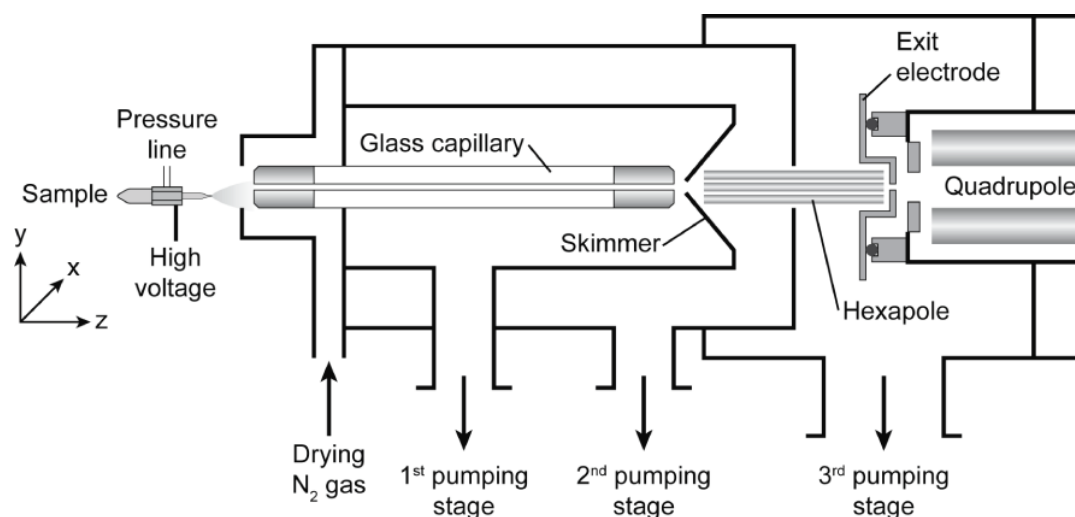


Figure 2.3: Schematic of the source used in our apparatus.

A Au/Pd coated borosilicate capillary, which serves as the nanospray needle, is filled with the sample solution and immersed in a 1.5 mL Eppendorf reservoir containing additional solution. The typical concentration of the sample is $2 \cdot 10^{-4}$ M in a 1:1 methanol/water mixture with 0.2% acetic acid added. The airtight assembly is mounted on an electrically insulated xyz-manipulator, which is needed for precise adjustment of the spray needle tip relative to the glass capillary inlet, and connected to a high-voltage power supply. The spray is initiated by submitting the solution to a gentle pressure, and once a small droplet is formed at the capillary tip, the needle is floated ~ 500 V to 1 kV above ground potential (in the positive ion mode). The charged spray droplets travel at atmospheric pressure towards the Ni-coated entrance end of a glass capillary, which is grounded and acts as the counter electrode. A counter-current flow of nitrogen gas can be used to assist desolvation of the droplets. The electrosprayed ions enter the glass capillary and are carried by the bath gas into the first vacuum stage.

A supersonic expansion takes place at the exit of the capillary, although the voltages applied between the exit of the capillary and the skimmer accelerates the ions and warms

them slightly, which helps prevent condensation of the ions with solvent molecules in the carrier gas and complete the desolvation process without disruption of the covalent bonds. Only the central core of the free jet expansion passes through the skimmer orifice towards the hexapole, which traverses two pumping stages significantly different in pressure. Therefore, the ions travel from the high-pressure side to the low-pressure side of the hexapole, passing from a region where they still undergo collisions with the background gas, to a region of molecular flow, where the mean free path is much larger than the instrument dimensions. The kinetic energy of the ions is then defined by the floating voltage of the hexapole rods (pole bias).

The hexapole is run in an RF-only mode, and as will be extensively discussed in *Section 2.1.3*, it can be used as an ion guide or trap. As a guide it serves to transfer the electrosprayed ions to the first quadrupole mass filter. Moreover, the ions can be trapped axially in the hexapole for a certain amount of time, applying proper voltages to the skimmer (which acts as the entrance electrode) and exit electrode. In doing so, the continuous ion signal from the nanospray source is turned in a packet of ions, which better matches the duty cycle of our pulsed laser experiment. In addition, when collected inside the trap, the ions are thermalized by collisional cooling. This implies a reduction in the spread of ion kinetic energy, with a consequent improvement of the transmission efficiency of the ions through the tandem mass spectrometer. However, excessively long accumulation time in the hexapole may lead to a significant degree of fragmentation when the space charge limit is reached [35-37]. This is especially critical when the studied species are weakly bound (i.e. solvated ions).

2.1.2 Quadrupole mass filtering

The principles of quadrupole mass spectrometry were introduced by Paul and Steinwedel at the beginning of 1950s [38], followed shortly after by the development of the first quadrupole ion trap from the same group [39]. Since then, many papers, as well as several reviews and text books, have been devoted to the characterization of this device, including computer simulations on the field geometry and ion motion inside quadrupole mass spectrometers [40-46]. The aim of this section is to give some insight into the fundamental principles underlying this technique.

An ideal quadrupole is formed by hyperbolic electrodes, aligned along the z -axis and equally spaced on an inscribed circle of radius r_0 (Figure 2.4).

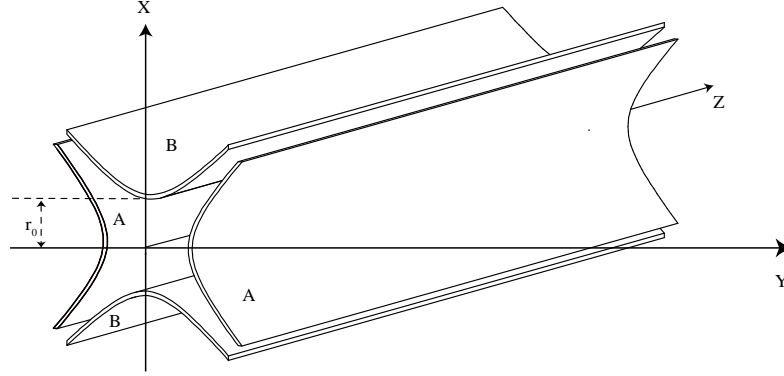


Figure 2.4: Ideal quadrupole mass filter with hyperbolic electrodes which serve to create a cylindrically symmetric field, being arranged at a distance r_0 from the z axis. (Adapted from March and Todd [46])

For mass analysis, both DC (U) and RF ($V \cos \Omega t$) voltages are applied to the electrodes with alternate polarity. Thus, the potential in the xy plane can be expressed by the following equation:

$$\phi = \phi_0 \left(\frac{x^2 - y^2}{r_0^2} \right) \quad \text{Eq. 2.2}$$

where

$$\phi_0 = U + V \cos \Omega t \quad \text{Eq. 2.3}$$

An ion entering the quadrupole mass filter along the z -axis experiences forces in the x and y directions perpendicular to the propagation direction. The ion motion is described mathematically by the exact solutions of a set of decoupled one dimensional differential equations, called Mathieu equations (cf. [42, 43, 47] for a detailed discussion). These solutions contain either a strictly growing exponential factor or an oscillatory term depending on the ion mass, leading to unstable or stable trajectories in the quadrupole. The latter are usually represented in a diagram (Figure 2.5) in which the stability regions are displayed as a function of the two Mathieu's dimensionless parameters, a and q , defined as:

$$a = \frac{8eU}{mr_0^2\Omega^2} \quad \text{and} \quad q = \frac{4eV}{mr_0^2\Omega^2} \quad \text{Eq. 2.4}$$

e being the elementary charge and m the mass of the given ion.

Under usual quadrupole operating conditions, the angular frequency Ω is fixed. Stable trajectories of ions of a chosen mass are, thus, obtained by a proper selection of U and V , respectively a and q in the stability region of the diagram of Figure 2.5. These charged molecules oscillate around the z -axis with finite amplitude and emerge from the end of the quadrupole mass filter. On the other hand, the motion of ions of higher or lower masses is unstable either in the x or y directions with their consequent ejection from the quadrupole.

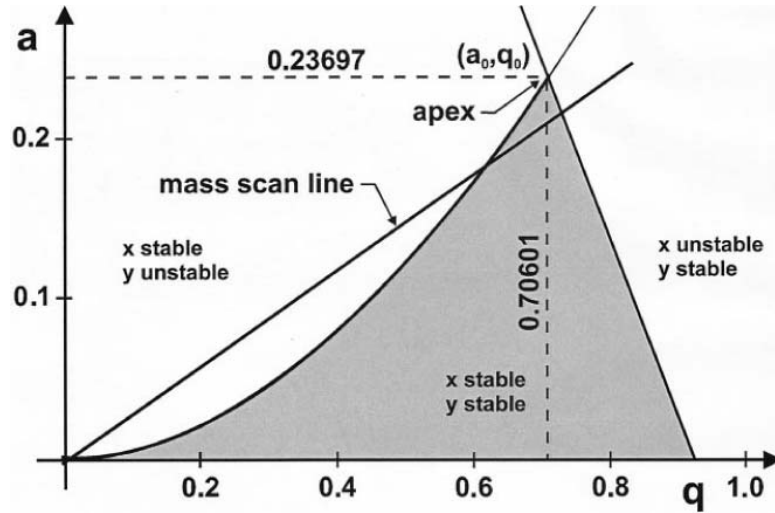


Figure 2.5: Stability diagram of a quadrupole mass filter. Figure from reference [45].

A mass spectrum is obtained by scanning simultaneously the amplitudes of U and V along a “mass scan line” of fixed ratio U/V equal to $a/2q$. The intersection of the mass scan line and the stability region defines the ions with stable trajectories in the quadrupole. Higher mass resolution is achieved when the slope of the mass scan line puts it closer to the apex of the stability island.

2.1.3 Linear multipoles ions traps and guides

The motion of a charged particle in a time- and space-varying electric field is described by non-linear, coupled differential equations, which cannot always be solved exactly. However, if the oscillation frequency of the field is high relative to the ion velocity, the equation of motion can be treated within the *adiabatic approximation*, which leads to the introduction of the so-called effective potential V^* [48]. The trajectory of a charged particle of mass m and charge q is then described as the superimposition of a rapidly oscillating motion with a smooth one. The latter can be derived from the effective potential, whose form

depends on the geometry of the electrode arrangement. An *adiabaticity parameter*, μ , is associated to a particular electrode configuration. According to the pioneering work of Teloy and Gerlich, the validity of the adiabatic approximation is guaranteed by a value of μ smaller than 0.3 [48, 49]. A slightly higher limit, ~ 0.36 , has been recently established by Wester and coworkers [50].

Linear multipoles consist of $2n$ cylindrical rods equally spaced on an inscribed circle of radius r_0 . An RF potential, $V_0 \cos \Omega t$, applied with opposite phase on alternate rods of a multipole generates an effective potential given by [49]:

$$V^* = \frac{1}{8} \frac{(qV_0)^2}{\varepsilon} \left(\frac{r}{r_0} \right)^{2n-2} \quad \text{Eq. 2.5}$$

associated to an adiabaticity parameter of the form:

$$\mu = \frac{n-1}{n} \frac{qV_0}{\varepsilon} \left(\frac{r}{r_0} \right)^{n-2} \quad \text{Eq. 2.6}$$

The *characteristic energy*, ε , which combines the mass of the ion with the frequency of the RF field and the inscribed radius of the multipole arrangement, is expressed as follows:

$$\varepsilon = \frac{1}{2n^2} m \Omega^2 r_0^2 \quad \text{Eq. 2.7}$$

Figure 2.6 displays the relative effective potential for a quadrupole, an octupole and a 22-pole as a function of the radial distance from the axis.

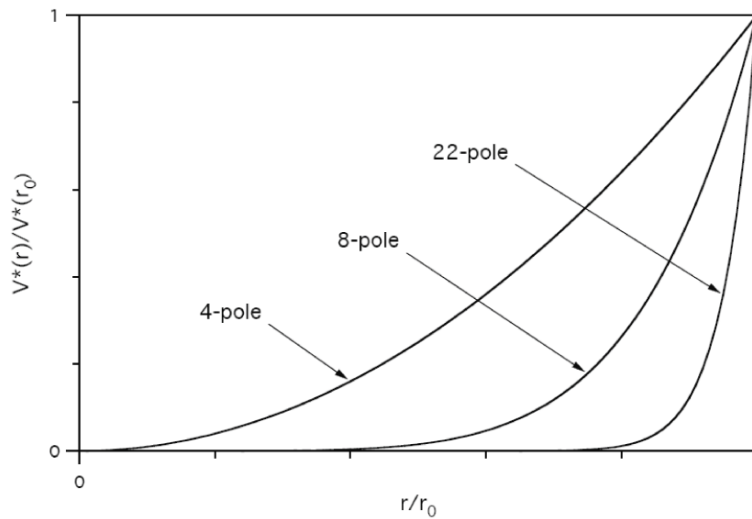


Figure 2.6: Relative effective potentials of a quadrupole, an octupole and a 22-pole.

As the number of poles increases, the repulsive wall becomes steeper and the field free region enlarges. The equipotential lines of the field for several multipoles are shown in Figure 2.7. The ions experience the field only in the vicinity of the rods and are thus confined in the radial direction of the device. The charged particles move undisturbed in the central part of the multipole, but once they approach the electrodes, they undergo an oscillatory micromotion at the characteristic frequency of the RF field [49, 51].

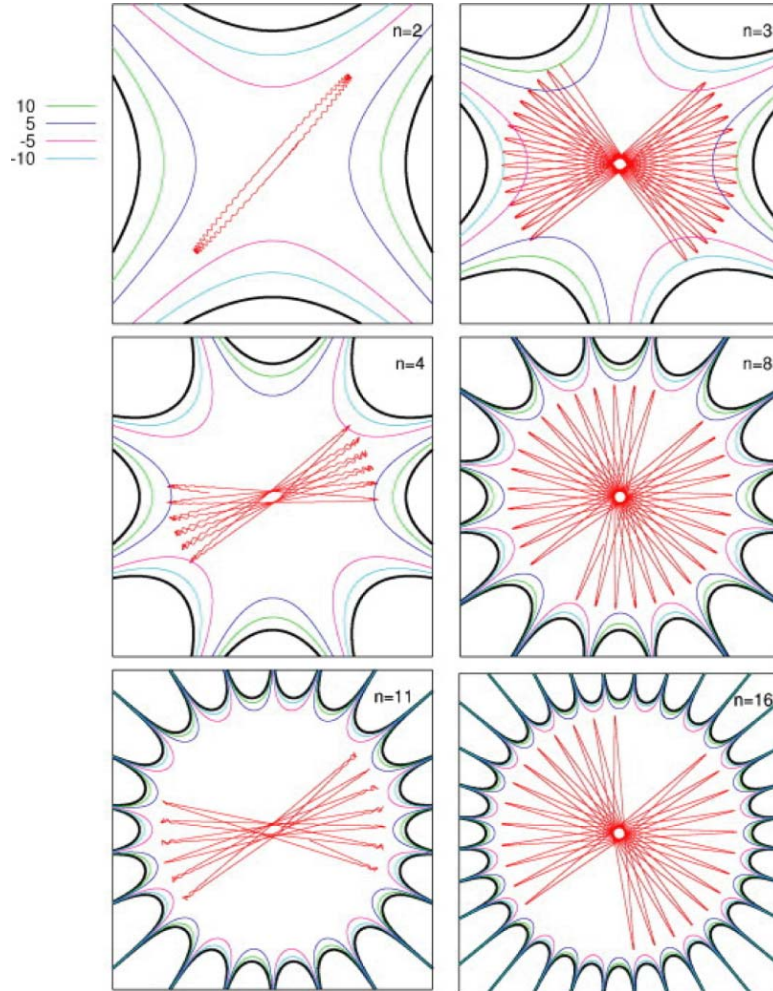


Figure 2.7: Visualization of RF fields generated by infinitely long multipoles for several values of n at a fixed time. The black lines represent the electrodes and the equipotential lines are colored coded. Some typical ion trajectories are included in each figure. (Taken from Asvany and Schlemmer [51])

Two cylindrical electrodes are usually placed on axis at the extremities of the multipole device. The confinement of the ions in the axial direction is achieved setting the voltages applied on these electrodes higher than the floating voltage of the rods (pole bias) and

avored by collisions with residual or buffer gas in the device. In this way, the latter serves as an ion trap. The ions are released from the trap by pulsing the voltage on the exit electrode to a level below the pole bias. The RF devices can also act as an ion guide, adjusting the end electrode voltages in such a way that the ions travel through the multipole.

In our apparatus we use RF-only multipoles in both configurations. As already mentioned in *Section 2.1.1*, the hexapole ion trap is an essential part of the electrospray source. In addition, we use an octupole to guide the ions through a differential pumping stage into a 22-pole ion trap. The latter is the central part of our apparatus, since it is where the ions are cooled to low temperature and interact with the laser light. The following paragraph gives a detailed description of the 22-pole ion trap.

The 22-pole ion trap

At the beginning of 1990s Gerlich and Horning introduced radiofrequency devices to study the chemistry of ion-molecule reactions that occur in the low density and low temperature environment found in interstellar clouds [52, 53]. They used both a ring electrode trap and a 22-pole ion trap because they can store charged molecules and allow long reaction times. Moreover, these devices allow efficient buffer-gas cooling of the ions. We focus here on a 22-pole ion trap.

As previously discussed, a 22-pole ion trap generates a potential with a wide field free region and steep wall close to the electrodes. Whenever the adiabaticity condition is fulfilled, the total energy of the ions is conserved on average, meaning the ions are not heated by the RF field. A buffer-gas can be introduced to increase the trapping efficiency and to thermalize the ions. Once entering the trap, charged particles can lose their kinetic energy by collisions with the buffer-gas, which allows them to be trapped more efficiently in the axial direction. Obviously, the collisions occur both in the field free region and during the reflection from the electrodes. This implies the thermalization of the charged molecules at the temperature of the ambient gas takes place in the central part of the trap, while in the vicinity of the electrodes the ions can be heated up. In the case of an ion trap with a wide field free region such as a 22-pole, measurements and numerical simulations have demonstrated the latter effect is almost negligible [49, 51-54]. Figure 2.8 illustrates the velocity distribution of the ions stored

in traps of different multipolarity n , when the temperature of the helium buffer-gas is 18 K. As the number of poles increases, simulations show that the thermal distribution approaches the Boltzmann distribution at the neutral buffer-gas temperature [51]. In a 22-pole ion trap, the charged species are slightly warmer than the buffer-gas molecules.

The other benefit of using a 22-pole consists in the characteristic storage time of the cold ions in the device. Gerlich and coworkers reported values ranging from μs up to min with no loss of ions from the trap [49, 52, 55].

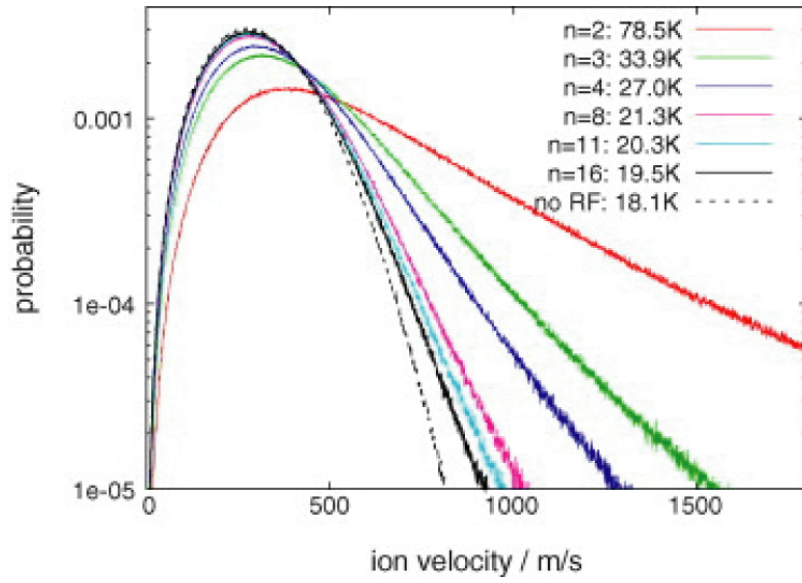


Figure 2.8: Velocity distribution of the ions stored in traps with different multipolarity n in the presence of helium buffer gas. The temperature of the latter is 18 K [51].

Particular attention must be devoted to the role of the end electrodes in a 22-pole ion trap since they generate a potential which has both longitudinal and radial components. The latter pushes the charged particles close to the rods of the trap where they can be heated by the RF field. Evidence of this phenomenon has been recently demonstrated by numerical simulations as well as in experiments [51, 56]. In particular, Wester and coworkers studied the photodetachment of OH^- molecules in a 22-pole ion trap. By performing transversal laser scans through the trap, they found a higher density of molecules toward the RF electrodes [56]. This effect becomes more pronounced as the voltages applied at the electrodes are increased [51].

The 22-pole trap we use in our apparatus has been designed and built by Dr. Oleg Boyarkin, based on the publications from the group of Dieter Gerlich [49, 52, 53]. Figure 2.9 illustrates the 22-pole trap mounted on the cold head as well as a picture of the trap uncovered.

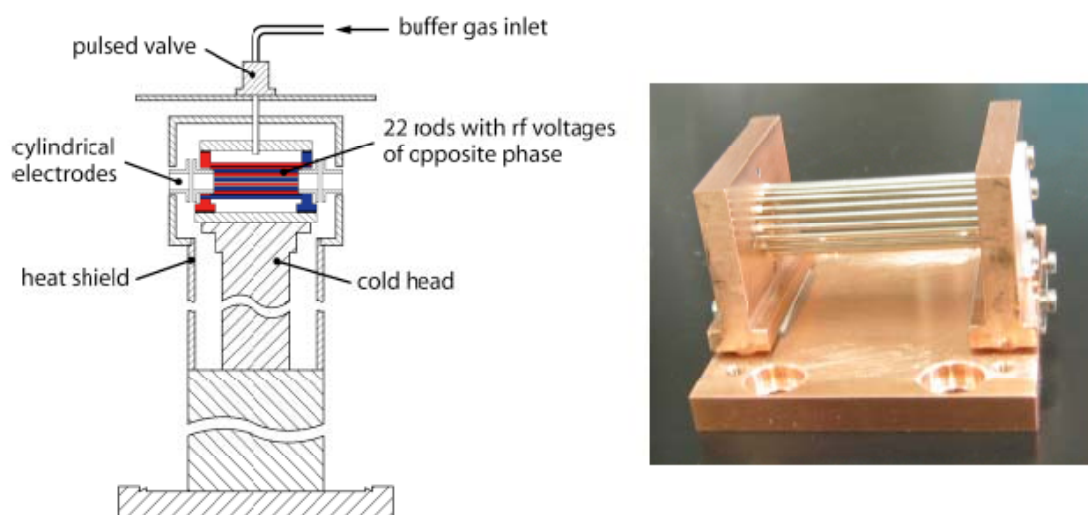


Figure 2.9: Schematic section view of the home-built 22-pole ion trap and cold head assembly, and picture of the 22 rods mounted onto their holders [57].

It consists of 22 stainless steel rods, 50 mm long and 1 mm in diameter, equally spaced on a 10 mm inscribed diameter. The rods are supported by two copper holders, each of them being electrically connected to a set of 11 alternate rods and insulated from the other 11. Equal RF voltage of opposite phase is applied to the holders, which are electrically insulated from the rest of the housing but in good thermal contact *via* a set of sapphire plates. Two sets of cylindrical electrodes (L_1 - L_4 along the ion path) are placed at the entrance and exit of the trap. These lenses are used to let the ions in, confine them and finally release them after the process we are interested in occurs. The voltage on each lens is controlled individually and the two closest to the trap can be pulsed for trapping purposes. The 22-pole trap is directly mounted on a cold head of a cryocooler, which can reach a nominal temperature of 6 K. Before the ions arrive, helium buffer-gas is injected in the trap through a pulsed valve. This ambient gas is thermalized at the cold head temperature by collisions with the wall surrounding the trap and serves as a heat exchanger between the ions and the trap.

Further details on the 22-pole trap assembly, as well as its characterization and operating conditions, have been described in the PhD thesis of Dr. Sebastien Mercier [57].

2.1.4 Machine overview

Figure 2.10 shows the schematic of our home-built mass spectrometer, displaying the seven differential pumping stages as well as the main ion optical systems needed to guide the ions through it.

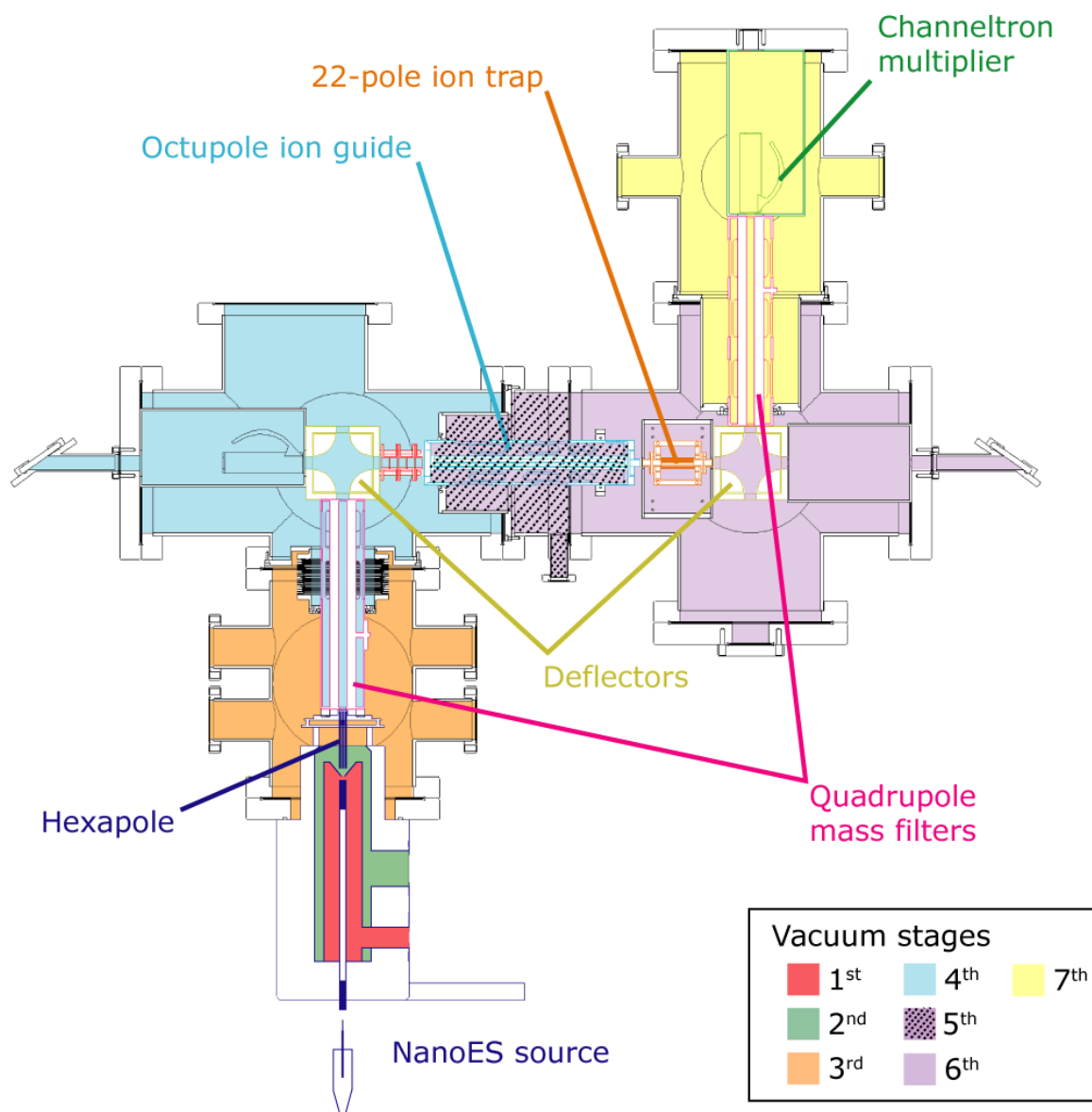


Figure 2.10: Section view of the tandem mass spectrometer

The ion source consists of a commercial electrospray ionization source, whose atmospheric part has been replaced by a nanospray source kit (cf. *Section 2.1.1*). The sample to investigate is put in solution and sprayed into atmospheric pressure from a metal-coated glass needle towards the entrance of a nickel-coated glass capillary. The ions are driven by

airflow to the end of the glass capillary and pass through a skimmer into a hexapole. An electrode, placed at the end of this device, can be submitted to a pulsed voltage, allowing one to trap and accumulate the ions in the hexapole and convert the continuous signal from the source into a dense ion packet.

The hexapole is followed by a first quadrupole mass filter (cf. *Section 2.1.2*) because, even if a single substance is put in solution, the electrospray produces a variety of species. Indeed if the solvent evaporation process is incomplete, water clusters of the starting species can be formed. The study of these complexes allows the analysis of the solvation process of a molecule. Moreover, if the molecule of interest is large enough, several different charge states may be present in the electrospray plume. This opens the possibility of examining the charge state dependence of conformation of a large molecule, for example.

The mass-selected ion packet can be deviated by 90° in either direction by a quadrupole deflector. There are several reasons for doing so. One is that the ions are separated from the beam of the neutral molecules, which will not experience the deflector field and fly directly towards the turbomolecular pump, which is positioned on the beam axis. Secondly, the charged molecules can be turned toward an intermediate ion detector, in order to optimize all the voltages of the first part of the machine for the best ion transmission. Finally, by turning the ion beam 90° before guiding it into the ion trap, one has a clear axis along with to send a laser beam for spectroscopic experiments.

When turned 90° toward the 22-pole ion trap, the ion beam is first decelerated by a stack of five cylindrical electrodes and then guided by an octupole guide into the trap. The 22-pole ion trap is mounted on the cold head of a closed-cycle helium refrigerator which can reach a temperature of 6 K. About 1ms prior to the arrival of the ion packet, the trap is filled by a pulse of helium gas provided by a pulsed valve. As already discussed in *Section 2.1.3*, the presence of the gas is twofold. First of all, the ions lose their kinetic energy by collisions with the helium buffer gas, so that they can be trapped axially in the electric potential well created by setting the pole bias voltage of the trap lower than those of its entrance and exit electrodes. Moreover, the gas serves as a heat exchanger between the ions and the surrounding walls of the trap, which are maintained at about 6 K. The pressure in the 22-pole ion trap, prior to the helium arrival, must be on the order of 10^{-8} mbar to prevent water or other species sticking on the rods during the cooling process.

While stored inside the trap, the parent ions interact with ultraviolet or infrared laser light. Photofragmentation will take place if the absorption of the photons promotes the internal energy of the molecule above the dissociation threshold. If fragmentation occurs inside the trap, both the parent and the daughter ions are stored for a certain amount of time and then released when the voltage on the exit electrode of the 22-pole is lowered. The exiting ion beam is turned 90° by a second deflector towards the last quadrupole mass filter. Several fragments can be produced upon photons absorption, and the quadrupole mass filter is used to select the ion with the m/z of interest, which is then guided into an ion detector. Transmitting the m/z of a chosen fragment, we can detect the amount of photodissociation of the parent ion into a specific fragment as a function of the laser wavelength. On alternate trapping cycle, the selection of the parent molecule in the second quadrupole allows one to account for the fluctuations of the source, since this signal can be used for normalization purposes.

The ion detectors consist of a conversion dynode and a channeltron multiplier. The former component is set at a high negative voltage (for positive ions), typically -5 kV, and emits electrons upon the impact of the accelerated ions. These electrons are collected by the channeltron multiplier, which further amplifies the electron current. The resulting signal is sent to a fast preamplifier and then to a gated pulse counter.

Further details on the home-built mass spectrometer, as well as the operating conditions and procedure to maximize the ion transmission through the entire machine, can be found in the PhD theses of Dr. Anthi Kamariotu [37] and Dr. Sébastien Mercier [57].

2.2 Description of the laser setup

2.2.1 Generation of UV laser light

The ultraviolet laser light is produced by frequency doubling of the visible output of a dye laser, pumped by a Nd:YAG laser, as schematically depicted in Figure 2.11.

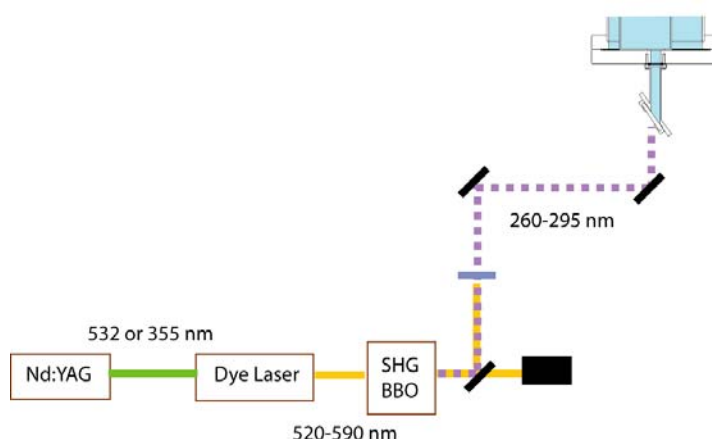


Figure 2.11: Schematic diagram of the UV generation.

The desired UV range can be covered using a variety of laser dyes. We have mainly used Exciton dyes Rhodamine 590 and 610 and Coumarin 540A and 503 (or 153 and 307 if bought from Radiant Dyes) in order to cover the visible range from 520 up to 590 nm. These laser dyes must be pumped by different frequencies, and we use either the first (532 nm) or the second (355 nm) harmonic of the 1064 fundamental from a Nd:YAG laser (Spectra Physics GCR-250). Typical pulse energies from the Nd:YAG laser, at repetition rates of 10 or 20 Hz, are on the order of 200 mJ and 150 mJ, respectively at 532 nm and 355 nm. The Nd:YAG laser power is adjusted to achieve a maximum pulse energy of 50 mJ out of the dye laser (Lumonics model HD-500). This limit is imposed by the damage threshold of the beta barium borate (BBO) crystal used to convert the visible output of the dye laser into the UV light by second harmonic generation (SHG). The crystal is mounted in an Autotraker III (Inrad, NJ, USA) and, together with a fused silica compensator, is rotated to the phase-matching angle as the visible wavelength is scanned.

The UV beam is separated from the remaining visible light *via* reflections on two dichroic mirrors and the use of a colored filter. The beam passes through a converging lens before it is deflected by a prism into the machine through a BaF₂ window placed at the Brewster angle. The UV pulse energy is 1-5 mJ, and the duration is 5-10 ns. The typical linewidth in the UV is $\sim 0.07 \text{ cm}^{-1}$.

2.2.2 Generation of IR laser light

The schematic diagram of the IR generation system is illustrated in Figure 2.12.

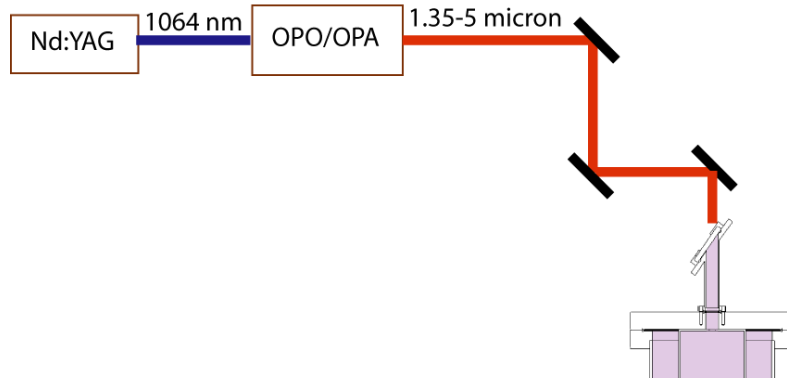


Figure 2.12: Schematic diagram of the IR generation.

The horizontally polarized 1064 fundamental harmonic of a Nd:YAG laser (Innolas Spitlight 600) pumps an Optical Parametric Oscillator/Optical Parametric Amplifier, (OPO/OPA system from LaserVision), a non linear device used to convert the fixed output of the pumping laser to a tunable mid-infrared laser light.

The Nd:YAG pulse length is 7 ns and the unseeded beam linewidth 0.5 cm^{-1} . The pulse energy at 5 or 10 Hz repetition rate is adjusted to $\sim 500 \text{ mJ}$ at maximum, to prevent damaging of the crystals in the OPO/OPA device, displayed in Figure 2.13.

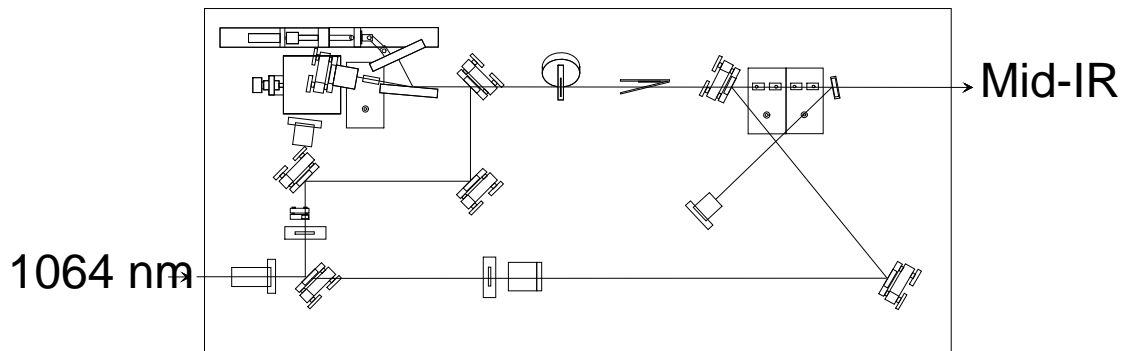


Figure 2.13: Layout of the OPO/OPA.

Inside the parametric converter, the 1064 nm light is split in two separate beams. The first one is frequency doubled in a Potassium Titanium Oxide Phosphate (KTP) crystal to provide the 532 nm light for the OPO stage, which makes use of a second KTP crystal. The output of this first stage consists of a horizontally polarized signal and a vertically polarized idler wave. In our parametric converter, the signal wave exits the housing while the idler passes through a quarter waveplate and is recombined with the remaining 1064 nm beam of

the Nd:YAG laser. The combined beams are then directed into the OPA stage for difference-frequency mixing. Four Potassium Titanyl Arsenate (KTA) crystals are employed in this second stage. Its output consists of a horizontally polarized signal (the idler of the OPO stage) and a vertically polarized idler, which is in the mid-infrared region between 1.35 and 5 μm . A Brewster plate polarizer isolates the idler from the combined output.

The mid-infrared beam enters the machine from the opposite side respect to the UV laser through a second BaF_2 window placed at Brewster angle. The incident beam must be horizontally polarized to reduce power loss when passing through the window. Thus, the polarization of the OPA idler output must be changed. This is achieved employing a periscope, where the lower mirror is turned 90° respects to the upper one. The horizontally polarized beam is then focused by means of a converging lens and sent in the machine by reflection off of a silver mirror mounted on a silicon substrate.

The pulse energy in the 3 μm region used in this thesis work ranges from 6 to 12 mJ and its linewidth is $\sim 1\text{ cm}^{-1}$, since we are pumping the OPO/OPA convertor with an unseeded beam from the Innolas Nd:YAG. The pulse duration, after frequency mixing, is $\sim 3\text{ ns}$.

2.2.3 TEA-CO₂ laser

A commercial TEA-CO₂ laser (Lumonics model 840/1) is used to produce light in the 10 μm region. This is a pulsed discharge pumped laser, whose laser medium consists of approximately 8% of CO₂, 8% of CO, 16% of N₂ and He for the remaining percentage. This laser is not continuously tunable and can operate only at the frequencies of the main rovibrational lines of the laser medium. The strongest CO₂ molecule vibrations are at 10.6 μm and 9.6 μm , and thus the TEA-CO₂ laser can emit light at a variety of wavelengths in this vicinity depending on which rotational line is used.

The repetition rate of the discharge can range from 1 Hz to 100 kHz, and the laser can deliver up to 1.6 J of energy per pulse. The pulse profile of this laser consists of a leading spike of 100-200 ns, caused by the molecules which have been directly excited by the discharge, and a low intense long tail. The latter lasts 4-5 μs and it is determined by collisional transfer from the N₂ to the CO₂ molecules.

The horizontally polarized CO₂ laser enters the machine from the infrared laser side. The two lasers are combined by means of a germanium plate placed at Brewster angle. The CO₂ laser is focused by a converging lens and passes unperturbed through the plate, while the vertically polarized mid-infrared laser is reflected by the germanium surface. The two beams are then sent through the mass spectrometer by reflection off the same silver mirror used for the infrared laser alone. Because of its vertical polarization, the mid-infrared laser power is reduced by ~25% when it passes through the BaF₂ window on entering the chamber.

References

1. Zeleny, J., *Phys. Rev.*, **1914**, 3(2): p. 69-91.
2. Zeleny, J., *Phys. Rev.*, **1917**, 10(1): p. 1.
3. Dole, M., Mack, L.L., Hines, R.L., Mobley, R.C., Ferguson, L.D., and Alice, M.B., *J. Chem. Phys.*, **1968**, 49(5): p. 2240-2249.
4. Yamashita, M. and Fenn, J.B., *J. Phys. Chem.*, **1984**, 88(20): p. 4671-4675.
5. Yamashita, M. and Fenn, J.B., *J. Phys. Chem.*, **1984**, 88(20): p. 4451-4459.
6. Fenn, J.B., Mann, M., Chin, K.M., Wong, S.F., and Whitehouse, C.M., *Science*, **1989**, 246: p. 64-71.
7. Polfer, N.C., Oomens, J., Suhai, S., and Paizs, B., *J. Am. Chem. Soc.*, **2007**, 129(18): p. 5887-5897.
8. Oomens, J., Polfer, N., Moore, D.T., van der Meer, L., Marshall, A.G., Eyler, J.R., Meijere, G., and von Helden, G., *Phys. Chem. Chem. Phys.*, **2005**, 7: p. 1345-1348.
9. Ideue, S., Sakamoto, K., Honma, K., and Clemmer, D.E., *Chem. Phys. Lett.*, **2001**, 337(1-3): p. 79-84.
10. Gabelica, V. and De Pauw, E., *Int. J. Mass Spectrom.*, **2002**, 219(1): p. 151-159.
11. Rodriguez-Cruz, S.E., Khoury, J.T., and Parks, J.H., *J. Am. Soc. Mass Spectrom.*, **2001**, 12(6): p. 716-725.
12. Joly, L., Antoine, R., Allouche, A.-R., and Dugourd, P., *J. Am. Chem. Soc.*, **2008**, 130(42): p. 13832-13833.
13. Kang, H., Jouvét, C., Dedonder-Lardeux, C., Martrenchard, S., Charrière, C., Grègoire, G., Desfrancoise, C., Schermann, J.P., Barat, M., and Fayeton, J.A., *J. Chem. Phys.*, **2005**, 122(8): p. 084307.
14. Breuker, K. and McLafferty, F.W., *Angew. Chem. Int. Ed.*, **2005**, 44: p. 4911-4914.
15. Nolting, D., Marian, C., and Weinkauff, R., *Phys. Chem. Chem. Phys.*, **2004**, 6: p. 2633-2640.
16. Kang, H., Jouvét, C., Dedonder-Lardeux, C., Martrenchard, S., Grègoire, G., Desfrancoise, C., Schermann, J.P., Barat, M., and Fayeton, J.A., *Phys. Chem. Chem. Phys.*, **2005**, 7: p. 394-398.
17. Nonose, S., Iwaoka, S., Mori, K., Shibata, Y., and Fuke, K., *Eur. Phys. J. D*, **2005**, 34: p. 315-319.
18. Nonose, S., Iwaoka, S., Tanaka, H., Okai, N., Shibakusa, T., and Fuke, K., *Eur. Phys. J. D*, **2003**, 24(1 - 3): p. 335-338.

19. Lucas, B., Barat, M., Fayeton, J.A., Perot, M., Jouvet, C., Gregoire, G., and Nielsen, S.B., *J. Chem. Phys.*, **2008**, 128(16): p. 7.
20. Baker, E.S., Dupuis, N.F., and Bowers, M.T., *Journal of Physical Chemistry B*, **2009**, 113(6): p. 1722-1727.
21. Kebarle, P. and Tang, L., *Anal. Chem.*, **1993**, 65(22): p. A972-A986.
22. Taylor, G., *Proc. R. Soc. Lon. Ser-A*, **1964**, 280(1382): p. 383-397.
23. Rayleigh, L., *Phil. Mag.*, **1882**, 14: p. 184-186.
24. Cole, B.R., *J. Mass. Spectrom.*, **2000**, 35(7): p. 763-772.
25. Kebarle, P., *J. Mass. Spectrom.*, **2000**, 35(7): p. 804-817.
26. Hogan, C.J., Carroll, J.A., Rohrs, H.W., Biswas, P., and Gross, M.L., *Anal. Chem.*, **2009**, 81(1): p. 369-377.
27. Schmelzeisen-Redeker, G., Bütfering, L., and Röllgen, F.W., *Int. J. Mass Spectrom. and Ion Proc.*, **1989**, 90(2): p. 139-150.
28. Iribarne, J.V. and Thomson, B.A., *J. Chem. Phys.*, **1976**, 64(6): p. 2287-2294.
29. Thomson, B.A. and Iribarne, V., *J. Chem. Phys.*, **1979**, 71(11): p. 4451-4463.
30. Fenn, J.B., *J. Am. Soc. Mass Spectrom.*, **1993**, 4(7): p. 524-535.
31. Felitsyn, N., Peschke, M., and Kebarle, P., *Int. J. Mass Spectrom.*, **2002**, 219(1): p. 39-62.
32. Smith, D.P.H., *Ieee T. Ind. Appl.*, **1986**, IA-22(3): p. 527-535.
33. Wilm, M.S. and Mann, M., *Int. J. Mass Spectrom. and Ion Proc.*, **1994**, 136: p. 167-180.
34. Wilm, M. and Mann, M., *Anal. Chem.*, **1996**, 68(1): p. 1-8.
35. Sannes-Lowery, K., Griffey, R.H., Kruppa, G.H., Speir, J.P., and Hofstadler, S.A., *Rapid Commun. Mass Spectrom.*, **1998**, 12(23): p. 1957-1961.
36. Sannes-Lowery, K.A. and Hofstadler, S.A., *J. Am. Soc. Mass Spectrom.*, **2000**, 11(1): p. 1-9.
37. Kamariotis, A., *Infrared Photofragment Spectroscopy of charged amino acid water clusters in the gas phase*, in *PhD Thesis, EPFL, Lausanne*. 2006.
38. Paul, W. and Steinwelden, Z., *Naturforsch*, **1953**, 448.
39. Paul, W., Reinhard, H.P., and von Zahn, U., *Zeitschrift für Physik A Hadrons and Nuclei*, **1958**, 152(2): p. 143-182.
40. Brubaker, W.M. and Tuul, J., *Rev. Sci. Instrum.*, **1964**, 35(8): p. 1007-&.
41. Dawson, P.H., *Quadrupole mass spectrometer and its applications*. 1976: Elsevier Scientific Pub. Co.: Amsterdam.
42. Dawson, P.H., *Mass Spectrom. Rev.*, **1986**, 5(1): p. 1-37.
43. March, R.E., *J. Mass. Spectrom.*, **1997**, 32(4): p. 351-369.
44. Nappi, M., Weil, C., Cleven, C.D., Horn, L.A., Wollnik, H., and Cooks, R.G., *Int. J. Mass Spectrom. and Ion Proc.*, **1997**, 161(1-3): p. 77-85.
45. Blaum, K., Geppert, C., Müller, P., Nörtershäuser, W., Otten, E.W., Schmitt, A., Trautmann, N., Wendt, K., and Bushaw, B.A., *Int. J. Mass Spectrom.*, **1998**, 181(1-3): p. 67-87.
46. March, R.E. and Todd, J.F.J., *Quadrupole ion trap mass spectrometry*, ed. 2nd. 2005: Wiley-Interscience: Hoboken, N.J.
47. Mathieu, E., *J. Math. Pure Appl. (J. Liouville)*, **1868**, 13: p. 137-.
48. Teloy, E. and Gerlich, D., *Chem. Phys.*, **1974**, 4: p. 417-427.
49. Gerlich, D., *Adv. Chem. Phys.*, **1992**, LXXXII: p. 1-176.
50. Mikosch, J., Fruhling, U., Trippel, S., Otto, R., Hlavenka, P., Schwalm, D., Weidemüller, M., and Wester, R., *Phys. Rev. A*, **2008**, 78(2): p. 13.
51. Asvany, O. and Schlemmer, S., *Int. J. Mass Spectrom.*, **2009**, 279(2-3): p. 147-155.

52. Gerlich, D. and Horning, S., *Chem. Rev.*, **1992**, 92(7): p. 1509-1539.
53. Gerlich, D., *J. Chem. Soc. Faraday Trans.*, **1993**, 89(13): p. 2199-2208.
54. Gerlich, D., *Physica scripta*, **1995**, T59: p. 256-263.
55. Luca, A., Schlemmer, S., Cermak, I., and Gerlich, D., *Rev. Sci. Instrum.*, **2001**, 72(7): p. 2900-2908.
56. Trippel, S., Mikosch, J., Berhane, R., Otto, R., Weidemuller, M., and Wester, R., *Phys. Rev. Lett.*, **2006**, 97(19): p. 4.
57. Mercier, S., *Electronic and Vibrational Spectroscopy of cold protonated amino acids in the gas phase*, in *PhD Thesis, EPFL, Lausanne*. 2008.

Chapter 3

Spectroscopic techniques and theoretical approach

The goal of this thesis was to measure and interpret conformer-specific vibrational spectra of closed-shell biological ions in a cold ion trap. This chapter describes in detail the techniques used to acquire such spectra. First, it illustrates the photophysical processes a molecule undergoes when interacting with laser light and the possible spectroscopic methods used to reveal this interaction, drawing particular attention to the technique adopted in this thesis work, electronic *photofragment spectroscopy*. Then, it presents the timing of the events taking place on a single ion packet, followed by the description of how a fragment mass spectrum is acquired and a discussion on the possible mechanisms leading to photodissociation. The chapter also explains the IR-UV double-resonance spectroscopy methods used to obtain conformer-specific vibrational spectra and the theoretical approach employed to assign a geometry to each conformer. Finally it discusses the photophysics of the three aromatic amino acids, which are used to probe the conformational preferences of the peptides in this thesis work.

3.1 Photofragment Spectroscopy

3.1.1 Introduction

In *photoactive* proteins, a *chromophore* is the part of the molecule responsible for the light absorption. Its response to photoabsorption can be used as a probe of protein structure

and dynamics, studying the effect of the environment on the absorption spectrum of the isolated chromophore [1-5].

In our apparatus any kind of direct absorption spectroscopy would be difficult if not impossible, because of the low density of ions in the 22-pole ion trap. Therefore, one has to measure a consequence of the photon absorption to record a spectrum (i.e., *action spectroscopy*).

To a first order approximation, the absorption of a UV photon preferentially promotes the molecules from a ground to an excited singlet electronic state, $S_0 \rightarrow S_n$, because the spin is a conserved quantum number in spectroscopic transitions. Several processes, illustrated in Figure 3.1, compete in the deactivation of this excited state.

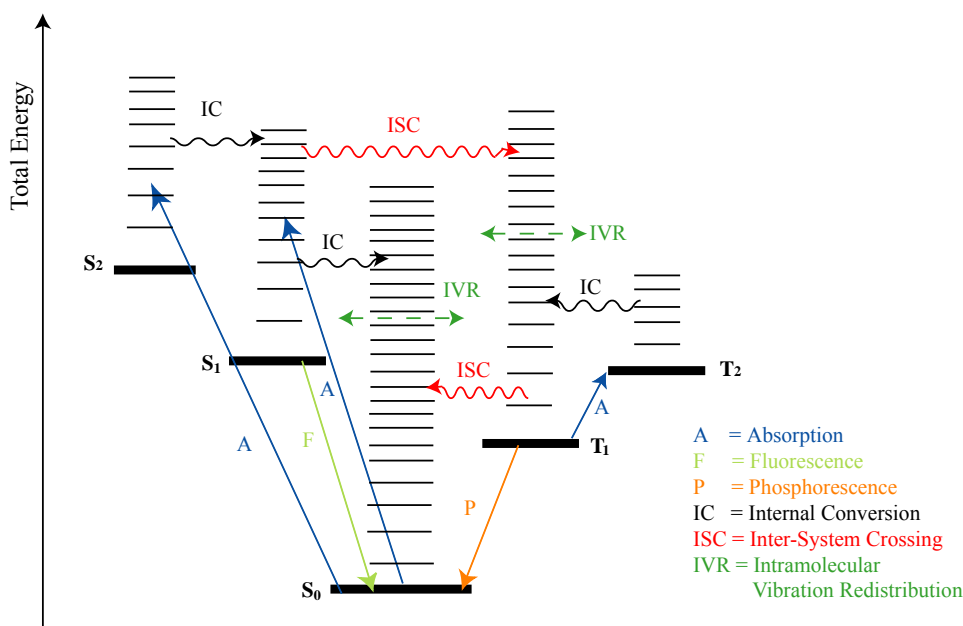


Figure 3.1: Schematic diagram of the various photophysical processes a molecule undergoes when interacting with laser light. The straight lines indicate processes with absorption and emission of light, the horizontal ones the radiationless processes. The wavy arrows denote transitions between electronic states with conversion of electronic energy into vibrational energy. Finally, the straight horizontal arrows represent vibrational energy redistribution in a process where the total vibrational energy is unchanged.

Electronic energy can be converted into vibrational energy *via internal conversion* (IC), a radiationless transition to a lower-lying state of the same spin-multiplicity. The time scale of IC depends on the geometry of the potential energy surfaces (PES) involved in the transition and on the electronic couplings. The IC rate from $S_1 \rightarrow S_0$ may be on the order of 10^5 - 10^8 s⁻¹. However, in the presence of a crossing point between the potential energy

surfaces (*conical intersection*), the internal conversion rate constant may be much faster, on the order of 10^{13} s^{-1} [6]. It is also possible to bring the system to a lower-lying state of different spin-multiplicity *via* radiationless *intersystem crossing* (ISC). The rate of intersystem crossing is a function of the spin-orbit coupling of the involved electronic states and it varies over a wide range. For $S_1 \rightarrow T_1$ transitions, it ranges from 10^6 to 10^9 s^{-1} for molecules that do not contain heavy atoms, whereas for $T_1 \rightarrow S_0$ it is on the order of 10^{-1} - 10^3 s^{-1} [6].

At high levels of vibrational excitation, molecular vibrations are anharmonically coupled. Thus, the energy will not remain in a single vibrational mode but it will be redistributed among all the $3N-6$ vibrational modes, N being the number of atoms in the molecule. This process is known as *intramolecular vibrational energy redistribution* (IVR).

The radiationless conversion from the higher-order electronic states, S_n and T_n with $n \geq 2$, to the lowest excited singlet state (S_1) and the lowest triplet state (T_1) is rapid (picoseconds time scale). Therefore, relaxation back to the ground state with emission of light occurs primarily from S_1 and T_1 , since radiationless processes are slower for these states (*Kasha's rule*). The phenomenon of *fluorescence* involves spontaneous light emission between two electronic states with the same *multiplicity*. It is a spin-allowed transition, and between singlet states (e.g., $S_1 \rightarrow S_0$) it typically occurs at a rate of 10^5 - 10^9 s^{-1} . The spin-forbidden transition $T_1 \rightarrow S_0$ is known as *phosphorescence* and it happens on a much longer time scale, its rate being 10^{-1} - 10^4 s^{-1} [6, 7].

The detection of fluorescence photons emitted by molecules is a common type of action spectroscopy used to reveal the absorption of laser light by the molecule itself [2, 7-11]. This technique is known as *laser induced fluorescence* (LIF). The ability to discriminate between the pumping and the emitted light is a fundamental requirement for LIF to work. This is difficult to achieve in our home built mass spectrometer, because of the unfavorable geometry of the 22-pole ion trap for photon detection (cf. *Section 2.1.4*). Moreover, in a typical experiment, the ion density in the 22-pole trap is $\sim 2 \cdot 10^3 \text{ atoms} \cdot \text{cm}^{-3}$, at the limit of what can be detected by laser induced fluorescence.

Alternatively, one could consider using *resonant enhanced multiphoton ionization* (REMPI) [12, 13]. After the molecule is promoted by a UV photon to an excited electronic state, further absorption of light can bring the molecule to an energy above the ionization

threshold. The molecule will then eject an electron and a positive ion will be formed. The ionization probability is greatly enhanced when the first UV photon is resonant with a molecular transition, while it is very small for non-resonant excitation. Therefore, a spectrum of the molecule can be recorded by monitoring the number of ions produced as a function of the wavelength of the first UV photon. Unfortunately, since the ions in our mass spectrometer start with a net positive charge, the energy required to remove an electron is much higher than in neutrals, making it more difficult to apply REMPI to detect the absorption of laser light.

Rather than using either LIF or REMPI to measure an action spectrum of the closed-shell biological ions in our cold, 22-pole ion trap, we use *photofragment spectroscopy*, which is illustrated schematically in Figure 3.2 for electronic excitation. The parent molecular ion MH^+ , taken here as an example, is singly charged and lies in the lowest vibrational state of its ground electronic state S_0 , since this is the case for most ions trapped in the 22-pole trap when this is cooled to 6 K [14-16].

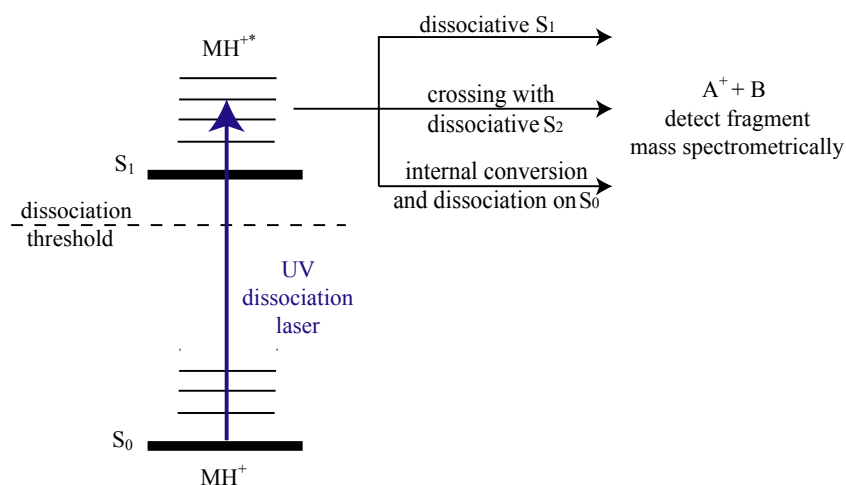


Figure 3.2: Photodissociation spectroscopic scheme after UV excitation. The detailed mechanism leading to fragmentation depends on the photophysics of the parent ion.

After the absorption of a UV photon, the parent ion reaches an excited electronic state S_1 , which can lie above the threshold for dissociating at least one of the bonds in the molecule. The UV excitation can lead either to a direct fragmentation of the molecule if the S_1 state is purely repulsive in the coordinate of a particular bond or to an indirect dissociation (i.e., predissociation) if the initially excited state crosses a repulsive state through which dissociation occurs. Finally, fragmentation can occur on the ground potential energy surface

if the molecule first undergoes internal conversion to a highly excited vibrational state of the electronic ground state. In this case vibrational energy will be redistributed among the vibrational modes of the molecule and there will be a non-zero probability of sufficient energy collecting in a particular bond of the molecule, thereby causing the fragmentation. For large molecules, one typically assumes that intramolecular vibrational energy redistribution (IVR) will be statistical. Consequently, one can use statistical theories to estimate the dissociation rate. Which of the aforementioned dissociation mechanisms (i.e., direct dissociation from an excited electronic state, electronic predissociation or dissociation on the ground state surface following internal conversion and IVR) holds for a given ion cannot be *a priori* established and depends on its electronic state structure. This issue will be further discussed in this chapter and in the rest of this thesis work.

Independent of the mechanism of dissociation, an electronic spectrum can be recorded by monitoring a particular fragment, A^+ (in the example of Figure 3.2), as a function of the UV laser frequency.

3.1.2 Timing of the events

In our home-built tandem mass spectrometer, a photodissociation experiment on a single ion packet, from the generation of the parent ions to the detection of the products, lasts typically 50, 100 or 200 ms. The experiment is then repeated at a rate of 20, 10 or 5 Hz respectively and the signals are averaged for a certain number of cycles to obtain a single point of a spectrum. The subsequent point is obtained by averaging a new set of data after changing a parameter by a small increment (e.g. the laser wavelength or the mass of the fragment to be detected). This process is iterated until a complete spectrum is acquired.

The sequence of events taking place during a single experiment can be illustrated by the timing diagram of Figure 3.3, which shows the set of pulses applied on the optical elements of the machine for a typical 20 Hz experiment. In this case, the laser repetition rate is set to 10 Hz, which allows us to obtain one data point with the laser on and one with it off and subtract the two to extract the laser-induced signal.

The ion packet, formed by collecting ions for ~ 40 ms in the hexapole, is released by lowering the exit lens potential of the latter. The parent ions are mass-selected in the first

quadrupole (Q_1) and then enter the 22-pole ion trap, where they are stored for ~ 35 ms and cooled by collisions with helium buffer gas pulsed ~ 1 ms prior their arrival. The laser is usually fired 10 ms before the ions are released from the 22-pole ion trap. After the opening of the trap, which is achieved by lowering the exit lens potential, both the parent and the daughter ions fly towards the second quadrupole mass filter (Q_3) which transmits a fragment with a given mass-to-charge ratio (m/z) for detection. The number of ions of the chosen dissociation product is then recorded on channel A of the pulse counter. During the subsequent trapping cycle, no laser is fired and Q_3 selects the parent ion mass. Therefore, the channel B of the counter detects the parent ion signal, which is then used for normalization purposes, to compensate for fluctuations of the nanospray source. This normalization procedure is not perfect, but since source fluctuations are rather slow, it helps nonetheless.

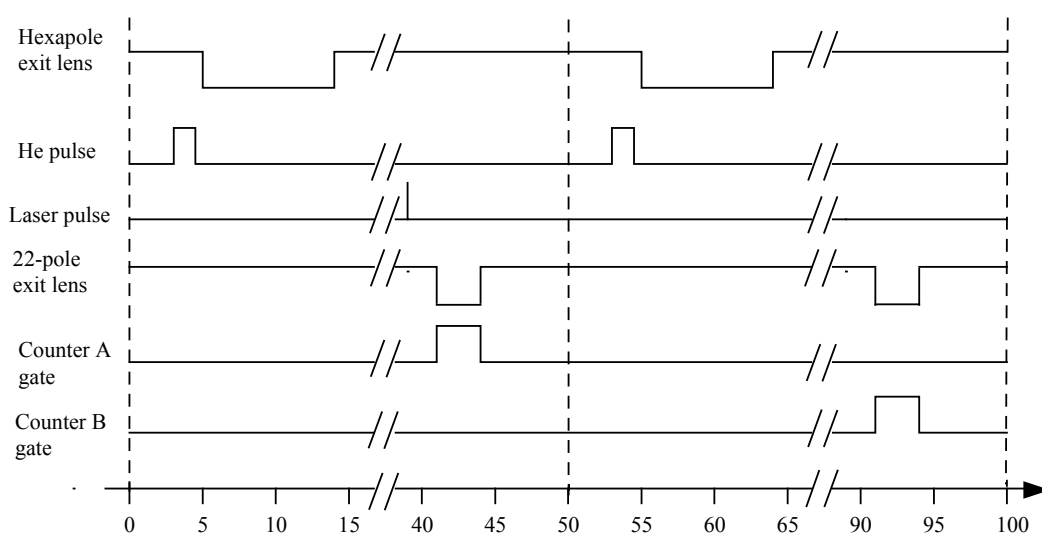


Figure 3.3: Typical timing diagram of the events taking place in a single photodissociation experiment at a repetition rate of 20 Hz.

The delay between the firing of the laser and the opening of the trap is properly chosen to maximize the fragmentation yield (ratio of dissociated to excited ions) of a given m/z species and it varies from 50 μ s to 20 ms for a 20 Hz experiment. The flight time of the ions released from the 22-pole ion trap to reach the detector is ~ 200 μ s and the spread of the ions in a typical ion packet is 1 ms. Therefore, the sum of these time periods and the delay between the laser firing and the trap opening represents the time the parent ion disposes for fragmentation.

In a 10 or 5 Hz photodissociation experiment, the widths of the pulses applied on the optical systems usually remain the same as in the timing diagram of Figure 3.3. However, the ions are collected in the hexapole longer than in a 20 Hz experiment, resulting in a more intense parent ion signal. Furthermore, because the trapping cycle extends over 100 ms and 200 ms respectively, it is possible to fire the laser earlier in the 22-pole trapping cycle, providing the ions more time to photofragment.

In experiments on weakly bound species, i.e. water clusters, the hexapole is simply used as an ion guide. In these cases, a pulse is applied on the entrance lens of the 22-pole ion trap to prevent the continuous flow of warm molecules into the trap and to synchronize the photodissociating laser with the 22-pole trapping cycle.

3.1.3 Measurement of photofragment mass spectra

As already discussed, in photofragment spectroscopy, an optical spectrum of a parent ion is acquired by measuring the intensity of a given photofragment as a function of the laser wavelength. Therefore, before recording any spectra, one should know the mass to charge ratio of the possible fragments and set the second quadrupole mass filter accordingly. Depending on the parent ion, fragmentation mass spectra can already be found in the literature. However, the techniques commonly used to fragment biomolecules (e. g., electron capture, collision-induced and electron impact dissociations) are fundamentally different from ours and could lead to different fragmentation patterns [17-24]. Moreover, the relative fragment intensities in a photodissociation experiment vary depending on the experimental conditions, e.g. laser wavelength or ion temperature [24-26]. For these reasons, we need to measure ourselves the photofragment mass spectrum of each parent ion.

By fixing the laser wavelength to an absorption transition of the parent ion, the fragment mass spectrum can be obtained by successively dissociating several ion packets while incrementing the mass of the daughter ion to be detected. This implies that a photofragment mass spectrum cannot be recorded without knowing the absorption transitions of the parent ion. Unfortunately, nothing is known *a priori* about the precise wavelengths of the transitions in the electronic spectrum of a new species. However, at room temperature the spectrum is typically broad because of inhomogeneous broadening. The laser wavelength is

then at the peak of the broad absorption and the fragment mass spectrum is acquired for the parent molecule at room temperature. This provides a first overview of the daughter ions produced by photodissociation, although their relative intensities can differ greatly from those at low temperature.

The spectroscopic transitions of a cold molecule are expected to be much narrower than those measured at room temperature. Therefore, once the masses of the main photofragments are identified, they can be monitored while scanning the laser wavenumber to measure the low temperature optical spectrum. Once this is obtained, one can measure photodissociation mass spectra by setting the laser wavelength on several sharp absorption bands of the cold parent ion. In this way, different fragmentation patterns can be obtained from transitions belonging to distinct conformers of the same parent ions [27, 28].

3.1.4 Molecular size and lifetime considerations

In photofragment spectroscopy, the intensity of the fragment signal would be proportional to the absorption cross-section at each point of the spectrum if the fragmentation yield and detection efficiency would be independent of the photon wavelength. Of course, this is usually not the case, since the dissociation efficiency depends on the internal energy of the ion and, hence, on photon energy.

The internal energy of a molecule must exceed a certain threshold, E_0 , to observe the cleavage of a bond. Information about dissociation activation energies of peptides, proteins or oligonucleotides are obtained by measurements of the dissociation kinetics as a function of temperature, by means of various dissociative techniques such as CID [29, 30], surface induced dissociation (SID) [30] or blackbody infrared radiative dissociation (BIRD) [31-36]. By applying the latter technique to several electrosprayed proteins, the Williams' group determined dissociation threshold energies on the order of 1.0 to 1.5 eV for leucine enkephaline (560 Da) [32], bradykinin (1.06 kDa) [31] and ubiquitin (8.6 kDa) [36]. This suggests that the absorption of a photon of at least this energy, about 10000 cm^{-1} , could lead to the fragmentation of these protein ions.

The three naturally occurring aromatic amino acids, tryptophan (Trp), tyrosine (Tyr) and phenylalanine (Phe), which we use as probe chromophores for peptides, absorb light in

the UV region around 260-280 nm, providing more than 35000 cm^{-1} in energy [37-39] and thus bringing the internal energy of any peptide ion far above its dissociation threshold energy. However, the excitation energy and the dissociation threshold are not the only parameters to consider when studying the possibility for a molecule to fragment. As previously discussed, the excitation energy, even if initially localized, can be rapidly redistributed among the vibrational modes of a molecule through IVR [40, 41]. Consequently, the average energy in each vibrational mode can drop below the dissociation threshold with a reduction of the probability to find enough energy concentrated in the reaction coordinate to induce fragmentation. This trend becomes more important as molecules get larger, because of the increasing number of vibrational modes between which the energy can be partitioned. Therefore, for a given excitation energy and dissociation threshold, the lifetime of a molecular ion is expected to get longer with increasing size. Indeed, Griffin and McAdoo performed Rice-Rampsberger-Kassel-Marcus (RRKM) calculations to evaluate the dissociation lifetimes of model ions as a function of their size and internal energy [42]. They predicted an increase of several orders of magnitude (from ~ 3 ms to 3 hours) in the dissociation lifetime of room temperature ions absorbing a 193 nm photon when going from a 2.1 kDa to a 13.7 kDa molecule. These considerations lead us to reflect on the maximum size of ions we can expect to photodissociate and detect on the time scale of our experiment, and on the ways to improve this limit.

Increasing the size limit of dissociable ions

The *kinetic shift* (KS) is the excess internal energy above the dissociation threshold of polyatomic ions required for their fragmentation on the time scale of a given mass spectrometer [41]. The KS increases dramatically with the ion size, resulting from a significant decrease of the dissociation rate. Therefore, the fragmentation lifetimes represent a limitation for photofragment spectroscopy when dealing with large biomolecular ions. Several methods have been applied to circumvent this limitation and achieve the dissociation of increasingly heavier ions. A first strategy is to extend the observation time by replacing linear quadrupoles or time-of-flight (TOF) by trapping mass spectrometers, such as Fourier transform ion cyclotron resonance (FT-ICR) instruments or quadrupole ion traps. This allows the detection of lifetimes of the order of milliseconds or seconds [43, 44].

Concerning our own apparatus, a careful optimization of the different voltages allows one to trap the photoexcited molecules in the 22-pole ion trap for several tens of millisecond without significant loss [16]. This suggests that we could easily probe photoexcited ions with dissociation lifetimes on the mentioned time scale. As in all trapping experiments, the observable fragmentation lifetime is limited by the residual pressure of background gas used to decelerate the incoming ions, since the excited ions can be collisionally deactivated. In our case where the buffer-gas is pulsed in and then pumped away, this restriction can be easily circumvented, if necessary, by increasing the delay between the gas introduction and the excitation of the parent ions by laser light. However, a lower limit on the observable dissociation rate of an ion is imposed by emission of infrared photons [41, 45]. This so-called IR radiative cooling, according to Dunbar, should limit the lifetime of a metastable ion to a few tens of milliseconds at most [45].

Another strategy is to accelerate the dissociation of large ions by increasing their internal energy. This can be achieved by using multiple-collision activation (MCA-CID), infrared multiphoton dissociation (IRMPD) or surface-induced dissociation (SID) [44]. Because the main purpose of our experiments is to get spectroscopic information of a given species using its photodissociation as a tool, any alternative excitation methods combined with single-photon absorption should not alter significantly the measured optical spectrum. Our chosen strategy is to assist the fragmentation of the UV pre-excited molecules with a CO₂ laser, implementing the *Infrared Laser Assisted Photofragment Spectroscopy* (IRLAPS) technique, which has been previously applied to measure high vibrational overtone spectra of small neutral molecules [46-49]. The main challenge is to find conditions for which the pre-excited ions show an important dissociation yield, while unexcited ones do not. A complete description of the basic principles of the method, the strategies developed to achieve our goal and the results obtained will be described in subsequent chapters.

Statistical vs non-statistical photofragmentation

The discussion above suggests that the amount of excitation energy imparted to the ions would determine the molecular size that is possible to dissociate in a given mass spectrometer. Since in our low-temperature experiments the initial internal energy of the peptides is almost negligible, one could expect a rather modest size of dissociable ions under

absorption of a single ultraviolet photon. However, a few studies have put into doubt the general assumption of energy redistribution among all the vibrational modes in large molecules prior to dissociation. Schlag and Levine suggested that the statistical theories cannot be applied when the excess of energy leads to levels of vibrational excitation below one quantum per mode [50]. Under such conditions, biomolecular ions fragment much more rapidly than predicted by RRK theory [50]. Weinkauff *et al.* experimentally supported the existence of such a rapid dissociation channel in di- and tri-peptides containing tyrosine as chromophore [51]. On the other hand, Hu *et al.* measured the lifetimes of the same ions and concluded that “the peptide length strongly correlates with the dissociation rates”, since the tripeptide fragments about 17-fold slower than the dipeptide [52]. Schlag and coworkers recently attempted to reconcile these different experimental results suggesting that two different processes, happening on distinct time scales, are responsible for the biomolecular ions to fragment [53]. According to them, a fraction of the excited molecules may undergo non-statistical fragmentation and produce daughter ions on an unexpected short time scale compared to RRK estimations. The remaining part would instead dissociate in accordance with statistical theory predictions [52, 53].

In the mid 1980s, the first peptide photodissociations by UV laser light (193 nm) in FT-ICR mass spectrometers have been reported [17, 18, 54, 55]. In 1989, Russel and coworkers observed the prompt dissociation of derivatized amino acids and peptides by visible and low-energy UV (~350 nm) excitations and estimated lifetimes in the submicrosecond time range [56]. After the development of ESI and MALDI, larger protein ions have been dissociated by UV laser radiation. For instance, protein such as bradykinin, mellitin, insulin and lysozyme fragment upon absorption of a single 193 nm photon with constant rate above 10^6 s^{-1} [57]. Gabryelski and Li reported photodissociation of small Trp- and Tyr-containing peptides on a μs time scale after interaction with a 266 nm laser light, although it is not clear if the fragmentation results from a single or multiphoton process [19]. Kim and coworkers observed photofragments of synthetic proteins and peptides induced by 266 nm laser excitation and noted enhancement of the fragmentation adjacent to the chromophore group [58, 59]. Leu-enkephalin and gramicidin A dissociate upon absorption of UV wavelengths in the 220-280 nm range, producing CID-type daughter ions together with fragments that involve the loss of the aromatic side chains or hydrogen atoms. These losses were attributed to direct dissociation at the UV chromophore before complete IVR takes

place [26]. Reilly and coworkers have used higher energy vacuum ultraviolet laser light (VUV; 157 nm) to photofragment oligopeptide ions and attributed the unusual products to a non-ergodic mechanism [60]. Recently, the Jouvet group, using coincidence and femtosecond pump/probe experiments, demonstrated the coexistence of statistical fragmentation following internal conversion from the electronic excited state and direct dissociation from the electronic excited surface in single protonated aromatic amino acid and small peptide ions interacting with UV laser radiation. The latter process leads to a fast dissociation, shorter than 100 ns, which induce the loss of the aromatic side chain [61-66].

All these experiments suggest that there may in fact be no practical upper limit to the size of molecular ions that we can photofragment in our instrument. Indeed, if dissociation occurs directly from the electronic excited state or non-statistically in the ground state, then it allows us to continue using photofragment-based detection schemes to measure electronic spectra of large peptide ions.

3.2 Conformer-specific spectra by IR-UV double-resonance spectroscopy

The selection of the parent ion mass-to-charge ratio in the first quadrupole mass analyzer assures that the measured electronic spectrum belongs to a unique ion species. In the case of flexible molecules such as peptides, several conformers (i.e. structures corresponding to local minima on the potential energy surface of a given molecule) can be found in the 22-pole ion trap at low temperature. Therefore, the optical spectrum can be the result of the superimposition of spectra of multiple conformers. Being able to disentangle the different contributions would help in characterizing spectroscopically each of the conformers.

In 1985 and 1986, the Levy group published a series of papers to demonstrate the presence of several conformers of tryptophan and some of its analogs in a supersonic expansion using R2PI saturation spectroscopy [9, 37, 67] and dispersed fluorescence spectroscopy [9, 68]. Analysis of the rotationally resolved $S_1 \leftarrow S_0$ fluorescence excitation spectrum can also assist in distinguishing different conformers and, with the help of quantum chemical computations, in assigning a specific geometry to each of them [69-74].

Colson and coworkers first applied UV-UV hole-burning spectroscopy to resolve the electronic spectrum of a single *m*-cresol conformer in the presence of isomers which absorb in the same region [75]. In this method, the pulsed laser (the “probe”) is tuned to a vibronic transition of the electronic spectrum previously measured and serves to monitor the ground state population of the corresponding conformer. A second pulsed laser (the “pump”) is fired ~ 400 ns earlier and is scanned across the spectrum. Population is transferred out from the probed level whenever the pump laser becomes resonant with a vibronic transition of the selected conformer. This is revealed by dips in the probe laser signal induced by the pump laser, producing a conformer-specific vibronic spectrum. Lee and coworkers studied the electronic and vibrational spectra of jet-cooled benzene and dimers employing IR-UV double-resonance methods [76, 77]. In these schemes, the UV pump laser is replaced by an IR laser, but the basic “ion-dip” approach remains the same. The frequency of the latter can be fixed on a vibrational transition specific of a particular conformer while the probe laser is scanned. The difference between the electronic spectra measured with or without the IR laser reveals the transitions belonging to the selected isomer. Moreover, by scanning the IR laser frequency while keeping the UV wavelength fixed, one can measure the vibrational spectrum of the conformer selected by the probe laser. This method is commonly referred to as resonant ion-dip or fluorescence-dip IR spectroscopy depending on the detection scheme used. Several groups have applied these double-resonance techniques to sort out the conformational preferences of flexible molecules or clusters in supersonic expansions. Some examples of the vast applicability of these methods are given in references [78-96] and extensively discussed in the reviews [10, 97].

3.2.1 Adaptation to the spectroscopy of cold trapped ions

In our apparatus, both the parent and the daughter ions are collected in the 22-pole trap until they are released and analyzed in the second quadrupole mass filter. As a consequence, the UV-UV hole-burning scheme cannot be easily employed to extract information on the molecular conformation because distinguishing between the photofragments produced by the first and the second UV laser pulses would not be trivial.

For the IR-UV double-resonance methods to work, the electronic absorption of the vibrationally excited state ions should differ from that of the ground state molecules, leading

to a less efficient fragmentation. This implies that whenever the infrared frequency coincides with a vibrational transition of the conformer selected by the UV laser, a dip is recorded in the UV photofragmentation signal. Hence, IR-UV double-resonance experiments, like the previously described IR-dip and the IR-UV hole-burning spectroscopy, can be carried out on the cold ions trapped in the 22-pole trap, to measure conformer-specific electronic and vibrational spectra. These spectroscopic schemes are illustrated in Figure 3.4. The possible mechanisms responsible for the changes in the UV absorption of the vibrationally pre-excited molecules respect to the ground state species are discussed below.

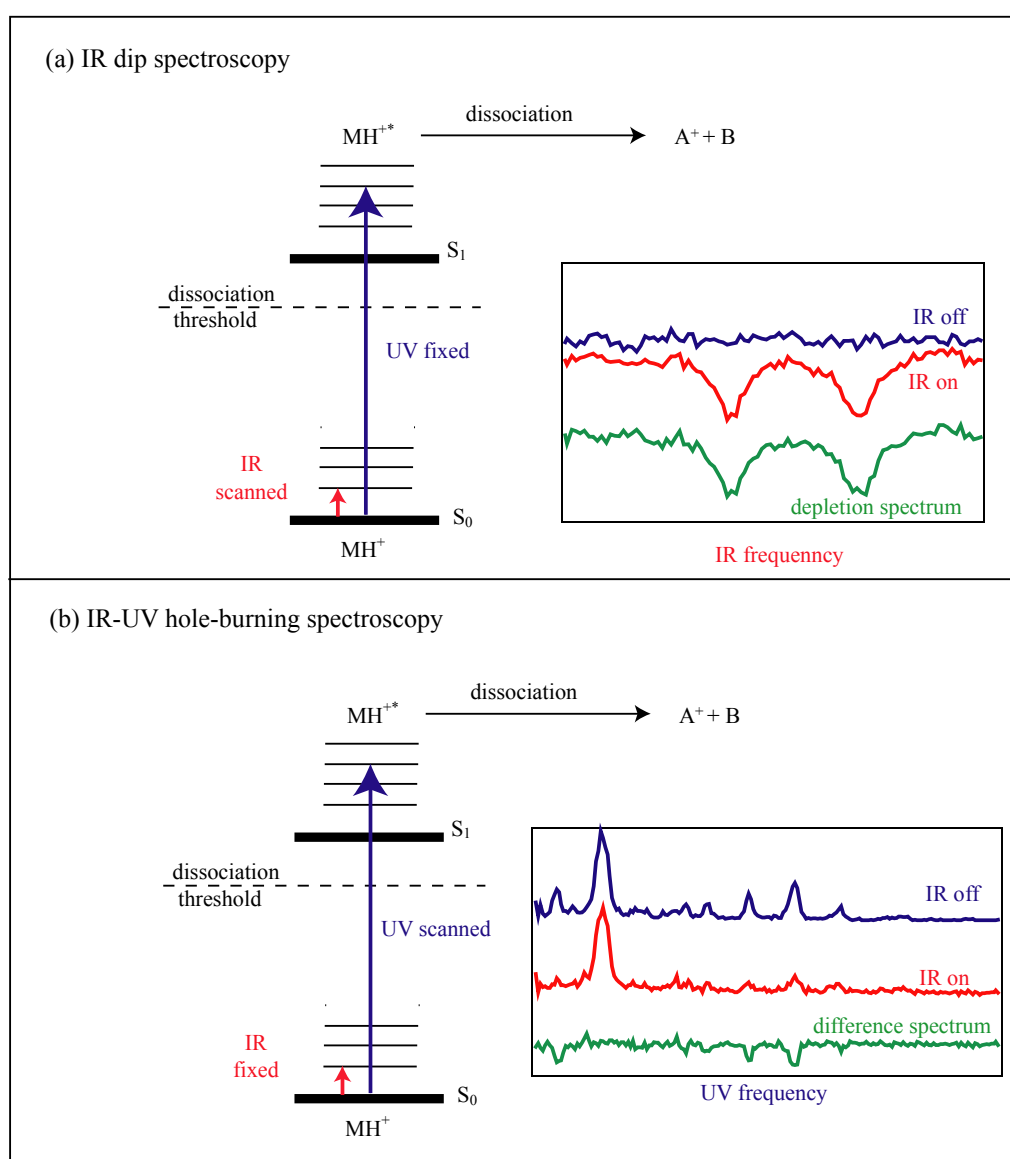


Figure 3.4: IR-UV double-resonance schemes adapted to the photodissociation of cold trapped molecules to measure conformer-specific vibrational (a) and electronic (b) spectra. The IR pulse is fired ~ 200 ns before the UV pulse.

Experimentally, an IR pulse from an OPO is fired ~200 ns before the UV pulse at half the repetition rate of the latter so that the IR-on and off signals are acquired on alternate ion packets. A vibrational spectrum is then obtained by fixing the UV wavelength on a transition of the electronic spectrum previously measured and monitoring the photofragment signal while scanning the IR frequency (Figure 3.4a). The ions belonging to the UV probed conformation are heated up by the IR photon absorption whenever the frequency becomes resonant with a vibrational transition, reducing the dissociation yield into the recorded mass channel. As a result, the IR-on photofragment signal presents dips where the selected isomer absorbed IR radiation. The conformer-specific vibrational spectrum is generated by subtracting the IR-off signal from the IR-on signal and normalizing this difference by the IR-off signal (to compensate for fluctuations in the electrospray source) and by the IR laser power.

Once the IR spectrum of a conformer is known, the IR frequency can be fixed on a vibrational transition while the UV wavelength is scanned (Figure 3.4b). If the chosen IR transition is unique to a particular conformer, all the vibronic transitions associated to the IR probed isomer are depleted by the IR laser. In this case, subtracting the IR-off signal from the IR-on signal and normalizing by the UV laser power generates the electronic spectrum of the selected conformer.

3.2.2 Mechanisms and limitations of the IR-UV double-resonance methods

The complexity of a conformer-specific infrared spectrum of a molecule depends on the number of vibrational bands that may be close in frequency and overlap. One then expects that the spectrum complexity increases with the molecular size. Exactly how many vibrational bands appear in the infrared spectrum depends upon the mechanism of IR-UV double-resonance method. As previously mentioned, the essential requirement for the IR-UV double-resonance technique to work is that the IR pre-excited molecules do not absorb the UV laser at the same frequency as the ground state species. It is thus important to understand why the UV absorption frequency of a molecule changes when the ions are vibrationally excited.

After the absorption of a resonant IR photon, the electronic absorption of a molecule might shift due to a coupling between the vibrational and the electronic degrees of freedom, and such a shift is necessary to observe a dip in ion signal upon IR excitation. The vibrational bands that possess strong Frank-Condon factors for $\Delta v \neq 0$ transitions in the electronic band will be most effective in causing such dips in the UV photofragment signal. If the molecules with a strong Frank-Condon factor for a $\Delta v = 0$ transition in the electronic band are excited to a particular $v=1$ level by an IR photon, the frequency of the electronic absorption may not differ significantly from the ground state molecules since it depends only on the difference in frequency of that particular mode between the ground and excited states, and if this difference is small, the photofragment signal will not be influenced by the IR photon absorption. On the other hand, if the Frank-Condon factor of the $\Delta v = 0$ transition of a particular vibrational mode is weak due to a change in geometry in the excited electronic state (implying stronger transitions for $\Delta v \neq 0$), after absorption of an IR photon the electronic absorption in the region of the band origin (i.e., the 0-0 band) will be weaker than that of the ground state species and the photofragment signal will be depleted. Another way to view this is that the strong transitions starting from the $v=1$ level might occur at the 1-0 frequency, which is significantly shifted from the band origin. Since only a small subset of vibrational modes experience the electronic excitation (i.e., those involving bond vibrations in the vicinity of the UV chromophore) leading to significant Franck-Condon factors for $\Delta v \neq 0$ transitions, this interpretation implies that only this subset will appear in the vibrational ion-dip spectrum.

The previous discussion, however, ignores the possibility that intramolecular vibrational energy redistribution (IVR) takes place in the ions on the timescale of the delay between the two lasers. Since the typical delay is ~ 200 ns, this scenario is improbable. More likely, after the IR photon absorption, the vibrational energy redistributes among the vibrational modes of the molecules, putting them in states of mixed vibrational character. The wave functions of such states will have components that represent population in many low frequency vibrational modes, because of the high density of dark states. The electronic spectrum of a molecule in such states will be broadened because the terms of their wave functions have slightly different UV absorption frequencies. Therefore, the intensity of the UV absorption of the vibrationally excited molecules will be lower at the resonant frequency of the cold ions, leading to a dip in the photofragment signal (cf. Figure 3.5).

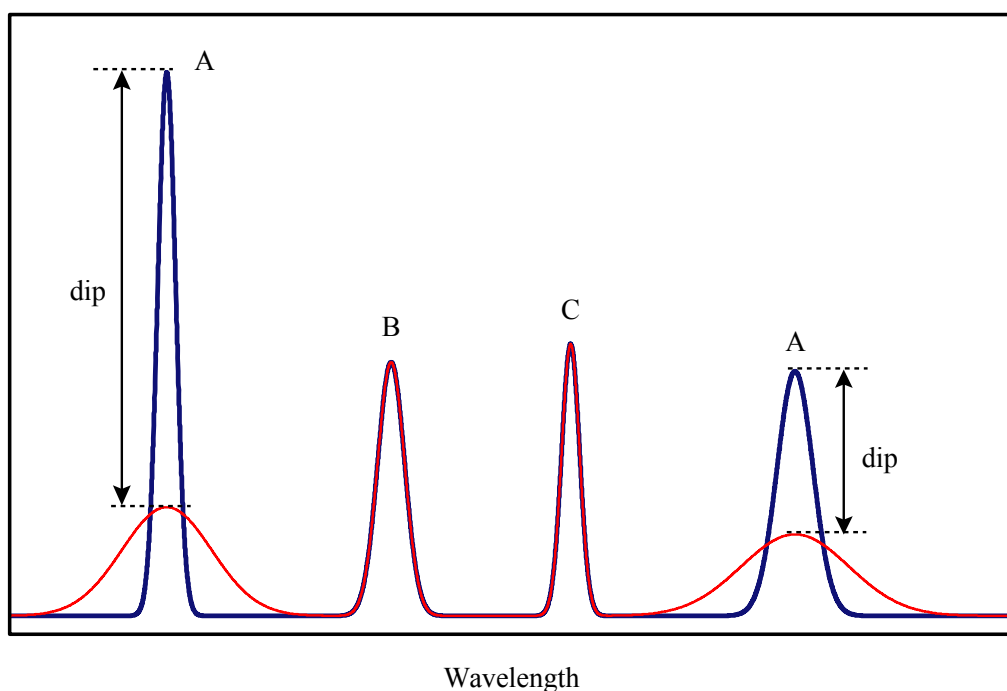


Figure 3.5: Electronic spectra of a cold molecule upon UV-only excitation (blue trace) and after absorption of an infrared photon prior to electronic excitation (red trace). In the example of the figure, the frequency of the infrared laser is resonant with a vibrational mode of conformer A so that all the vibronic transitions belonging to this conformer are depleted by the IR laser.

How the complexity of the infrared spectra scales with molecular size depends upon the mechanism. If the energy is not statistically redistributed, only those modes in the vicinity of the chromophore would appear in the spectrum. Indeed, these are the only modes that one would expect to experience the electronic excitation of the chromophore and thus they have greater possibility of having strong Franck-Condon factors for $\Delta v \neq 0$ transitions. On the other hand, if the energy is statistically redistributed after IR excitation, all the vibrations of the molecule will contribute to the IR-dip spectrum, which will not be a local probe of the chromophore region. In this case the complexity of the vibrational spectrum will increase with the size of the molecule. However, as the molecule gets larger, vibrational modes far away from the chromophore will contribute to the wave functions of the mixed states. Since these modes will not experience the electronic excitation of the chromophore, they will tend to have strong Frank-Condon factors for $\Delta v = 0$ transitions and will not contribute to the broadening of the electronic absorption. The degree of broadening will then decrease roughly proportionally to $1/(\text{SQRT}(S))$, S being the number of mixed states. This implies that with

increasing molecular size the degree of dips in the spectrum will decrease, making it increasingly difficult to measure IR spectra.

The mechanism of IR-UV double-resonance spectroscopy and the complexity of the conformer-specific vibrational spectra with increasing the molecular size will be extensively analyzed in *Chapter 4*.

3.3 Theoretical methods

Progress in theory has contributed significantly to the explosion of interest in the IR-UV double-resonance techniques. A conformer-specific vibrational spectrum constitutes a fingerprint of the conformer itself. Theoretical methods provide the means to convert the spectroscopic data into structural assignments. Indeed, one can associate a geometry to the probed conformer by comparing the measured and the calculated conformer-specific spectra. The general approach is to explore classically the conformational space in order to identify the structures corresponding to local minima on the potential energy surface and then calculate their vibrational spectra at the quantum mechanical level.

For the conformational search, the quantum mechanical potential energy surface is approximated by a classical surface, dubbed a force field, which is a function of bond lengths, bond angles and dihedral angles. In principle one could use several methods for searching the conformational space on this surface for stable minima: simulated annealing, replica-exchange molecular dynamics (REMD) and random search. The first technique is a molecular dynamics method where a starting configuration at high temperature is cooled down slowly until the system freezes and no further changes occur. At each step, the simulation must be long enough to reach a steady state. The process is then iterated to identify several local minima of the potential energy surface with energies close to the global minimum [98, 99]. The REMD is another molecular dynamics method in which many replicas of the system with different temperatures are simulated simultaneously and allowed to pass any energy barrier in the PES. In this way the replica escapes from local minima-energy states and it is possible to explore the conformational space of the system in a single simulation run [100, 101]. The third method for conformational searching consists in

changing randomly the internal coordinates of the input configuration. The new structure is retained and optimized if its energy falls inside an energy window initially defined. If this is not the case, that structure is discarded and the randomization step starts again from the previously minimized structure. The randomization is successful if the minimized energy of the new structure is lower than that of the starting configuration. Once the new structure is identified as unique, it acts as the input structure for an additional step. This procedure is then iterated to generate a set of candidate geometries [102]. The results of both methods depend critically on the force field employed to describe the potential energy surface. In this work, the random search method is adopted to identify the starting structures since it is less computationally intensive than simulated annealing. The AMBER force field [103] within the commercial software, MACROMODEL [104], is used to generate structures for a given molecule. Among all of them, the geometries with a relative energy below 50 kJ/mol are retained to carry out optimization using density functional theory (DFT) in GAUSSIAN03 [105].

The low computational costs of DFT compared to *ab initio* Hartree-Fock (HF) and post-HF methods contributed to its popularity for calculations of the electronic structure in chemistry and in solid state physics. The theoretical derivation of density functional theory is outside the scope of this thesis work, so only some relevant aspects are discussed below (for a detailed treatment see [106] and references therein). The basic idea behind DFT is that the energy of a many-electron system can be expressed as a function of its spatially dependent electron probability density, $\rho(r)$. The electronic energy is, then, said to be a functional¹ of the electron density. Therefore, the kinetic energy of the electrons, the electron-nucleus attraction, the Coulomb interaction between the total charge distribution and the exchange-correlation energy, whose sum gives the total electronic energy of the system, are all functionals of the electron probability density. The last term takes into account the nonclassical electron-electron interactions, and it is the only one that cannot be obtained exactly. Several different schemes have been developed to obtain approximate forms for the exchange-correlation energy functional, allowing efficient and accurate calculations of many molecular properties using DFT [106, 107]. However, the traditional approximations fail in treating the long range dispersion effects (i.e., Van der Waals (VdW) interactions). To overcome this limitation, new density functionals for a first-principles treatment of the VdW

¹ A functional is a function of a function.

interactions or semiempirical approaches have been proposed [108-110]. Both strategies are not entirely satisfactory because the former methods are quite complex and computationally demanding compared to the standard DFT calculations, while the latter ones are far from being broadly applicable because they are developed on specific systems.

We normally employ the hybrid functional B3LYP, which incorporates exact exchange terms from HF theory with approximated or empirical exchange-correlation terms and neglects the Van der Waals interactions. The basis set is then chosen depending on the size of the studied molecules. After optimization of the candidate geometries identified in the conformational search, final energy minimizations and harmonic frequency calculations are performed at the appropriate level of theory. All harmonic frequencies are scaled to account for systematic errors and anharmonicity. Finally, it is the quality of agreement between the calculated and the measured vibrational spectra that allows one to associate a geometry to the selected conformer.

In order to reduce the number of optimized structures to be further analyzed by DFT calculations, we can sort the geometries into families by individuating common structural features. However, this strategy is applicable for small peptide ions or for systems which are expected to be very stable in the gas phase, i.e. charged helical peptides [111], but it is less efficient when treating flexible systems. The specific approach adopted for each ion in this thesis work will be discussed in the next chapters along with the interpretation of the experimental results.

3.4 Overview of the photophysics of the aromatic amino acids

The three aromatic amino acids, tryptophan (Trp), tyrosine (Tyr) and phenylalanine (Phe), are natural UV *chromophores* in proteins. Tryptophan has been the chromophore of choice for spectroscopic studies of peptides and proteins in solutions because of its strong UV absorption and high fluorescence yield. Consequently, much of the gas-phase work has been focused on tryptophan in order to distinguish its intrinsic spectral properties from those induced by its local environment. However, the high fluorescence yield of tryptophan suggests it might not be the most suitable chromophore to employ for photofragment-based

spectroscopic techniques. Photofragment spectroscopy relies on non radiative processes occurring in the excited state that lead to fragmentation as a means to detect the laser absorption. If a high fraction of the pre-excited molecules fluoresce, then the fraction undergoing dissociation would be correspondingly lower. In this sense, it might be an advantage to use phenylalanine, which has the lowest fluorescence quantum yield, even though it has a lower oscillator strength. On the other hand, the non-radiative processes leading to dissociation should not be too fast, because this will broaden the electronic spectrum and inhibit our ability to resolve individual conformations. It is the balance between these two competing factors which determines the best chromophore to use in our experiments. Therefore, it is fundamental to understand the spectroscopy and photophysics of the three aromatic amino acids before using them as a probe of gas-phase peptides and proteins.

The first electronic spectrum of gas-phase tryptophan was measured in a supersonic expansion by Rizzo *et al.* more than 20 years ago [37]. The presence of six conformers, identified by R2PI saturation spectroscopy and dispersed fluorescence spectroscopy (cf. *Section 3.2*), was later confirmed by UV-UV hole-burning and IR dip spectroscopy [81, 112, 113]. At the beginning of the 90s, Martinez *et al.* recorded the electronic spectra of phenylalanine and tyrosine *via* LIF, identifying five and ten conformers respectively [39]. A combination of double-resonance methods, rotational band contour analysis and *ab initio* calculations were used to investigate in detail the conformational preferences of neutral phenylalanine [80, 114, 115]. These studies allowed identifying an additional isomer with respect to those earlier found in Levy's group and to associate a structure to all of them. Concerning tyrosine, UV hole-burning experiments, together with quantum mechanical calculations, performed by de Vries and coworkers, confirmed the existence of ten different conformers even though their spectral assignments slightly differ from the ones proposed by Levy [12, 116]. Recently, Inokuchi *et al.* interpreted the electronic spectrum of tyrosine as the superimposition of the spectra of eight different conformers, whose structures could be identified by comparing infrared depletion spectra with quantum mechanical calculations [117].

All the studies mentioned up to now have investigated neutral chromophores cooled in a supersonic jet. Since we are interested in closed-shell ions, we need to investigate the effect of the charge on the amino acid photophysics. In 2004, Weinkauff and coworkers reported the

first gas-phase electronic spectrum of protonated tryptophan (TrpH^+) obtained by ultraviolet photodissociation in a cooled Paul trap [118]. Their spectrum is in the same range as the S_0 - S_1 transition of neutral tryptophan, but much broader, which they attributed to the congestion caused by multiple vibronic transitions and hot bands, as well as possible lifetime broadening. Moreover, in the same paper, quantum mechanical calculations allowed them to identify the most stable isomer of TrpH^+ as the one with the protonation site on the amino group, as previously established by Maksic [119] and O'Hair [120] for all three aromatic amino acids. In 2005, Talbot *et al.* published the room temperature electronic spectrum of trapped TrpH^+ over a wider spectral range, which also exhibited only broad spectral features. Using multistage mass spectrometry (MS^n) experiments in their quadrupole ion trap, they also deduced possible structures and dissociation mechanisms for various photofragments [121]. In particular, they associated the loss of the hydrogen atom to a specific laser-induced dissociation pattern that serves as a marker of direct fragmentation on the excited-state surface.

In 2006, Boyarkin *et al.* published the electronic spectra of protonated tryptophan and tyrosine measured in our home-built tandem mass spectrometer (cf. *Chapter 2*). These measurements constitute the first demonstration of the power of our methodology to determine optical spectra of protonated species [15, 27]. The electronic spectrum of TrpH^+ , obtained monitoring the photofragment due to the loss of the amino group as a function of the laser wavelength, is relatively broad [15]. This suggested that the cooling in the 22-pole ion trap might not be complete, if the width of the spectral features arises from thermal inhomogeneous broadening (i.e., hot bands). On the other hand, the observation of clusters of protonated amino acids with one or two helium atoms in the trap suggested that the internal temperatures of the ions should be on the order of 15 K [16]. In addition, the ultraviolet spectra of protonated tyrosine and phenylalanine exhibit well-resolved vibronic transitions, with internal temperatures estimated to be ~ 10 K from the analysis of hot band intensities in the electronic spectra [15, 27]. These observations indicate that efficient cooling was achieved in the 22-pole ion trap also for protonated tryptophan.

The Jouvét group investigated the electronic excited states of both protonated tryptophan and tyrosine, measuring their excited-state lifetimes with femtosecond laser pump-probe experiments [61, 122-125]. They use a 266 nm photon to promote the ions into an excited electronic state, while a second delayed 800 nm photon monitors the time

evolution of that state by modifying the branching ratios of the subsequent dissociations. Their data revealed an excited-state lifetime of 22 ps for protonated tyrosine (TyrH^+) [122] whereas TrpH^+ exhibits a decay with two time constants of about 380 fs and 15 ps [61, 125]. These lifetimes are explained, with the support of *ab initio* calculations, by the presence of a dissociative $\pi\sigma^*$ state in the vicinity of the optically accessible $\pi\pi^*$ excited state located on the aromatic chromophore. The $\pi\sigma^*$ state is a charge transfer state located on the protonated amino group with strong antibonding character along the free NH coordinate and crosses the $\pi\pi^*$ state at a certain NH distance. Coupling between these two states permits an electron to transfer from the aromatic ring to the ammonium group, creating an unstable hypervalent C-NH₃ radical, which leads to the fast detachment of an H atom. At still further N-H distance, the $\pi\sigma^*$ state crosses the ground-state potential energy surface. These results indicate that two competing processes, H-atom loss through the dissociative $\pi\sigma^*$ state and internal conversion to S_0 , might be responsible for the deactivation of the electronic excited state of the aromatic amino acids. Kang *et al.* explain the very different excited-state lifetimes of TyrH^+ and TrpH^+ by the height of the barrier formed by the crossing of the initially excited $\pi\pi^*$ state with the dissociative $\pi\sigma^*$ state [122]. They estimated that the H atom dissociation energy, which correlates with the position of the $\pi\sigma^*$ state, is mainly determined by the IP of the neutral aromatic amino acid. Since the IP of tyrosine is much higher than that of Trp, the barrier height for the H atom dissociation in tyrosine is higher than that of tryptophan, then causing the shorter lifetime of the latter.

Jouvet and coworkers initially attributed the two lifetimes of TrpH^+ to the existence of two conformers with different $\pi\pi^*$ - $\pi\sigma^*$ energy gaps [124, 125]. They later performed additional *ab initio* calculations, including geometry optimizations of the excited states, on TyrH^+ and TrpH^+ [123]. Their results show that for several conformers of both ions a proton transfer reaction from the NH_3^+ group to the aromatic ring occurs through a small barrier for TyrH^+ and no barrier for TrpH^+ but at the cost of significant geometrical rearrangement. On the other hand, the H-loss reaction presents a high energetic barrier for TyrH^+ and a smaller one for TrpH^+ . They thus attributed the lifetime of TyrH^+ and the long decay component of TrpH^+ to the geometrical rearrangement necessary for the proton transfer reaction, while the entropically favored H-atom loss is responsible for the short lifetime component of the protonated tryptophan [123].

In light of the femtosecond laser pump-probe experiments of Jouvet [61, 122-125], the width of the electronic spectrum of TrpH^+ can be justified by the inherent lifetime broadening due to the fast excited state decay. Furthermore, the electronic spectra of the other protonated amino acids, considerably narrower than that of TrpH^+ , reflect the longer excited state lifetime predicted in the time-resolved work of the Jouvet group. An exhaustive interpretation of the electronic spectra of protonated tryptophan and tyrosine can be found in the PhD thesis of Dr. Sébastien Mercier [16]. The discussion above suggests that tyrosine or phenylalanine might be better candidates as spectroscopic probes of charged, gas-phase peptides.

Stearns *et al.* measured the electronic spectra of protonated tyrosine and phenylalanine, monitoring their most abundant photofragments, that is the side chain radical cation (m/z 107) for TyrH^+ and the amino acid backbone (m/z 74) radical cation for the PheH^+ [27]. Both photofragments involve cleavage of the $\text{C}_\alpha\text{-C}_\beta$ bond and, because neither of them is abundant in collision-induced dissociation experiments [23], they must result from a direct dissociation on an excited electronic state. Lucas *et al.* recently reported results of coincidence experiments as well as *ab initio* calculations on protonated tryptophan and tyrosine and proposed two mechanisms responsible for the $\text{C}_\alpha\text{-C}_\beta$ bond cleavage [65]. Laser absorption can induce an electron transfer from the aromatic ring either to the ammonium group or to the carbonyl oxygen. As previously discussed, the former process leads to fast H-atom loss, followed by slow dissociation of the remaining open-shell species *via* $\text{C}_\alpha\text{-C}_\beta$ bond cleavage. The latter mechanism involves the formation of a biradical cation, which induces the same rupture but on a much shorter time scale (less than 100 ns) [65]. They observed the presence of both dissociation channels in protonated tryptophan, while only the fast process occurs in protonated tyrosine. These results suggest that, assuming that phenylalanine behaves similar to tyrosine, the photofragments we observe in the case of TyrH^+ and PheH^+ originate from the $\text{C}_\alpha\text{-C}_\beta$ bond cleavage due to the electron transfer to the carboxylic oxygen.

The conformer-specific infrared spectra of both protonated phenylalanine and tyrosine were measured in our apparatus using infrared depletion spectroscopy and interpreted by comparison with DFT calculations at the B3LYP/6-31++G** level of theory (cf. *Section 3.2*) [27]. All detected conformations possess two stabilizing H-bond interactions of the NH_3^+ group, one with the π cloud of the ring and one with the carbonyl oxygen, and can be classified accordingly to the orientation of the carboxylic acid group with respect to the ring,

either in *anti* or *gauche* arrangement. Two conformers are identified for PheH⁺ and four in the case of TyrH⁺ (since in the latter case the two backbone orientations can be combined with the two possible orientations of the phenol OH). Finally, the two classes of conformations in protonated tyrosine, *anti* and *gauche*, exhibit different photodissociation dynamics [27].

References

1. Munro, I., Pecht, I., and Stryer, L., *Proc. Natl. Acad. Sci. U. S. A.*, **1979**, 76(1): p. 56-60.
2. Rodriguez-Cruz, S.E., Khoury, J.T., and Parks, J.H., *J. Am. Soc. Mass Spectrom.*, **2001**, 12(6): p. 716-725.
3. Ideue, S., Sakamoto, K., Honma, K., and Clemmer, D.E., *Chem. Phys. Lett.*, **2001**, 337(1-3): p. 79-84.
4. Andersen, L., Nielsen, I., and Kristensen, M., *J. Am. Chem. Soc.*, **2005**, 127: p. 12347-12350.
5. Gonnelli, M. and Strambini, G.B., *Photochem. Photobiol.*, **2005**, 81(3): p. 614-622.
6. Turro, N., *Modern Molecular Photochemistry*. 1978: Benjamin/Cummings Publishing Company, Inc.
7. Lakowicz, J.R., *Principles of Fluorescence Spectroscopy*. 2nd ed. 1999, New York: Kluwer Academic / Plenum Publisher.
8. Kinsey, J.L., *Laser-Induced Fluorescence*. 1977. p. 349-372.
9. Park, Y.D., Rizzo, T.R., Petenau, L.A., and Levy, D.H., *J. Chem. Phys.*, **1986**, 84(12): p. 6539-6549.
10. Zwier, T.S., *J. Phys. Chem. A*, **2001**, 105: p. 8827-8839.
11. Zalesskaya, G.A., Yakovlev, D.L., Sambor, E.G., and Bely, N.N., *Phys. Chem. Chem. Phys.*, **2002**, 4(22): p. 5634-5639.
12. Cohen, R., Brauer, B., Nir, E., Grace, L., and de Vries, M., *J. Phys. Chem. A*, **2000**, 104: p. 6351-6355.
13. Hunig, I., Seefeld, K.A., and Kleineremanns, K., *Chem. Phys. Lett.*, **2003**, 369: p. 173-179.
14. Mercier, S.R., Boyarkin, O.V., Kamariotis, A., Guglielmi, M., Tavernelli, I., Cascella, M., Rothlisberger, U., and Rizzo, T.R., *J. Am. Chem. Soc.*, **2006**, 128(51): p. 16938-16943.
15. Boyarkin, O.V., Mercier, S.R., Kamariotis, A., and Rizzo, T.R., *J. Am. Chem. Soc.*, **2006**, 128: p. 2816.
16. Mercier, S., *Electronic and Vibrational Spectroscopy of cold protonated amino acids in the gas phase*, in *PhD Thesis, EPFL, Lausanne*. 2008.
17. Bowers, W.D., Delbert, S.S., and McIver, R.T., *Anal. Chem.*, **1986**, 58(4): p. 969-972.
18. Williams, E.R., Furlong, J.J.P., and McLafferty, F.W., *J. Am. Soc. Mass Spectrom.*, **1990**, 1(4): p. 288-294.
19. Gabryelski, W. and Li, L., *Rev. Sci. Instrum.*, **1999**, 70(11): p. 4192-4199.
20. Rogalewicz, F., Hoppilliard, Y., and Ohanessian, G., *Int. J. Mass Spectrom.*, **2000**, 195-196: p. 565-590.

21. Horn, D.M., Breuker, K., Frank, A.J., and McLafferty, F.W., *J. Am. Chem. Soc.*, **2001**, 123(40): p. 9792-9799.
22. Breuker, K. and McLafferty, F.W., *Angew. Chem. Int. Ed.*, **2003**, 42: p. 4900-4904.
23. El Aribi, H., Orlova, G., Hopkinson, A.C., and Siu*, K.W.M., *J. Phys. Chem. A*, **2004**, 108: p. 3844-3853.
24. R. Antoine, M.B.J.C.-R.C.D.C.D.P.D.G.G.C.J.D.O.P.P.T.T.G.v., *Rapid Commun. Mass Spectrom.*, **2006**, 20(11): p. 1648-1652.
25. Gabryelski, W. and Li, L., *Rapid Commun. Mass Spectrom.*, **2002**, 16: p. 1805-1811.
26. Tabarin, T., Antoine, R., Broyer, M., and Dugourd, P., *Rapid Commun. Mass Spectrom.*, **2005**, 19: p. 2883-2892.
27. Stearns, J.A., Mercier, S., Seaiby, C., Guidi, M., Boyarkin, O.V., and Rizzo, T.R., *J. Am. Chem. Soc.*, **2007**, 129(38): p. 11814-11820.
28. Stearns, J.A., Guidi, M., Boyarkin, O.V., and Rizzo, T.R., *J. Chem. Phys.*, **2007**, 127: p. 154322.
29. Busman, M., Rockwood, A.L., and Smith, R.D., *J. Phys. Chem.*, **1992**, 96(6): p. 2397-2400.
30. Meot-Ner, M., Dongré, A.R., Somogyi, Á., and Wysocki, V.H., *Rapid Commun. Mass Spectrom.*, **1995**, 9(9): p. 829-836.
31. Schnier, P.D., Price, W.D., Jockusch, R.A., and Williams, E.R., *J. Am. Chem. Soc.*, **1996**, 118(30): p. 7178-7189.
32. Schnier, P.D., Price, W.D., Strittmatter, E.F., and Williams, E.R., *J. Am. Soc. Mass Spectrom.*, **1997**, 8(8): p. 771-780.
33. Price, W.D. and Williams, E.R., *J. Phys. Chem. A*, **1997**, 101(47): p. 8844-8852.
34. Strittmatter, E.F., Schnier, P.D., Klassen, J.S., and Williams, E.R., *J. Am. Soc. Mass Spectrom.*, **1999**, 10(11): p. 1095-1104.
35. Lemoff, A.S., Bush, M.F., and Williams, E.R., *J. Am. Chem. Soc.*, **2003**, 125(44): p. 13576-13584.
36. Price, W.D., Schnier, P.D., and Williams, E.R., *Anal. Chem.*, **1996**, 68(5): p. 859-866.
37. Rizzo, T.R., Park, Y.D., Petenau, L.A., and Levy, D.H., *J. Chem. Phys.*, **1985**, 83(9): p. 4819-4820.
38. Li, L. and Lubman, D.M., *Appl. Spectrosc.*, **1988**, 42(3): p. 418-424.
39. Martinez, S.J., Alfano, J.C., and Levy, D.H., *J. Mol. Spectroscop.*, **1992**, 156(2): p. 421-430.
40. Lifshitz, C., *J. Phys. Chem.*, **1983**, 87(13): p. 2304-2313.
41. Lifshitz, C., *Int. J. Mass Spectrom. Ion Processes*, **1992**, 118-119: p. 315-337.
42. Griffin, L.L. and McAdoo, D.J., *J. Am. Soc. Mass Spectr.*, **1993**, 4: p. 11-15.
43. Rakov, V.S. and Futrell, J.H., *Eur. J. Mass Spectrom.*, **2002**, 8(3): p. 253-262.
44. Laskin, J. and Futrell, J.H., *Mass Spectrom. Rev.*, **2005**, 24(2): p. 135-167.
45. Dunbar, R.C., *Int. J. Mass Spectrom. and Ion Proc.*, **1983**, 54(1-2): p. 109-118.
46. Lubich, L., Boyarkin, O.V., Settle, R.D.S., Perry, D.S., and Rizzo, T.R., *Faraday Discuss.*, **1995**, 102: p. 167-178.
47. Boyarkin, O.V. and Rizzo, T.R., *J. Chem. Phys.*, **1996**, 105: p. 6285-6292.
48. Boyarkin, O.V., Lubich, L., Settle, R.D.S., Perry, D.S., and Rizzo, T.R., *J. Chem. Phys.*, **1997**, 107: p. 8409-8422.
49. Boyarkin, O.V., Rizzo, T.R., Rueda, D., Quack, M., and Seyfang, G., *J. Chem. Phys.*, **2002**, 117(21): p. 9793-9805.
50. Schlag, E.W. and Levine, R.D., *Chem. Phys. Lett.*, **1989**, 163(6): p. 523-530.
51. Weinkauff, R., Schanen, P., Metsala, A., Schlag, E.W., Burgle, M., and Kessler, H., *J. Phys. Chem.*, **1996**, 100(47): p. 18567-18585.

52. Hu, Y., Hadas, B., Davidovitz, M., Balta, B., and Lifshitz, C., *J. Phys. Chem. A*, **2003**, 107(34): p. 6507-6514.
53. Schlag, E.W., Selzle, H.L., Schanen, P., Weinkauf, R., and Levine, R.D., *J. Phys. Chem. A*, **2006**, 110(27): p. 8497-8500.
54. Bowers, W.D., Delbert, S.S., Hunter, R.L., and McIver, R.T., *J. Am. Chem. Soc.*, **1984**, 106(23): p. 7288-7289.
55. Hunt, D.F., Shabanowitz, J., and Yates, J.R., *J. Chem. Soc. Chem. Commun.*, **1987**(8): p. 548-550.
56. Tecklenburg, R.E., Miller, M.N., and Russell, D.H., *J. Am. Chem. Soc.*, **1989**, 111(4): p. 1161-1171.
57. Gimon-Kinsel, M.E., Kinsel, G.R., Edmondson, R.D., and Russell, D.H., *J. Am. Soc. Mass Spectrom.*, **1995**, 6(7): p. 578-587.
58. Oh, J.Y., Moon, J.H., and Kim, M.S., *J. Mass. Spectrom.*, **2005**, 40(7): p. 899-907.
59. Oh, J.Y., Moon, J.H., and Kim, M.S., *Rapid Commun. Mass Spectrom.*, **2004**, 18(22): p. 2706-2712.
60. Cui, W., Thompson, M.S., and Reilly, J.P., *J. Am. Soc. Mass Spectrom.*, **2005**, 16(8): p. 1384-1398.
61. Kang, H., Dedonder-Lardeux, C., Jouvét, C., Martrenchard, S., Gregoire, G., Desfrancois, C., Schermann, J.P., Barat, M., and Fayeton, J.A., *Phys. Chem. Chem. Phys.*, **2004**, 6(10): p. 2628-2632.
62. Kang, H., Jouvét, C., Dedonder-Lardeux, C., Martrenchard, S., Charrière, C., Grègoire, G., Desfrancoise, C., Schermann, J.P., Barat, M., and Fayeton, J.A., *J. Chem. Phys.*, **2005**, 122(8): p. 084307.
63. Gregoire, G., Kang, H., Dedonder-Lardeux, C., Jouvét, C., Desfrancois, C., Onidas, D., Lepere, V., and Fayeton, J.A., *Phys. Chem. Chem. Phys.*, **2006**, 8(1): p. 122-128.
64. Gregoire, G., Dedonder-Lardeux, C., Jouvét, C., Desfrancois, C., and Fayeton, J.A., *Phys. Chem. Chem. Phys.*, **2007**, 9(1): p. 78-82.
65. Lucas, B., Barat, M., Fayeton, J.A., Perot, M., Jouvét, C., Gregoire, G., and Nielsen, S.B., *J. Chem. Phys.*, **2008**, 128(16): p. 7.
66. Lucas, B., Barat, M., Fayeton, J.A., Jouvét, C., Carcabal, P., and Gregoire, G., *Chem. Phys. Lett.*, **2008**, 347(1-3): p. 324-330.
67. Rizzo, T.R., Park, Y.D., Peteanu, L.A., and Levy, D.H., *J. Chem. Phys.*, **1986**, 84(5): p. 2534-2541.
68. Rizzo, T.R., Park, Y.D., and Levy, D.H., *J. Chem. Phys.*, **1986**, 85: p. 6945-6951.
69. Philips, L.A. and Levy, D.H., *J. Chem. Phys.*, **1986**, 85(3): p. 1327-1332.
70. Philips, L.A. and Levy, D.H., *J. Chem. Phys.*, **1988**, 89(1): p. 85-90.
71. Felker, P.M., *J. Phys. Chem.*, **1992**, 96(20): p. 7844-7857.
72. Wu, Y.R. and Levy, D.H., *J. Chem. Phys.*, **1989**, 91(9): p. 5278-5284.
73. Connell, L.L., Corcoran, T.C., Joireman, P.W., and Felker, P.M., *Chem. Phys. Lett.*, **1990**, 166(5-6): p. 510-516.
74. Dickinson, J.A., Joireman, P.W., Randall, R.W., Robertson, E.G., and Simons, J.P., *J. Phys. Chem. A*, **1997**, 101(4): p. 513-521.
75. Lipert, R.J. and Colson, S.D., *J. Phys. Chem.*, **2002**, 93(10): p. 3894-3896.
76. Page, R.H., Shen, Y.R., and Lee, Y.T., *J. Chem. Phys.*, **1988**, 88(8): p. 4621-4636.
77. Page, R.H., Shen, Y.R., and Lee, Y.T., *J. Chem. Phys.*, **1988**, 88(9): p. 5362-5376.
78. Carney, J.R. and Zwier, T.S., *J. Phys. Chem. A*, **2000**, 104: p. 8677-8688.
79. Unterberg, C., Jansen, A., and Gerhards, M., *J. Chem. Phys.*, **2000**, 113: p. 7945-7954.

80. Snoeck, L.C., Robertson, E.G., Kroemer, R.T., and Simons, J.P., *Chem. Phys. Lett.*, **2000**, 321: p. 49-56.
81. Snoeck, L.C., Kroemer, R.T., Hockridge, M.R., and Simons, J.P., *Phys. Chem. Chem. Phys.*, **2001**, 3: p. 1819-1826.
82. Nir, E., Janzen, C., Imhof, P., Kleineremanns, K., and De Vries, M.S., *Phys. Chem. Chem. Phys.*, **2002**, 4: p. 740-750.
83. Plutzer, C., Hunig, I., and Kleineremanns, K., *Phys. Chem. Chem. Phys.*, **2003**, 5(6): p. 1158-1163.
84. Fricke, H., Gerlach, A., Unterberg, C., Rzepecki, P., Schrader, T., and Gerhards, M., *Phys. Chem. Chem. Phys.*, **2004**, 6: p. 4636-4641.
85. Carcabal, P., Kroemer, R.T., Snoek, L.C., Simons, J.P., Bakker, J.M., Compagnon, I., Meijer, G., and von Helden, G., *Phys. Chem. Chem. Phys.*, **2004**, 6(19): p. 4546-4552.
86. Chin, W., Mons, M., Piuzzi, F., Tardivel, B., Dimicoli, I., Gorb, L., and Leszczynski, J., *J. Phys. Chem. A*, **2004**, 108(40): p. 8237-8243.
87. Hunig, I. and Kleineremanns, K., *Phys. Chem. Chem. Phys.*, **2004**, 6: p. 2650-2658.
88. Crews, B., Abo-Rziq, A., Grace, L., Callahan, M., Kabelac, M., Hobza, P., and de Vries, M.S., *Phys. Chem. Chem. Phys.*, **2005**, 7: p. 3015-3020.
89. Abo-Rziq, A., Grace, L., Nir, E., Kabelac, M., Hobza, P., and De Vries, M.S., *Proc. Natl. Acad. Sci. U. S. A.*, **2005**, 102: p. 20-23.
90. Carcabal, P., Jockusch, R.A., Hunig, I., Snoek, L.C., Kroemer, R.T., Davis, B.G., Gamblin, D.P., Compagnon, I., Oomens, J., and Simons, J.P., *J. Am. Chem. Soc.*, **2005**, 127(32): p. 11414-11425.
91. Chin, W., Piuzzi, F., and Dognon, J.-P., *J. Am. Chem. Soc.*, **2005**, 127: p. 11900-11901.
92. Chin, W., Piuzzi, F., Dimicoli, I., and Mons, M., *Phys. Chem. Chem. Phys.*, **2006**, 8(9): p. 1033-1048.
93. Brenner, V., Piuzzi, F., Dimicoli, I., Tardivel, B., and Mons, M., *J. Phys. Chem. A*, **2007**, 111(31): p. 7347-7354.
94. Callahan, M.P., Crews, B., Abo-Riziq, A., Grace, L., de Vries, M.S., Gengeliczki, Z., Holmes, T.M., and Hill, G.A., *Phys. Chem. Chem. Phys.*, **2007**, 9(32): p. 4587-4591.
95. Shubert, V.A. and Zwier, T.S., *J. Phys. Chem. A*, **2007**, 111(51): p. 13283-13286.
96. Callahan, M.P., Gengeliczki, Z., and de Vries, M.S., *Anal. Chem.*, **2008**, 80(6): p. 2199-2203.
97. Robertson, E.G. and Simons, J.P., *Phys. Chem. Chem. Phys.*, **2001**, 3: p. 1-18.
98. Kirkpatrick, S., Gelatt, C.D., and Vecchi, M.P., *Science*, **1983**, 220(4598): p. 671-680.
99. Filizola, M., Centeno, N.B., and Perez, J.J., *J. Pept. Sci.*, **1997**, 3(2): p. 85-92.
100. Hukushima, K. and Nemoto, K., *J. Phys. Soc. Jpn.*, **1996**, 65(6): p. 1604-1608.
101. Sugita, Y. and Okamoto, Y., *Chem. Phys. Lett.*, **1999**, 314(1-2): p. 141-151.
102. Ferguson, D.M. and Raber, D.J., *J. Am. Chem. Soc.*, **2002**, 124(12): p. 4371-4378.
103. Cornell, W.D., Cieplak, P., Bayly, C.I., Gould, I.R., Merz, J.K.M., Ferguson, D.M., Spellmeyer, D.C., Fox, T., Caldwell, J.W., and Kollman, P.A., *J. Am. Chem. Soc.*, **1995**, 117: p. 5179-5197.
104. MACROMODEL, *version 9.1*. **2005**, Schrödinger, LLC: New York.
105. M. J. Frisch, G.W.T., H. B. Schlegel, G. E. Scuseria, M. A. Robb, J. R. Cheeseman, J. A. Montgomery, T. Vreven, K. N. Kudin, J. C. Burant, J. M. Millam, S. S. Iyengar, J. Tomasi, V. Barone, B. Mennucci, M. Cossi, G. Scalmani, N. Rega, G. A. Petersson, H. Nakatsuji, M. Hada, M. Ehara, K. Toyota, R. Fukuda, J. Hasegawa, M. Ishida, T. Nakajima, Y. Honda, O. Kitao, H. Nakai, M. Klene, X. Li, J. E. Knox, H. P. Hratchian, J. B. Cross, V. Bakken, C. Adamo, J. Jaramillo, R. Gomperts, R. E.

- Stratmann, O. Yazyev, A. J. Austin, R. Cammi, C. Pomelli, J. W. Ochterski, P. Y. Ayala, K. Morokuma, G. A. Voth, P. Salvador, J. J. Dannenberg, V. G. Zakrzewski, S. Dapprich, A. D. Daniels, M. C. Strain, O. Farkas, D. K. Malick, A. D. Rabuck, K. Raghavachari, J. B. Foresman, J. V. Ortiz, Q. Cui, A. G. Baboul, S. Clifford, J. Cioslowski, B. B. Stefanov, G. Liu, A. Liashenko, P. Piskorz, I. Komaromi, R. L. Martin, D. J. Fox, T. Keith, M. A. Al-Laham, C. Y. Peng, A. Nanayakkara, M. Challacombe, P. M. W. Gill, B. Johnson, W. Chen, M. W. Wong, C. Gonzalez, and J. A. Pople, *GAUSSIAN 03, Revision D.01* **2004**, Gaussian, Inc.: Pittsburgh PA.
106. Ziegler, T., *Chem. Rev.*, **2002**, 91(5): p. 651-667.
107. De Proft, F., Martin, J.M.L., and Geerlings, P., *Chem. Phys. Lett.*, **1996**, 250(3-4): p. 393-401.
108. Kohn, W., Meir, Y., and Makarov, D.E., *Phys. Rev. Lett.*, **1998**, 80(19): p. 4153.
109. Schwabe, T. and Grimme, S., *Phys. Chem. Chem. Phys.*, **2007**, 9(26): p. 3397-3406.
110. Silvestrelli, P.L., *J. Phys. Chem. A*, **2009**, 113(17): p. 5224-5234.
111. Jarrold, M.F., *Phys. Chem. Chem. Phys.*, **2007**, 9(14): p. 1659-1671.
112. Piuze, F., Dimicoli, I., Mons, M., Tardivel, B., and Zhao, Q., *Chem. Phys. Lett.*, **2000**, 320(3-4): p. 282-288.
113. Bakker, J.M., Aleese, L.M., Meijer, G., and von Helden, G., *Phys. Rev. Lett.*, **2003**, 91(20): p. 203003.
114. Lee, Y., Jung, J., Kim, B., Butz, P., Snoek, L.C., Kroemer, R.T., and Simons, J.P., *J. Phys. Chem. A*, **2003**, 108(1): p. 69-73.
115. Hashimoto, T., Takasu, Y., Yamada, Y., and Ebata, T., *Chem. Phys. Lett.*, **2006**, 421(1-3): p. 227-231.
116. Grace, L.I., Cohen, R., Dunn, T.M., Lubman, D.M., and de Vries, M.S., *J. Mol. Spectroscop.*, **2002**, 215(2): p. 204-219.
117. Inokuchi, Y., Kobayashi, Y., Ito, T., and Ebata, T., *J. Phys. Chem. A*, **2007**, 111(17): p. 3209-3215.
118. Nolting, D., Marian, C., and Weinkauff, R., *Phys. Chem. Chem. Phys.*, **2004**, 6: p. 2633-2640.
119. Maksic, Z.B. and Kovacevic, B., *Chem. Phys. Lett.*, **1999**, 307(5-6): p. 497-504.
120. Lioe, H., O'Hair, R.A.J., and Reid, G.E., *J. Am. Soc. Mass Spectrom.*, **2004**, 15(1): p. 65-76.
121. Talbot, F.O., Tabarin, T., Antoine, R., Broyer, M., and Dugourd, P., *J. Chem. Phys.*, **2005**, 122: p. 074310.
122. Kang, H., Jouvét, C., Dedonder-Lardeux, C., Martrenchard, S., Grégoire, G., Desfrancoise, C., Schermann, J.P., Barat, M., and Fayeton, J.A., *Phys. Chem. Chem. Phys.*, **2005**, 7: p. 394-398.
123. Grégoire, G., Jouvét, C., Dedonder, C., and Sobolewski, A.L., *J. Am. Chem. Soc.*, **2007**, 129(19): p. 6223-6231.
124. Grégoire, G., Jouvét, C., Dedonder, C., and Sobolewski, A.L., *Chem. Phys.*, **2006**, 324(2-3): p. 398-404.
125. Kang, H., Dedonder-Lardeux, C., Jouvét, C., Grégoire, G., Desfrancois, C., Schermann, J.P., Barat, M., and Fayeton, A., *J. Phys. Chem. A*, **2005**, 109(11): p. 2417-2420.

Chapter 4

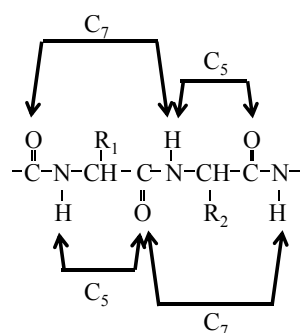
Photofragmentation spectroscopy of small charged peptides

4.1 Tyrosine-based protonated dipeptides: H^+AlaTyr and H^+TyrAla

4.1.1 Introduction

Dipeptides represent the natural step along the road to examine large systems with our photofragment spectroscopy technique. Indeed, they are the smallest unit containing a peptide bond and as such they allow one to understand the first stages of polypeptide structure.

The secondary structure of peptides is typically characterized by hydrogen bonding interaction among the backbone amide groups. A weak hydrogen bond between an amide NH and the carbonyl oxygen of the same amino acid forms a five-member ring and is termed a C_5 interaction. A seven-member ring (C_7) is formed when the hydrogen bond is between the NH hydrogen and the carboxylic oxygen of two adjacent amino acids, and in this case the added flexibility allows for a stronger interaction. The C_5 and C_7 interactions seem to characterize neutral dipeptides and dipeptide mimics containing phenylalanine [1-4] or tryptophan [5-7] as a chromophore that have been studied in supersonic expansions. In the case of protonated dipeptides, the stabilization of the charge by interactions with various functional groups provides additional driving forces for peptide structure and it could alter the conformational landscape and dynamics with respect to the neutral species.



Scheme 4.1: C₅ and C₇ intramolecular NH···O=C interactions in peptides.

Cohen *et al.* measured the ultraviolet spectra of laser-desorbed X-Tyr and Tyr-X, X being alanine (Ala) or glycine (Gly) by resonance-enhanced multiphoton ionization [8]. The X-Tyr spectra are similar to those of the single aromatic amino acid, while the peaks are red-shifted for Tyr-X dipeptides. This is attributed to the interaction between the carbonyl and the phenol groups, which gives rise to a folded conformation. However, they could not classify the structures of the conformers in *anti* or *gauche* forms. In this section, we investigate the preferred structural motifs of the protonated dipeptides H⁺AlaTyr and H⁺TyrAla by a combination of IR-UV double-resonance spectroscopy and density functional theory calculations to better understand the role of the charge.

4.1.2 H⁺TyrAla

Figure 4.1 shows the ultraviolet spectrum of H⁺TyrAla (*m/z* 253), recorded monitoring the two main photofragments *m/z* 136 (Figure 4.1a) and *m/z* 146 (Figure 4.1b). The former daughter ion corresponds to the protonated imine NH₂⁺=CH-CH₂-Ph-OH, which results from cleavage of the C_α-C_{amide} bond, a common dissociation pattern of dipeptides in CID experiment known as the a₁-y₁ pathway [9]. The *m/z* 146 photofragment results from the loss of the tyrosine side chain radical cation, which, as already discussed in Section 3.4, is attributed to a direct dissociation on an excited electronic state in TyrH⁺ [10-13]. The lowest energy transition, occurring at 35174.8 cm⁻¹, has almost the same intensity in each spectra of Figure 4.1, which corresponds to fragmentation of ~1% of the parent ion population. On the other hand, the strongest peak in the spectrum of Figure 4.1a, which occurs at 35223.2 cm⁻¹, shows a completely different behavior depending on the monitored daughter ion. Indeed, the fragmentation yield is nearly 5% of the parent ion population when detecting *m/z* 136, but only 0.2% when monitoring *m/z* 146. The different dissociation patterns subsequent to excitation of these two transitions are confirmed by their photofragment mass spectra, shown

in Figure 4.2. As in the case of protonated tyrosine [12], this suggests that the two transitions are the band origins of two different conformations, labeled A and B in Figure 4.1a and b.

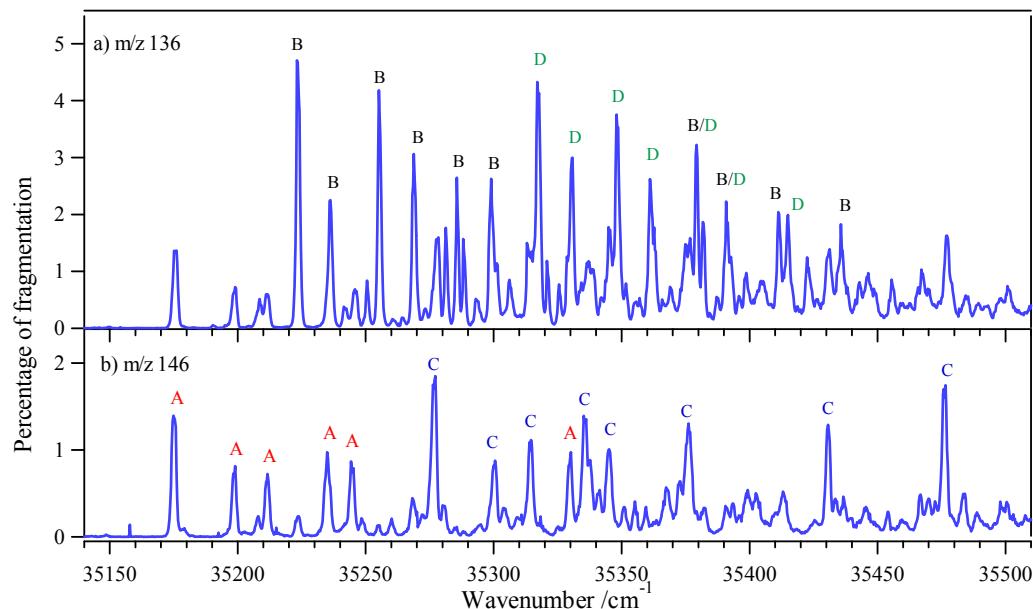


Figure 4.1: Electronic spectra of H^+ TyrAla recorded monitoring the photofragments (a) m/z 136 and (b) m/z 146. The transitions are labeled by conformation, as determined by IR-UV double-resonance spectroscopy. The same transitions are present in both spectra with different intensities, but are labeled only in one for clarity.

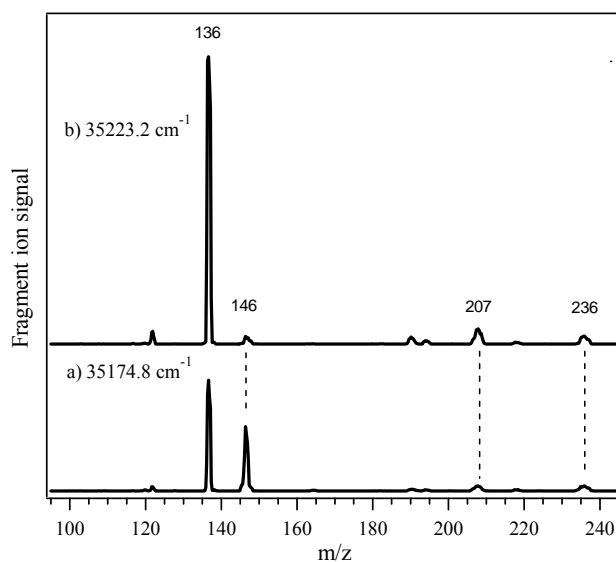


Figure 4.2: Fragmentation mass spectra of H^+ TyrAla recorded at (a) 35174.8 cm^{-1} and (b) 35223.2 cm^{-1} .

Although the conformer A origin appears less intense than that of conformer B, the total fragmentation yields of the two conformers is similar when taking into account all the

photofragments. The energy difference between the conformers' band origins is $\sim 48\text{ cm}^{-1}$, comparable to the 30 cm^{-1} splitting observed for the *anti* and *gauche* conformations of TyrH^+ [12].

Assuming the dipeptide is protonated on the N-terminus, we performed a conformational search using the Amber force field [14] in MACROMODEL [15] in order to find the low-energy conformations. We then carried out reoptimization and harmonic frequency analysis on the lowest-energy structures from this search using DFT in GAUSSIAN 03 [16] at the B3LYP/6-31++G**. The relative energies of the geometries from the molecular mechanics search, reported in Figure 4.3, include zero-point energy corrections based on the calculated harmonic frequencies.

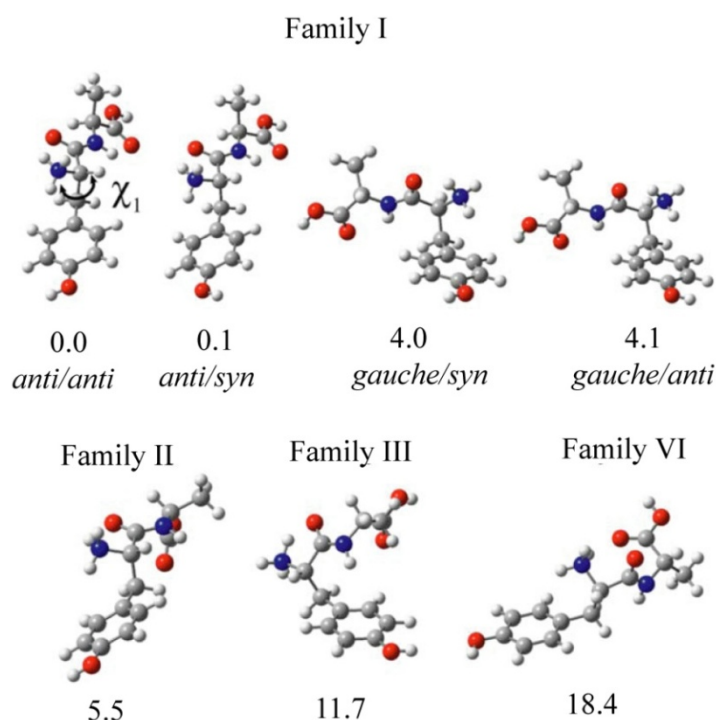


Figure 4.3: Structures and zero-point corrected energies in kJ/mol of H^+TyrAla calculated at the B3LYP/6-31++G** level of theory.

The calculated structures can be sorted into four different conformational families depending on their hydrogen bonding patterns (Figure 4.3). The lowest-energy geometries of H^+TyrAla , belonging to family I, are all characterized by three hydrogen bonding interactions: an $\text{NH}\cdots\pi$ hydrogen bond between the ammonium group and the aromatic ring and two $\text{NH}\cdots\text{O}=\text{C}$ C_5 interactions on both the ammonium group and the neutral amide NH with the carboxylic groups. Within family I, there are two possible rotations about the

tyrosinyl C $_{\alpha}$ -C $_{\beta}$ bond such that the COOH group is *anti* or *gauche* to the ring and two orientations of the phenolic oxygen lone pair of electrons with respect to the ammonium group (*syn* or *anti*). The latter rotation has a little effect on the conformer energy, while the *anti* backbone conformations are stabilized 4 kJ/mol relative to the *gauche* structures. In family II, the ammonium group has a C $_5$ interaction and a π -hydrogen bond, but the amide NH is free from any H bonding. The interaction between the carboxylic acid C=O and the C $_{\beta}$ hydrogens of tyrosine provides an additional stabilizing force for the structures belonging to family II. The lowest-energy member of this family is 5.5 kJ/mol above the global minimum. The third group, lying 11.7 kJ/mol higher in energy, is characterized by the absence of an NH $_3$ $\cdots\pi$ -hydrogen bond, with an amide NH $\cdots\pi$ -hydrogen bond in its place. The structures belonging to family IV, with energy of 18.4 kJ/mol and higher, do not exhibit extended backbone structures but form an eight-member hydrogen bonded ring. This C $_8$ ring is formed by the hydrogen bond between the NH group of one amino acid and the carbonyl of the next amino acid, while the C $_7$ ring observed in the neutral peptide connects an amide NH with the carbonyl of the previous amino acid [7, 17]. Therefore, the C $_7$ ring is found in dipeptides mimics capped at both ends or in larger molecules, but not in uncapped dipeptides.

Figure 4.4 illustrates the NH stretch region of the calculated infrared spectra of the lowest-energy conformer of each family in comparison with the experimental spectra recorded with the UV laser set to the presumed electronic band origins of conformers A and B. The calculated harmonic frequencies are scaled by a factor of 0.954, which gives good agreement with the measured frequencies in our previous work on the protonated aromatic amino acids [12]. Each of the measured spectra exhibits two NH stretch peaks in the region of 3350-3400 cm $^{-1}$, which we assigned to free NH stretches. The peaks are split by 22 cm $^{-1}$ in conformer A and 14 cm $^{-1}$ in B and the vibrational spectrum of the latter is blue-shifted from that of the former by about 15 cm $^{-1}$. Moreover, the bands in the lower frequency region, 3100-3200 cm $^{-1}$, where different absorption of the two conformers is also observed, are assigned to the ammonium NH stretches involved in hydrogen bonds. Consequently, A and B are distinct conformers and, as it appears evident from Figure 4.4, the calculated infrared spectra of family I match best the experimental spectra. We can assign conformers A and B more precisely by comparison with the calculated spectra of the four conformers in family I, as shown in Figure 4.5. The 15 cm $^{-1}$ difference between the free NH stretches of A and B is reflected in the calculated spectra as the difference between the *anti* and the *gauche* backbone

orientations. Therefore, we assign conformer A to an *anti* structure and conformer B to a *gauche* one, with a slightly higher energy.

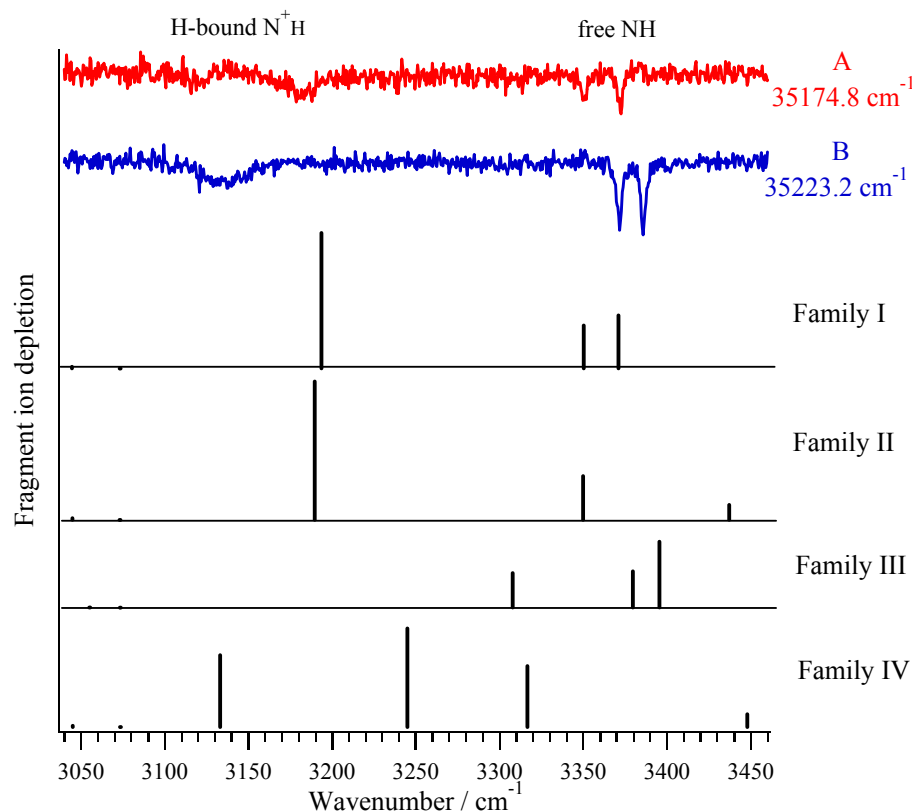


Figure 4.4: Infrared spectra of H^+TyrAla in the NH stretch region recorded with the UV laser set to (A) 35174.8 cm^{-1} and (B) 35223.2 cm^{-1} identified by means of the IR-UV double-resonance technique. The sticks indicate the vibrational spectra calculated at the B3LYP/6-31++G** level of theory for four conformational families.

Based on the results on protonated tyrosine [12], we expect to find two additional conformers with the same structure as A and B but opposite phenol OH orientation. The band origin of a third conformer (C) is found at 35277.2 cm^{-1} , 102 cm^{-1} above the band origin of conformer A. The difference between the two infrared spectra is in the free ammonium NH stretch, which appears reproducibly one wave number lower in A than in C. The origin of the fourth conformer (D) is located at 35317.1 cm^{-1} , 94 cm^{-1} above the B origin. Again the infrared spectra differ in the free NH stretch region, with a 14 cm^{-1} splitting for the free NH peaks in B and 10 cm^{-1} in D. The predicted splitting between the free NH peaks for the *anti/syn* and the *anti/anti* or the *gauche/syn* and *gauche/anti* calculated structures are too close to allow a definitive assignment to conformers A/C or B/D. Moreover, the vibrational bands assigned to the carboxylic acid and the phenolic OH stretches, respectively at

$\sim 3567\text{ cm}^{-1}$ and $\sim 3641\text{ cm}^{-1}$ for all the four conformers, are indistinguishable, leaving the absolute orientation of the COOH group and the phenolic OH group remain uncertain.

The transitions in the electronic spectra of Figure 4.1a and b are assigned to the four conformers using IR-UV hole-burning spectroscopy, setting the infrared laser to unique vibrational bands for each conformer, and labeled accordingly.

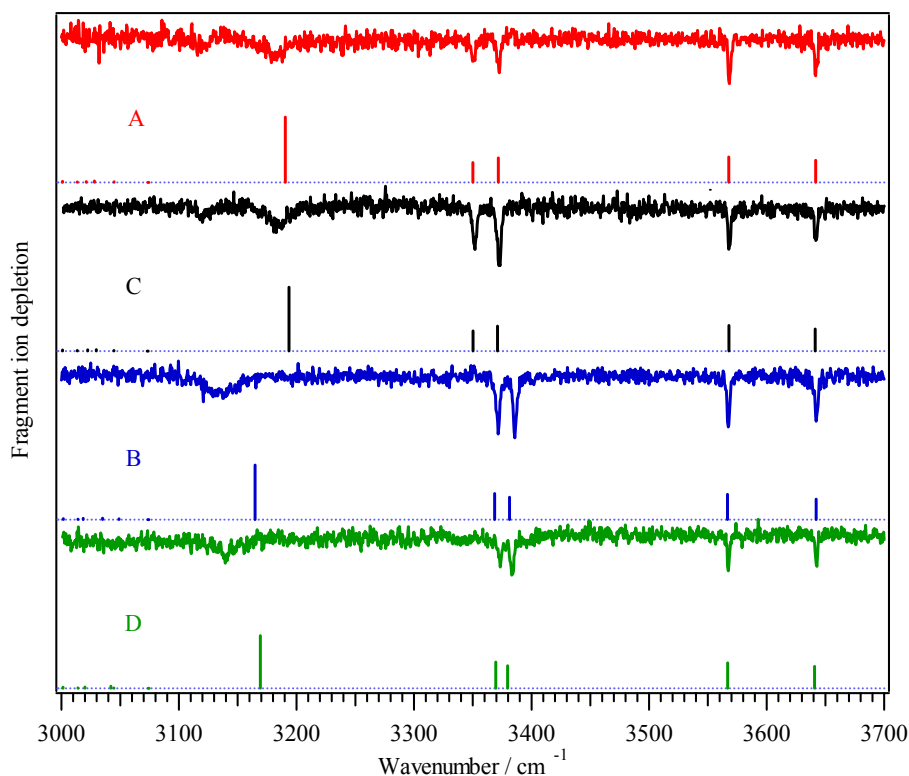


Figure 4.5: Infrared spectra of the four conformers of H^+TyrAla at (A) 35174.8 cm^{-1} , (B) 35223.2 cm^{-1} , (C) 35277.2 cm^{-1} , (D) 35317.1 cm^{-1} identified by means of the IR-UV double-resonance technique. The sticks indicate the vibrational spectra calculated at the B3LYP/6-31++G** level of theory. The calculated harmonic frequencies are scaled by a factor of 0.954.

The conformers observed in H^+TyrAla are analogous to those identified in TyrH^+ and both of them exhibit excited-state fragmentation involving loss of the side chain radical cation [12]. The excited-state dissociation channel accounted for nearly all the products observed in TyrH^+ , although more in the *anti* than in the *gauche* conformers. In the H^+TyrAla *anti* conformers, excited-state fragmentation accounts for almost one-third of the photofragments, while it is at most 2% for the *gauche* structures. As already discussed in Section 3.4, two dissociation mechanisms are proposed to explain the $\text{C}_\alpha\text{-C}_\beta$ bond cleavage in protonated aromatic amino acids. The UV absorption can induce an electron transfer from the

phenolic ring to the ammonium group followed by the H-atom detachments or to the carboxylic oxygen with the consequent formation of a biradical cation [10, 11, 13, 18, 19]. The two mechanisms lead respectively to a slow (longer than 1 ms) or fast (shorter than 100 ns) C_{α} - C_{β} bond cleavage. In the case of protonated tyrosine, the side chain photofragment (m/z 107) is formed promptly after the UV excitation and no H-atom loss is observed [10, 12]. Recently, Lucas *et al.* demonstrated only the biradical cation formation mechanism is responsible for the C_{α} - C_{β} bond cleavage in TyrH^+ [13]. The excited-state photofragment for H^+TyrAla is m/z 146, indicating the charge stays on the peptide chain. Indeed, the release of the fragments as neutrals or charged depends on the ionization potential (IP) of the peptide chain as compared to that of the aromatic ring. For small peptide, the charge is situated on the aromatic ring since its IP is smaller than that of the peptide chain. As the latter lengthens, its IP decreases and the charge remains located on the chain [13]. Therefore, we can imagine that the biradical cation is also responsible for the C_{α} - C_{β} rupture observed in H^+TyrAla .

4.1.3 H^+AlaTyr

Figure 4.6 shows the electronic spectrum of H^+AlaTyr (m/z 253). The band origin appears at 34525.2 cm^{-1} , shifted $\sim 650\text{ cm}^{-1}$ to the red of the lowest-energy band origin of H^+TyrAla , denoting a relative stabilization of the excited state. Indeed, since the charge located on the NH_3^+ group is now separated from the aromatic ring by six bonds, it can get much closer to the π cloud than in H^+TyrAla , where only three bonds separate the charge from the ring. This should provide a stronger interaction between the NH_3^+ and the π system with the consequent stabilization of the excited state.

The fragmentation yield of H^+AlaTyr is nearly 25%, significantly higher than that of H^+TyrAla or the protonated aromatic amino acids, which was only a few percent [12]. One explanation for this apparently higher yield is the fragmentation patterns of H^+AlaTyr , which is shown in Figure 4.7 for the band origin but remains the same for the first three vibronic bands in the electronic spectrum. Most of the H^+AlaTyr dissociation occurs into the single mass channel m/z 182, which corresponds to the mass of protonated tyrosine. This photofragment results from the a_1 - y_1 dissociation pathway, commonly observed in the CID of dipeptides [9]. Moreover, there is no indication of excited-state dissociation in H^+AlaTyr ,

evidenced by the absence of fragments due to the breakage of the tyrosinyl C_α - C_β bond. On the other hand, several photofragments are detected for H^+ TyrAla or the protonated aromatic amino acids (cf. Figure 4.2 and ref. [12]). Therefore, the total fragmentation yields of these parent molecules are similar when taking into account all the produced daughter ions.

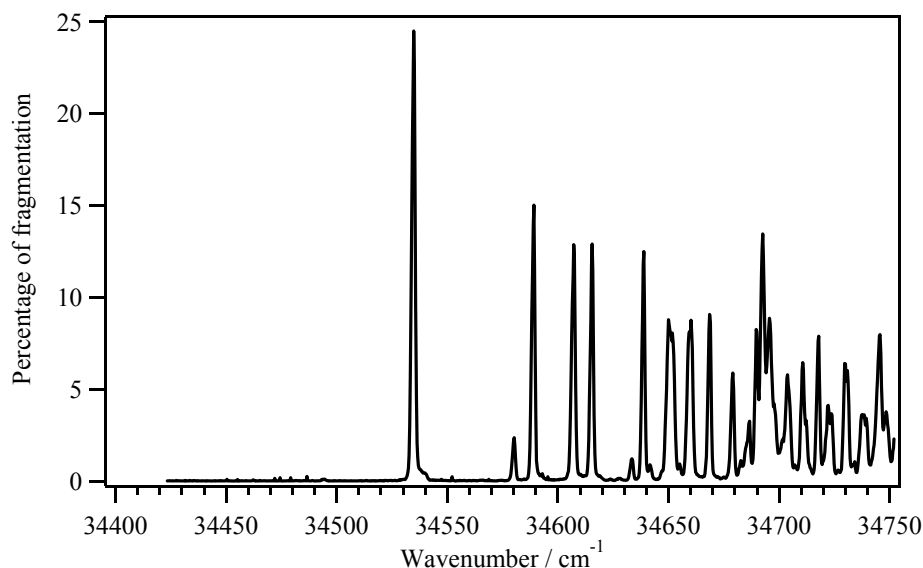


Figure 4.6: Ultraviolet spectrum of H^+ AlaTyr, recorded monitoring m/z 182.

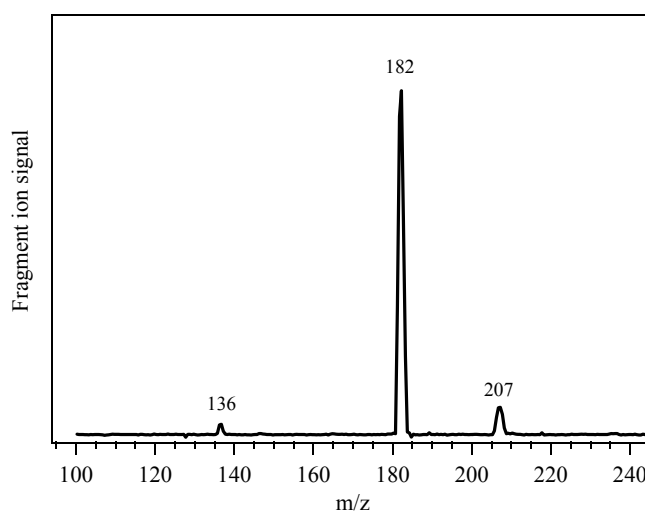


Figure 4.7: Fragmentation mass spectrum of H^+ AlaTyr, recorded at the electronic band origin at 34525.2 cm^{-1} . The same spectrum is obtained fixing the UV laser on the first three vibronic transitions.

DFT calculations performed at the B3LYP/6-31++G** level of theory predict several families of conformations, whose lowest-energy representatives are illustrated in Figure 4.8 and which give rise to unique infrared spectra. The global minimum belongs to family I and

has a strong interaction between the ammonium group and the phenol ring, in addition to the C_5 interactions of the ammonium and amide NH bonds with the carbonyls. The corresponding *gauche* conformer has the ammonium group positioned far away from the ring (family III of Figure 4.8) with the loss of the favorable hydrogen bonding interaction. Surprisingly, this family lies only 1.7 kJ/mol higher in energy than family I, whereas the energy difference between the *anti* and *gauche* structures of H^+ TyrAla is 4 kJ/mol. Both family II and IV lack the $NH_3 \cdots \pi$ interaction but have an amide $NH \cdots \pi$ interaction instead. The difference in the two families is in the orientation of the COOH group, *gauche* to the ring in family II and *anti* in family IV. Finally, the last family exhibits an eight-member hydrogen bonded ring between the N-terminus and the C-terminus of the dipeptides and is much higher in energy, 11.5 kJ/mol, than the other conformations.

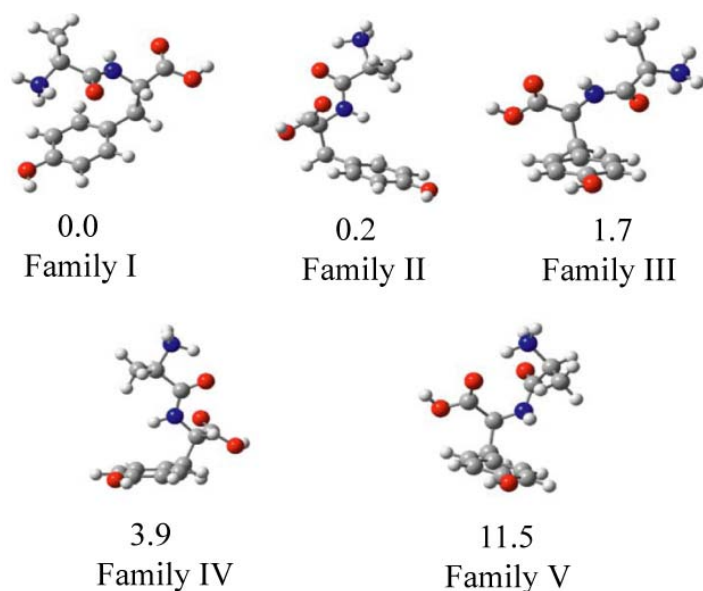


Figure 4.8: Structures and zero-point corrected energies in kJ/mol of H^+ AlaTyr calculated at the B3LYP/6-31++G** level of theory.

The calculated IR spectrum of each of these families, along with the experimental spectrum recorded with the UV laser set at the band origin of H^+ AlaTyr, is shown in Figure 4.9. The spectrum of family I is the only reasonable match to the measured vibrational spectrum. Indeed, it predicts two bands in the $3300\text{--}3400\text{ cm}^{-1}$ region arising from the free ammonium NH and amide NH stretches and two strong bands below 3100 cm^{-1} from the symmetric and antisymmetric combination of the π -hydrogen-bonded and C_5 ammonium NH stretches. However, this calculated spectrum is not unique since there are three conformers in family I in addition to that shown in Figure 4.8, which differ only in the orientation of the

COOH or the phenolic OH groups but have indistinguishable spectra. These isomers are all calculated to be more than 6 kJ/mol higher in energy than the conformer of Figure 4.8 so they are unlikely to have measurable populations.

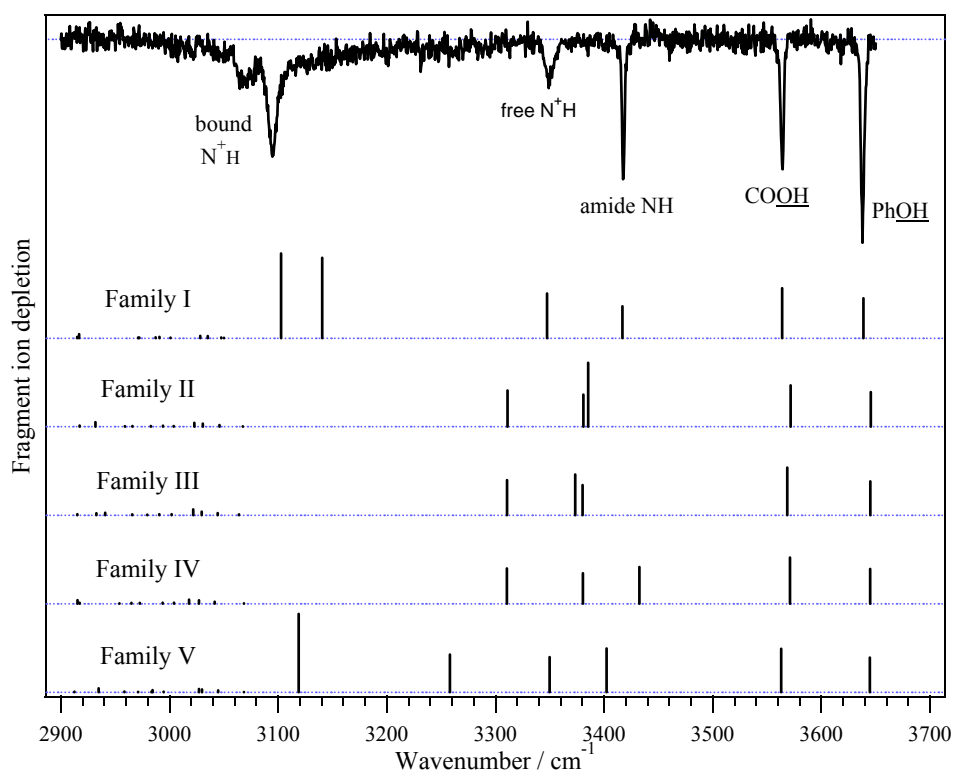


Figure 4.9: Infrared spectrum of the conformer of H⁺AlaTyr identified by means of the IR-UV double-resonance technique. The sticks indicate the vibrational spectra calculated at the B3LYP/6-31++G** level of theory for the five families determined from the random conformational search.

We used IR-UV double-resonance techniques to search for other conformers, but the vibrational spectra associated with the UV peaks we examined were the same. We also performed IR-UV hole-burning experiments, finding the IR transitions at 3095, 3349 and 3428 cm⁻¹ deplete every UV peaks, indicating that they are associated with a single conformer or with conformers that have the same vibrational spectrum. Therefore, the vibronic spectrum of Figure 4.6 is assigned to a unique group of conformers, having the same IR spectrum as the representative structure of family I in Figure 4.8. The concentration of the population in a single conformer is consistent with the large fragmentation yield of H⁺AlaTyr relative to the aromatic amino acids and H⁺TyrAla, in which the population is spread over several conformers. The high yield is thus a consequence of a single conformer fragmenting into a significant mass channel, in addition to the possibility of an inherently stronger absorption.

The absence of the excited-state fragmentation pattern in H^+AlaTyr is not straightforward to explain. We can hypothesize that the stronger C_5 interaction between the charged ammonium group and the carbonyl of tyrosine observed in the conformers of family I prevents the electron transfer from the aromatic ring to the $\text{C}=\text{O}$ of tyrosine residue such that internal conversion dominates.

4.1.4 Conclusions

These results on the IR-UV double-resonance spectra of the cold, protonated dipeptides H^+TyrAla and H^+AlaTyr verify the role of the charge in driving the conformational preferences in small peptides. Indeed, in both dipeptides the charge on the ammonium group is stabilized by C_5 and π -hydrogen-bonding interactions, weaker in H^+TyrAla than H^+AlaTyr because of the smaller number of bonds between the ammonium group and the aromatic ring. Consequently, H^+TyrAla can adopt four stable conformers while in H^+AlaTyr the stronger interaction between the charge and the phenol group seemingly stabilizes only a single conformer compared to other possibilities. The photodissociation dynamics of the H^+TyrAla dipeptide is similar to that of the protonated tyrosine, because of the same number of bonds between the charge and the aromatic ring. On the other hand, the H^+AlaTyr photofragmentation pattern differs from that of the other dipeptide and the aromatic amino acid, since it lacks the excited-state products. Indeed, more bonds separate the charged N-terminus from the phenol ring, leading to a stronger interaction, which may favor internal conversion with respect to excited-state fragmentation pattern.

4.2 Single- and double-chromophore seven-amino-acid peptides

4.2.1 Introduction

The primary structure of a peptide is defined as its sequence of amino acids, linked by covalent bonds. The secondary structure is the three-dimensional form of local segments in the protein, while the tertiary structure is its overall shape. These three-dimensional arrangements are determined by weak non-covalent interactions between the amino acids, i.e.

hydrogen bonds. One of the most common secondary structural elements in proteins is the helix, which also represents the first level of complexity in the folding process. Different types of helices are defined accordingly to their hydrogen-bonding patterns. In the α -helix, the most common helical structure, the amide carbonyl oxygen on the i th residue is hydrogen-bonded to the amide NH of the $(i + 4)$ th residue forming rings of 13 atoms, denoted C_{13} . The 3_{10} helix is a tighter structure formed by 10-membered rings (C_{10}) of an $i, i + 3$ bonding pattern.

Helical structures have been identified in several gas-phase proteins and peptides using IR spectroscopy. For instance, IRMPD studies reveal a mostly α -helical structure for gas-phase cytochrome C, in keeping with its known solution structure [20], while 3_{10} helical motifs are identified in gas phase Ac-Ala-Phe-Ala-NH₂ and Ac-Aib-Phe-Aib-NH₂ by measuring their infrared spectra in the NH stretch region [21, 22]. Moreover, de Vries and coworkers reported the infrared spectra of the pentapeptide FDASV and of several 15-residue gramicidins in the hydride stretch region, suggesting the presence of gas phase helical structures. In particular, the former peptide contains a C_{13} α -helix, while the unresolved band in the gramicidin NH-stretch region is attributed to hydrogen bonds involved in a helix [23, 24].

Very recently, Stearns *et al.* used our experimental approach to measure the electronic and vibrational spectra of cold, protonated, lysine-capped polyalanine molecules, which are expected to be helical in the gas-phase [25-27]. The basis of this work lies in the ion mobility studies of Jarrold and coworkers performed on a series of alanine-containing peptides, Ac-(Ala)_n-LysH⁺, Ac-LysH⁺-(Ala)_n and (Ala)_nH⁺, n being the number of alanine residue in the peptide [28-30]. By converting the measured drift times of each of these species into average cross sections and, subsequently, comparing the latter with molecular dynamics calculations, they can detect the difference between helical or non-helical structures. They establish that the helix formation occurs only in peptides consisting of seven or more alanines with the lysine at the C-terminus, while putting it at the N-terminus or eliminating it altogether results in non-helical structures. Indeed, Vaden *et al.* have recently confirmed the globular nature of small polyalanine peptides lacking the protonated C-terminus lysine by IRMPD spectroscopy in the high frequency stretch region [31]. The protonated side chain of the lysine at the C-terminus plays a double role in helix formation. First, it is involved in

hydrogen-bonding with dangling carbonyl groups at the end of the peptide chain, inducing helix formation. Second, the charge on the lysine side chain stabilizes the helix macro-dipole, formed by alignment of the amide NH and CO groups, through a favourable electrostatic interaction.

In order to measure conformer-specific infrared spectra with our photofragmentation spectroscopic techniques, we need to introduce a UV chromophore in the peptide chain without interfering with the formation of secondary structure. Therefore, we started by substituting the N-terminus alanine residue with a phenylalanine and, hence, investigating Ac-Phe-(Ala)₅-LysH⁺ and Ac-Phe-(Ala)₁₀-LysH⁺. A complete analysis of the electronic and conformer-specific vibrational spectra of these peptides is outside the scope of this thesis work, so only some results relevant for our following discussion are presented below (for a detailed analysis cf. ref. [25-27]).

Despite the large size of the two parent ions, their ultraviolet spectra show sharp features without significant congestion from Franck-Condon activity, a large number of conformers or thermal congestion. Using IR-UV double-resonance spectroscopy, four and two different conformers have been identified for Ac-Phe-(Ala)₅-LysH⁺ and Ac-Phe-(Ala)₁₀-LysH⁺ respectively. The vibrational spectra of the small peptide conformers are characterized by seven well-resolved bands in the NH stretch region, while the conformers of the larger one have a more congested spectrum with distinguishable vibrational bands. In the case of Ac-Phe-(Ala)₅-LysH⁺, a geometry can be associated to each conformer by comparing the measured infrared spectrum with calculated ones at the B3LYP/6-31G** level of theory. In accordance to the ion mobility studies of Jarrold, nearly all the lowest-energy geometries are found to be helical. The geometries of Ac-Phe-(Ala)₅-LysH⁺ are, then, classified accordingly to the hydrogen-bonding scheme of the peptide backbone and the rotation around the C_α-C_β bond of the phenylalanine. The four conformers are, finally, assigned to two distinct helical families, having C₁₀-C₁₀-C₁₀-C₁₃ and C₁₀-C₁₀-C₁₃-C₁₃ backbone arrangements. Each conformer in a family differs from the other member for the orientation of the phenyl ring. Systematic isotopic substitution of the nitrogen-14 by nitrogen-15 in the amide group of different alanine residues of the peptide confirms the correct calculated assignments to the measured NH stretch bands, giving confidence in attributing a particular spectrum to a specific, calculated conformer [27]. On the other hand, a full set of calculations on the larger peptide Ac-Phe-(Ala)₁₀-LysH⁺ cannot be performed with

our current computational capabilities. Therefore, it is by comparison with the assigned spectra of the smaller peptides that one can identify important structural features in the infrared spectra of the larger peptide [25-27].

The following sections explore the ability to probe helical structures with a different aromatic amino acid, tyrosine instead of phenylalanine, as the chromophore. We also explore the effect of chromophore location. After having studied the properties of peptides containing a single aromatic amino acid as chromophore, the next level of complexity is to add another one. This will allow us to explore the possibility to investigate the same infrared spectrum using two different probes to understand the mechanism responsible for the IR-UV double-resonance technique to work.

4.2.2 Ac-Tyr-(Ala)₅-LysH⁺

The electronic excitation spectrum of the tyrosine containing peptide Ac-Tyr-(Ala)₅-LysH⁺ (*m/z* 708) illustrated in Figure 4.10 appears more congested than that measured for Ac-Phe-(Ala)₅-LysH⁺ [25-27]. The analysis of the ultraviolet spectrum of Ac-Tyr-(Ala)₅-LysH⁺ as a function of the laser pulse energy indicates that the transitions are not saturated in the electronic spectrum of Figure 4.10 so that the background noise in this spectrum can be attributed to the electronic activity of tyrosine.

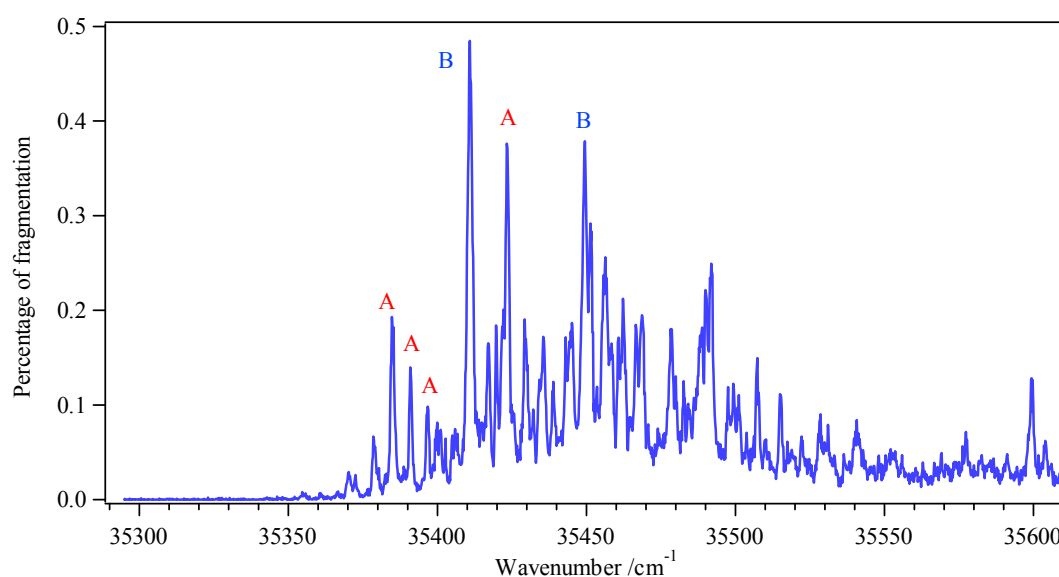
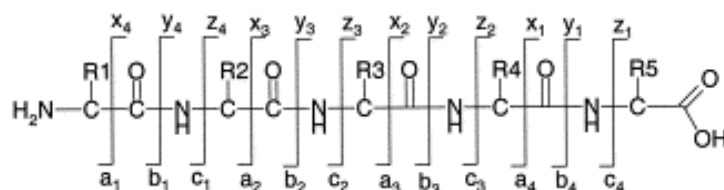


Figure 4.10: Electronic spectrum of Ac-Tyr-(Ala)₅-LysH⁺ recorded monitoring the photofragment *m/z* 602. The transitions are labeled by conformation, as determined by IR-UV double-resonance spectroscopy.

Figure 4.11 shows the photofragment mass spectrum of Ac-Tyr-(Ala)₅-LysH⁺ recorded by setting the ultraviolet laser at the most intense transition of its electronic spectrum since the fragmentation pattern seems to be independent of the vibronic band used for excitation. The nature of the photofragments is the same as for the corresponding phenylalanine helix. Indeed, both peptides produce mainly b-type ions and charged fragments that involve the loss of the aromatic amino acid side chain. The former species derives from the common b_x-y_z pathways in CID experiments, whose typical fragmentation products are depicted in Scheme 4.2 [32, 33]. For this reason we attribute them to a ground state dissociation process. The daughter ions produced by the C_α-C_β bond cleavage are, instead, attributed to direct dissociation on the excited state surface, as already determined for the bare protonated aromatic amino acids and the doubly-charged tyrosine-based dipeptides [12, 34].



Scheme 4.2: Nomenclature used for the common b_x-y_z fragmentation products in CID experiments.

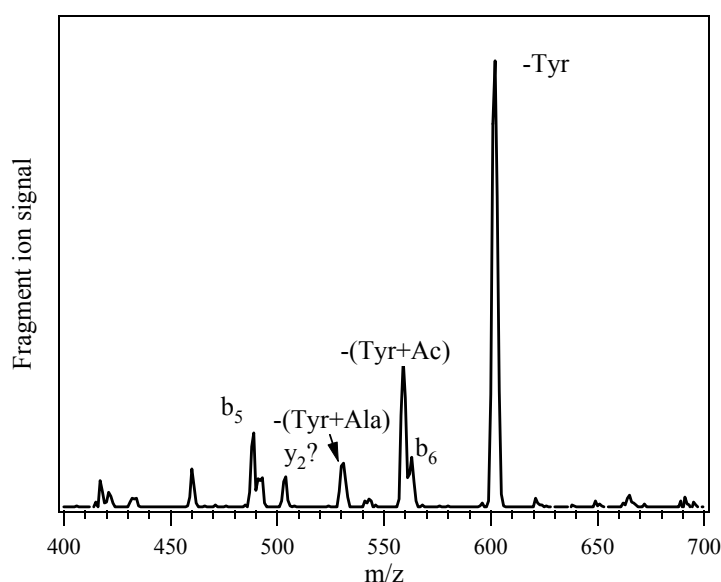


Figure 4.11: Photofragment mass spectra of Ac-Tyr-(Ala)₅-LysH⁺ recorded at 35410.8 cm⁻¹, the most intense ultraviolet transition of the electronic spectrum of Figure 4.10.

The infrared spectra associated with several ultraviolet transitions were measured employing IR-UV double-resonance spectroscopy to identify the conformers of Ac-Tyr-(Ala)₅-LysH⁺ contributing to its electronic spectrum. Only two different vibrational spectra

were observed, suggesting the existence of two distinct conformers, labeled A and B (Figure 4.12), whose band origins appear at 35384.7 cm^{-1} and 35410.8 cm^{-1} respectively. Based on our results on TyrH^+ and the protonated dipeptides [12, 34], we expected to find two additional conformers that differ in the orientation of the phenolic OH from the identified ones. These were not observed, most probably because our resolution is not sufficient to resolve the small vibrational shifts induced by the phenolic OH flipping in $\text{Ac-Tyr-(Ala)}_5\text{-LysH}^+$. In addition to IR-dip spectroscopy measurements, IR-UV hole-burning spectroscopy was performed by setting the infrared laser on unique vibrational bands of A and B to assign other vibronic transitions to one of the two conformers.

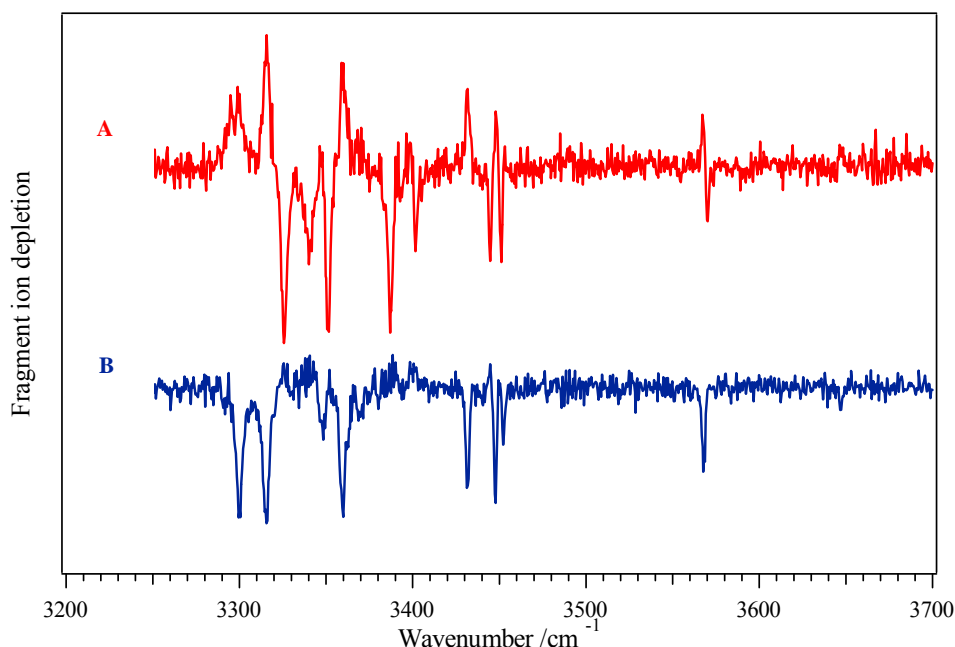


Figure 4.12: Infrared spectra of $\text{Ac-Tyr-(Ala)}_5\text{-LysH}^+$ recorded setting the UV laser at 35384.7 cm^{-1} and 35410.8 cm^{-1} , the band origins of conformer A and B respectively. The gains in the spectrum of conformer A are due to conformer B.

As previously discussed, in IR-UV double-resonance experiments the infrared laser usually causes depletions in the ultraviolet induced fragmentation signal (cf. *Section 3.2*). However, there are some gains in the vibrational spectrum of conformer A. Indeed, the infrared excitation of conformer B spreads a small amount of absorption intensity to the wavelengths at which conformer A is probed because of statistical broadening [35]. The fragmentation signal of conformer A thus increases whenever the frequency of the infrared laser is in resonance with a vibrational transition characteristic of conformer B. These gains are on the same scale as the IR-induced depletions in conformer A because its fragmentation

signal is significantly smaller than that associated to B. For the same reason, the transfer of absorption intensity from the minor to the major conformer is not perceptible. Each of the infrared spectra of Figure 4.12 contains the C-terminal carboxylic acid OH stretch around 3570 cm^{-1} and shows seven well-resolved amide NH bands. The substantial differences in the NH stretch region between the two conformers suggest different hydrogen-bonding patterns. In general, the amide NH stretches below 3400 cm^{-1} belong to the NH groups involved in stronger hydrogen-bonds, whereas the higher-frequency NH stretch bands arise from those in weaker interactions. The infrared spectrum of conformer B presents the phenolic OH stretch band around 3647 cm^{-1} , while the infrared spectrum of conformer A shows no depletions in this high-energy region but a small gain at the same frequency as the conformer B phenolic OH stretch. This suggests that the phenolic OH band in A is buried underneath the gain due to conformer B absorption.

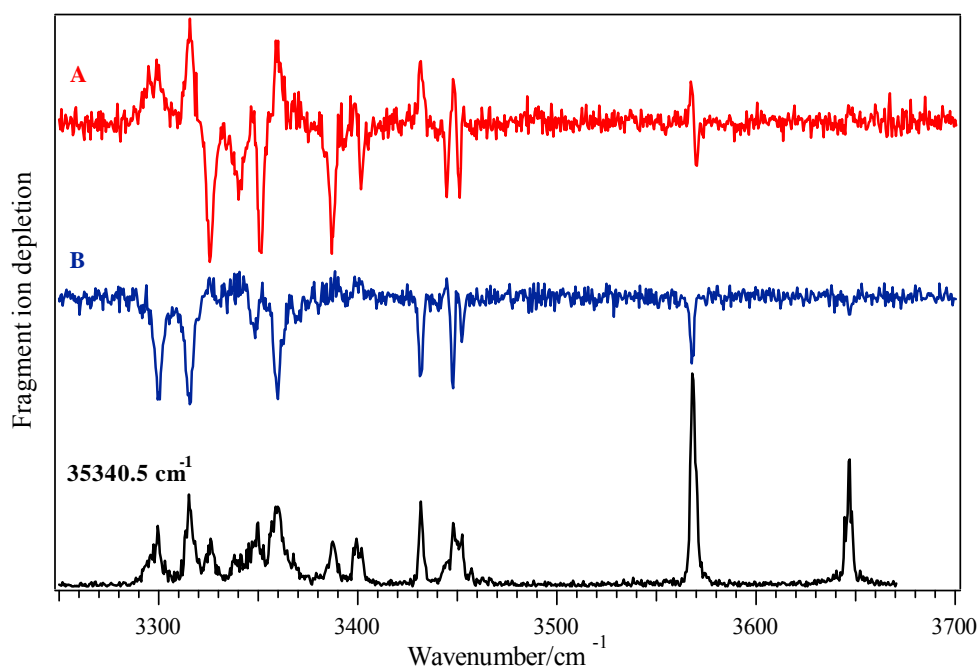


Figure 4.13: Comparison between the conformer-specific infrared spectra of Ac-Tyr-(Ala)₅-LysH⁺ with that recorded setting the UV laser at 35340.51 cm^{-1} .

Figure 4.13 compares the conformer-specific vibrational spectra of Ac-Tyr-(Ala)₅-LysH⁺ with that recorded by setting the ultraviolet laser $\sim 44\text{ cm}^{-1}$ to the red of the vibronic band origin, at 35340.5 cm^{-1} . This vibrational spectrum shows gains at the same frequencies as the vibrational bands of conformers A and B, supporting the observation that these are the unique conformational families giving rise to the electronic spectrum of Ac-Tyr-(Ala)₅-

LysH⁺. In addition, the existence of gains when the UV probe laser is to the red of the electronic absorption of the cold peptides indicates that the electronic spectrum of the IR pre-excited molecules is broader than that of the ground state species, suggesting that the resonant vibrational energy initially pumped in the peptide is redistributed among all its vibrational modes (cf. Section 3.2.2).

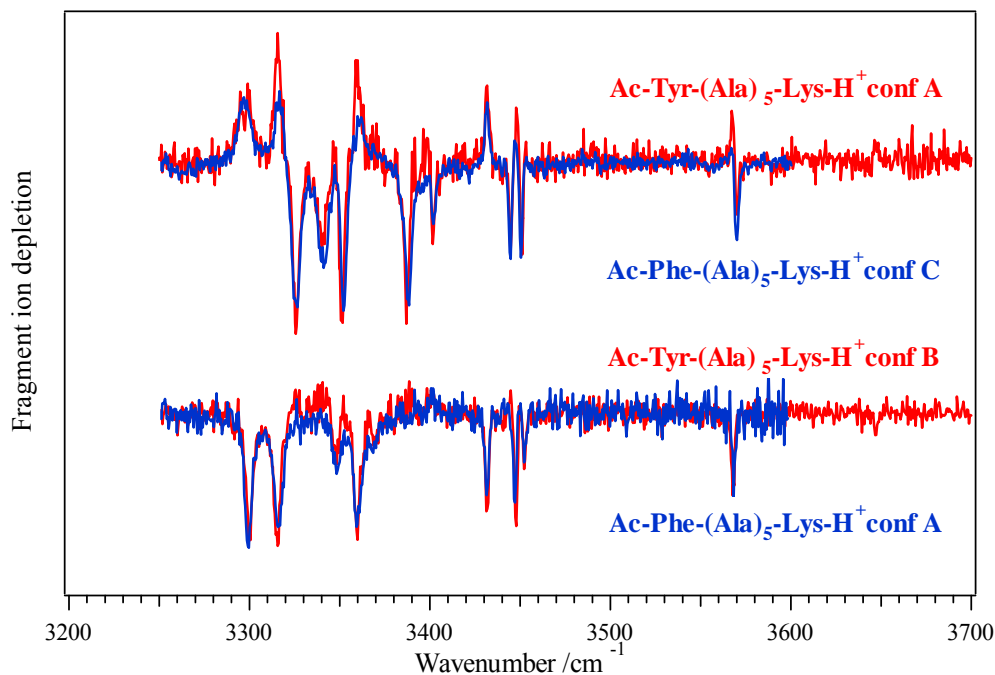


Figure 4.14: Comparison between the infrared spectra of Ac-Tyr-(Ala)₅-LysH⁺ conformer A and B (red traces) with the infrared spectra of Ac-Phe-(Ala)₅-LysH⁺ conformer C and A (blue traces) [25, 27].

Figure 4.14 shows the overlaps between the infrared spectra of the conformers A and B of Ac-Tyr-(Ala)₅-LysH⁺ with those of conformers C and A of Ac-Phe-(Ala)₅-LysH⁺, which are two helices with C₁₀-C₁₀-C₁₃-C₁₃ and C₁₀-C₁₀-C₁₀-C₁₃ backbones and the phenylalanine side chain rotated respect the C_α-C_β bond of 60° along the N-C^α-C^β-C^γ atoms (*g*⁺ configuration) [25, 27]. The perfect match between these infrared spectra suggests that conformers A and B of Ac-Tyr-(Ala)₅-LysH⁺ will have the same structures as conformers C and A of Ac-Phe-(Ala)₅-LysH⁺ respectively. In light of this observation and the presence of four distinct conformers in Ac-Phe-(Ala)₅-LysH⁺, *a priori* we expected the existence of additional conformers of Ac-Tyr-(Ala)₅-LysH⁺ but, as already discussed, no other infrared spectra were observed. A possible explanation to the fewer number of conformations in the tyrosine containing molecule is a stronger interaction between the helix macrodipole and the aromatic side chain dipole, which may preferentially stabilize certain conformations.

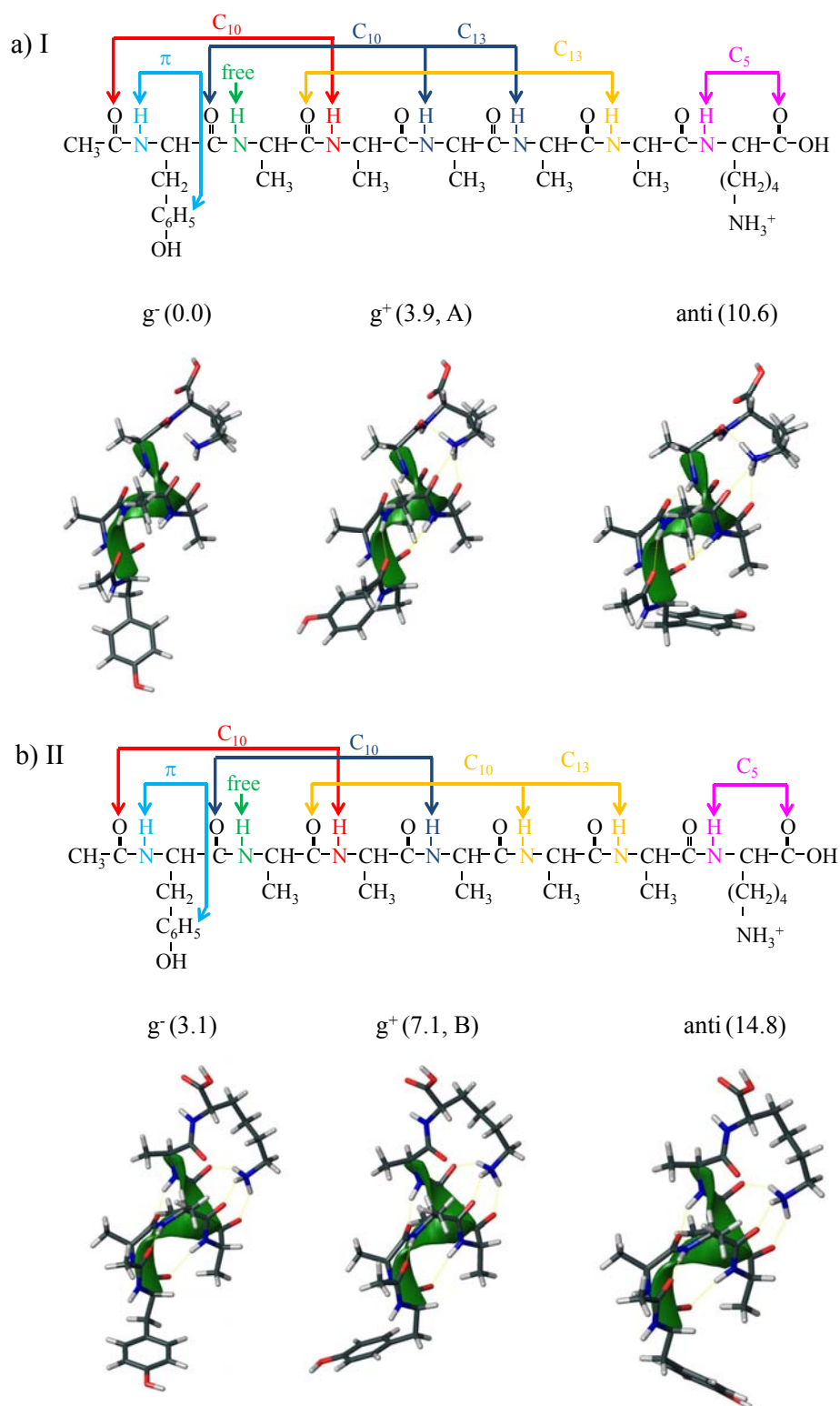


Figure 4.15: Lowest-energy calculated conformers of Ac-Tyr-(Ala)₅-LysH⁺ with the hydrogen-bonding schemes of the helices on top and the calculated structures below. The latter ones have the helix axes aligned to better show the orientations of the tyrosine ring: g^+ , g^- or *anti*. The zero-point-corrected energy in kJ/mol are also reported, along with their conformational assignments.

To confirm the backbone assignments of conformers A and B made by comparison with Ac-Phe-(Ala)₅-LysH⁺ infrared spectra, we carried out calculations on Ac-Tyr-(Ala)₅-LysH⁺, following the same procedure as the one employed for the small phenylalanine helix described in ref [27]. A conformational search, performed using the AMBER force field [14] in MACROMODEL [15], gives an initial collection of nearly all helical structures below 50 kJ/mol. Since calculations on protonated aromatic amino acids show that AMBER tends to overestimate the stabilizing effect of an NH⁺⋯OH C₅ interaction at the C-terminus by about 10-15 kJ/mol [12], all the structures with this type of interaction were eliminated from further consideration, retaining instead those with the more favorable NH⁺⋯O=C C₅ interaction. Single-point energies were then calculated using B3LYP/6-31G** in GAUSSIAN03 [16] for the remaining structures but a full geometry optimization and harmonic frequencies analysis were performed only on a subset of geometries that included all major flexible coordinates as described below.

The calculated geometries of Ac-Tyr-(Ala)₅-LysH⁺ are first classified accordingly to the hydrogen-bonding scheme of the peptide backbone. The global minimum at the B3LYP/6-31G** level of theory is a helix with two C₁₀ and two C₁₃ rings, as shown schematically in Figure 4.15a, and denoted backbone I. The hydrogen-bonded rings involve the amide NH groups of Ala³, Ala⁴, Ala⁵ and Ala⁶ in such a way that the middle two share a carbonyl, while the amide NH groups located at the end of the molecules do not participate in C₁₀ or C₁₃ interactions. The lysine NH amide group forms a C₅ arrangement with the C-terminus carbonyl, and the tyrosine amide NH can be in a π -hydrogen bond, depending on the orientation of the phenol ring. Finally, there is a free amide NH group located on Ala². The backbone of the second lowest-energy hydrogen-bonding pattern (II) has three C₁₀ rings and a C₁₃ ring, as illustrated in Figure 4.15b, with the Ala⁵ and Ala⁶ amide NH groups hydrogen-bonded to the same carbonyl. The hydrogen bonding schemes for the end residues are the same as backbone I. Backbones forming an α -helix with one C₁₀ and three C₁₃ rings (III) were also considered. In all the backbones, the ammonium group of Lys⁷ participates to hydrogen-bonds with a particular subset of carbonyl groups, providing additional stabilization interactions.

Within each family defined by a specific backbone, there are other degrees of freedom which give rise to different conformers. First, the orientation of the tyrosine side chain by

rotation with respect to the C_α - C_β bond, such that the Tyr¹ χ_1 angle, measured along the N- C^α - C^β - C^γ atoms, takes values of approximately 180° , $+60^\circ$ or -60° , corresponding to labels of *anti*, *gauche* + (g^+) and *gauche* - (g^-). In all the structures we examined, the *gauche* configurations were lower in energy than the *anti* ones because they allow a favorable π -hydrogen bond between the Tyr¹ amide NH group and the aromatic ring. This interaction seems stronger in the g^- structures (cf. Figure 4.15). Two other flexible coordinates involve the lysine. In addition to the C_5 interaction with the C-terminal carboxylic acid group previously discussed, the butyl side chain of lysine can be puckered in different ways without significantly altering the hydrogen bonding with the ammonium group. However, these changes increase the energy by at least 8kJ/mol so these structures are not considered further.

Family	Backbone	Tyr χ_1	Energy (kJ/mol)	Assignment
I	C ₁₀ -C ₁₀ -C ₁₃ -C ₁₃	g^-	0	A
I	C ₁₀ -C ₁₀ -C ₁₃ -C ₁₃	g^+	3.9	
I	C ₁₀ -C ₁₀ -C ₁₃ -C ₁₃	<i>anti</i>	10.6	
II	C ₁₀ -C ₁₀ -C ₁₀ -C ₁₃	g^-	3.1	B
II	C ₁₀ -C ₁₀ -C ₁₀ -C ₁₃	g^+	7.1	
II	C ₁₀ -C ₁₀ -C ₁₀ -C ₁₃	<i>anti</i>	14.8	
III	C ₁₀ -C ₁₃ -C ₁₃ -C ₁₃	g^-	11.3	
III	C ₁₀ -C ₁₃ -C ₁₃ -C ₁₃	g^+	15.5	
III	C ₁₀ -C ₁₃ -C ₁₃ -C ₁₃	<i>anti</i>	33.8	

Table 4.1: Structures of the calculated conformations of Ac-Tyr-(Ala)₅-LysH⁺ at the B3LYP/6-31G** level of theory, their zero-point corrected energies and assignments.

Table 4.1 summarizes the nine types of conformations that arise from the three types of backbones and the three orientations of the tyrosine side chain. In the case of Ac-Phe-(Ala)₅-LysH⁺, 3₁₀ helices with four C₁₀ rings in the backbone were identified in the calculation and found to be energetically favorable respect the C₁₀-C₁₃-C₁₃-C₁₃ arrangement [27]. Instead, Ac-Tyr-(Ala)₅-LysH⁺ lacks this 3₁₀ helical conformation, at least for the structures we examined at the B3LYP/6-31G** level of theory. Finally, we did not include the rotation of the phenolic OH as an important degree of freedom for the characterization of the helical conformations. Indeed, calculations predict slight shifts in the vibrational bands of structures which differ solely by OH orientation, suggesting each of the infrared spectra of Figure 4.12

could be associated to two helices with the same backbone and Tyr side chain orientation but opposite phenolic OH. Therefore, the orientation of the latter remains uncertain in the Ac-Tyr-(Ala)₅-LysH⁺ conformers.

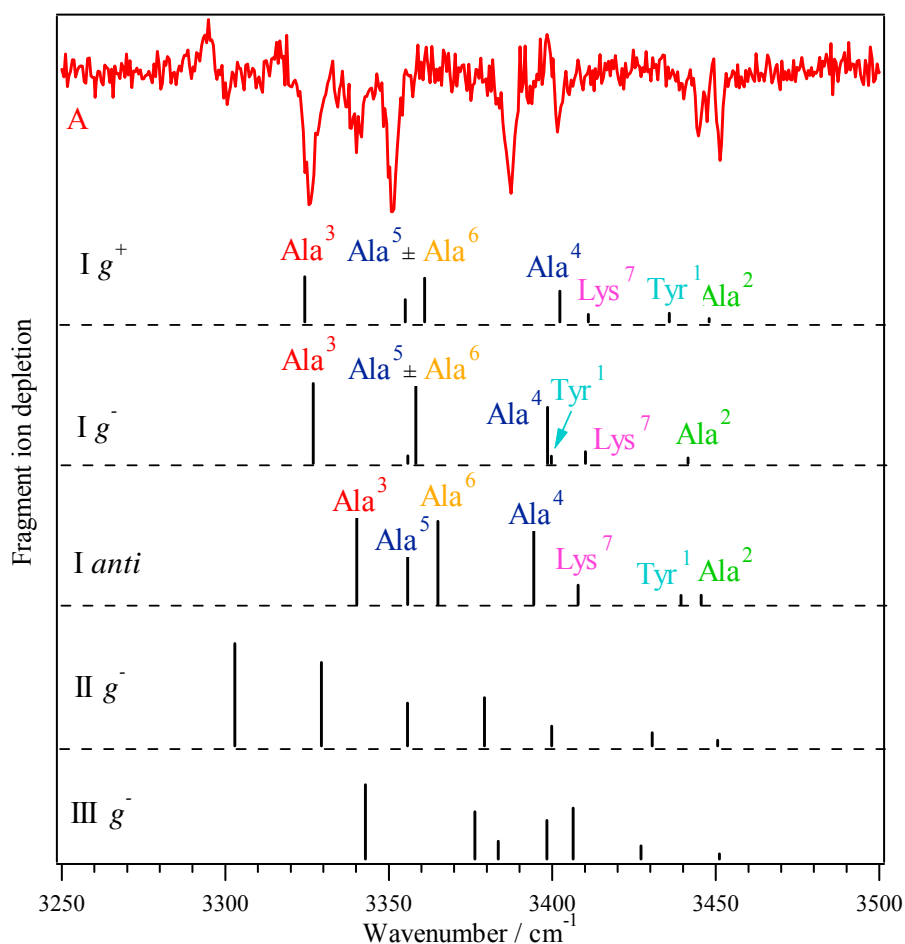


Figure 4.16: Comparison between experimental and calculated spectra at the B3LYP/631G** level of theory for conformer A of Ac-Tyr-(Ala)₅-LysH⁺. The representatives of the family with the best-matching calculated spectrum are presented directly under the experimental spectrum. The lowest-energy representatives of the other families are shown right below for comparison. The calculated spectra are scaled by 0.952

Figure 4.16 illustrates the infrared spectrum of the minor conformer A, together with several calculated spectra. The experimental data are the same as those shown in Figure 4.9, but the gains have been removed by subtracting the spectrum of conformer B. The comparison between the infrared spectrum of conformer B and some of the calculated vibrational spectra is displayed in Figure 4.17. The calculated structures matching the best the measured spectra of conformers A and B have a C₁₀-C₁₀-C₁₃-C₁₃ and a C₁₀-C₁₀-C₁₀-C₁₃ backbone respectively. Both the *anti* and *g*⁺ configurations in families I and II are reasonable

matches to conformers A and B. However, the *anti* structures are high in energy, as shown in Table 4.1, so we presume that the g^+ conformers are more likely to appear in the low-temperature conditions of our experiment. These conformers lie respectively 3.9 and 7.1 kJ/mol above the global minimum, which, however, does not fit our experimental data.

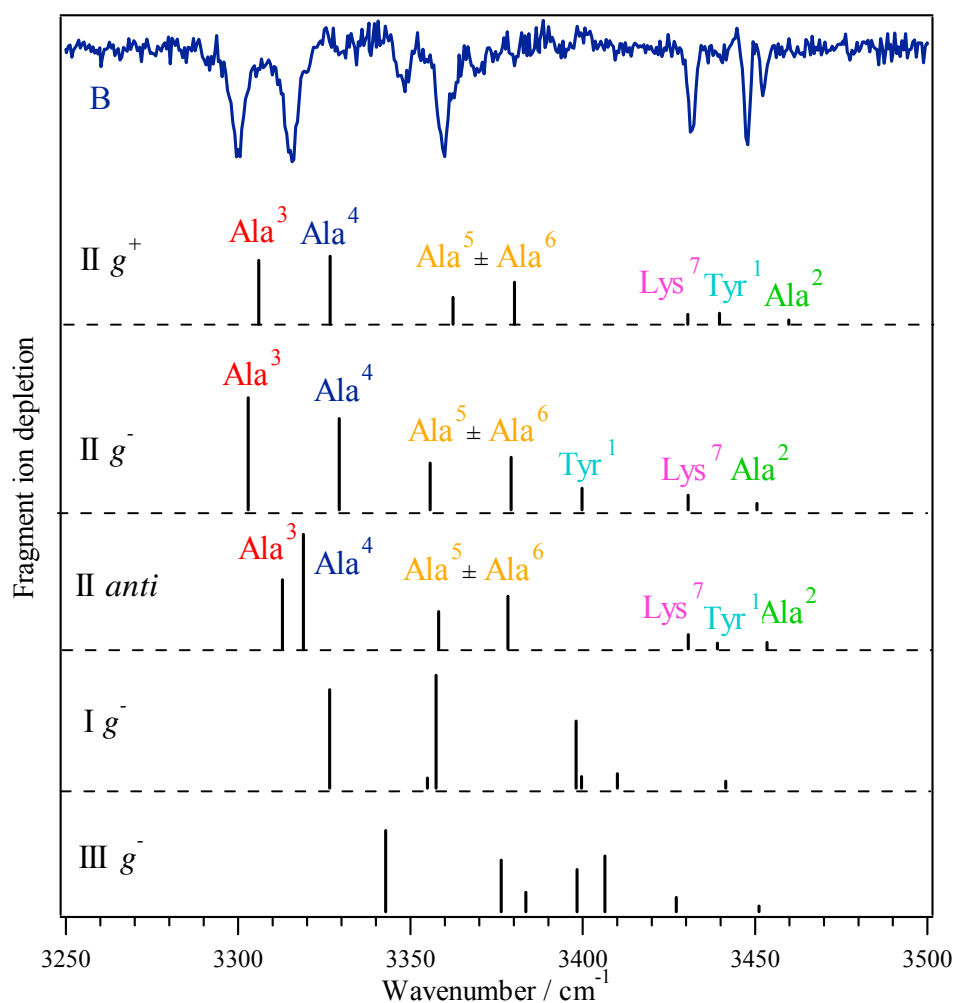


Figure 4.17: Comparison between experimental and calculated spectra at the B3LYP/6-31G** level of theory for conformer B of Ac-Tyr-(Ala)₅-LysH⁺. The representatives of the family with the best-matching calculated spectrum are presented directly under the experimental spectrum. The lowest-energy representatives of the other families are shown right below for comparison. The calculated spectra are scaled by 0.952.

These findings confirm the predictions on the conformational preferences of Ac-Tyr-(Ala)₅-LysH⁺ made by comparison with the infrared spectra of Ac-Phe-(Ala)₅-LysH⁺. As already mentioned, in the case of the latter peptide isotopic substitution was employed to assign the vibrational bands in the infrared spectrum independently from the calculations [27]. The good match between the assignments made by calculation and on the basis of

isotopic substitution for Ac-Phe-(Ala)₅-LysH⁺ conformer “C” and “A” further confirms the association between the conformations *I g*⁺ and *II g*⁺ with the minor and major conformers of Ac-Tyr-(Ala)₅-LysH⁺ respectively.

4.2.3 Ac-(Ala)₅-Phe-LysH⁺

Our interest is to investigate the influence of the position of the chromophore on the conformational preferences of a peptide. We thus decided to study Ac-(Ala)₅-Phe-LysH⁺, where the proximity of the phenyl ring to the protonated lysine side chain should give rise to a stronger interaction between the chromophore and the charge.

Figure 4.18 illustrates the electronic spectrum of Ac-(Ala)₅-Phe-LysH⁺ (*m/z* 692), recorded monitoring the *b*₅ ion (*m/z* 400) as a function of the laser wavelength. This photofragment originates by the breakage of the peptide bond between the fifth alanine and the phenylalanine residues and is attributed to dissociation on the electronic ground surface. The absorption of a UV photon also induces phenylalanine side chain loss but the signal is less intense than in the case of Ac-Tyr-(Ala)₅-LysH⁺. The band origin of Ac-(Ala)₅-Phe-LysH⁺ appears at 37437.6 cm⁻¹, ~100 cm⁻¹ to the red of the lowest-energy band origin of Ac-Phe-(Ala)₅-LysH⁺, which is at 37525.6 cm⁻¹ [27]. This shift confirms the strong interaction between the charge and the phenyl ring, as observed in the case of the tyrosine-based protonated dipeptides [34]. The ultraviolet spectra of the two seven-amino-acid, phenylalanine-containing peptides show well-resolved peaks without any background, as it happens, by contrast, in the case of Ac-Tyr-(Ala)₅-LysH⁺. It thus seems that it is the intrinsic properties of the chromophore and not its position in the peptide chain that determine the congestion in the electronic spectrum of a peptide at least of the size considered in this thesis work.

IR-UV double-resonance spectroscopy allows us to identify two distinct conformers, labeled A and B in Figure 4.18b, whose infrared spectra are illustrated in Figure 4.19. Their band origins appear at 37437.6 cm⁻¹ and 37451.9 cm⁻¹ respectively. The other transitions in the ultraviolet spectrum are, then, assigned to each conformer by IR-UV hole-burning spectroscopy by setting the infrared laser to unique vibrations of the two conformers.

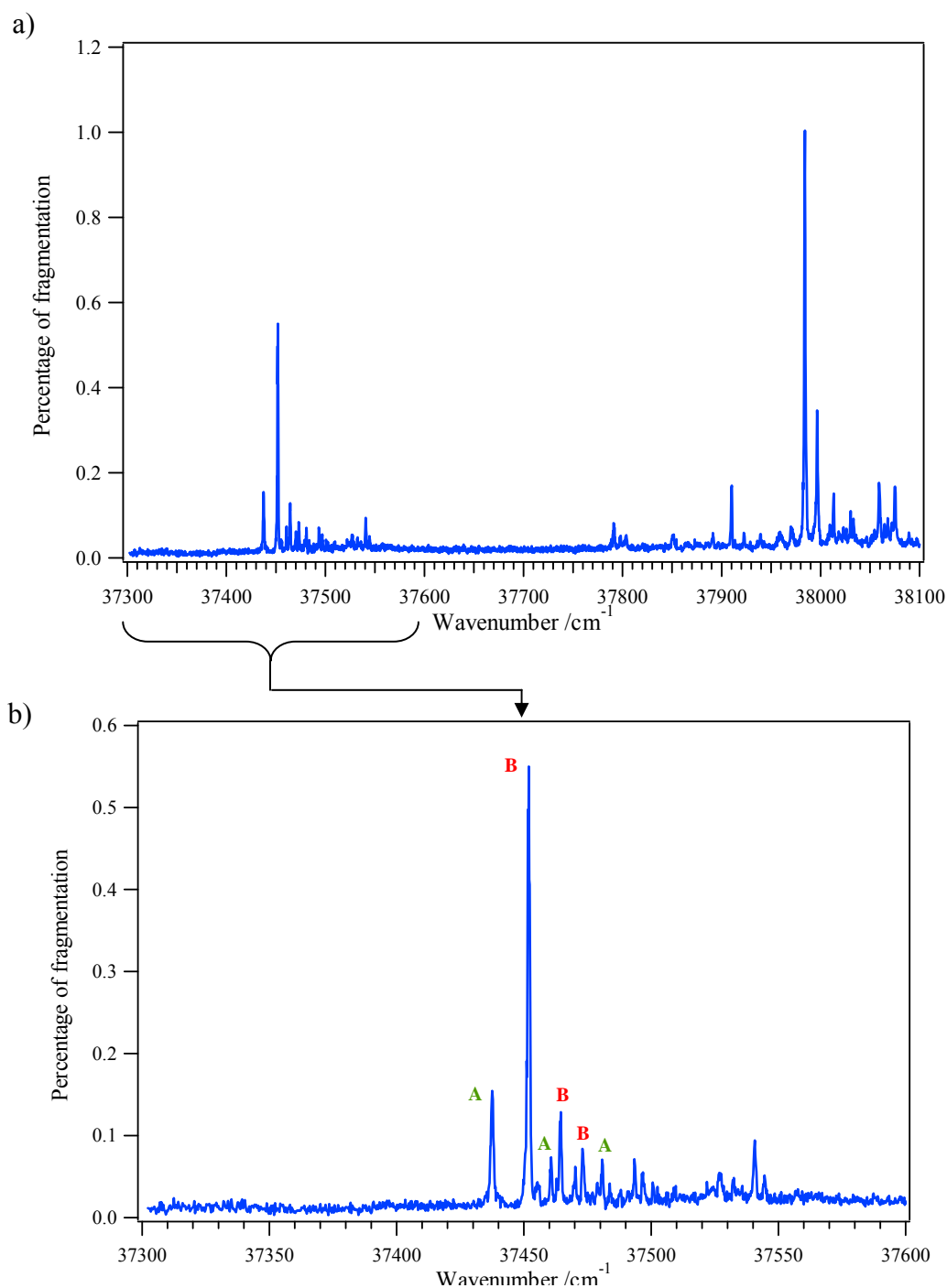


Figure 4.18: (a) Electronic spectrum of Ac-(Ala)₅-Phe-LysH⁺ recorded monitoring the photofragment m/z 400; (b) enlargement of the first 300 cm⁻¹ of the spectrum. The transitions in (b) are labeled by conformation, as determined by IR-UV double-resonance spectroscopy.

The vibronic bands at ~ 530 cm⁻¹ above the band origins of conformers A and B in Figure 4.18b correspond to the 6b vibration of benzene and its derivatives, which appears at 530 cm⁻¹ in the excited state of toluene [36]. The intensity of this transition in toluene and

other substituted benzenes derives from vibronic coupling between the L_b and $L_a \pi\pi^*$ excited states, and this is likely to be also in the case of PheH^+ [12] and $\text{Ac-(Ala)}_5\text{-Phe-LysH}^+$.

Each of the infrared spectra of Figure 4.19 contains the C-terminal carboxylic acid OH stretch around 3570 cm^{-1} . The NH stretch region of the infrared spectrum of conformer A shows seven well-resolved transitions, while in conformer B there are five resolved bands and two partially overlapped bands, which appear at 3453.6 cm^{-1} and 3456.2 cm^{-1} . Moreover, the infrared spectrum of conformer B looks like the vibrational spectrum of conformer “A” of $\text{Ac-Phe-(Ala)}_5\text{-LysH}^+$, suggesting a $\text{C}_{10}\text{-C}_{10}\text{-C}_{10}\text{-C}_{13}$ backbone rearrangement. The infrared spectrum of conformer A resembles the overall structure of that of conformer “C” of $\text{Ac-Phe-(Ala)}_5\text{-LysH}^+$, thus a $\text{C}_{10}\text{-C}_{10}\text{-C}_{13}\text{-C}_{13}$ backbone, but it is red-shifted with respect to the latter one.

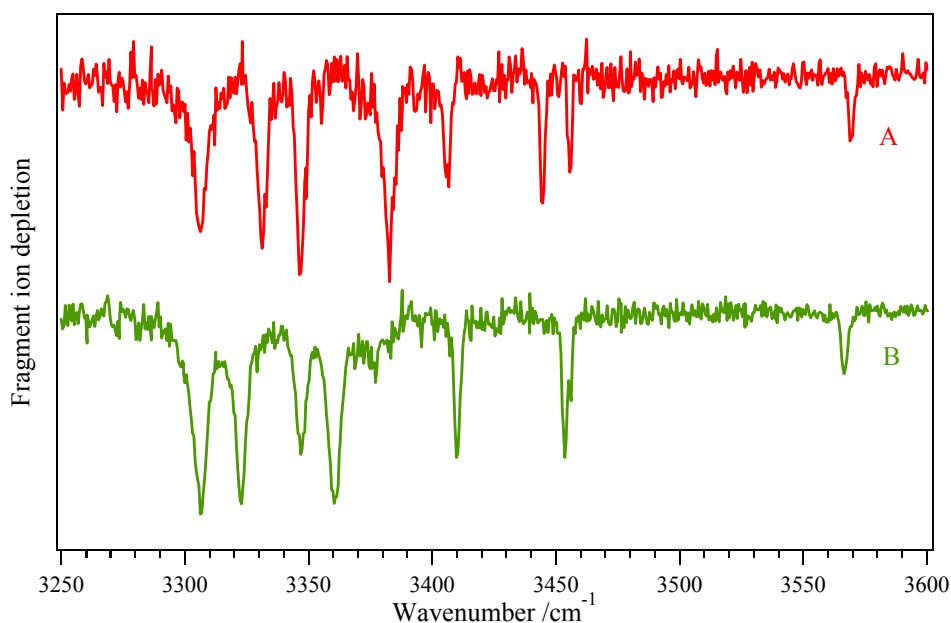


Figure 4.19: Infrared spectra of $\text{Ac-(Ala)}_5\text{-Phe-LysH}^+$ recorded setting the UV laser at 37437.6 cm^{-1} and 37451.9 cm^{-1} , the band origins of conformer A and B respectively.

Calculations were performed to associate a geometry to each conformer following the same procedure described for $\text{Ac-Tyr-(Ala)}_5\text{-LysH}^+$ in the previous section. A conformational search, carried out employing the AMBER force field [14] in MACROMODEL [15], serves to generate starting structures, whose single-point energies are evaluated using B3LYP/6-31 G** in GAUSSIAN [16]. These geometries are then sorted into families accordingly to the hydrogen-bonding patterns of the peptide backbone. Finally, full geometry optimization and harmonic frequencies analysis are performed on a subset of structures

within each family that differ by the rotation of the phenylalanine side chain with respect to the C_α - C_β bond. The global minimum at the B3LYP/6-31 G** level of theory has a C_{10} - C_{10} - C_{13} - C_{13} backbone rearrangement (family I) with the phenyl ring in the *anti* configuration. With respect to the Ac-Tyr-(Ala)₅-LysH⁺, the family with one C_{10} and three C_{13} rings is missing while two new ones are identified, the 3_{10} helix (III), present in Ac-Phe-(Ala)₅-LysH⁺ [25, 27], and the C_{10} - C_{13} - C_{13} - C_{10} (IV), which is completely different from all the backbones found up to now. Table 4.2 summarizes the structures considered for frequency calculations that arise from the different backbone families and phenylalanine side chain orientations. In addition to the helical structures previously described, several non-helical backbones higher in energy were considered, but only the C_{16} - C_{18} - C_7 - C_7 is discussed in this paragraph, as an example. This backbone rather corresponds to a globular structure, where the C-terminal carboxylic acid OH does not participate in any hydrogen-bonds since its stretch vibration appears at $\sim 3579.4\text{ cm}^{-1}$ close to that calculated for the helical peptides.

Family	Backbone	Phe χ_1	Energy (kJ/mol)	Assignment
I	C_{10} - C_{10} - C_{13} - C_{13}	<i>anti</i>	0	
I	C_{10} - C_{10} - C_{13} - C_{13}	g^-	5.1	
I	C_{10} - C_{10} - C_{13} - C_{13}	g^+	35.3	
II	C_{10} - C_{10} - C_{10} - C_{13}	g^-	2.8	
II	C_{10} - C_{10} - C_{10} - C_{13}	<i>anti</i>	5.5	
II	C_{10} - C_{10} - C_{10} - C_{13}	g^+	16.5	
III	C_{10} - C_{10} - C_{10} - C_{10}	<i>anti</i>	7.5	B
III	C_{10} - C_{10} - C_{10} - C_{10}	g^-	9.2	
III	C_{10} - C_{10} - C_{10} - C_{10}	g^+	40.3	
IV	C_{10} - C_{13} - C_{13} - C_{10}	g^+	25.6	
V	C_{16} - C_{18} - C_7 - C_7	<i>anti</i>	30.8	

Table 4.2: Structures of the calculated conformations of Ac-(Ala)₅-Phe-LysH⁺ at the B3LYP/6-31G** level of theory, their zero-point corrected energies and assignments.

Figure 4.20 compares the infrared spectrum of conformer A with several calculated spectra at the B3LYP/6-31 G** level of theory. The infrared spectrum of the C_{10} - C_{10} - C_{13} - C_{13} g^- geometry resembles that of conformer A, but it seems not to be the right structure since the frequencies of the hydrogen-bonded NH stretches appear higher in energy than those of the

measured spectrum. In fact, none of the calculated spectra show an acceptable level of agreement with the vibrational spectrum of conformer A, even when considering non-helical geometries. Thus it was not possible for us to assign a structure to conformer A and determine whether it is a helical or a globular peptide.

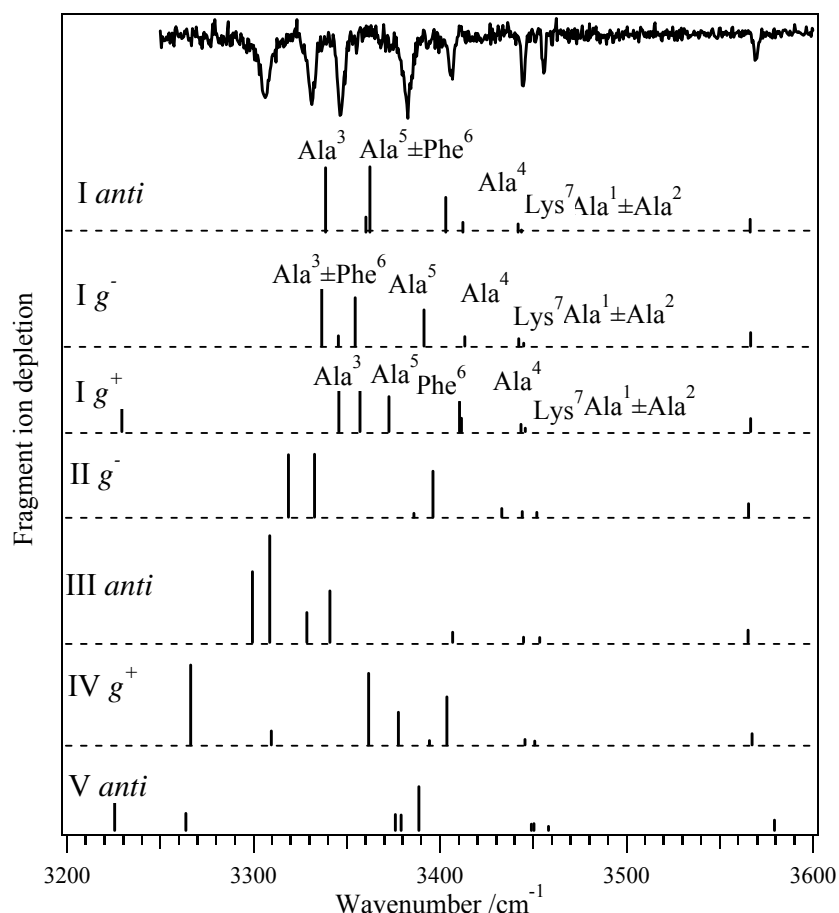


Figure 4.20: Comparison between experimental and calculated spectra at the B3LYP/6-31G** level of theory for conformer A of Ac-(Ala)₅-Phe-LysH⁺. The calculated IR spectra of the lowest-energy family are presented under the experimental spectrum. The lowest-energy representatives of the other families are shown right below for comparison. The calculated spectra are scaled by 0.952.

Figure 4.21 shows the infrared spectrum of conformer B and those calculated for several representatives of the identified families. The vibrational spectrum associated to the 3_{10} *anti* geometry matches the best that of conformer B, which thus seems to be a helical peptide. These results demonstrate the difficulty of predicting the geometry associated with a given infrared spectrum by comparing the measured vibrational spectra of peptides that differ by only the position of the chromophore even if their spectra resembles each other. Indeed, the infrared spectrum of Ac-(Ala)₅-Phe-LysH⁺ conformer B resembles that of Ac-Phe-(Ala)₅-LysH⁺ conformer C [25, 27] but calculations at the B3LYP/6-31 G** level of

theory suggests that the former is a 3_{10} helix while the backbone of the latter has two C_{10} and two C_{13} rings.

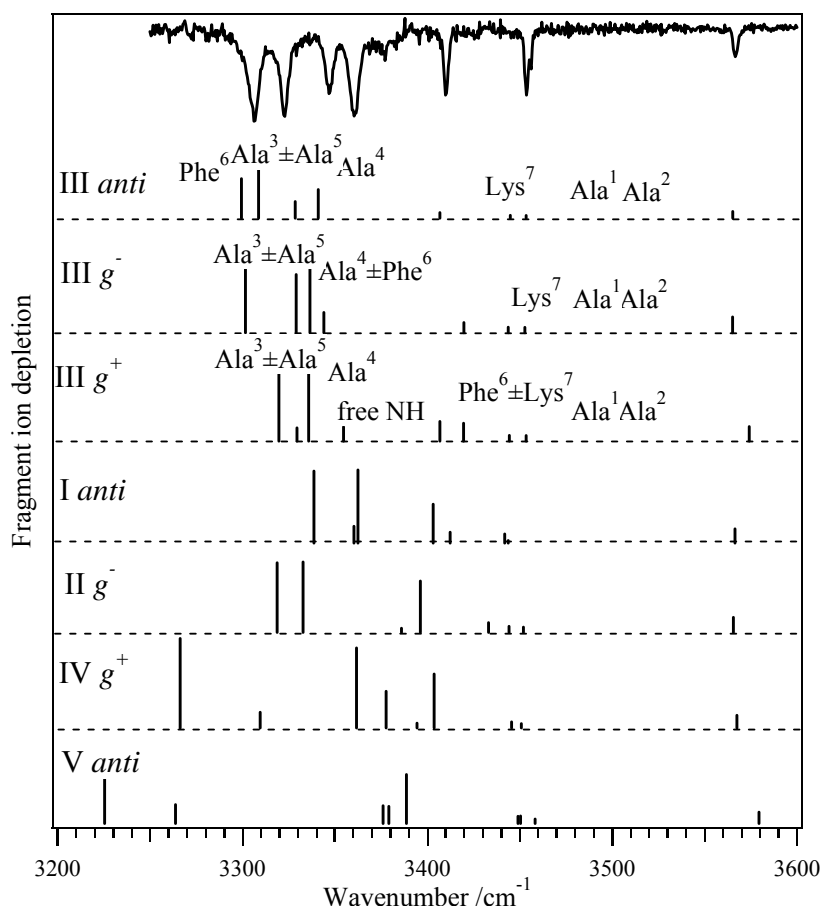


Figure 4.21: Comparison between experimental and calculated spectra at the B3LYP/6-31G** level of theory for conformer B of Ac-(Ala)₅-Phe-LysH⁺. The best-matching calculated spectrum is presented directly under the experimental spectrum. The other members of this family together with the lowest-energy representatives of the other families are shown right below for comparison. The calculated spectra are scaled by 0.952.

4.2.4 Ac-Tyr-(Ala)₄-Phe-LysH⁺

As already mentioned, after having analyzed the properties of peptides containing a single aromatic amino acid, the next level of complexity is to investigate molecules containing two chromophores, since natural peptides typically contain several of them. In addition, studying a double-chromophore peptide can help elucidate the mechanism of IR-UV double-resonance spectroscopy. Indeed, assuming that intramolecular vibrational energy redistribution (IVR) does not take place in the peptides on the time scale of the delay between the IR and the UV lasers, the absorption of a resonant IR photon might shift the electronic spectrum of a molecule due to the coupling between the vibrational and electronic degrees of

freedom (Section 3.2.2). In order to observe dips in the UV induced photofragment signal, the electronic transitions from the ground and the vibrationally excited states should have significantly different Frank-Condon factors. If this is the correct mechanism of the IR-UV double-resonance technique, then only the vibrational modes involving bonds vibration in the vicinity of the UV probe chromophore, for which one might expect a geometry change upon electronic excitation, will contribute to the infrared spectrum. This would imply that, in the case of a double-chromophore peptide, two different vibrational spectra might be recorded depending on the chromophore used as a probe.

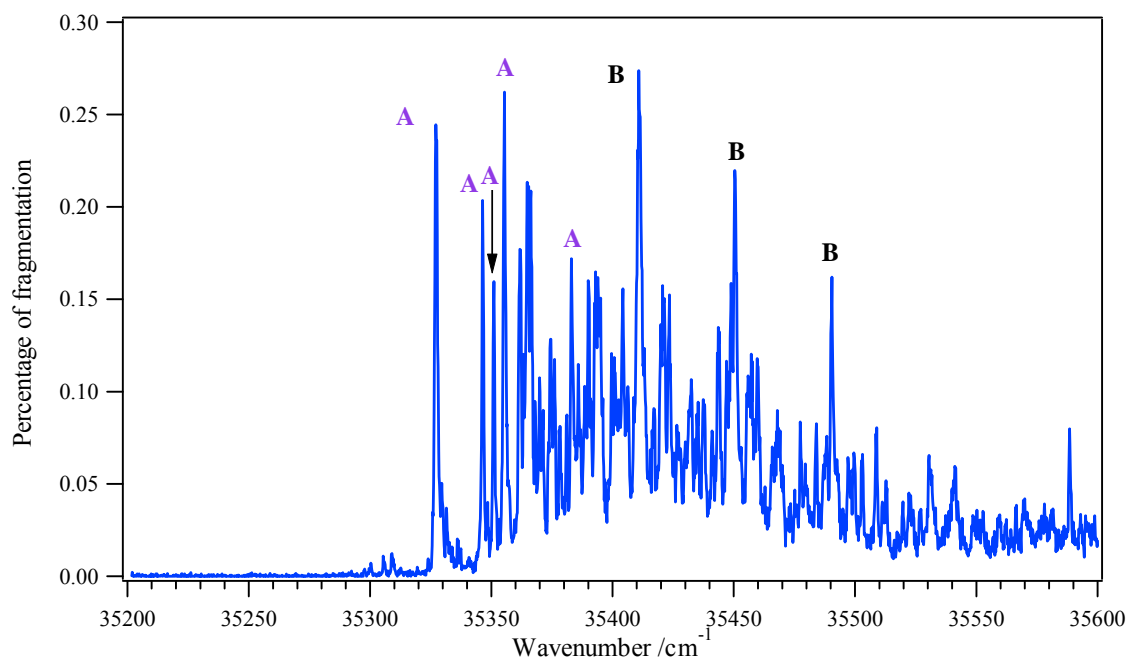


Figure 4.22: Electronic spectrum of Ac-Tyr-(Ala)₄-Phe-LysH⁺ in the first 400 cm⁻¹, recorded monitoring the photofragment m/z 677. The transitions are labeled by conformation, as determined by IR-UV double-esonance spectroscopy.

In light of the complete analysis on the electronic and vibrational spectra of Ac-Tyr-(Ala)₅-LysH⁺ and Ac-(Ala)₅-Phe-LysH⁺ discussed in the previous sections, a seven-amino-acid peptide containing a tyrosine at the N-terminus and a phenylalanine close to the C-terminal lysine, namely Ac-Tyr-(Ala)₄-Phe-LysH⁺ (m/z 784), was studied. These chromophores absorb in two distinct regions of the ultraviolet spectrum so our expectation is to distinguish easily between them. Figure 4.22 illustrates the ultraviolet spectrum of the double-chromophore peptide in the low-energy region, where tyrosine is responsible for the absorption. The spectrum is recorded monitoring the photofragment due to the C_α-C_β cleavage of the tyrosine residue, the main LID product of Ac-Tyr-(Ala)₄-Phe-LysH⁺, as shown in Figure 4.23. All its major dissociation products involve the tyrosine side chain loss,

while the photofragment due to the phenylalanine side chain loss, also marked in the photofragment mass spectrum of Figure 4.23, is not a significant dissociation channel.

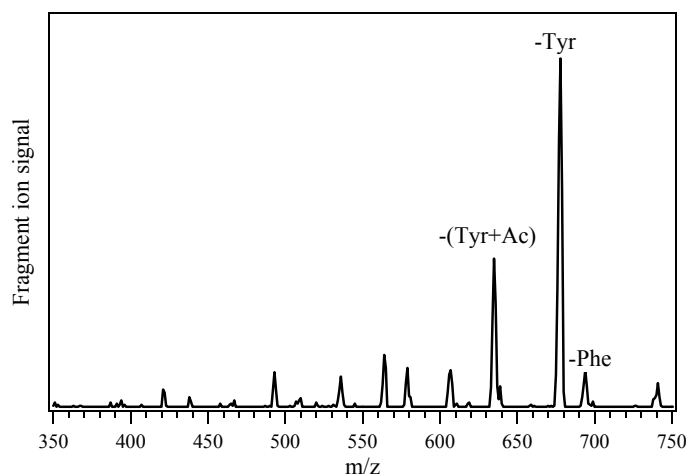


Figure 4.23: Fragment mass spectrum of Ac-Tyr-(Ala)₄-Phe-LysH⁺ measured fixing the ultraviolet laser at the molecule band origin, 35327.1 cm⁻¹. The same spectrum is obtained setting the laser at 35410.9 cm⁻¹, band origin of conformer B, and at 37419.6 cm⁻¹, which is attributed to phenylalanine absorption.

In order to characterize the coupling of the two chromophores in Ac-Tyr-(Ala)₄-Phe-LysH⁺, its electronic spectrum is compared to those of the single-chromophore peptides Ac-Tyr-(Ala)₅-LysH⁺ and Ac-(Ala)₅-Phe-LysH⁺ in Figure 4.24a. The two enlargements in the tyrosine and phenylalanine absorption region, respectively Figure 4.24b and Figure 4.24c, shows that the electronic spectrum of Ac-Tyr-(Ala)₄-Phe-LysH⁺ differs slightly from that of Ac-Tyr-(Ala)₅-LysH⁺. Indeed, even if it appears red-shifted respect that of the tyrosine-containing helix, the strength of the absorptions and the overall pattern of bands seem to be determined uniquely by the tyrosine vibronic activity, suggesting a weak coupling between the two chromophores. However, the Ac-Tyr-(Ala)₅-LysH⁺ lacks of an intense peak in the phenylalanine absorption region. Therefore, the strong vibronic transition at 37419.6 cm⁻¹ in the electronic spectrum of Ac-Tyr-(Ala)₄-Phe-LysH⁺ is attributed to phenylalanine photoabsorption. The ultraviolet spectrum of the double-chromophore peptide in the phenylalanine region is red-shifted also respect to Ac-(Ala)₅-Phe-LysH⁺. This might indicate no more than a weak coupling between the two chromophores. Indeed, in the case of an interaction between the two aromatic amino acids one would expect a symmetric shift in their electronic absorptions, so that the intense peak in the ultraviolet spectrum of Ac-Tyr-(Ala)₄-Phe-LysH⁺ should be blue-shifted respect to that of Ac-(Ala)₅-Phe-LysH⁺.

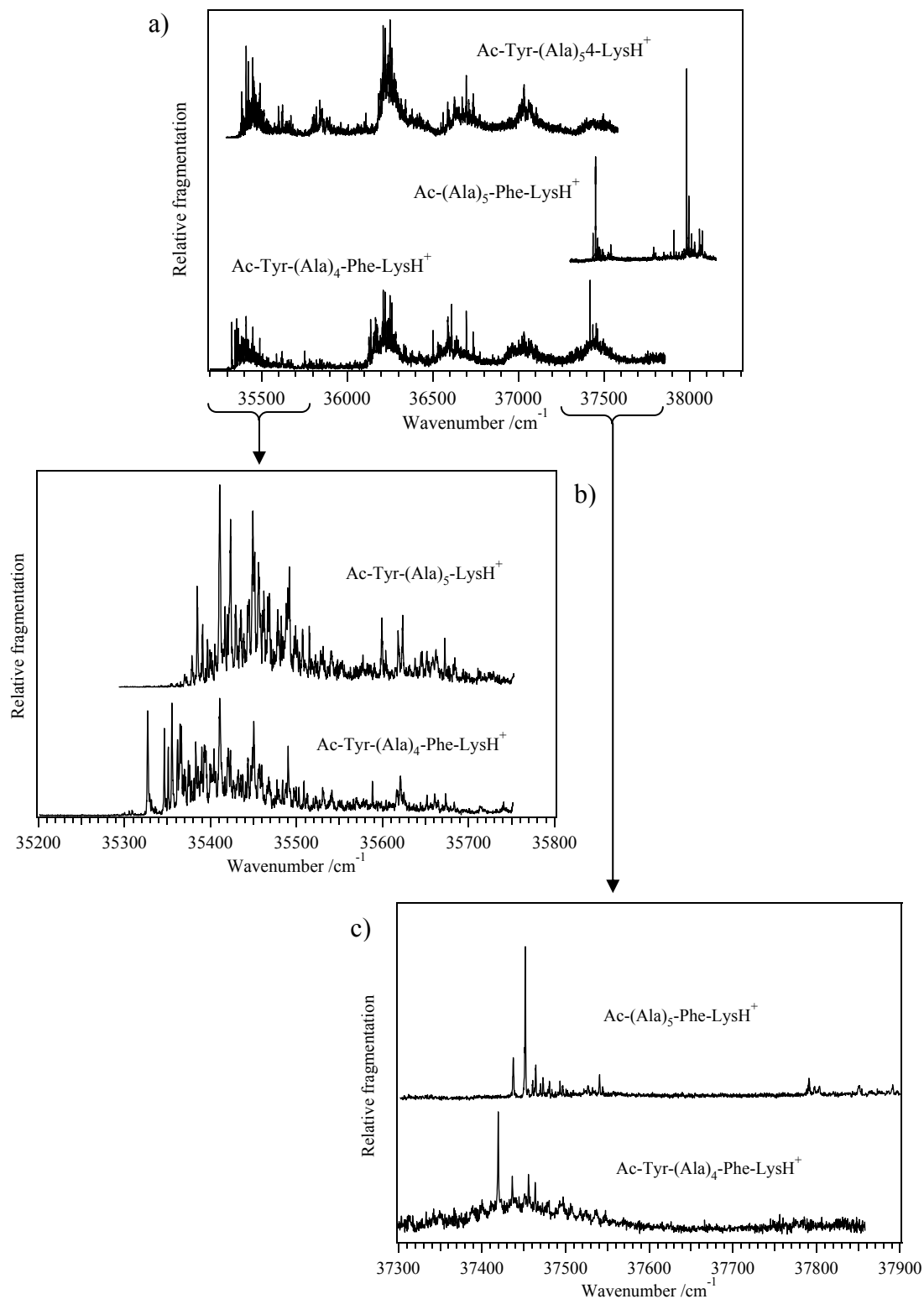


Figure 4.24: Comparison between the electronic spectra of $\text{Ac-Tyr-(Ala)}_4\text{-Phe-LysH}^+$ and $\text{Ac-Tyr-(Ala)}_5\text{-LysH}^+$ and $\text{Ac-(Ala)}_5\text{-Phe-LysH}^+$ (a). The enlargements of the spectra in the tyrosine and phenylalanine absorption regions are respectively illustrated in (b) and (c).

It is worth mentioning that the photofragment mass spectrum of the double-chromophore peptide presents the same features independent of the wavelength of the pumping laser, also when considering the phenylalanine absorption peak at 37419.6 cm^{-1} . This suggests a transfer of electronic energy from the higher-energy chromophore, phenylalanine, to the lowest-energy one, tyrosine.

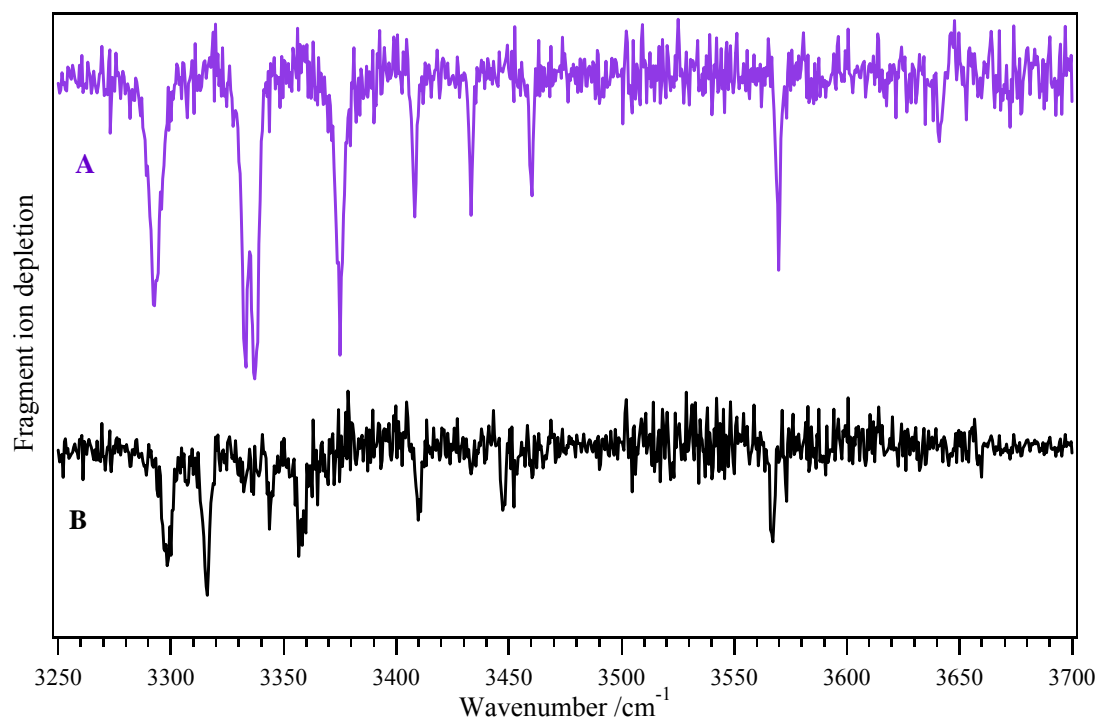


Figure 4.25: Infrared spectra of Ac-Tyr-(Ala)₄-Phe-LysH⁺ recorded setting the UV laser at 35327.1 cm^{-1} (violet trace) and 35410.9 cm^{-1} (black trace), band origins of conformer A and B respectively.

IR-UV double-resonance spectroscopy allows us identifying two conformers, labeled A and B in Figure 4.22, whose band origins appear at 35327.1 cm^{-1} and 35410.9 cm^{-1} . Figure 4.25 depicts their vibrational spectra, already corrected by the mutual gains each conformer exhibits due to infrared bands of the other one. The carboxylic acid OH vibrations occur at $\sim 3567.2\text{ cm}^{-1}$ for conformer A and $\sim 3569.8\text{ cm}^{-1}$ for conformer B, while the phenolic OH stretch is distinguishable only for the former structure $\sim 3641.1\text{ cm}^{-1}$. In analogy with Ac-Tyr-(Ala)₅-LysH⁺, this vibration in the infrared spectrum of B might lie underneath the gain due to the population spanned by conformer A. Since the subtraction process, employed to get rid of the gains in both infrared spectra, is not perfect, the OH vibration of the tyrosine ring remains difficult to observe in the infrared spectrum of conformer B. Seven well-resolved bands appear in the NH stretch region for both conformers, as it is in the case

of the single-chromophore helices. The infrared spectrum of conformer B resembles that of conformer “A” in Ac-Phe-(Ala)₅-LysH⁺ [25, 27], suggesting a C₁₀-C₁₀-C₁₀-C₁₃ backbone rearrangement. On the other hand, the spectrum of A is quite different from those measured for all the other protonated, seven-amino-acid, single-chromophore peptides investigated in this thesis work. Hence, calculations were performed, following the same procedure as for the single-chromophore peptides, in order to assign a structure to the two conformers. Also in the case of Ac-Tyr-(Ala)₄-Phe-LysH⁺, the geometries generated by a conformational search in MACROMODEL [15] are sorted into different families depending on their backbone arrangements after DFT single-point energy calculations at the B3LYP/6-31 G** level of theory. However, it is necessary to consider the orientations of the two aromatic rings, which can be *g*⁺, *g*[−] or *anti*, to define a complete set of candidate structures for further frequency analysis.

Family	Backbone	Phe χ_1	Tyr χ_2	Energy (kJ/mol)	Assignment
I	C ₁₀ -C ₁₀ -C ₁₀ -C ₁₃	<i>g</i> [−]	<i>g</i> [−]	0	
I	C ₁₀ -C ₁₀ -C ₁₀ -C ₁₃	<i>anti</i>	<i>g</i> [−]	3.2	B
I	C ₁₀ -C ₁₀ -C ₁₀ -C ₁₃	<i>g</i> [−]	<i>g</i> ⁺	4.1	
I	C ₁₀ -C ₁₀ -C ₁₀ -C ₁₃	<i>anti</i>	<i>g</i> ⁺	6.3	B
I	C ₁₀ -C ₁₀ -C ₁₀ -C ₁₃	<i>g</i> [−]	<i>anti</i>	12.7	
I	C ₁₀ -C ₁₀ -C ₁₀ -C ₁₃	<i>anti</i>	<i>anti</i>	14.7	
I	C ₁₀ -C ₁₀ -C ₁₀ -C ₁₃	<i>g</i> ⁺	<i>g</i> ⁺	17.9	
I	C ₁₀ -C ₁₀ -C ₁₀ -C ₁₃	<i>g</i> ⁺	<i>anti</i>	26.1	
II	C ₁₀ -C ₁₀ -C ₁₃ -C ₁₃	<i>g</i> ⁺	<i>anti</i>	0.7	
II	C ₁₀ -C ₁₀ -C ₁₃ -C ₁₃	<i>anti</i>	<i>g</i> [−]	3.6	
II	C ₁₀ -C ₁₀ -C ₁₃ -C ₁₃	<i>g</i> [−]	<i>g</i> ⁺	6.1	
II	C ₁₀ -C ₁₀ -C ₁₃ -C ₁₃	<i>anti</i>	<i>anti</i>	6.5	
II	C ₁₀ -C ₁₀ -C ₁₃ -C ₁₃	<i>g</i> [−]	<i>anti</i>	11.8	
III	C ₇ -C ₁₀ -C ₁₀ -C ₁₃	<i>anti</i>	<i>anti</i>	19.9	

Table 4.3: Structures of the calculated conformations of Ac-Tyr-(Ala)₄-Phe-LysH⁺ at the B3LYP/6-31G** level of theory, their zero-point corrected energies and assignments.

The lowest-energy structure at the B3LYP/6-31 G** level of theory is a C₁₀-C₁₀-C₁₀-C₁₃ helix with both the phenylalanine and the tyrosine side chains in the *g*[−] configuration. Among all the structures investigated, it is possible to identify only one other helical family,

characterized by a C₁₀-C₁₀-C₁₃-C₁₃ backbone. Table 4.3 shows the helical conformations and one representative of the non-helical structures considered for frequencies calculations. The number of different geometries in Table 4.3 that arise from the helical families and the orientations of the two aromatic rings is clearly lower than that one would expect *a priori* considering all the possible combinations of the aromatic rings orientations.

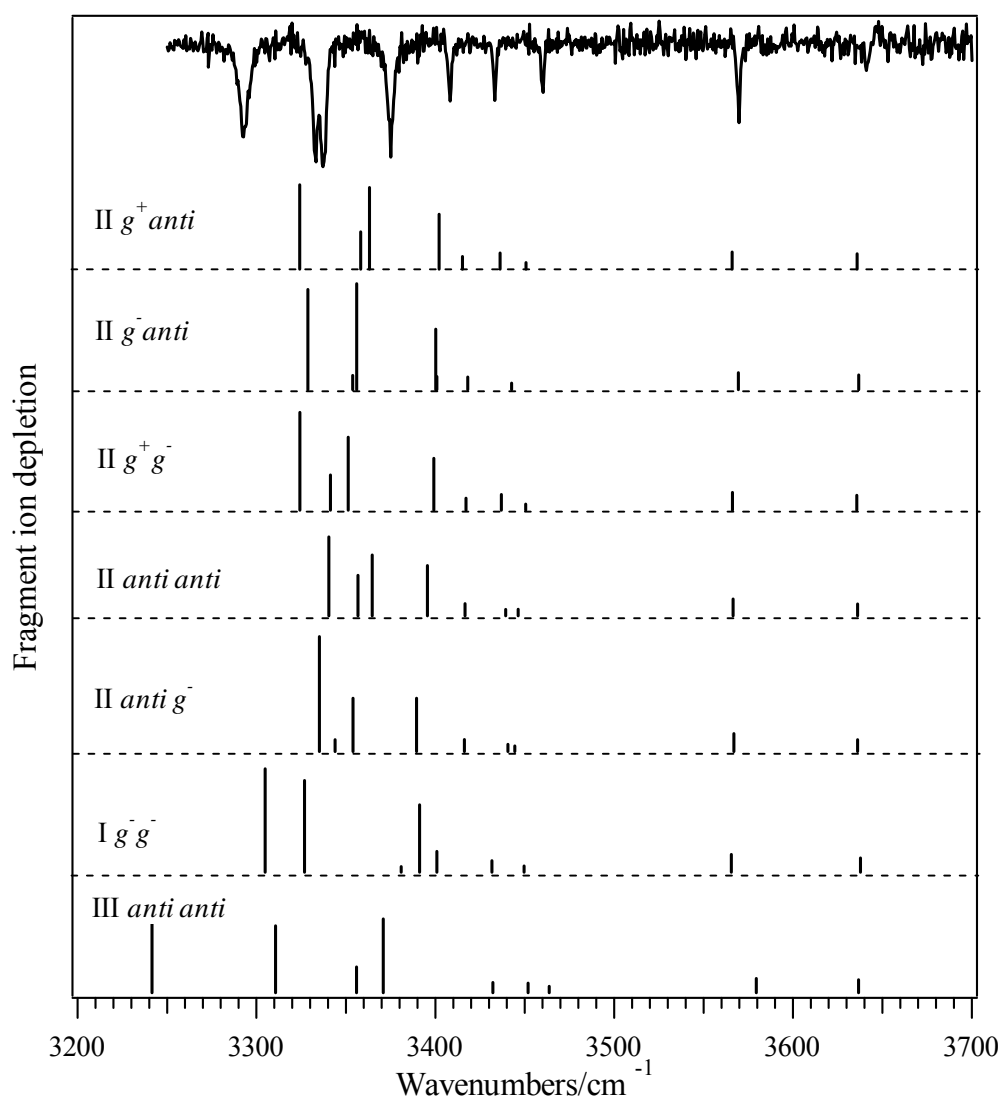


Figure 4.26: Comparison between experimental and calculated spectra at the B3LYP/6-31G** level of theory for conformer A of Ac-Tyr-(Ala)₄-Phe-LysH⁺. The calculated IR spectra of the family II and of the other lowest energy families are presented under the experimental spectrum. The calculated spectra are scaled by 0.952.

Figure 4.26 compares the infrared spectrum of conformer A with several calculated vibrational spectra. None of the calculated spectra match the experimental data for conformer A very well. The infrared spectra of both the I *anti g*⁻ and the I *anti g*⁺ geometries represent a

good match with the vibrational spectrum of conformer B (cf. Figure 4.27). This suggests that the conformer B could be a C₁₀-C₁₀-C₁₀-C₁₃ helix with the phenylalanine side chain in the *anti* configuration, although nothing can be inferred about the tyrosine ring orientation.

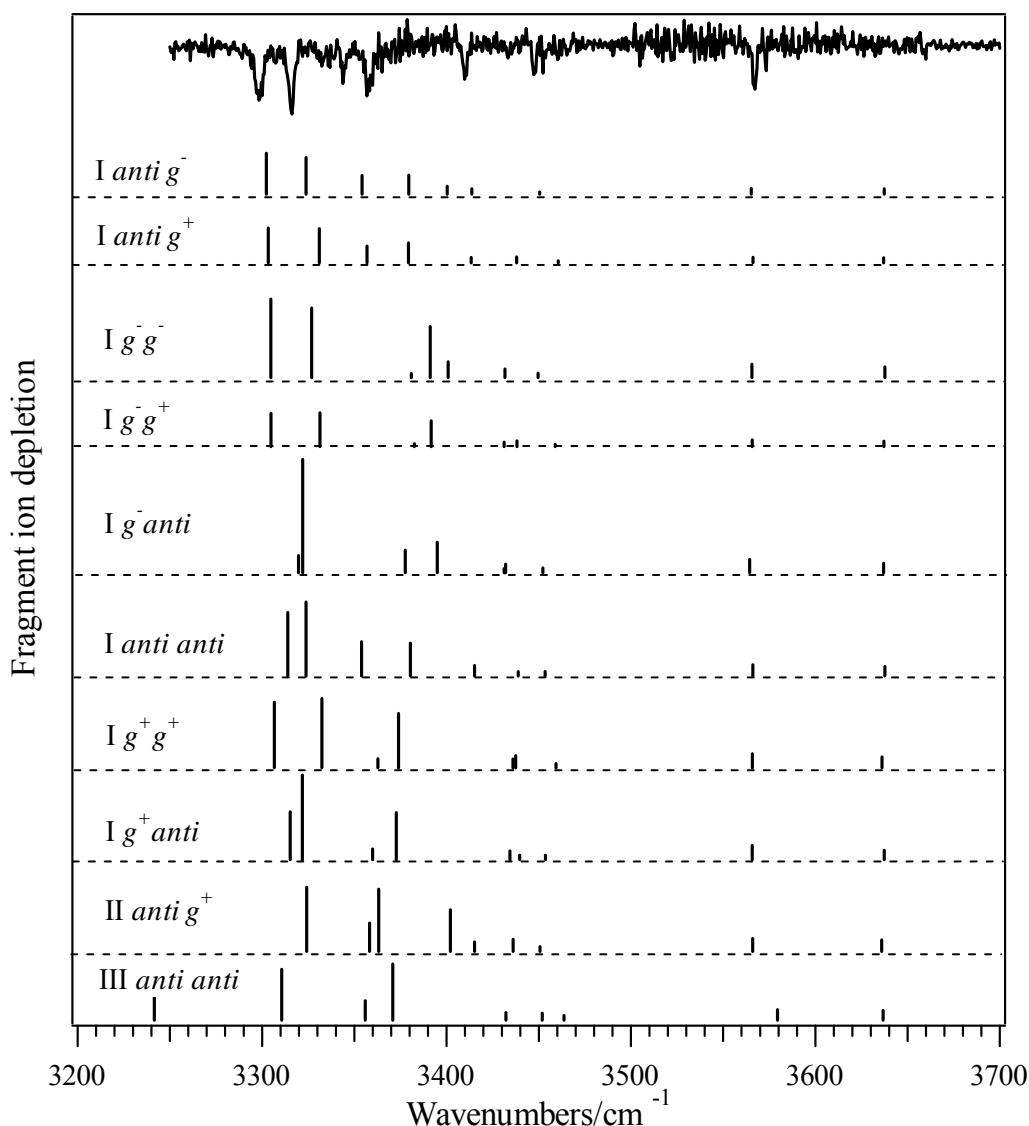


Figure 4.27: Comparison between experimental and calculated spectra at the B3LYP/6-31G** level of theory for conformer B of Ac-Tyr-(Ala)₄-Phe-LysH⁺. The best-matching calculated spectra are presented directly under the experimental spectrum. The other members of this family together with the lowest-energy representatives of the other families are shown right below for comparison. The calculated spectra are scaled by 0.952.

Figure 4.28 displays the infrared spectra of Ac-Tyr-(Ala)₄-Phe-LysH⁺ measured at the vibronic band origin of conformer A, where tyrosine is responsible for the absorption, and at 37419.6 cm⁻¹, which was previously attributed to phenylalanine photabsorption. The perfect match between these spectra demonstrates that this vibronic band belongs to conformer A.

Unfortunately, it is impossible to attribute with absolute confidence other vibronic transitions to phenylalanine absorption in the higher-energy region of the ultraviolet spectrum and, thus, to assign any vibronic bands belonging to conformer B to this chromophore absorption.

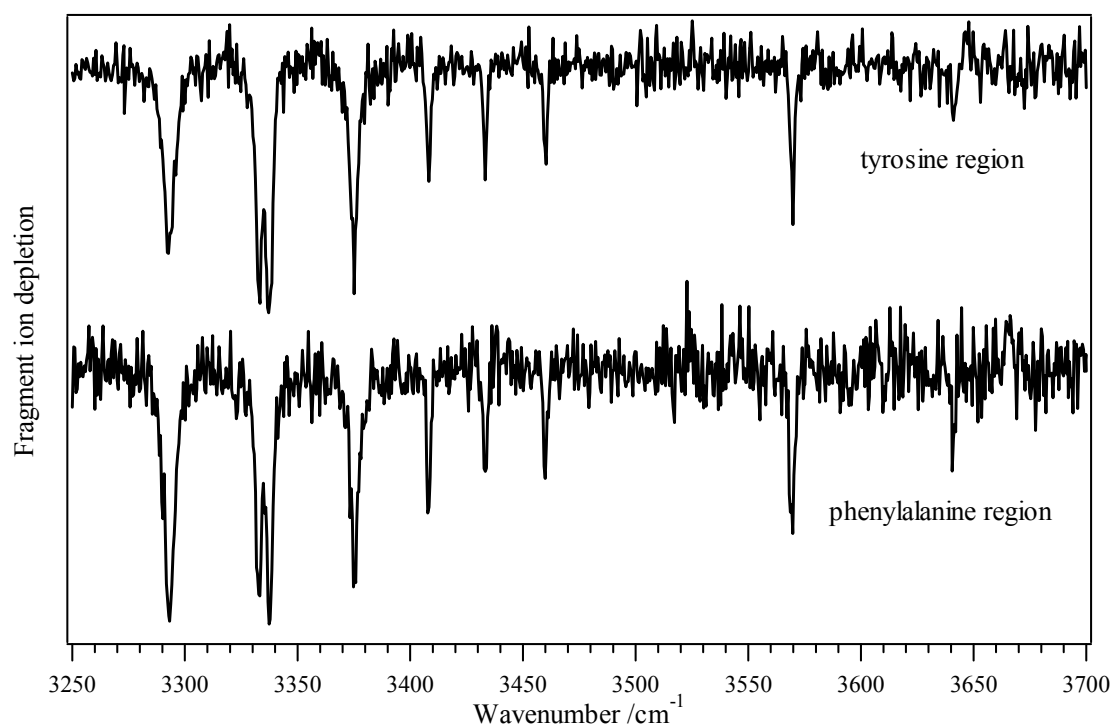


Figure 4.28: Comparison between the infrared spectrum of Ac-Tyr-(Ala)₄-Phe-LysH⁺ recorded setting the UV laser at 35327.1 cm⁻¹ (upper trace) with that measured at 37419.6 cm⁻¹ (lower trace), respectively band origin of conformer A and absorption peak in the phenylalanine region.

The result obtained on conformer A nevertheless suggests that all the vibrational modes of Ac-Tyr-(Ala)₄-Phe-LysH⁺ contribute to its infrared spectra independent of the pumped chromophores. This indicates that IVR takes place in the peptide on the timescale of the typical delay between the IR and the UV lasers in the IR-UV double-resonance spectroscopy experiments, i.e. ~200 ns. Indeed, as already mentioned, if one were to assume that IVR does not occur in the peptide on this time scale, the Franck-Condon factors of the ground and the excited vibrational states would have to be significantly different to observe dips in the UV induced signal. It is however unlikely that the couplings between electronic and vibrational degrees of freedom remain exactly the same for all the vibrational modes in the peptide when pumping different chromophores, as suggested by the perfect match of the infrared spectra of Figure 4.28. These considerations support the idea that the dips in an IR-UV double-resonance experiment occur from the broadening that results from IR-induced heating.

4.2.5 Discussion and Conclusions

The previous sections demonstrate that our photofragment-based detection scheme can be employed to measure electronic and vibrational spectra of protonated, seven-amino-acid peptides containing one or two chromophores.

IR-UV double-resonance spectroscopy of the tyrosine-containing peptide Ac-Tyr-(Ala)₅-LysH⁺ reveals the existence of two distinct conformations. The comparison of their infrared spectra with those of Ac-Phe-(Ala)₅-LysH⁺ measured in a previous work [25, 27] allows us to assign helical structures for both Ac-Tyr-(Ala)₅-LysH⁺ conformers prior to any theoretical analysis, which simply serves to confirm these assignments. Substituting the probe seems not to alter the conformational preferences of a peptide of the size considered here. However, four distinct conformers are identified in the case of protonated, phenylalanine-based helix, while only two for Ac-Tyr-(Ala)₅-LysH⁺, characterized by the phenol ring in the g^+ configuration. A possible explanation for the reduction of the number of conformations when changing the probe is a stronger interaction between the helical macrodipole with the tyrosine side chain dipole which acts as an additional stabilization factor for the helix that will be conformation dependent. Since the g^+ conformations are not calculated to be the lowest-energetic structures, these results clearly indicate that calculations neglect this stabilization feature (cf. *Section 4.3*).

Two conformers contribute to the electronic spectrum of Ac-(Ala)₅-Phe-LysH⁺, where the chromophore is close to the charge and thus able to interact with it, as suggested by the red-shift of its electronic spectrum with respect to that of Ac-Phe-(Ala)₅-LysH⁺. Calculations suggest that the predictions on the conformers structures based on comparing the infrared spectra with those of Ac-Phe-(Ala)₅-LysH⁺ are wrong. Moreover, only one of the two conformers is found to be helical while nothing can be inferred about the other conformer.

Analysis of the electronic spectrum of the double-chromophore peptide Ac-Tyr-(Ala)₄-Phe-LysH⁺ suggests a weak interaction between the two aromatic amino acid side chains. Indeed, the comparison between the electronic spectrum of the double-chromophore peptide with those of Ac-Tyr-(Ala)₅-LysH⁺ and Ac-(Ala)₅-Phe-LysH⁺ allows us to assign vibronic transitions to tyrosine or phenylalanine photoabsorptions. The ultraviolet spectrum of Ac-Tyr-(Ala)₄-Phe-LysH⁺ differs only slightly from that of

Ac-Tyr-(Ala)₅-LysH⁺, indicating tyrosine drives the photoabsorption of the double-chromophore peptide. In addition, this spectrum is red-shifted with respect to those of both the single-aromatic amino acid peptides. Since one would expect a symmetric shift of the electronic absorption of the two chromophores in case of a strong coupling between them, this supports the idea of a weak interaction between the chromophores. IR-UV double-resonance spectroscopy reveals that the electronic spectrum of Ac-Tyr-(Ala)₄-Phe-LysH⁺ arises from two different conformers, only one of which calculations show to be helical. As in the case of Ac-(Ala)₅-Phe-LysH⁺, we cannot conclude anything on the other conformer. The reasons why the theoretical approach employed up to now fails for these peptides will be discussed in the next section. Finally, the comparison between the infrared spectra of the double-chromophore helix measured by fixing the ultraviolet laser on vibronic transitions due to tyrosine and phenylalanine absorption demonstrates that the two chromophores probe the same vibrational bands.

The results obtained from the IR-UV double-resonance experiments help elucidate the mechanism that makes this technique work. As discussed in *Section 3.2.2*, alternative mechanisms can be proposed assuming that, after the absorption of a resonant IR photon, intramolecular energy redistribution (IVR) does or does not take place in the peptides on the 200 ns timescale of the delay between the IR and UV lasers. In the latter situation, the absorption of the IR photon might shift the electronic absorption of the peptide because of the coupling between the vibrational and electronic excitations. If the Franck-Condon factors for the vibronic excitation of the IR pre-excited molecules differ significantly from that of the ground state ones, the UV-induced photofragment signal would show depletions when the IR laser is in resonance with a vibrational transition. Since one might expect that only the vibrational modes involving bond vibrations close to the pumped chromophore would experience its electronic excitation, the infrared spectrum would show depletions only in correspondence of such vibrations. All the vibrational spectra of the protonated, seven-amino-acid peptides recorded by IR-UV double-resonance spectroscopy and discussed in this chapter contain seven well-resolved NH stretches, which might indicate that IVR occurs prior electronic excitation. It is however possible to object that this is simply due to a size issue so that all the vibrational modes in the peptide experience the electronic excitation even if IVR does not occur. On the other hand, setting the ultraviolet laser to the red of the electronic absorption of the cold molecule allows one to record infrared gain spectra, which

are not conformer-specific and can be regarded as the sum of the individual infrared spectra. These measurements indicate that the electronic absorption of the IR pre-excited molecules is broader than that of the cold ones, supporting the idea that IVR takes place after the absorption of an IR photon (cf. *Section 3.2.2*). In favor of this statement is the perfect match of the infrared spectra of double-chromophore peptide recorded pumping the two chromophores. Indeed, if IVR does not occur and assuming that the peptide chain is small enough that all the bond vibrations experience the electronic excitation, one would expect different couplings of the electronic and vibrational degrees of freedom for each chromophore. The observation that the infrared spectra are identical in the double-chromophore peptide pumping different chromophores, together with the possibility of measuring gain vibrational spectra, strongly supports the idea that IVR takes place in the peptides of the size considered here. The vibrational energy of the molecule is thus redistributed among all the vibrational modes of the molecule, broadening its electronic spectrum (cf. *Section 3.2.2*). As a consequence, the intensity of the UV absorption of the IR pre-excited molecules will be lower at the resonant frequency of the cold ions, leading to a dip in the photofragment signal.

4.3 State of comparison with theory

The results on protonated peptides presented in this chapter clearly demonstrate the role of calculations in interpreting the infrared spectra of biomolecular ions. As already discussed in *Section 3.3*, non-empirical *ab initio* calculations should be ideally performed for each conformation of the peptide. This approach is however still far from being practical because of the enormous computational time required. The general strategy is thus to use more modest methods based on lower-level potentials, i.e. force fields that are classical approximation of the quantum mechanical potential energy surface to generate the conformational landscape of the peptide. Only a subset of the classical structures is then selected for more accurate quantum mechanical treatment. The comparison between the calculated and the measured vibrational spectra allows one to connect a geometry to the selected conformer. In the case of Ac-Tyr-(Ala)₅-LysH⁺, the perfect match of the infrared spectra with those of Ac-Phe-(Ala)₅-LysH⁺, where isotopic substitution supports the

theoretical assignments, gives confidence in associating the spectra to specific helical conformations [27]. However, theory and experiment do not completely agree and our general approach cannot always be applied, as demonstrated in the calculations on Ac-(Ala)₅-Phe-LysH⁺ and Ac-Tyr-(Ala)₄-Phe-LysH⁺. In addition, even for Ac-Tyr-(Ala)₅-LysH⁺ the theoretical conformations whose vibrational spectra match the best the experimental data are not calculated to be the lowest-energy ones. This section outlines the strengths and the weaknesses of our chosen procedures and discusses methods that might improve the calculations on larger molecules.

The AMBER force field we employed in the random search method for conformational searching normally generates thousands of unique structures. Among these, the conformers with a relative energy below 50 kJ/mol are retained to carry out optimization using DFT. When calculating the energy of the molecular mechanics structures with DFT, the relative energy ordering changes significantly. For example, the global minimum conformation of Ac-Tyr-(Ala)₅-LysH⁺ according to DFT calculations at the B3LYP/6-31G** level of theory was the 75th lowest energy structure according to AMBER. Changing the force field, among the available ones, does not solve the problem of correctly selecting low-energy conformers. Indeed, a conformational search on the same peptide was performed using the MMFF94 force field [37]. In this case, the structure that is the global minimum at the DFT level of theory turns out to be the 239th lowest-energy structure determined using this force field and that with the best match to one of the experimental infrared spectra was predicted to be the 497th. Moreover, the geometry of the global minimum changes when using different force fields. If, on the other hand, a molecule is thought to have a stable structure, like in the case of the helix, one might use chemical intuition to select candidate geometries generated by the conformational search to be further analyzed. By contrast, the lack of constraints in the structures of a flexible peptide renders almost impossible the task of guessing *a priori* the possible geometries and sorting them into distinct families, so that one can extensively study only representatives of these groups. The fundamental question is, of course, how similar the geometries identified by the force fields are to those determined by quantum chemistry. Hobza and coworkers have recently shown that force fields perform poorly in predicting the structures and the relative energies of different conformations of isolated small peptides containing aromatic amino acids [38, 39]. There is hence a general need to improve the

existing force fields, since in addition to the calculations presented here, they are used to make predictions about biochemical processes.

Another question to address is how well DFT performs when it comes to predict conformer structures, relative energies and vibrational frequencies. Usually, we perform harmonic frequency calculations at the B3LYP/6-31G** level of theory which are then scaled to account for systematic errors and anharmonicity. Including the latter in the calculations, even if computationally expensive, improves the agreement between the theoretical and the experimental spectra with the advantage of requiring no scaling factor. However, standard DFT calculations generally fail in treating dispersion forces, which greatly influence biomolecular structure, and which are found to be the major attractive forces in the peptide backbone-aromatic side chain intramolecular interactions [39]. Since the B3LYP functional that we employed in our frequency calculations lacks these dispersion corrections, it might predict incorrect geometries, relative energies and thus frequencies of the conformers structures [38]. Moving to a higher level of theory, including anharmonicity and dispersion corrections in DFT calculations would ameliorate to some extent the accuracy of the energies and the frequencies predictions, even if computationally expensive.

One way to reduce the computational time for DFT calculations is to use resolution-of-the-identity (RI) approximation, which offers a less expensive route to MP2 energies [40]. The TURBOMOLE program package has been employed to calculate the energies and the frequencies by means of the RI approximation with DFT [41]. The method was tested on Ac-Tyr-(Ala)₅-LysH⁺ calculating at different levels of theory the frequencies of the structure whose B3LYP/6-31G** infrared spectrum matches best the conformer A experimental data. We use the BP86 functional with different basis sets, finding that the frequencies obtained with the higher basis match the experimental ones as well as the B3LYP/6-31G** ones. On the other hand, the inclusion of the dispersion corrections in the BLYP functional with the small basis does not give a good match between the experimental and the theoretical infrared spectra. This might indicate that we are not investigating the correct theoretical conformer, because if this is the case then all the higher level of theory calculations should give the same results.

The discussion above underlines the limitations of the actual strategy to identify the geometries associated with the conformations of a peptide. The first issue is to explore

extensively the conformational space of a molecule and then identify suitable candidate geometries for further analysis. The second question arises from the proper method to calculate reliable energies and frequencies of the different conformers. A possible way to solve these issues is to investigate force fields, basis sets, functionals and time-saving approximations to develop a trustful methodology to compute the conformational space and calculate the frequencies of smaller peptides. The calculated results must then be calibrated with the type of high-resolution, conformer-selected infrared spectra presented in this thesis. Once this is accomplished, the methods could be extended to progressively larger molecules.

References

1. Gerhards, M., C. Unterberg, A. Gerlach, *Phys. Chem. Chem. Phys.*, **2002**. 4: p. 5563-5565.
2. Gerhards, M., C. Unterberg, *Phys. Chem. Chem. Phys.*, **2002**. 4: p. 1760-1765.
3. Gerhards, M., Unterberg, C., Gerlach, A., and Jansen, A., *Phys. Chem. Chem. Phys.*, **2004**. 6: p. 2682-2690.
4. Chin, W., Mons, M., Dognon, J.P., Mirasol, R., Chass, G., Dimicoli, I., Piuze, F., Butz, P., Tardivel, B., Compagnon, I., vonHelden, G., and Meijer, G., *J. Phys. Chem. A*, **2005**. 109: p. 5281-5288.
5. Hunig, I. and Kleinermanns, K., *Phys. Chem. Chem. Phys.*, **2004**. 6: p. 2650-2658.
6. Hunig, I., Seefeld, K.A., and Kleinermanns, K., *Chem. Phys. Lett.*, **2003**. 369: p. 173-179.
7. Dian, B.C., Longarte, A., Mercier, S., Evans, D.A., Wales, D.J., and Zwier, T.S., *Journal of Chemical Physics*, **2002**. 117: p. 10688-10702.
8. Cohen, R., Brauer, B., Nir, E., Grace, L., and de Vries, M., *J. Phys. Chem. A*, **2000**. 104: p. 6351-6355.
9. Paizs, B., Schnolzer, M., Warnken, U., Suhai, S., and Harrison, A.G., *Phys. Chem. Chem. Phys.*, **2004**. 6: p. 2691-2699.
10. Kang, H., Juvet, C., Dedonder-Lardeux, C., Martrenchard, S., Grègoire, G., Desfrancoise, C., Schermann, J.P., Barat, M., and Fayeton, J.A., *Phys. Chem. Chem. Phys.*, **2005**. 7: p. 394-398.
11. Gregoire, G., Juvet, C., Dedonder, C., and Sobolewski, A.L., *J. Am. Chem. Soc.*, **2007**. 129: p. 6223-6231.
12. Stearns, J.A., Mercier, S., Seaiby, C., Guidi, M., Boyarkin, O.V., and Rizzo, T.R., *J. Am. Chem. Soc.*, **2007**. 129: p. 11814-11820.
13. Lucas, B., Barat, M., Fayeton, J.A., Perot, M., Juvet, C., Gregoire, G., and Nielsen, S.B., *J. Chem. Phys.*, **2008**. 128: p. 7.
14. Cornell, W.D., Cieplak, P., Bayly, C.I., Gould, I.R., Merz, J.K.M., Ferguson, D.M., Spellmeyer, D.C., Fox, T., Caldwell, J.W., and Kollman, P.A., *J. Am. Chem. Soc.*, **1995**. 117: p. 5179-5197.
15. MACROMODEL, *version 9.1*. **2005**, Schrödinger, LLC: New York.

16. M. J. Frisch, G.W.T., H. B. Schlegel, G. E. Scuseria, M. A. Robb, J. R. Cheeseman, J. J. A. Montgomery, T. Vreven, K. N. Kudin, J. C. Burant, J. M. Millam, S. S. Iyengar, J. Tomasi, V. Barone, B. Mennucci, M. Cossi, G. Scalmani, N. Rega, G. A. Petersson, H. Nakatsuji, M. Hada, M. Ehara, K. Toyota, R. Fukuda, J. Hasegawa, M. Ishida, T. Nakajima, Y. Honda, O. Kitao, H. Nakai, M. Klene, X. Li, J. E. Knox, H. P. Hratchian, J. B. Cross, V. Bakken, C. Adamo, J. Jaramillo, R. Gomperts, R. E. Stratmann, O. Yazyev, A. J. Austin, R. Cammi, C. Pomelli, J. W. Ochterski, P. Y. Ayala, K. Morokuma, G. A. Voth, P. Salvador, J. J. Dannenberg, V. G. Zakrzewski, S. Dapprich, A. D. Daniels, M. C. Strain, O. Farkas, D. K. Malick, A. D. Rabuck, K. Raghavachari, J. B. Foresman, J. V. Ortiz, Q. Cui, A. G. Baboul, S. Clifford, J. Cioslowski, B. B. Stefanov, G. Liu, A. Liashenko, P. Piskorz, I. Komaromi, R. L. Martin, D. J. Fox, T. Keith, M. A. Al-Laham, C. Y. Peng, A. Nanayakkara, M. Challacombe, P. M. W. Gill, B. Johnson, W. Chen, M. W. Wong, C. Gonzalez, and J. A. Pople, *GAUSSIAN 03, Revision D.01* **2004**, Gaussian, Inc.: Pittsburgh PA.
17. Chin, W., Piuzzi, F., Dimicoli, I., and Mons, M., *Phys. Chem. Chem. Phys.*, **2006**. 8: p. 1033-1048.
18. Lepere, V., Lucas, B., Barat, M., Fayeton, J.A., Picard, V.J., Jouvet, C., Carcabal, P., Nielsen, I., Dedonder-Lardeux, C., Gregoire, G., and Fujii, A., *J. Chem. Phys.*, **2007**. 127: p. 134313.
19. Gregoire, G., Lucas, B., Barat, M., Fayeton, J.A., Dedonder-Lardeux, C., and Jouvet, C., *Eur. Phys. J. D*, **2009**. 51: p. 109-116.
20. Oomens, J., Polfer, N., Moore, D.T., van der Meer, L., Marshall, A.G., Eyler, J.R., Meijere, G., and von Helden, G., *Phys. Chem. Chem. Phys.*, **2005**. 7: p. 1345-1348.
21. Chin, W., Piuzzi, F., and Dognon, J.-P., *J. Am. Chem. Soc.*, **2005**. 127: p. 11900-11901.
22. Brenner, V., Piuzzi, F., Dimicoli, I., Tardivel, B., and Mons, M., *J. Phys. Chem. A*, **2007**. 111: p. 7347-7354.
23. Abo-Riziq, A., Bushnell, J.E., Crews, B., Callahan, M., Grace, L., and de Vries, M.S., *Chem. Phys. Lett.*, **2006**. 431: p. 227-230.
24. Abo-Riziq, A., Crews, B.O., Callahan, M.P., Grace, L., and de Vries, M.S., *Angew. Chem. Int. Ed.*, **2006**. 45: p. 5166-5169.
25. Stearns, J.A., Boyarkin, O.V., and Rizzo, T.R., *J. Am. Chem. Soc.*, **2007**. 129: p. 13820-13821.
26. Stearns, J.A., Boyarkin, O.V., and Rizzo, T.R., *Chimia*, **2008**. 62: p. 240-243.
27. Stearns, J.A., Seaiby, C., Boyarkin, O.V., and Rizzo, T.R., *Phys. Chem. Chem. Phys.*, **2009**. 11: p. 125-132.
28. Hudgins, R.R., Ratner, M.A., and Jarrold, M.F., *J. Am. Chem. Soc.*, **1998**. 120: p. 12974-12975.
29. Hudgins, R.R. and Jarrold, M.F., *J. Am. Chem. Soc.*, **1999**. 121: p. 3494-3501.
30. Kohtani, M., Jones, T.C., Schneider, J.E., and Jarrold, M.F., *J. Am. Chem. Soc.*, **2004**. 126: p. 7420-7421.
31. Vaden, T.D., de Boer, T.S.J.A., Simons, J.P., Snoek, L.C., Suhai, S.n., and Paizs, B.I., *J. Phys. Chem. A*, **2008**. 112: p. 4608-4616.
32. Paizs, B. and Suhai, S., *J. Am. Soc. Mass Spectrom.*, **2004**. 15: p. 103-113.
33. Paizs, B. and Suhai, S., *Rapid Commun. Mass Spectrom.*, **2002**. 16: p. 375-389.
34. Stearns, J.A., Guidi, M., Boyarkin, O.V., and Rizzo, T.R., *J. Chem. Phys.*, **2007**. 127: p. 154322.
35. Bossart, R., Boyarkin, O.V., Makarov, A.A., and Rizzo, T.R., *J. Chem. Phys.*, **2007**. 126: p. 054302.

36. Hopkins, J.B., Powers, D.E., and Smalley, R.E., *J. Chem. Phys.*, **1980**. 72: p. 5039-5048.
37. Halgren, T.A., *J. Comput. Chem.*, **1996**. 17: p. 490-519.
38. Valdes, H., Pluhackova, K., Pitonak, M., Rezac, J., and Hobza, P., *Phys. Chem. Chem. Phys.*, **2008**. 10: p. 2747-2757.
39. Valdes, H., Spiwok, V., Rezac, J., Reha, D., Abo-Riziq, A.G., de Vries, M.S., and Hobza, P., *Chem. Eur. J.*, **2008**. 14: p. 4886-4898.
40. Weigend, F., Häser, M., Patzelt, H., and Ahlrichs, R., *Chem. Phys. Lett.*, **1998**. 294: p. 143-152.
41. Ahlrichs, R., Bär, M., Häser, M., Horn, H., and Kölmel, C., *Chem. Phys. Lett.*, **1989**. 162: p. 165-169.

Chapter 5

Toward larger peptides

5.1 Introduction

The data presented and discussed in *Chapter 4* demonstrates our ability to measure highly-resolved infrared spectra of small gas-phase peptides by means of photofragment spectroscopy. These spectra provide a benchmark for theory and, as previously discussed, provide evidence of its limits. Nevertheless, our ultimate goal is to be able to extract useful structural information, even if only qualitative, on naturally-occurring peptides and proteins by applying our photofragment techniques to even larger molecules. We have indeed been mostly focused in characterizing the secondary structure of peptide chains containing at maximum 10-12 amino acids [1, 2]. Increasing the size of the molecules would allow us to observe elements of tertiary structure. Moreover, it is more likely that larger molecules will retain something that resembles their condensed-phase structure in the gas phase, since the accumulation of many non-covalent interactions will make a considerable contribution to the overall stabilization energy.

The first issue that arises in considering the extension of our techniques to still larger molecules is whether their electronic spectra will be simple enough to extract any information. Thermal inhomogeneous broadening, large number of Franck-Condon active low-frequency vibrations and conformational heterogeneity could all potentially contribute to the complexity of the electronic spectra of a large peptide and thus render difficult the applicability of our spectroscopic methods. Collisional cooling has been demonstrated to be efficient for protonated aromatic amino acids as well as for peptide chains containing up to twelve amino acids [1-4]. The ultimate temperature achieved does not change significantly with the size of the molecules as long as we allow them to have a sufficient number of

collisions in the ion trap, suggesting thermal inhomogeneous broadening should not complicate significantly their electronic spectra. On the other hand, the number of low-frequency vibrational modes with Franck-Condon activity could be an important source of spectral complexity since vibrational progressions near the band origin might prevent the resolution of individual conformers. The number of vibrational modes increases rapidly with the number of residues in a peptide but not all of them will appear in the electronic spectra. Indeed, the vibrational modes with strong Franck-Condon factors will be those for which the bond lengths and angles associated with the vibrational motion change in geometry upon excitation to the excited electronic state. Since we are using aromatic amino acids as chromophores, one expects that the bond lengths and angles near to or associated with the aromatic moiety are the most likely to feel the change and thus those appearing as vibrational progressions in the electronic spectrum, while those remote from the chromophore should not experience the effect of the electronic excitation. Finally, conformational heterogeneity, that is, the increasing number of possible stable conformations assumed by a peptide as it becomes larger, may be the limiting factor to the applicability of our spectroscopic methods. At that point, combining our techniques with other experimental methods, such as ion mobility, might help reduce the problem. For the moment, not much can be argued *a priori* about when we will reach this point and the problem of conformational heterogeneity is better addressed experimentally. Figure 5.1 compares the electronic spectra of three protonated, phenylalanine-containing peptides to investigate the degree of spectral complexity with increasing molecular size.

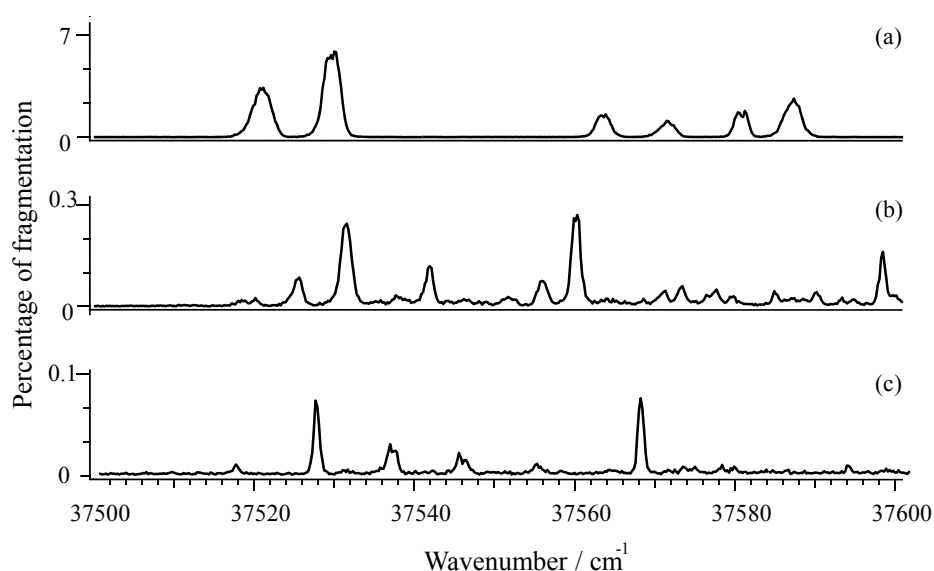


Figure 5.1: Ultraviolet spectra of (a) PheH^+ , (b) $\text{Ac-Phe-(Ala)}_5\text{-LysH}^+$ and (c) $\text{Ac-Phe-(Ala)}_{10}\text{-LysH}^+$ [1, 3].

The spectrum remains uncongested even for the 12 amino-acid peptide, allowing us to measure its conformer-specific infrared spectra without difficulty [1, 2]. This indicates that conformational heterogeneity and Frank-Condon activity of the low-frequency vibrations do not represent a limitation to our spectroscopic methods at least for the size and class of peptides considered up to now. We would like to push these methods further to see where the limits exist.

The second major issue that we need to address in considering the extension of our approach to larger ions is their dissociation rate. The use of spectroscopic techniques based on UV-induced photofragmentation requires that the molecules initially promoted to an electronic excited state will dissociate on a short timescale compared to competing processes. If the dissociation occurs in the electronic ground state after internal conversion from the excited state followed by statistical vibrational energy redistribution and unimolecular fragmentation, the lifetime of the molecule might scale strongly with the molecular size. In this case, processes that compete with unimolecular dissociation, such as collisional relaxation by residual helium in the trap or infrared fluorescence, might reduce the fraction of molecules that dissociate, rendering photofragment spectroscopy of large species difficult, if not impossible. On the other hand, if the molecules fragment directly from the electronic excited state, the process is typically fast, and the lifetime would not necessarily scale with molecular size. In this case, photofragment spectroscopy might work perfectly well on larger species. However, the internal conversion from the excited electronic state to the ground electronic state would compete more effectively with the direct dissociation from the electronic excited state as the molecule gets larger because of the significant difference in the vibrational densities of states [5]. The deactivation of the electronic excited state by the radiationless IC might actually limit the size of the molecules possible to investigate with photofragment spectroscopy.

The electronic spectra of Figure 5.1 show that the fragmentation yield decreases as the size of the peptide chain increases, independent from which dissociation channel is monitored to record the spectra. Indeed, it ranges from ~7% fragmentation for the single protonated phenylalanine, to ~0.3% for Ac-Phe-(Ala)₅-LysH⁺ and less than 0.1% for Ac-Phe-(Ala)₁₀-LysH⁺ [1-3]. Meanwhile, it must be noted that the vibronic transitions are still sharp even for the twelve amino acid peptide, whose electronic spectrum is recorded by monitoring a fragment associated with a direct dissociation on the excited electronic surface

[1, 2]. This indicates that the IC to the ground electronic state is not too fast and the lifetime of the electronic excited state is at least on the order of tens of ps.

In the 20 Hz experiments described in the previous chapter, the molecules are allowed only ~ 10 ms to dissociate, which is the time between the laser firing and the arrival of the ions to the detector, in the sense explained in *Section 3.1.2*. If the dissociation process is statistical, the lifetime of the molecules before they dissociate can easily become much longer than this as the molecules increase in size. Running the trapping cycle at half the repetition rate or less would give the ions up to 100 ms for dissociation. Unfortunately, on this timescale, radiative cooling can become significant and, thus, compete with dissociation [6]. Another solution to this problem would be to accelerate the dissociation of large ions by increasing their internal energy so that fragmentation effectively competes with collisional relaxation or infrared radiation. This is the strategy employed in this thesis work.

This chapter describes the recent experimental developments that allow us to use our photofragment-based detection scheme for even larger molecules than those described in the previous chapter. The basic idea is to implement the *Infrared Laser Assisted Photofragment Spectroscopy* (IRLAPS) technique used for photofragment spectroscopy of weak vibrational overtone transitions of light neutral molecules [7-11] and which Lee and coworkers applied to protonated water clusters [12]. The following sections present the method first in its original application and then as adapted for measuring the electronic and vibrational spectra of biomolecular ions, underlining the expected differences between the two applications. Finally, this chapter illustrates the results on several peptide ions of up to seventeen amino acids and discusses different mechanisms to explain these findings.

5.2 Infrared laser assisted photofragment spectroscopy

5.2.1 Measurements of weak overtone transitions of small molecules

Figure 5.2 depicts the IRLAPS spectroscopic technique employed to measure the weak overtone transitions in the specific case of methanol cooled in a supersonic jet [7, 8, 10, 11]. A pulsed dye laser excites molecules from their ground vibrational state to a vibrational

overtone level. After ~ 100 ns, a pulse from a TEA-CO₂ laser selectively pumps some fraction of the vibrationally pre-excited molecules to a level above the threshold for dissociating the CO bond *via* multiphoton excitation. Finally, a third laser pulse detects the OH fragments resulting from the unimolecular dissociation *via* LIF.

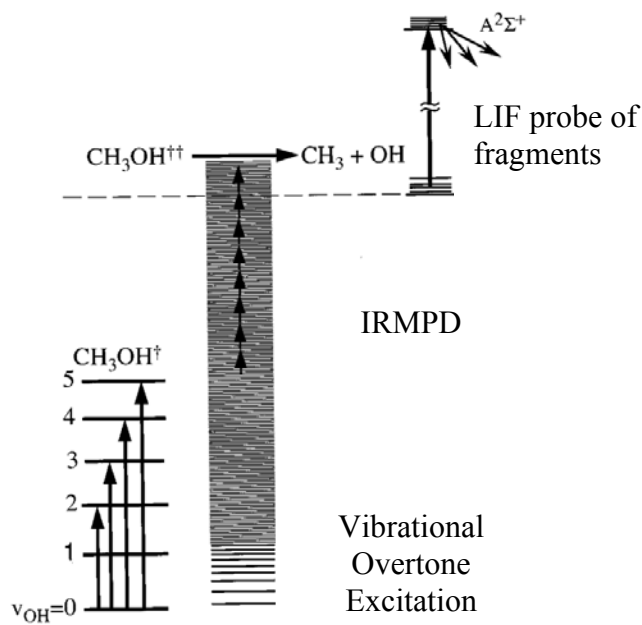


Figure 5.2: IRLAPS scheme to measure the overtone transitions of CH₃OH cooled in a supersonic jet. (Adapted from ref [10])

In order for this approach to work as a spectroscopic tool, two requirements must be satisfied. First, the dissociation efficiency of the CO₂ laser should be insensitive to the exciting laser frequency. If this is the case, fixing the frequency of the CO₂ and the LIF probe lasers and scanning the frequency of the overtone excitation laser generates a vibrational overtone excitation spectrum. The fact that the vibrational overtone spectrum obtained with the assistance of *infrared multiphoton dissociation* (IRMPD) matches that measured by photoacoustic spectroscopy demonstrates that the CO₂ simply probes the effect of the exciting laser [7]. The second requirement is that the CO₂ laser should selectively dissociate only those molecules that have first undergone vibrational overtone excitation. Several properties of the IRMPD process help us discriminate against dissociation of the ground-state molecules. First, it exhibits a threshold fluence, which has been associated with pumping through the quasi continuum. Adjusting the CO₂ laser fluence below this threshold suppresses the dissociation of the ground-state molecules, while the pre-excited molecules are already

half-way to the dissociation energy and fragment at the lower fluence. An additional factor that enables discrimination against IRMPD of ground-state molecules is a shift of the CO₂ laser absorption when the amount of vibrational energy increases. Indeed, two-color CO₂ multiphoton dissociation studies have shown that the dissociative laser absorption frequency tends to red-shift with increasing vibrational frequency owing to off-diagonal anharmonicities [13, 14]. Thus, tuning the CO₂ laser frequency to the red of the optimum absorption of the ground-state molecules allows one to pump selectively only the pre-excited molecules. The last factor that contributes to discriminating against ground-state molecule fragmentation is the nonlinear intensity dependence of the IRMPD process [15].

The sensitivity of the IRLAPS technique allows detection of high vibrational overtone transitions in polyatomic molecules cooled in a supersonic expansion. Moreover, when combined with double-resonance spectroscopic methods it allows measuring rotationally resolved spectra [8-11].

5.2.2 Adaptation of IRLAPS to measure electronic and vibrational spectra of biomolecular ions

The challenge for us is to measure the ultraviolet and the infrared spectra of larger peptide ions by implementing the IRLAPS technique previously described. Figure 5.3 shows the basic idea as applied to the current experiments [16]. Suppose that, after UV excitation of large, gas-phase protonated molecules, the dissociation is slow and only a small fraction of these ions fragments before the trap is emptied. By introducing a CO₂ laser pulse subsequent to the UV pulse, the protonated species that have been previously electronically excited may undergo *infrared multiphoton excitation* (IRMPE). This increases their internal energy and hence their dissociation rate. As a consequence, a larger fraction of pre-excited molecules should fragment during the fixed time before the trap is emptied.

For this approach to work, the CO₂ laser pulse must selectively excite only those molecules that are first promoted to the excited electronic state by the absorption of a UV photon and not those remaining in the ground electronic state. Moreover, the IRMPE process should not distort the UV-only electronic spectrum. If these requirements are achieved, an

electronic spectrum can be recorded by monitoring the fragment ion signal as a function of the UV laser frequency, as in the usual photofragment spectroscopic scheme.

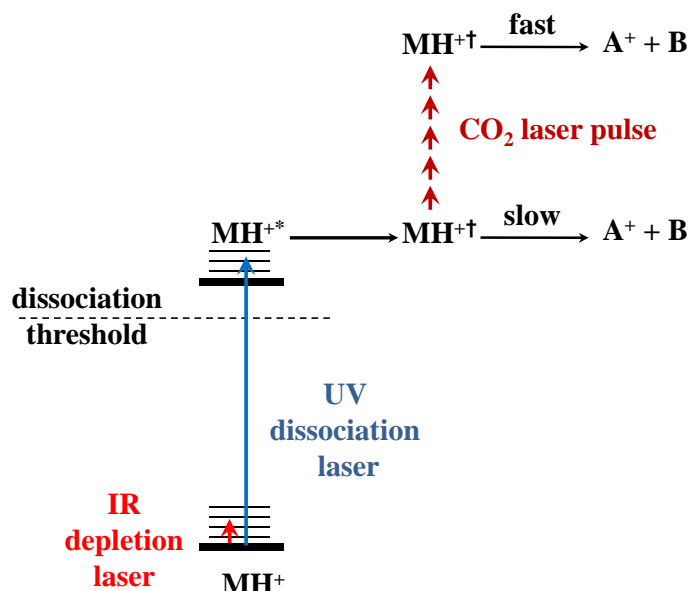


Figure 5.3: IRLAPS scheme to obtain electronic and vibrational spectra of a singly protonated molecule. For the measurements of vibrational spectra, the IR laser is run at half the repetition rate of the UV laser and fired 200 ns prior the UV laser, as for the double-resonance experiments described in *Chapter 4*. The delay between the latter and the CO_2 laser pulse is adjusted to maximize the photofragmentation signal.

The main difference between the IRLAPS technique applied to small polyatomic molecules and to large biomolecular ions lies in the factors that may allow discriminating against dissociation of the ground state molecules. It is worth mentioning that achieving this goal is less critical for electronic excitation of protonated peptides than for vibrational overtone excitation of polyatomic molecules. Indeed, in the case of forbidden overtone transitions one might excite only one molecule every 10^5 and hence a discrimination ratio of 10^6 is needed to get a signal-to-noise of 10. In the case of an electronic excitation, a discrimination ratio on the order of 10^3 is required to obtain the same signal-to-noise level, since the UV laser promotes a few percent of molecules in the electronic excited state.

The enormous density of vibrational states of large peptides leads to a low average occupation number of most vibrational modes following electronic excitation and internal conversion. Thus, one expects only a small anharmonic shift of the resonant frequency pumped by the CO_2 laser and insignificant statistical broadening in the IR absorption spectra [14], in contrast to the case of small molecules. This suggests that tuning the CO_2 laser away

from a resonant frequency of the cold, ground state molecules might not help dissociating only the pre-excited ions. On the other hand, these molecules have on the order of 35000 cm^{-1} of internal energy so they need to absorb fewer photons from the CO_2 laser, compared to the unexcited ions, to reach an energy at which the dissociation rate becomes sufficiently fast. These considerations lead us to suppose that, in the current approach, the CO_2 laser fluence is the critical parameter one needs to adjust to fragment those ions that have been already promoted to an electronic excited state after the absorption of a UV photon.

Once the effectiveness of the IRLAPS method for electronic spectroscopy is demonstrated, one should verify whether it is suitable to measure conformer-selective infrared spectra, because our final aim is to extract structural information. In this case, an IR spectroscopic laser would precede the UV laser in the same way as described for the smaller systems in *Chapter 4* (cf. Figure 5.3). The CO_2 laser would then be set to maximize the UV-induced dissociation signal as for electronic spectra measurements and the infrared absorption would be detected as a dip on the constant fragment ion signal.

The following paragraphs demonstrate the power of the IRLAPS detection scheme to measure the electronic and vibrational spectra of peptide ions of up to seventeen amino acids, independently of the chromophore used as a probe.

5.3 Results

5.3.1 Phenylalanine containing peptides

The natural candidate peptide for us to test the IRLAPS scheme was $\text{Ac-Phe-(Ala)}_5\text{-LysH}^+$, since this molecule was extensively studied with our standard photofragment spectroscopy techniques and its electronic spectrum is relatively simple [1, 2]. Figure 5.4 displays the ultraviolet spectra of this helical peptide measured with and without the assistance of the CO_2 laser. The UV-only spectrum in Figure 5.4 is multiplied by 20 to show that the two spectra are essentially identical in all main features, thus demonstrating that IRMPE is insensitive to the details of the UV excitation and thus does not distort the

spectrum¹. The striking feature of this result is the increase of the dissociation yield by more than two orders of magnitude induced by the additional absorption of the CO₂ laser, set at the 9P(16) line of the CO₂ laser (1050.1 cm⁻¹) where the fragmentation yield exhibits its maximum.

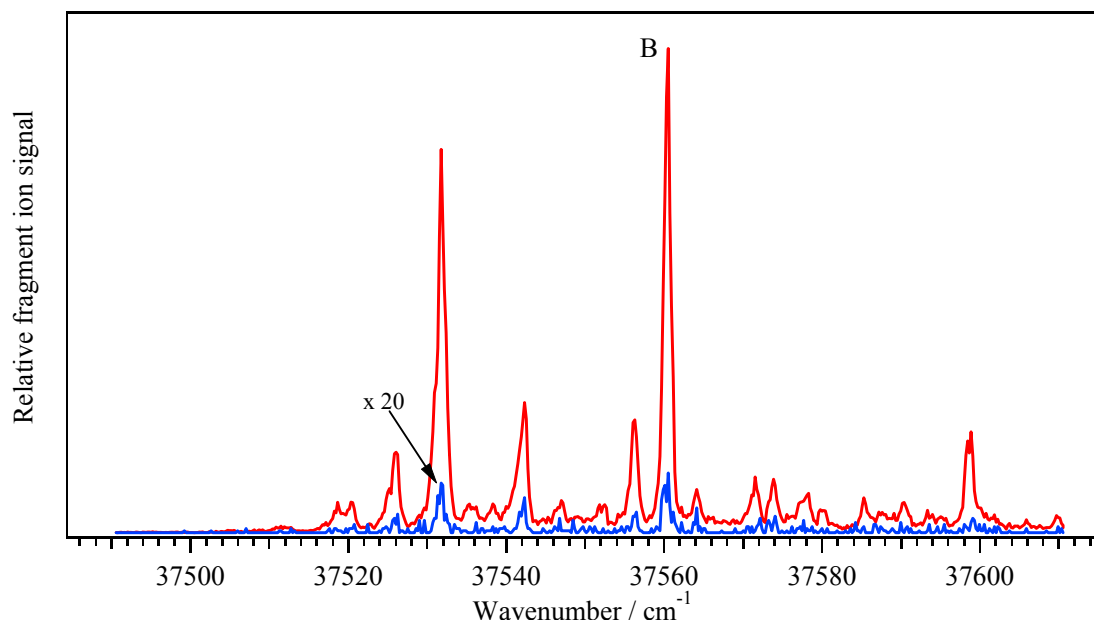


Figure 5.4: Electronic spectra of Ac-Phe-(Ala)₅-LysH⁺ obtained by UV-only photofragmentation (blue trace) and by UV excitation assisted by IRMPE (red trace). The blue trace is multiplied by 20 to evidence the two electronic spectra present the same spectroscopic features. The CO₂ laser is at 9P(16) line for both molecules.

This remarkable result on Ac-Phe-(Ala)₅-LysH⁺ encouraged us to push further the limit of applicability of the IRLAPS technique. We thus investigated a doubly-charged, seventeen-amino-acid peptide, namely Ac-Phe-(Ala)₇-LysH⁺-(Pro)₂-(Ala)₅-LysH⁺ (*m/z* 756) by means of this new method. Molecules such as Ac-(Ala)_{*n*}-LysH⁺-(Gly)_{*m*}-(Ala)_{*p*}-LysH⁺ have helix-turn-helix motifs and, according to the ion mobility studies of Jarrold and coworkers, assume extended helical and coiled-coil conformations in the gas phase [17, 18]. The latter geometry has two helical sections aligned antiparallel and is stabilized by favorable electrostatic interactions between the helices and by interactions between the C-terminus carboxylic group and the N-terminus amide groups. The extended helical conformations have two uncoupled helices, connected by the glycine bridge, and are energetically more favored

¹ The experimental conditions used to record the electronic spectra in Figure 5.4 are optimum for the IRLAPS technique. By changing some machine settings, i.e. the quadrupole resolution and the photofragment to monitor, it is however possible to have enough UV-induced photofragment signal to record a highly-resolved electronic spectrum of Ac-Phe-(Ala)₅-LysH⁺ without the assistance of the CO₂ laser [1, 2].

than the coiled-coil structures. In the peptide we investigated here, prolines replace glycines to decrease the flexibility and phenylalanine is substituted for the alanine at the N-terminus as a UV chromophore so that photofragment-based detection schemes can be employed.

Figure 5.5 illustrates the ultraviolet spectra of $\text{Ac-Phe-(Ala)}_7\text{-LysH}^+\text{-(Pro)}_2\text{-(Ala)}_5\text{-LysH}^+$, obtained with and without IRMPE assistance. As for $\text{Ac-Phe-(Ala)}_5\text{-LysH}^+$, the dissociation yield increases two orders of magnitude when the fragmentation is assisted by the CO_2 laser. It is evident that the UV-only fragmentation signal does not allow us to identify clearly the vibronic transitions of molecules of this size. On the other hand, using the IRLAPS technique we can record a well resolved electronic spectrum. Figure 5.6 displays the electronic spectrum of $\text{Ac-Phe-(Ala)}_7\text{-LysH}^+\text{-(Pro)}_2\text{-(Ala)}_5\text{-LysH}^+$ as its percentage of fragmentation, that is, the photofragment signal measured employing the IRLAPS technique normalized by the parent ion signal, as a function of the laser wavenumber in a wider range than that shown in Figure 5.5. In analogy with the other phenylalanine-containing peptides (cf. ref. [3] and Section 4.2.3), the intense vibronic transitions $\sim 530\text{ cm}^{-1}$ above the peaks labeled as A, B, C and D in Figure 5.5 correspond to the 6b vibration of benzene and its derivatives, which appears at 530 cm^{-1} in the excited state of toluene [19].

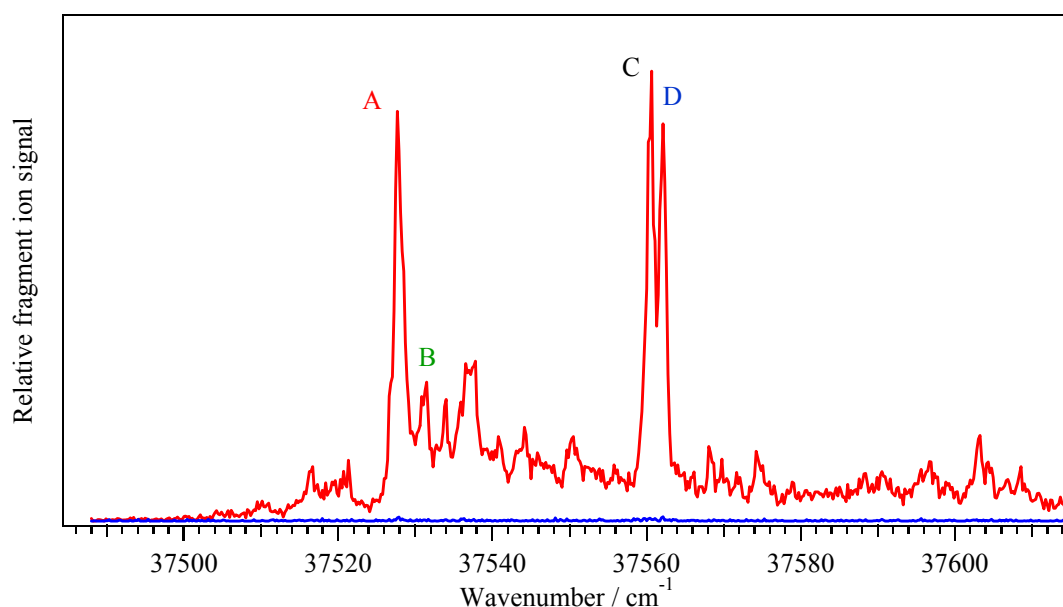


Figure 5.5: Electronic spectra of $\text{Ac-Phe-(Ala)}_7\text{-LysH}^+\text{-(Pro)}_2\text{-(Ala)}_5\text{-LysH}^+$ obtained by UV-only photofragmentation (blue trace) and by UV excitation assisted by IRMPE (red trace). The transitions are labeled accordingly to conformations as found by double-resonance spectroscopy. The CO_2 laser is at 9P(16) line for both molecules.

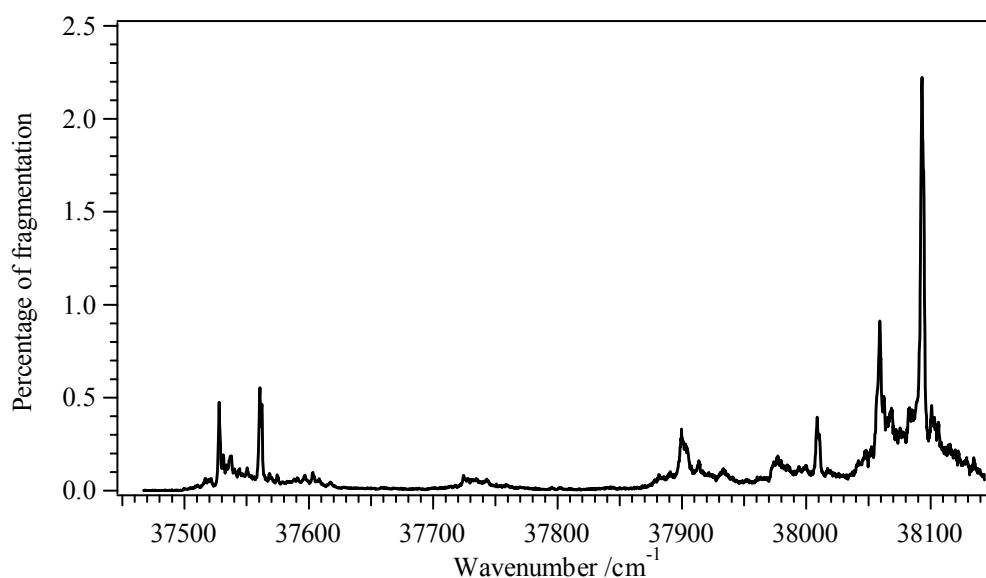


Figure 5.6: Electronic spectrum of Ac-Phe-(Ala)₇-LysH⁺-(Pro)₂-(Ala)₅-LysH⁺. In this graph, the photofragment signal recorded applying the IRLAPS scheme is normalized by that of the parent molecule to account for the source fluctuations. The electronic spectrum of Ac-Phe-(Ala)₇-LysH⁺-(Pro)₂-(Ala)₅-LysH⁺ is thus shown as its percentage of fragmentation as a function of the laser wavenumber in a wider range than that of Figure 5.5.

The next hurdle for us is to investigate whether the IRLAPS scheme allows measurement of conformer-selected vibrational spectra. Figure 5.7 compares the conformer-specific infrared spectra of Ac-Phe-(Ala)₅-LysH⁺, measured with the IR-UV double-resonance scheme with and without assistance of the CO₂ laser.

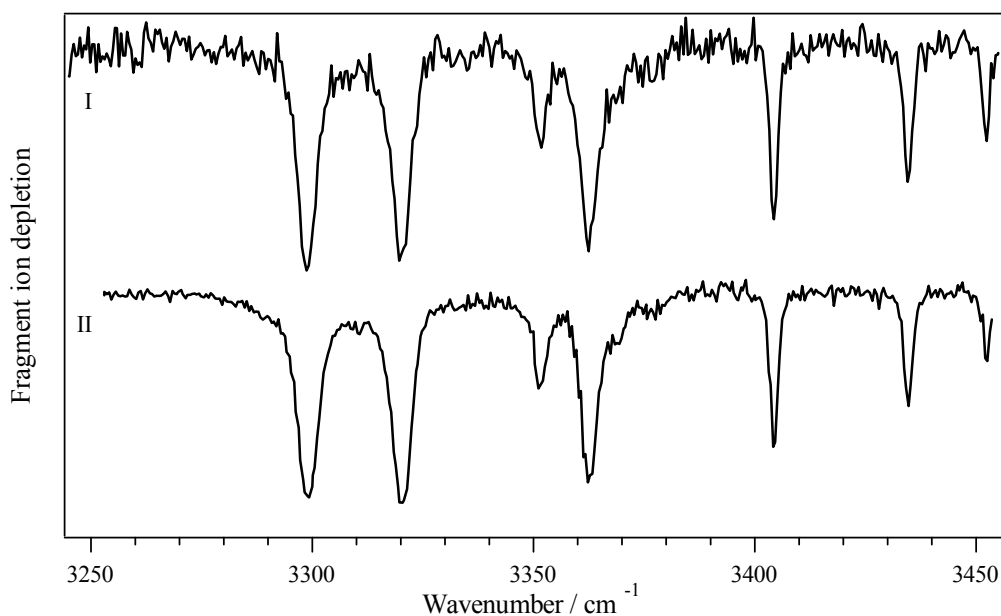


Figure 5.7: Infrared spectra of conformer “B” of Ac-Phe-(Ala)₅-LysH⁺ obtained with and without the assistance of the CO₂ laser, respectively I and II traces in the figure.

The UV laser is tuned to the band origin of Ac-Phe-(Ala)₅-LysH⁺ conformer “B” [1, 2] and the assisting laser is at the 9P(16) line, which gives the maximum UV-induced fragmentation signal. The two spectra are essentially identical, with no-distortion induced by CO₂ laser assisted dissociation. In addition, the noise level of the vibrational spectrum recorded with the IRLAPS scheme is significantly less than that measured with the usual photofragment spectroscopy, because of the increased dissociation efficiency.

Figure 5.8 shows the conformer-specific infrared spectra of Ac-Phe-(Ala)₇-LysH⁺-(Pro)₂-(Ala)₅-LysH⁺ with the assistance of the CO₂ laser and by fixing the UV laser frequency on peaks A, B, C and D of Figure 5.5. It is important to note that because of the poor signal-to-noise ratio of the UV-only fragmentation signal, no IR-induced depletion was detected without IRMPE assistance.

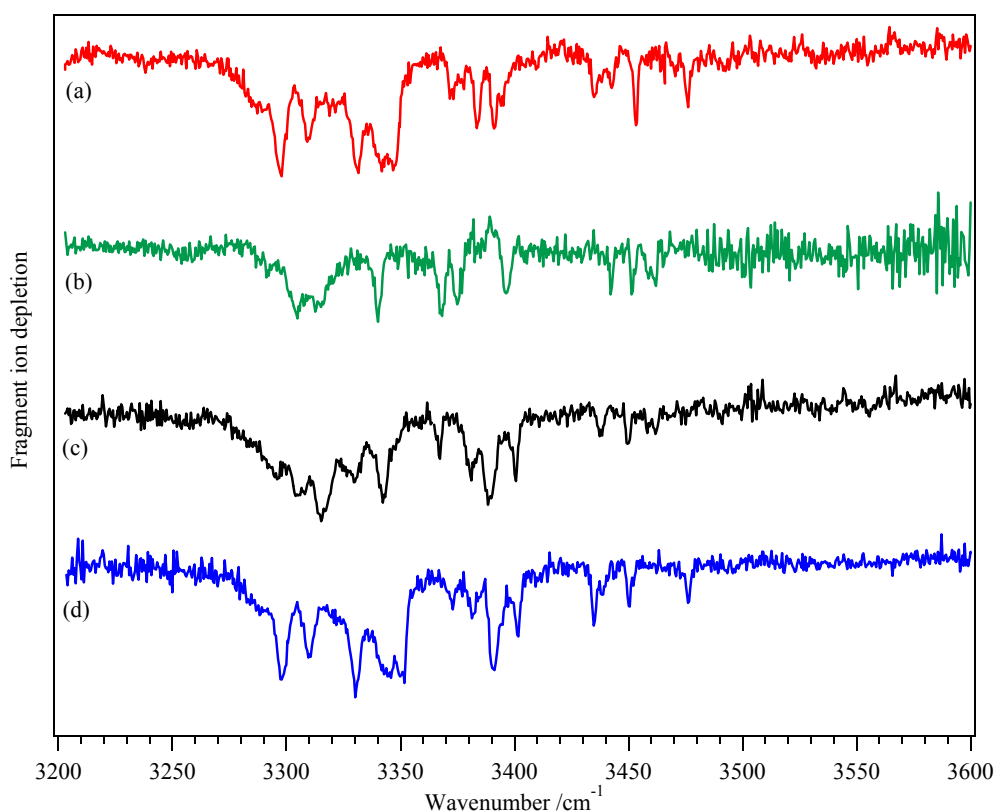


Figure 5.8: Conformer specific infrared spectra of Ac-Phe-(Ala)₇-LysH⁺-(Pro)₂-(Ala)₅-LysH⁺ obtained with the assistance of the CO₂ laser setting the UV laser at (a) 37527.9 cm⁻¹, (b) 37531.3 cm⁻¹, (c) 37560.7 cm⁻¹ and (d) 37562.2 cm⁻¹.

The degree of depletion achieved by the IR spectroscopic laser is as much as 70%, which indicates that for a molecule of this size, adding 3400 cm⁻¹ of vibrational energy is still

sufficient to broaden and shift the electronic spectrum to result in a dip at the UV probe frequency. Although these four spectra are not completely resolved, one can clearly see they are different, suggesting that the corresponding features in the electronic spectrum arise from distinct conformers. Unfortunately, peptides of this size are above the limit of what can be calculated with our present computational capabilities, meaning that we cannot presently deduce any structural information from the vibrational spectra. They thus represent a real challenge to theory.

5.3.2 Tyrosine containing peptides

The IRLAPS scheme also works with tyrosine as the probe chromophore, as demonstrated by the electronic spectra of Ac-Tyr-(Ala)₅-LysH⁺ in Figure 5.9, measured with and without the CO₂ laser assistance. The 9P(16) line of the latter gives the best photofragmentation signal also for the tyrosine-based peptides. However, upon IRMPE, its dissociation yields increases less than that of Ac-Phe-(Ala)₅-LysH⁺, i.e. one instead of two orders of magnitude. This suggests that the properties of the chromophore determine the enhancement of the photofragment signal upon IRMPE, since it is the only difference between the two peptide chains.

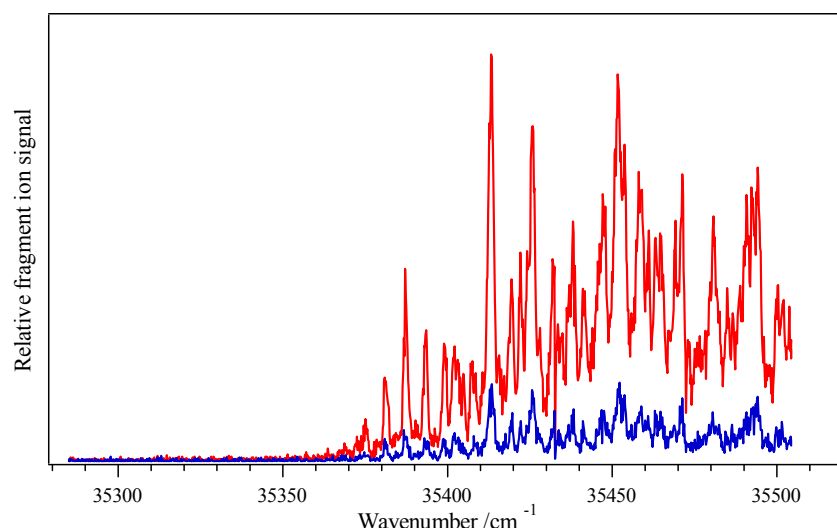


Figure 5.9: Electronic spectra of Ac-Tyr-(Ala)₅-LysH⁺ obtained by UV photofragmentation (blue trace) and by UV excitation assisted by IRMPE (red trace).

The enhancement observed in Ac-Tyr-(Ala)₅-LysH⁺ led us to apply the IRLAPS technique to a doubly charged segmented helix analogous to the one previously studied but

with tyrosine as chromophore, namely $\text{Ac-Tyr-(Ala)}_7\text{-LysH}^+\text{-(Pro)}_2\text{-(Ala)}_5\text{-LysH}^+$ (m/z 764). Its electronic spectrum obtained with assistance of the CO_2 laser is highly congested (cf. Figure 5.10). However, the results on $\text{Ac-Tyr-(Ala)}_5\text{-LysH}^+$, where the electronic spectra show the same features with UV-only excitation and IRLAPS technique, give us confidence that this spectrum is a faithful monitor of the UV absorption.

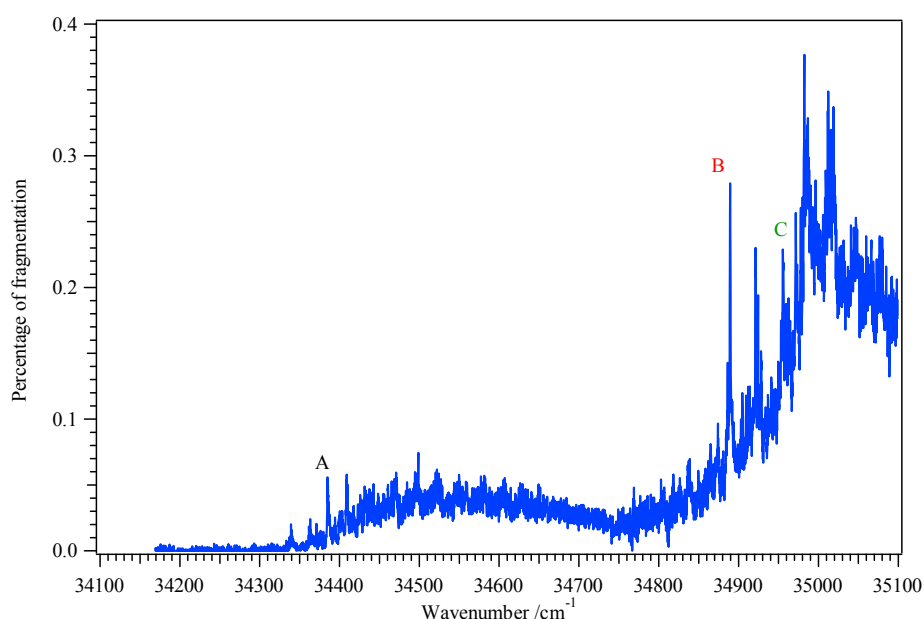


Figure 5.10: Electronic spectra of $\text{Ac-Tyr-(Ala)}_7\text{-LysH}^+\text{-(Pro)}_2\text{-(Ala)}_5\text{-LysH}^+$ obtained applying the IRLAPS detection scheme.

As discussed in *Section 5.1*, the complexity of the electronic spectra of large molecules could arise from incomplete cooling, conformational heterogeneity and Franck-Condon activity of the low-frequency vibrational modes of the bond lengths and angles near to or associated with the aromatic chromophore. The analysis of the electronic spectrum of $\text{Ac-Phe-(Ala)}_7\text{-LysH}^+\text{-(Pro)}_2\text{-(Ala)}_5\text{-LysH}^+$ (Figure 5.6) demonstrates that molecules of this size are efficiently cooled down to ~ 10 K by collisions with the helium buffer gas in our 22-pole ion trap. This indicates that we can exclude the incomplete cooling as the reason of the complexity of $\text{Ac-Tyr-(Ala)}_7\text{-LysH}^+\text{-(Pro)}_2\text{-(Ala)}_5\text{-LysH}^+$ electronic spectrum. Conformational heterogeneity can also be ruled out because, as it will be discussed below, only three different conformers give rise to the electronic spectrum of $\text{Ac-Tyr-(Ala)}_7\text{-LysH}^+\text{-(Pro)}_2\text{-(Ala)}_5\text{-LysH}^+$. On the other hand, we have attributed in *Section 4.2.2* the congestion of the electronic spectrum of $\text{Ac-Tyr-(Ala)}_5\text{-LysH}^+$ to the Franck-Condon activity of the chromophore, which can then also be used to explain the complexity of the electronic spectrum of $\text{Ac-Tyr-(Ala)}_7\text{-LysH}^+\text{-(Pro)}_2\text{-(Ala)}_5\text{-LysH}^+$. The electronic spectrum of this

positively charged, seventeen-amino-acid, tyrosine-containing peptide is red shifted respect to those of the protonated tyrosine [3], the dipeptide H^+TyrAla [20] and the seven-amino-acid molecule $\text{Ac-Tyr-(Ala)}_5\text{-LysH}^+$ (cf. *Section 4.2.2* and Figure 5.9) indicating a strong interaction between the charge and the chromophore as in the case of H^+AlaTyr (cf. *Section 4.1.3* and ref. [20]).

Figure 5.11 illustrates the conformer-specific infrared spectra of $\text{Ac-Tyr-(Ala)}_7\text{-LysH}^+ \text{-(Pro)}_2\text{-(Ala)}_5\text{-LysH}^+$ measured tuning the frequency of the UV laser on the transitions labeled as A, B and C in the electronic spectra of Figure 5.10. The vibrational spectra of this segmented helix are not completely resolved but one can see they are clearly different. Therefore, the three vibronic transitions in the electronic spectrum associated with these vibrational spectra belong to distinct conformers.

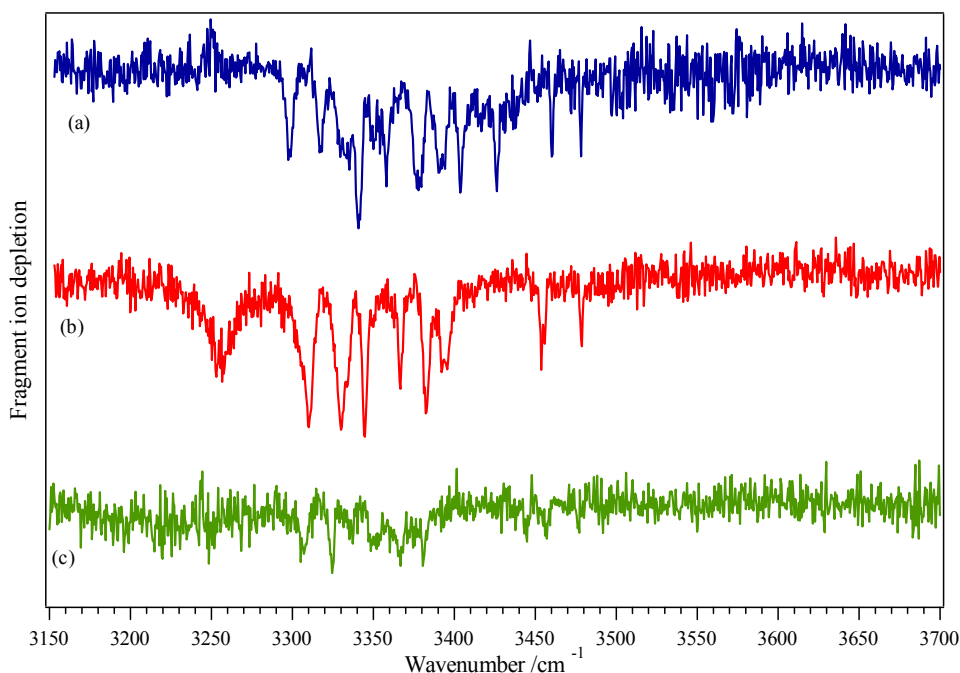


Figure 5.11: Conformer specific infrared spectra of $\text{Ac-Tyr-(Ala)}_7\text{-LysH}^+ \text{-(Pro)}_2\text{-(Ala)}_5\text{-LysH}^+$ obtained with the assistance of the CO_2 laser setting the UV laser at (a) 34384.8 cm^{-1} , (b) 34889.3 cm^{-1} and (c) 34955.4 cm^{-1} .

In *Section 4.2.2*, the conformer-specific infrared spectra of $\text{Ac-Tyr-(Ala)}_5\text{-LysH}^+$ could be interpreted by the comparison with those of $\text{Ac-Phe-(Ala)}_5\text{-LysH}^+$ before performing any calculations because of the similarity between the vibrational spectra. By contrast, the infrared spectra of the segmented helices with different probe chromophores presented in this chapter differ significantly.

5.3.3 Tryptophan containing peptide

We have demonstrated that the IRLAPS method also works for a tryptophan-containing peptide. Figure 5.12 illustrates the electronic spectra of Ac-Trp-(Ala)₅-LysH⁺ [21], measured with and without the CO₂ laser assistance. As for all the peptides investigated up to now with the IRLAPS technique, the 9P(16) rovibrational line of the CO₂ laser induces the maximum photofragmentation yield. Finally, the enhancement of the signal due to IRMPE is on the same order of magnitude as in the tyrosine containing peptides.

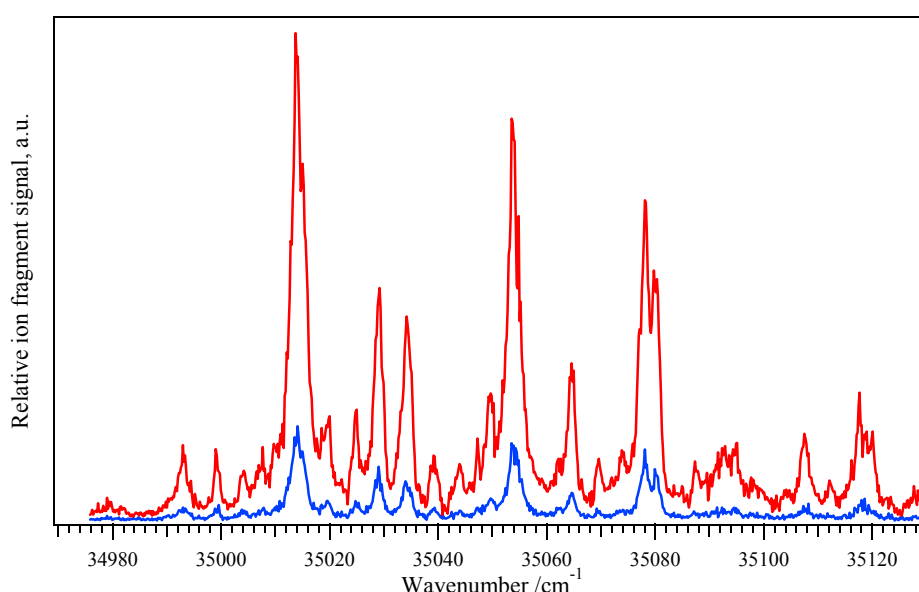


Figure 5.12: Electronic spectra of Ac-Trp-(Ala)₅-LysH⁺ obtained by UV photofragmentation (blue trace) and by UV excitation assisted by IRMPE (red trace).

5.3.4 Double-chromophore peptide

The last molecule that we investigated with the assistance of the CO₂ laser is Ac-Tyr-(Ala)₄-Phe-LysH⁺, whose electronic spectra in the tyrosine and phenylalanine absorption regions are illustrated in Figure 5.13 a and b. The IRLAPS method works also in this type of molecule and the 9P(16) rovibrational line still corresponds to the CO₂ laser frequency associated to the maximum in the IRLAPS photofragmentation signal. It should be mentioned that the dissociation yield for this double-chromophore helix is on the same order as that of the tyrosine containing peptides, which is smaller than that of the molecules where phenylalanine is the unique chromophore.

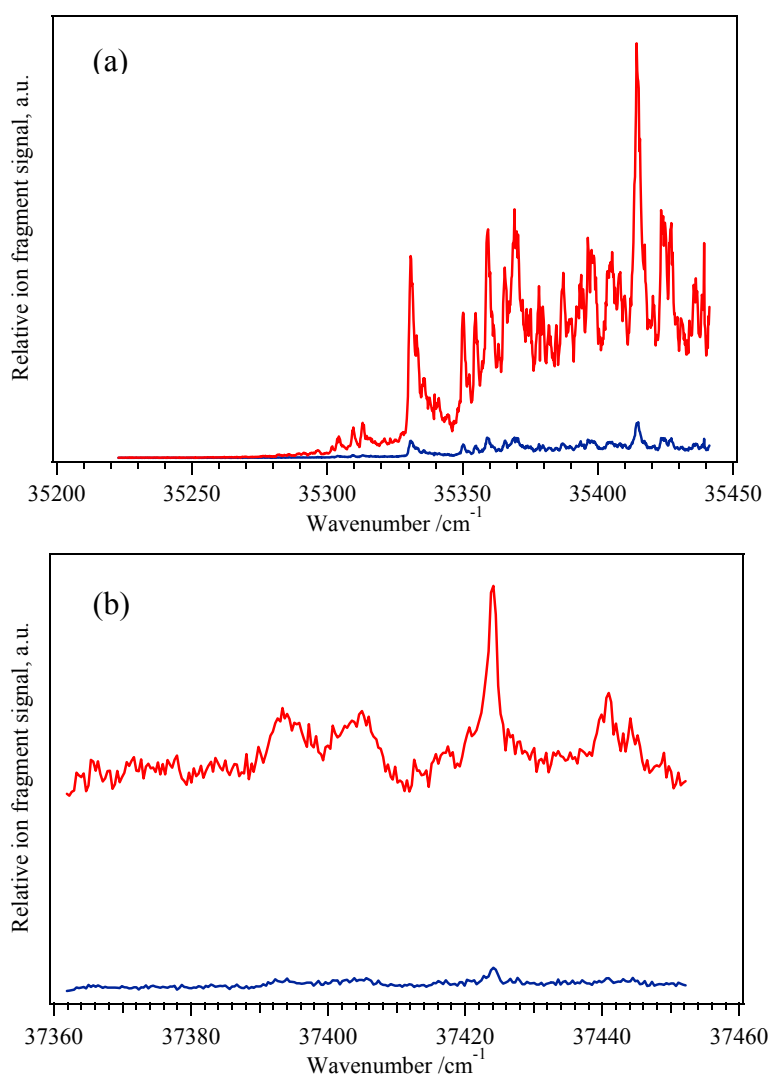


Figure 5.13: Electronic spectra of Ac-Tyr-(Ala)₄-Phe-LysH⁺ obtained by UV photofragmentation (blue trace) and by UV excitation assisted by IRMPE (red trace) in tyrosine and phenylalanine absorption regions respectively (a) and (b) in the graph.

5.3.5 Fragment mass spectra

The previous sections demonstrate the power of the IRLAPS method to measure electronic and vibrational spectra of several protonated peptides, without specifying which dissociation products were monitored to record such spectra. As already mentioned, we expected *a priori* to act on statistical dissociation channels, since IRMPE of the UV pre-excited molecules increases their internal energy and thus their dissociation rate. This paragraph shows the photofragment mass spectra of molecular ions obtained by UV-only excitation and IRLAPS technique, focusing on the seven-amino-acid peptides since the larger

molecules behave in the same way. The comparison between such spectra reveals the existence of a major dissociation channel upon IRMPE of UV pre-excited molecules, associated with the fragmentation on an excited electronic surface, which is not predicted by our initial hypothesis. Hence, the analysis of the photofragment mass spectra of the protonated peptides upon IRMPE subsequent to UV excitation indicates that the IRLAPS mechanism is not completely clear.

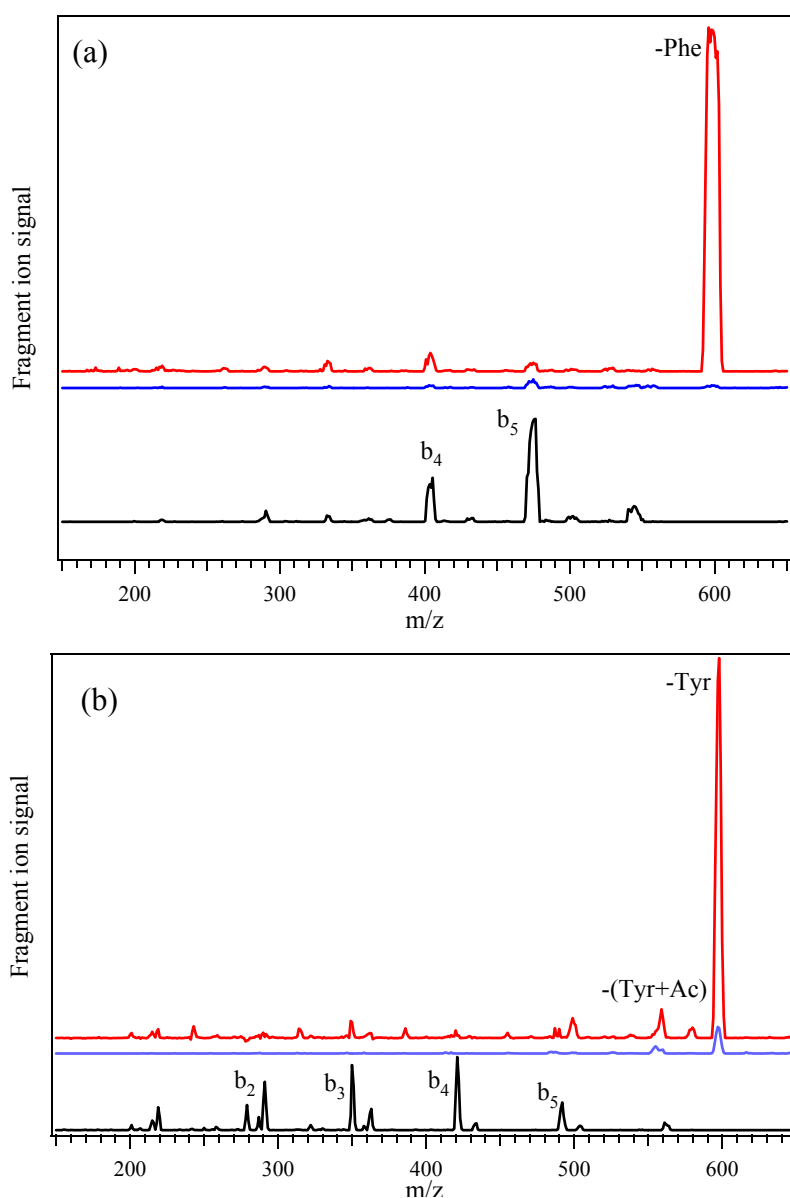


Figure 5.14: Photofragment mass spectra of (a) $\text{Ac-Phe-(Ala)}_5\text{-LysH}^+$ and (b) $\text{Ac-Tyr-(Ala)}_5\text{-LysH}^+$ obtained by UV photofragmentation (blue trace) and by UV excitation assisted by IRMPE (red trace). The black traces are the CO_2 laser only photofragment spectra at the 9P(16) rovibrational line. The UV laser in (a) is tuned to 37560.5 cm^{-1} and in (b) to 35410.8 cm^{-1} , band origin of the “B” conformers (cf. [1, 2] and Section 4.2.2).

Figure 5.14a and b show the photofragment mass spectra of Ac-Phe-(Ala)₅-LysH⁺ and Ac-Tyr-(Ala)₅-LysH⁺ with and without the assistance of the CO₂ laser. In these measurements, the UV laser is tuned to the conformers “B” band origins, which are the most intense vibronic transitions in the ultraviolet spectra of both charged peptides (cf. ref. [1, 2] and *Section 4.2.2*), and the assisting laser is fixed at 9P(16), the rovibronic line giving the maximum photofragmentation yield. For both peptides, IRMPE after UV excitation greatly enhances only the fragments due to the loss of the neutral aromatic side chain *via* cleavage of the C_α-C_β bond. These fragments disappear when the UV laser is blocked and only the CO₂ laser interacts with the peptides. On the other hand, IRMPD of the ground state molecules produces only the b-type daughter ions, which derive from the common b_x-y_z pathways in CID experiments and which we thus associate with a ground state dissociation process [22, 23].

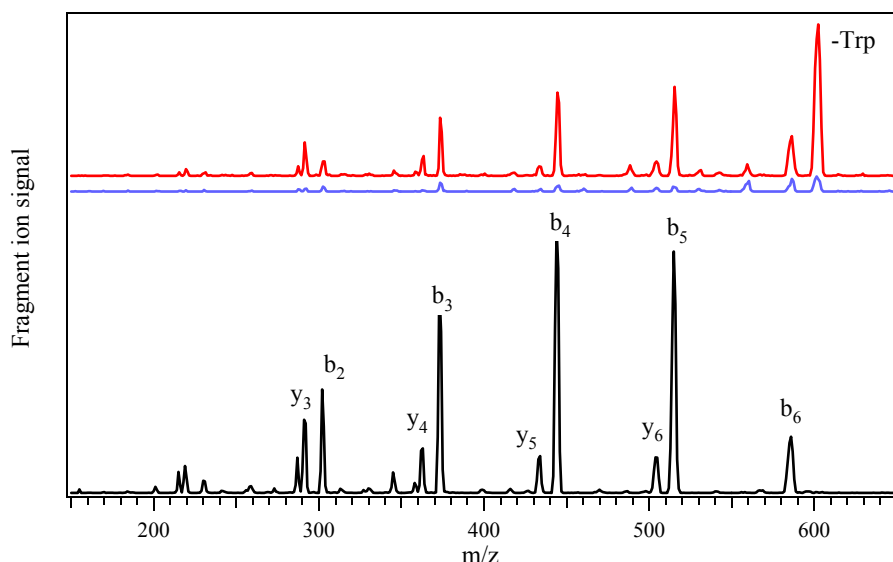


Figure 5.15: Photofragment mass spectra of Ac-Trp-(Ala)₅-LysH⁺ obtained by UV photofragmentation (blue trace), by UV excitation assisted by IRMPE (red trace) and by the CO₂ laser alone set at the 9P(16) rovibrational line (black trace). The UV laser is tuned at 35013.7 cm⁻¹.

Application of the IRLAPS scheme to Ac-Trp-(Ala)₅-LysH⁺ produces both b- and y-type fragment ions in addition to species involving the cleavage of the C_α-C_β bond (Figure 5.15). This indicates that for tryptophan-based peptides the IRLAPS technique enhances also signals due to ground-state dissociation process, even if the fragment due to the loss of the chromophore side chain remains the preferred dissociation channel. It should also be observed that the b- and y-type photofragment ions are the main dissociation channels upon

CO₂ laser-only absorption, which, on the other hand, does not produce fragments associated to the C_α-C_β bond cleavage.

In the analysis of the IRLAPS photofragment channels of the double-chromophore peptide Ac-Tyr-(Ala)₄-Phe-H⁺, one should consider both tyrosine and phenylalanine absorption regions of the ultraviolet spectrum. As previously observed, the dissociation yield of this peptide upon IRMPE subsequent to UV excitation is on the same order of magnitude than that of tyrosine-containing peptides independent of the pumped chromophore. The population of the dissociation products enhanced by the IRLAPS method reflects that of the UV-only induced photofragment mass spectrum (cf. *Section 4.2.4*). Thus, pumping either phenylalanine or tyrosine, the daughter ion due to the cleavage of the C_α-C_β bond at the tyrosine residue provides the most intense signal upon additional absorption of the CO₂ laser after UV pre-excitation.

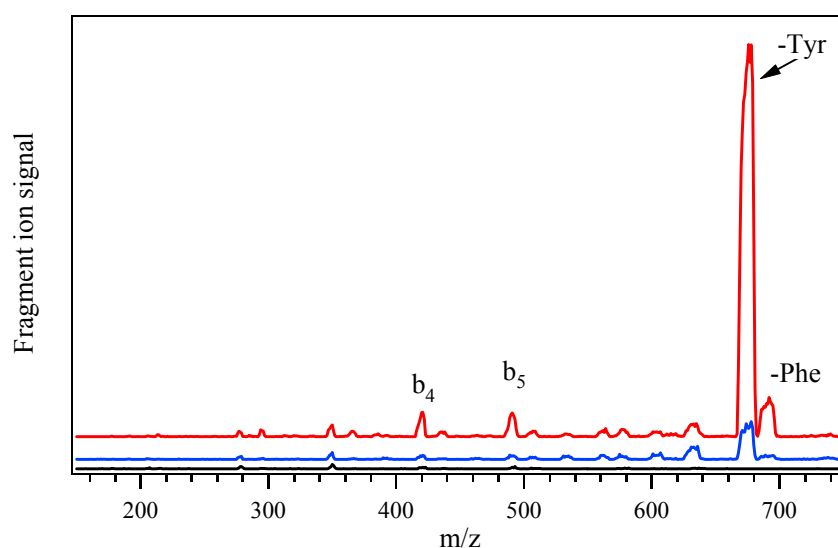


Figure 5.16: Photofragment mass spectra of Ac-Tyr-(Ala)₄-Phe-LysH⁺ obtained by UV photofragmentation (blue trace), by UV excitation assisted by IRMPE (red trace) and by the CO₂ laser alone set at the 9P(16) rovibrational line (black trace). The UV laser is tuned at 35327.1 cm⁻¹.

The fact that for all the protonated peptides investigated here, IRMPD of the ground-state molecules does not produce the fragment due to the C_α-C_β cleavage suggests that the latter is an excited state dissociation channel.

5.4 Discussion on the IRLAPS mechanism

The implementation of the IRLAPS method allows us to measure the electronic and conformer-specific vibrational spectra of singly- or doubly-charged biomolecular ions of different size, containing one or two chromophores. The comparison between the ultraviolet and infrared spectra of such peptides recorded with and without the assistance of the CO₂ laser provides evidence that the latter does not distort the spectra measured by monitoring the UV or the IR-UV photofragment signals. Furthermore, IRMPE subsequent to UV pre-excitation increases the dissociation yield by as much as two orders of magnitude when phenylalanine is the probe chromophore and of one order of magnitude for tyrosine and tryptophan. For all the charged peptides investigated by the IRLAPS technique, the photofragmentation yield of the daughter ions changes weakly with the frequency of the tunable CO₂ laser and exhibits a maximum around the 9P(16) line, independent of the chromophore used as a probe.

As already mentioned, our basic idea was to accelerate the dissociation of the charged peptides by IRMPE subsequent to UV pre-excitation. This implies we expected to act on statistical dissociation channels. In the case of Ac-Trp-(Ala)₅-LysH⁺, the additional absorption of the CO₂ laser after UV pre-excitation can enhance the photofragment signal of the b-type ions, which are associated with dissociation on the ground electronic state after IC from the excited electronic state. However, the fragmentation due to the aromatic side chain loss is the preferred dissociation channel in all the peptides that we investigated. Thus, IRMPE subsequent to UV pre-excitation always preferentially enhances the signal of the photofragments formed by the cleavage of the C_α-C_β bond, which is not the weakest in these molecules. Indeed, these are minor fragmentation channels when performing IRMPD-only of the parent ions, which should proceed on the ground-electronic surface at the CO₂ laser fluence typically used in our experiments (3-4 J/cm²). In addition, the dissociation appears to happen promptly after the CO₂ laser excitation. This observation, together with the strength of the C_α-C_β bond, suggests that the dissociation induced by IRMPE may occur on an excited electronic state or on an intermediate species that is promptly formed after the UV excitation.

The aim of the present section is to understand the possible mechanisms leading to the C_α-C_β bond cleavage in charged peptides. The first section treats the dependence of the

IRLAPS signal associated with this photofragment on the delay between the CO₂ and the UV lasers, which provides an estimate of the lifetime of the state populated after the absorption of a UV photon. The following paragraphs discuss two possible mechanisms for IRLAPS, both of which involve the formation of a biradical cation to explain the formation of the photofragment due to the chromophore side chain loss. The first model relies on the studies of the excited state dissociation of protonated aromatic amino acids by Jouvét and coworkers [24-32]. The second model involves the *electron driven proton transfer* (EDPT) process in hydrogen-bonded systems extensively studied in the group of Domcke and Sobowleski [33-39]. Results obtained applying the IRLAPS technique on phenylalanine-containing peptides are discussed to test the proposed mechanisms.

5.4.1 Timing of the lasers in the IRLAPS experiment

As explained in *Section 3.1.2*, the time-delay between the firing of the laser and the opening of the 22-pole ion trap plus the arrival time of the ions to the detector represents the time available to a molecule to dissociate. This time must be adjusted to achieve the maximum fragmentation signal. In the IRLAPS experiments described in the previous section, the excitation and the assisting lasers are ~200 ns apart and are fired ~10 ms before the ions are released from the 22-pole trap.

The electronic and vibrational spectra of the protonated peptides we investigated show exactly the same spectroscopic features whether they are measured with and without the assistance of the CO₂ laser. This demonstrates that the IRLAPS technique monitors faithfully the UV or the IR absorptions and that the assisting laser simply probes the effect of the spectroscopic lasers. It is then necessary to characterize the state initially populated by the UV excitation to understand the possible mechanisms that make the IRLAPS technique to work. The analysis of the photofragment signal due to the cleavage of the C_α-C_β bond as a function of the delay between the UV and the CO₂ lasers will give an indication of the lifetime of the UV pre-excited state.

Figure 5.17 shows the IRLAPS signal associated to the chromophore side chain loss as a function of the UV and CO₂ lasers-delay in the case of Ac-Phe-(Ala)₅-LysH⁺. It is worth to mention that the same behavior is observed for all the protonated peptides investigated with

the IRLAPS technique, independently from the length and the chromophore used as a probe. The initial exponential decay of the photofragmentation signal, characterized by a time constant of $\sim 15 \mu\text{s}$, is followed by an increase of the signal with a maximum at $\sim 65 \mu\text{s}$. The signal then decreases again and reaches an asymptotic value at 2 ms, which surprisingly does not coincide with the UV-only induced photofragmentation signal.

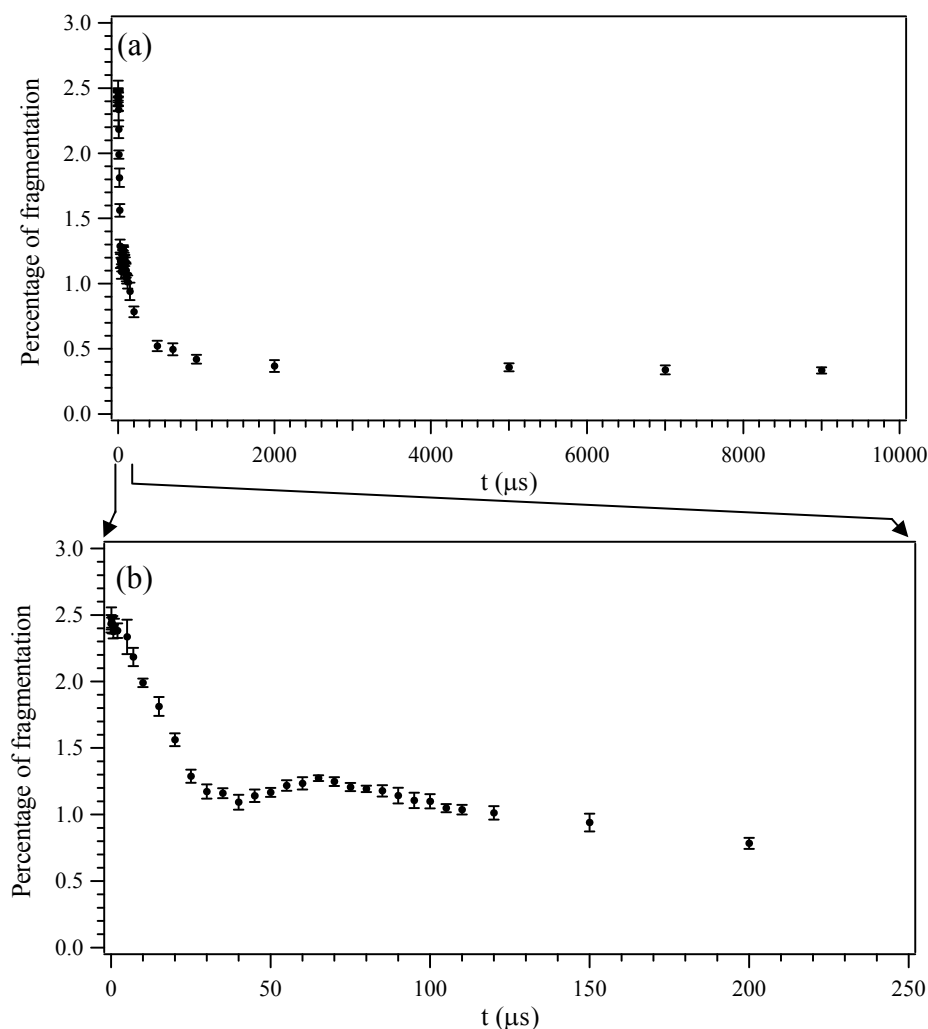


Figure 5.17: Percentage of fragmentation of Ac-Phe-(Ala)₅-Lys-H⁺, obtained with the IRLAPS technique, monitoring the m/z 601 fragment, as a function of the time delay between the CO₂ and the UV lasers (a), (b) enlargement in the first 200 μs . The CO₂ laser is tuned at the 9P(16) rovibrational line and the UV at conformer “B” frequency. The lasers are fired 10 ms before the trap opens.

Photophysical processes, such as fluorescence, internal conversion to the ground electronic state and phosphorescence, can occur after electronic excitation (cf. *Section 3.1.1*). The deactivation of the UV pre-excited molecules by means of these processes could be considered to explain the initial decay of the photofragment signal shown in Figure 5.17.

Both fluorescence and IC to the ground electronic state can be excluded because they occur on a much shorter time scale than the observed 15 μ s initial decay. After electronic excitation, a molecule might undergo intersystem crossing to a triplet electronic state, but the lifetime of the resulting phosphorescence is typically longer than the 15 μ s decay that we observe in Fig. 17b. This indicates that also this photophysical process cannot justify our experimental observations.

After absorbing a UV photon the molecules can still undergo collisions with residual helium in the 22-pole ion trap, which in principle could be responsible for the deactivation of the UV pre-excited molecules. If this were the case, changing the helium pressure would affect the decay of the photofragment signal shown in Figure 5.17. To test this hypothesis, the photofragment signal associated with the chromophore loss as a function of the delay between the UV and the CO₂ lasers was recorded at 20, 10 and 5Hz repetition rate of the machine cycle and shining the lasers always 10 ms before the trap opens. In doing so, the helium pumping out time increases and thus the number of collisions between the UV pre-excited molecules and the helium buffer gas in the 22-pole ion trap diminishes. Since the trend of the photofragmentation signal as a function of the laser delay remains the same changing the helium pressure in the 22-pole ion trap, we can conclude that collisions are not responsible for the deactivation of the UV pre-excited molecules.

Up to now, the discussion has focused on explaining the initial decay of the photofragment signal observed as the delay between the UV and the CO₂ lasers increases. The existence of the subsequent recurrence in the signal after the initial decrease led us to consider the possibility of an unfolding/refolding process induced by electronic excitation in the peptides. The fact that the trend of the photofragment signal is the same independently of the size of the molecule and the probe chromophore suggests that also this hypothesis can be excluded.

Another possible hypothesis is that the UV pre-excited molecules move in the 22-pole ion trap inducing the trend of the signal in Figure 5.17. Indeed, the UV and the CO₂ laser beams are initially focused and overlapped to get the maximum signal at a fixed time delay between the lasers. As this time increases, the UV pre-excited molecules might move away from the original volume and consequently from the region probed by the CO₂ laser, resulting in the initial decrease of the photofragment signal in Figure 5.17. The subsequent increase

would be due to the return of the electronically-activated ions in the region of the CO₂ laser beam, which would escape again from the CO₂-excitation volume leading to the long tail of Figure 5.17a. The latter can also indicate the existence of some long decay mechanisms occurring in the pre-excited molecules. Indeed, after redistribution inside the trap, the pre-excited ions spread over the entire trap volume giving rise to a certain signal level. These molecules can then lose their electronic energy by means of some deactivation mechanisms, whose characteristic decay time leads to the long tail of Figure 5.17a. If the motion of the parent ions in the trap is the correct explanation to the trend of the signal in Figure 5.17, then the same behavior should be observed for any signal induced by the absorption of two lasers. Figure 5.18 shows the depletion signal of conformer “B” of Ac-Phe-(Ala)₅-LysH⁺ with the IR laser tuned at 3401.6 cm⁻¹ as a function of the time-delay between the IR and the UV lasers. The close match between this trend and that of the IRLAPS photofragmentation signal of Figure 5.17 strongly supports the idea that they arise from the motion of the ions in the 22-pole.

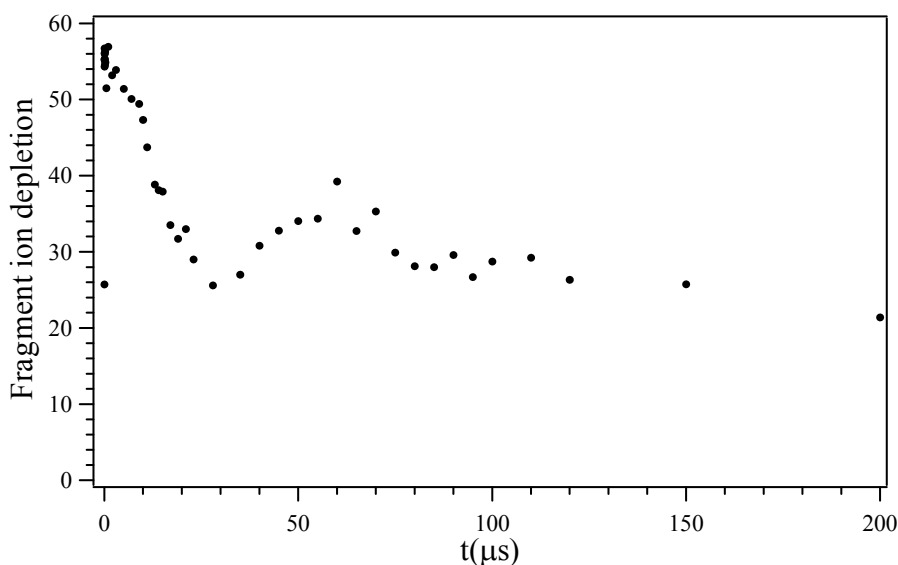


Figure 5.18: Depletion signal of Ac-Phe-(Ala)⁵-Lys-H⁺ conformer B with IR tuned at 3401.6 cm⁻¹ as a function of the time delay between the IR and UV lasers. The lasers are fired 5 ms before the trap opens.

Svendsen et al. have recently simulated the ion-motion inside a 22-pole trap, demonstrating that the charged molecules move as described above [40]. Furthermore, they explain the presence of a single recurrence in the experimental data because of the collisions with residual helium in the trap that randomize the ions trajectories. The trends of the IRLAPS photofragment and the ion depletion signals shown in Figure 5.17 and Figure 5.18

are thus due to the movement of the parent molecules in the trap and not to the existence of some deactivation mechanisms taking place in the pre-excited molecules.

In all the peptides studied by the IRLAPS method, the photofragment signal associated with the chromophore side chain loss is constant upon varying the delay between the lasers and the trap, while fixing the timing between the assisting and the exciting lasers. Moreover, the discussion above demonstrates that this fragment is formed promptly after the CO₂ laser absorption by the UV pre-excited molecules. These two observations indicate that the formation of this fragment ion is fast on the timescale of our experiment and thus suggests that such fragment is an excited state dissociation product. As already mentioned, the IRLAPS photofragment signal associated to the chromophore side chain loss reaches an asymptotic value when the delay between the lasers is ~2 ms, which however is higher than the UV only induced signal. This implies that the lifetime of the electronic excited state to which the biomolecular ions are promoted by UV absorption is at least on the order of milliseconds.

5.4.2 C_α-C_β bond cleavage in protonated aromatic amino acids

The discussion above indicates that the absorption of a UV photon promotes the molecules to a long-lived excited electronic state and that the additional absorption of a CO₂ laser pulse by these pre-excited molecules leads to the prompt cleavage of the C_α-C_β bond, which is not the weakest bond in the charged peptides investigated in this thesis work (cf. *Section 5.3.5*). This section discusses the nature of the long-lived electronic excited state and the origin of the C_α-C_β bond cleavage upon electronic absorption in single aromatic amino acids. The aim is thus to explain the mechanism of the IRLAPS technique from the excited state properties of the charged aromatic amino acids.

The coincidence experiment developed by Jouvet and coworkers allows the detection of charged and neutral photofragments simultaneously. It is, then, possible to extract information on the kinetic energy released in the dissociation process, the number of neutral fragments associated with an ion, the order of the fragmentation steps and the dissociation time scale in a wide window, ranging from tens of nanoseconds to milliseconds [29-31].

Coincidence experiments on protonated tryptophan reveal that its fragmentation *via* the loss of the neutral chromophore side chain occurs on two distinct time scales [29, 30]. This suggests that two different processes, a fast one happening in less than 100 ns and a slow one in few ms, can induce the C_α - C_β bond cleavage in TrpH^+ . The analysis of the experimental results, in combination with *ab initio* calculations, allowed Jouvet and coworkers to propose two distinct fragmentation mechanisms that lead to the C_α - C_β bond rupture in molecules containing the indole ring [29, 30]. Figure 5.19 illustrates the two suggested mechanisms giving rise to the loss of the chromophore side chain. In the scheme in the left-hand side of the figure, the absorption of a UV photon induces the transfer of an electron from the aromatic ring to the NH_3^+ group. This leads to a fast H loss and a consequent formation of a radical cation, which then fragments slowly by breaking the C_α - C_β bond. In the second mechanism (right-hand side of Figure 5.19), the UV laser excitation induces an electron transfer from the aromatic ring to the carboxylic acid oxygen. This causes a fast proton transfer from the charged amino group to the CO bond of the COOH group forming a biradical cation, which then dissociates *via* the C_α - C_β bond cleavage in less than 100 ns.

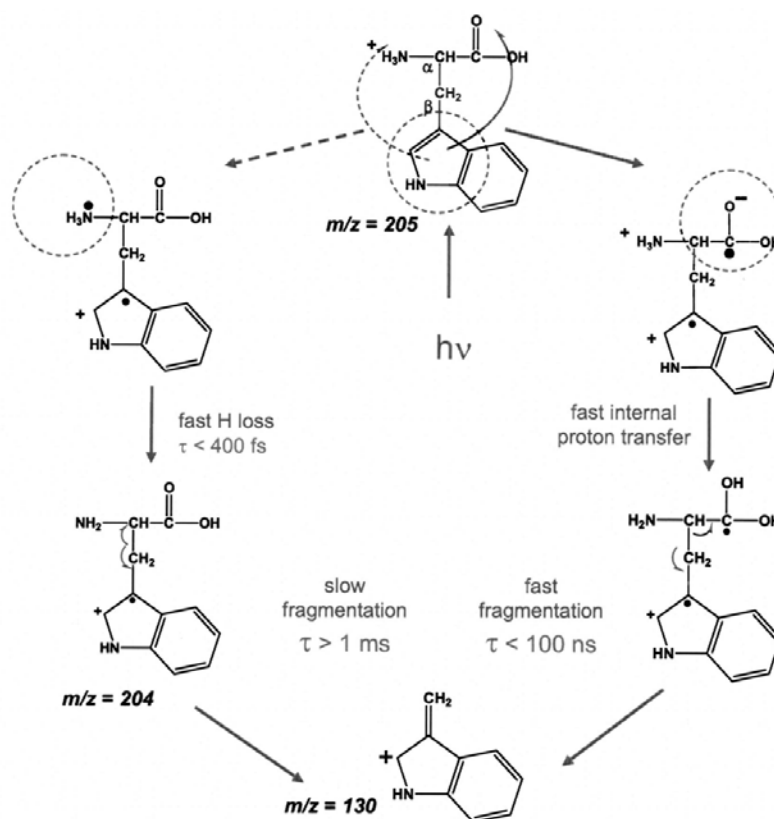


Figure 5.19: Schematic of the two mechanisms giving the C_α - C_β rupture in protonated tryptophan. Right-hand side: The excited state mechanism, through proton transfer toward the carbonyl. Left-hand side: The two-step mechanism. Slow dissociation of the radical cation subsequent to the H loss. Taken from ref. [30].

The analysis of the coincidence results on protonated tyrosine suggests that only the fast mechanism occurs when the phenol group is the chromophore [30]. Furthermore, the H-loss pathway has not been experimentally observed in TyrH^+ while multi-stage photodissociation (MS^n) [41] and femtosecond pump/probe experiments [26, 42] confirm the existence of such reaction in protonated tryptophan and other indole containing molecules. *Ab initio* calculations attribute the H-loss channel to a direct coupling between the locally excited state $\pi\pi^*$ with a low-lying $\pi\sigma^*$ state that is dissociative along the NH bond of the amide group [27, 28]. This fragmentation channel seems less accessible in the case of the protonated tyrosine because the potential energy surface of the dissociative state is higher in energy. Coincidence experiments on protonated tyramine and tryptamine, which have the same aromatic rings as tyrosine and tryptophan without the carboxylic acid group, reveal the lack of the fast fragmentation channels in these molecules, thus confirming the role of the carboxylic CO for the activation of this fast mechanism [30]. Jouvet and coworkers, with the support of *ab initio* calculations, suggest that the fast dissociation *via* the $\text{C}_\alpha\text{-C}_\beta$ rupture occurs directly on the excited electronic surface [30].

Phenylalanine vs. phenethylamine

As already discussed, the analysis of the IRLAPS results of several charged peptides indicate that the CO_2 laser acts on the state initially populated by the absorption of a UV photon. The formation of a biradical cation promptly after UV excitation followed by the chromophore side chain loss in less than 100 ns could explain our results. Indeed, this intermediate species, observed for small, protonated molecules containing indole or phenol as chromophore, could fragment upon IRMPD, enhancing the signal due to the neutral chromophore side chain loss. The release of the aromatic ring as neutral or charged depends on the relative ionization potential (IP) of the chromophore side chain with respect to the peptide backbone. In single protonated aromatic amino acids and, generally, in small charged systems, the charge is localized on the aromatic ring because its ionization potential is lower than that of the peptide chain. As the chain lengthens, its IP decreases and the charge remains on the peptide chain, which explains why in the peptides investigated with the IRLAPS technique the primary photofragment detected is the cation due to the chromophore loss. Since in IRLAPS experiments on phenylalanine containing peptides this is the preferred

fragmentation channel, UV excitation should produce an intermediate species also in molecules having the phenyl ring as the chromophore group. This subsection explores the photofragmentation induced by IRMPE after electronic excitation of protonated phenylalanine and a molecule with its same structure except for the carboxylic group, phenethylamine (m/z 122). According to Lucas *et al.* [30] and assuming that the molecules containing the phenyl group behave like those with phenol as chromophore, only the fast dissociation mechanism, which involves the formation of a biradical cation, should be responsible for the cleavage of the C_α - C_β bond in protonated phenylalanine. In addition, the absence of the COOH group in phenethylamine should completely prevent the formation of fragment ions due to this bond rupture, supporting the idea that the phenyl group behaves similar to the phenol ring. Therefore, the study of these two molecules employing the IRLAPS technique would help us verify the formation of a biradical, intermediate species in phenylalanine-containing peptides.

Figure 5.20 shows the photofragment mass spectrum of PheH^+ recorded with and without the assistance of the CO_2 laser.

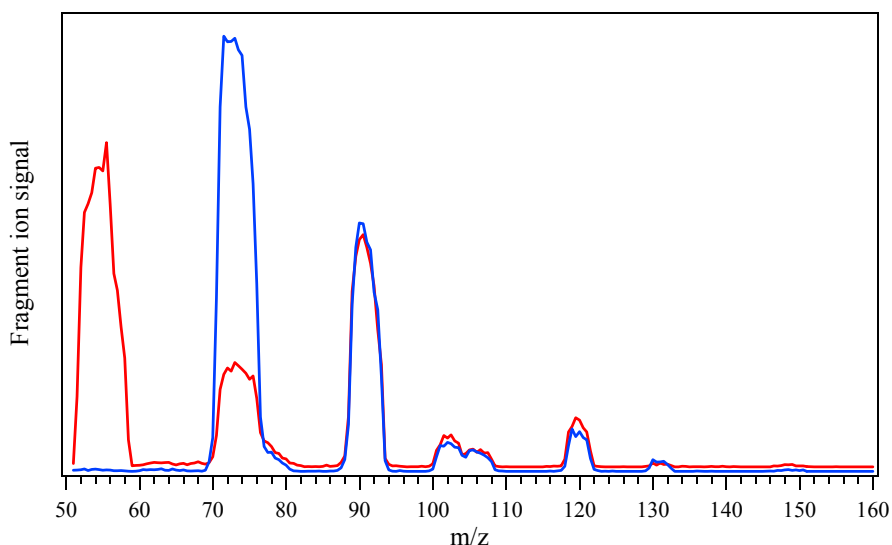


Figure 5.20: Photofragment mass spectra of PheH^+ obtained by UV photofragmentation (blue trace) and by UV excitation assisted by IRMPE (red trace). The UV laser is fixed at the conformer B band origin at 37527.9 cm^{-1} [3] and the CO_2 laser set at the 9P(16) rovibrational line.

The most intense UV only fragment signal, m/z 74, corresponds to $\text{NH}_2\text{-CH-COOH}$, the radical cation left upon the cleavage of the C_α - C_β bond [3]. The other major UV-only fragment is spread over the mass channels 91-93. The m/z 93 ion might come from the

production of di-hydrogenated chromophore, a channel also observed in positively charged tryptophan and tyrosine [29, 30]. The m/z 91 corresponds to the side chain radical cation but it is not clearly distinguishable from the other charged fragment. The subsequent absorption of the CO_2 laser after the UV excitation induces the formation of a new dissociation product, m/z 56, absent in the UV-only photofragment mass spectrum, and the simultaneous reduction of the m/z 74. The connection between these channels appears evident when monitoring the photofragment signals as a function of the UV- CO_2 laser delay. Indeed, the m/z 56 signal decreases as much as that associated with m/z 74 with increasing laser delay. The m/z 56 daughter ion might derive from the loss of a water molecule from the $\text{NH}_2\text{-CH-COOH}$ fragment and thus could be a secondary dissociation product induced by the absorption of the CO_2 laser by the primary fragment. Moreover, the $\text{C}_\alpha\text{-C}_\beta$ bond rupture in protonated phenylalanine seems to occur right after the electronic excitation, since the maximum signal of the m/z 56 photofragment is achieved when the delay between the UV and the CO_2 lasers is ~ 100 ns. In the case of protonated phenylalanine, the UV laser seems thus to induce the $\text{C}_\alpha\text{-C}_\beta$ bond cleavage *via* a fast mechanism.

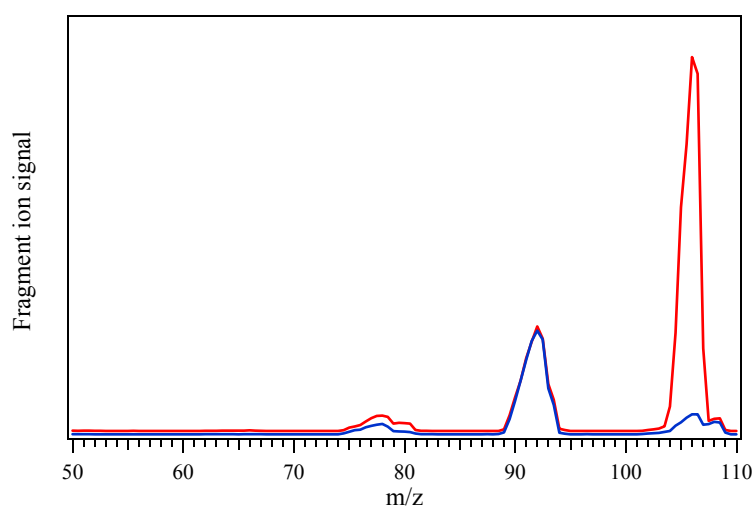


Figure 5.21: Photofragment mass spectra of protonated phenethylamine obtained by UV photofragmentation (blue trace) and by UV excitation assisted by IRMPE (red trace). The UV laser is fixed at the band origin at 37699.22 cm^{-1} and the CO_2 laser set at the 9P(16) rovibrational line.

Figure 5.21 shows the photofragment mass spectra of protonated phenethylamine measured with and without the assistance of the CO_2 laser. IRMPE subsequent to UV excitation seems to enhance most the m/z 105 fragment, which corresponds to the loss of the charged ammonium group. However, this channel turns out to be induced by the absorption

of the CO₂ laser pulse alone. The m/z 77 fragment could be the phenyl ring and its signal increases slightly upon IRMPD following UV excitation. It is worth noticing that for protonated phenethylamine, the additional absorption of the CO₂ laser after electronic excitation does not induce the formation of secondary dissociation products.

The results obtained applying the IRLAPS method on protonated phenylalanine and phenethylamine seems to support the initial assumption that these phenyl containing molecules behave like those containing phenol as chromophore. Indeed, IRMPD subsequent to electronic excitation induces dissociation of the primary fragment only in PheH⁺, suggesting the prompt formation of an intermediate species after UV absorption, which then dissociates *via* the cleavage of the C_α-C_β bond. A fast mechanism must be responsible for this channel, since the CO₂ laser induces secondary fragmentation also when it is fired 100 ns after the UV excitation. The absence of new fragments upon IRMPD after absorption of a UV photon in positively charged phenethylamine helps confirm the role of the COOH group in a fast mechanism, which involves electron transfer to the CO group with the consequent formation of a biradical cation. Moreover, in analogy with the coincidence experiment on tyramine and tryptamine [30], the m/z 93 fragment of phenethylamine could correspond to the di-hydrogenated side chain, suggesting that the dissociation of phenethylamine does not involve the C_α-C_β bond rupture.

The results discussed in this section might explain the enhancement of the fragment due to the neutral side chain loss in the protonated peptides studied in this thesis work upon IRMPD subsequent to electronic excitation. For all the three aromatic amino acids, the absorption of a UV photon leads to the fast formation of a biradical cation and one could imagine that the CO₂ laser acts on this intermediate species, enhancing the signal associated to the protonated chromophore side chain. In larger peptides, the latter is emitted as neutral because the IP of the chain is smaller than that of the aromatic ring. However, according to the mechanism proposed by Jouvét and coworkers, the lifetime of the biradical cation is really short, since it dissociates *via* the cleavage of the C_α-C_β bond in less than 100 ns [30]. By contrast, the intermediate state populated by the UV excitation in the protonated peptides investigated by the IRLAPS technique lives at least a few hundreds of μs (cf. *Section 5.4.1*). Therefore, while the fast dissociation model discussed here might explain the behavior

observed in protonated phenylalanine, it does not clarify the results obtained for larger peptides.

Role of the charge: Ac-Phe-(Ala)₅-LysH⁺+Crown Ether

In both models proposed by Lucas *et al.* to explain the dissociation of singly-protonated aromatic amino acids, the charge on the ammonium group plays an essential role [30]. Indeed, the fast mechanism predicts the electron transfer from the aromatic ring to the carboxylic oxygen, which then leads to a fast proton transfer from the NH₃⁺ group to the CO group and the formation of a biradical cation. On the other hand, in the slow process the UV absorption induces the electron transfer directly to the protonated amino group followed by hydrogen loss (cf. Figure 5.19). In accordance with these models, preventing movement of the charge after electronic excitation should avoid the fragmentation of protonated peptides *via* the C_α-C_β bond cleavage and consequently the IRLAPS method should work less effectively. The size of 18-crown-6 ether (CE) is optimum to form three hydrogen bonds with an ammonium group and thus it binds to lysine when the latter is present in the peptide chain [43-45]. Nielsen and coworkers have recently demonstrated that tagging the ammonium groups by crown ether serves to eliminate the process involving the H loss and to sequester the protons [46]. These results suggest that studying the complex of the Ac-Phe-(Ala)₅-Lys-H⁺ with CE (m/z 957) by means of the IRLAPS method would disentangle the role of the charge in the formation of an intermediate state.

Figure 5.22 shows the photofragment mass spectrum of this complex obtained by UV excitation alone and with subsequent IRMP. As it happens for all the large peptides investigated with the IRLAPS technique up to now, the most enhanced fragments involve the loss of the neutral phenylalanine side chain. Indeed, the m/z 693 ion is due to the detachment of the crown ether and it is induced by the absorption of the CO₂ laser alone. The m/z 865 corresponds to the loss of the chromophore *via* cleavage of the C_α-C_β bond and the additional detachment of the crown ether leads to the m/z 601 fragment. This latter species is observed also when the delay between the exciting and assisting lasers is ~100 ns, suggesting it results from a primary fragmentation of the complex and not from a secondary dissociation process of the m/z 865 cation. These findings indicate that the charge does not play an active role in the formation of an intermediate state after the electronic excitation.

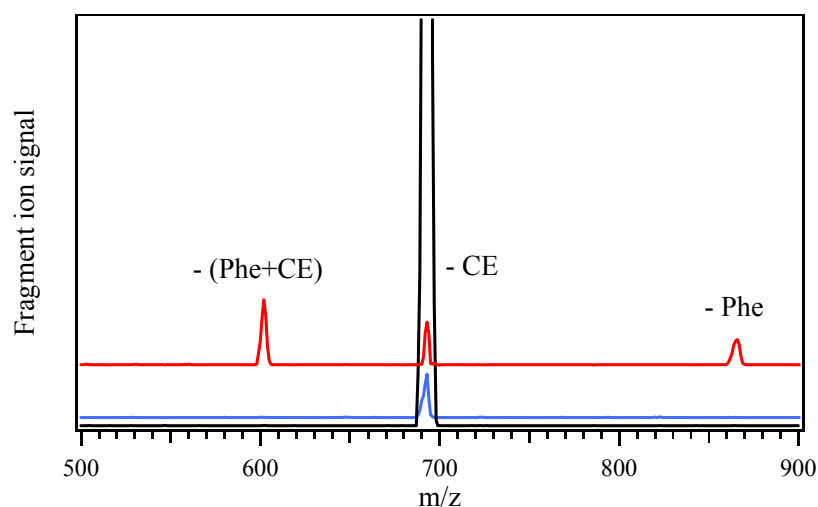


Figure 5.22: Photofragment mass spectra of the complex $\text{Ac-Phe-(Ala)}_5\text{-LysH}^+$ with 18-crow-6 ether obtained by UV photofragmentation (blue trace), by UV excitation assisted by IRMPE (red trace) and by the CO_2 laser alone set at the 9P(16) rovibrational line (black trace). The UV laser is tuned at 35327.1 cm^{-1} .

The discussion above suggests that the models proposed by Jouvet and coworkers to describe the fragmentation of the aromatic amino acids *via* breakage of the $\text{C}_\alpha\text{-C}_\beta$ bond cannot be used to explain the improvement of the dissociation signal due to the loss of the neutral chromophore in large peptide in the IRLAPS experiment. However, the fast mechanism involving the formation of the biradical cation upon electronic excitation which then leads to the cleavage of the $\text{C}_\alpha\text{-C}_\beta$ bond can explain the existence of this dissociation channel in the UV-only induced photofragment mass spectrum of the protonated peptides.

5.4.3 Electron-driven proton-transfer reaction

The group of Sobolewski and Domcke has devoted particular attention to studying the photophysics of hydrogen-bonded molecular systems with *ab initio* electronic-structure calculations [33-39]. The main idea behind their work lies on the need of understanding the role of hydrogen bonds in the UV-induced photochemistry of biological macromolecules. Indeed, UV exposure of peptides or proteins results in a complex photochemistry that eventually leads to structural changes and the loss of functionality. Therefore, mechanisms which suppress undesired photoinduced reactions in proteins are of fundamental importance to understand.

Shemesh *et al.* have recently reported the excited-state *ab initio* calculations of the neutral tripeptide Gly-Phe-Ala, providing evidence for an efficient excited-state deactivation pathway in the conformer shown in Figure 5.23, which contains the γ hydrogen-bond motif commonly found in the backbone of peptides [39]. The most important feature of the mechanism is an electron-driven proton-transfer (EDPT) reaction along a pre-existing $\text{C}=\text{O}\cdots\text{N}-\text{H}$ hydrogen-bond in a charge-transfer (CT) excited state of the tripeptide.

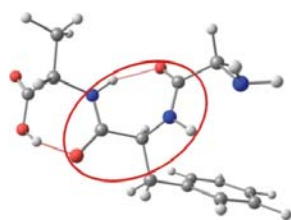


Figure 5.23: Ground state equilibrium geometry of Gly-Phe-Ala.

Figure 5.24a illustrates schematically the potential energy surfaces implicated in the EDPT process along the $\text{C}=\text{O}\cdots\text{N}-\text{H}$ hydrogen-bond. The absorption of a UV photon populates the lowest bright excited electronic state of the phenyl ring, the $^1\pi\pi^*$ state. This spectroscopic state is higher in energy than the locally excited state on the aromatic amino acid backbone (^1LE), which involves the excitation of an electron from a nonbonding orbital of the backbone to an unoccupied orbital localized on the same branch of the backbone (Figure 5.24b). Moreover, the two surfaces intersect at a point only slightly above the minimum of the $^1\pi\pi^*$ surface. An additional low-lying singlet state exists, involving the excitation of an electron from an orbital located in the region of the hydrogen-bonded NH group to an unoccupied orbital located in the region of the hydrogen-bonded CO group (Figure 5.24b). This can be classified as a charge-transfer (^1CT) state and it has conical intersections with the ^1LE state and the ground electronic state (S_0) [39].

The *ab initio* electronic-structure calculations suggest the following mechanism for deactivation of the excited electronic surface. The absorption of a UV photon populates the $^1\pi\pi^*$ state, which then relaxes to the ^1LE state *via* a low-lying conical intersection. This state intersects, in turn, the ^1CT surface. The population of the latter corresponds to the transfer of an electron from the NH to the CO groups along the intramolecular hydrogen-bond. The proton then follows the electron leading to a pronounced stabilization of the ^1CT state. This corresponds to the formation of a stable biradical species because of the presence of two unpaired electrons, one localized on the phenyl ring and the other on the peptide backbone.

The intermediate species relaxes back to the S_0 state *via* a conical intersection between the ^1CT and S_0 surfaces. In this way, the electronic excitation energy is converted by means of three conical intersections into vibrational energy in the electronic ground surface [39].

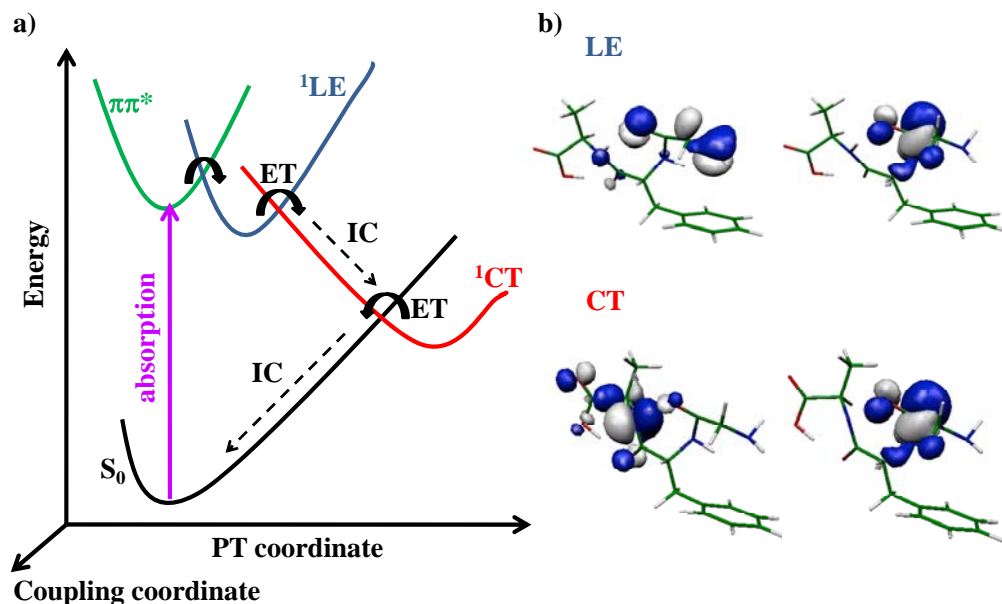


Figure 5.24: (a) Schematic view of the EDPT process in intermolecular hydrogen-bonded systems; (b) occupied and unoccupied orbitals in the local excited (LE) and charged transfer (CT) states (adapted from Sobolewski and Domcke [36]).

Visible laser assisted photofragment spectroscopy

The results discussed above suggest that the intermediate species, i.e. a biradical, is a short-lived species, in contrast with the findings in the IRLAPS experiments discussed in Section 5.4.1. However, its formation involves orbitals located on part of the backbone near the aromatic amino acid. Thus, if the aromatic amino acid belongs to a protonated peptide, the formation of a biradical should be independent of the presence of the positive charge. A recent study on a doubly deprotonated pentapeptide seems to confirm the latter statement [47]. Joly *et al.* performed multi-stage (MS^n , where n is the number of stages) photodissociation experiments on a tryptophan radical containing peptide, the doubly dehydrogenated WVVVV [47].

In MS^2 experiments, the precursor ions, isolated in a trap, interact with two different laser beams. The absorption of a 266 nm photon generates a radical species by electron photodetachment in less than 100 ns, which then fragments upon absorption of a 490 nm

photon. Hence, also in negatively charged peptides, the electronic excitation produces an intermediate species, a radical in the specific case. In the MS^3 experiments, the radical species produced after the absorption of the pump laser is isolated in a second stage and irradiated by the tunable probe laser.

The main dissociation product upon electronic excitation of WVVVV-2H is that due to the loss of the dehydrogenated tryptophan side chain, as shown in the left-hand side of Figure 5.25 [47]. This indicates that the cleavage of the C_α - C_β bond, which finally leads to the loss of the aromatic side chain, is the preferred dissociation channel not only in positively charged peptides. In addition, the intermediate species can be trapped in the MS^3 stage for several tens of milliseconds, which then represents an estimation of the radical lifetime [47]. As discussed in Section 5.4.1, the intermediate species formed in protonated peptides promptly after the UV excitation is a long-lived species and its lifetime is then comparable to that found for the radical species from Joly *et al.* Finally, the right hand side of Figure 5.25 illustrates the electronic spectrum of the radical species measured in the MS^3 experiments of the Dugourd group by monitoring the fragment due to the tryptophan side chain loss while scanning the visible laser [47]. This experimental photodissociation spectrum is in good agreement with the visible calculated absorption spectrum for the neutral indolyl radical, meaning that the rest of the molecule has a weak influence on the optical properties of the radical. The visible band in this open-shell species is associated with a strong transition from an inner π orbital to the single occupied π HOMO [48].

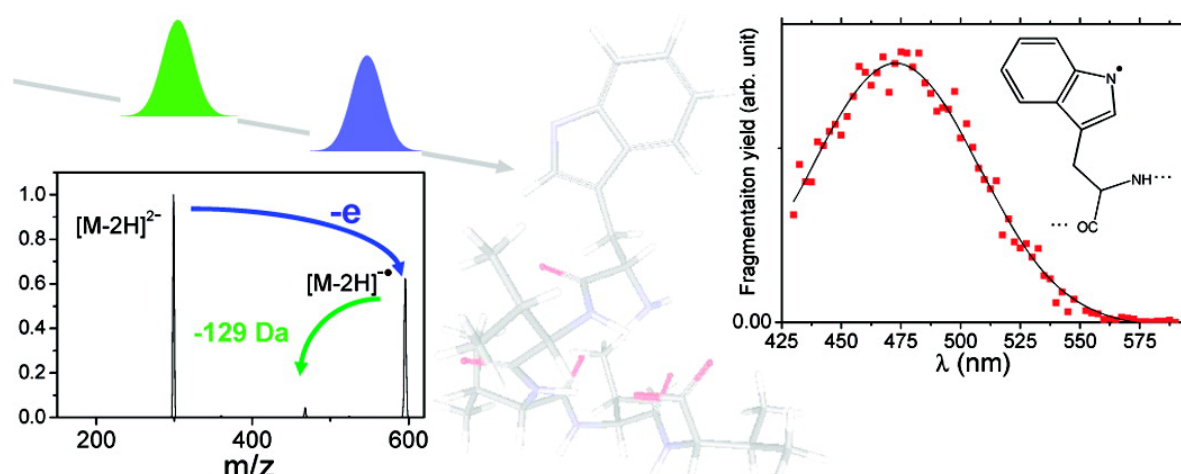


Figure 5.25: Left-hand side: photofragment mass spectrum of the doubly deprotonated $[M-2H]^{2-}$ WVVVV obtained upon absorption of 266 nm and 490 nm photons. Right-hand side: electronic spectrum of the radical species measured by detecting the fragment due to the tryptophan side chain loss. Taken from Joly *et al.*[47].

The discussion above suggests that in our IRLAPS experiment if the species generated by the absorption of a UV photon is a biradical, then it should absorb in the visible region. The spectroscopic scheme employed to verify this statement is analogous to that used in the usual IRLAPS experiment (Figure 5.3), but replacing the CO₂ laser with a tunable visible laser (Figure 5.26).

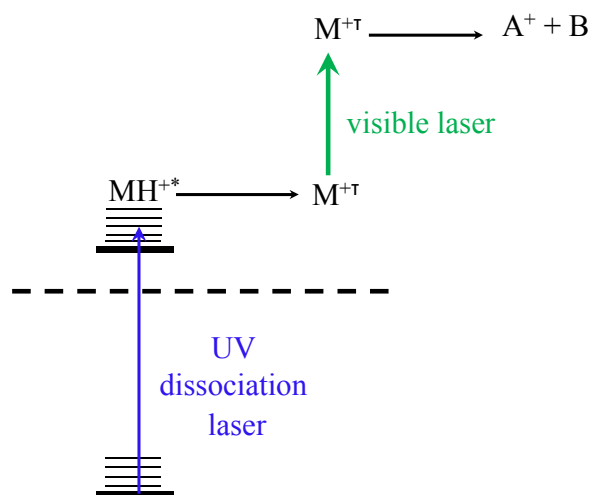


Figure 5.26: VISLAPS scheme to obtain electronic spectrum of the biradical cation, presumably formed right after the UV excitation of protonated peptides. The visible laser is fired 200 ns after the UV laser, as in the usual IRLAPS scheme (Figure 5.3).

The photofragment mass spectrum of Ac-Phe-(Ala)₅-LysH⁺ in Figure 5.27 demonstrates that this protonated peptide absorbs in the VIS region only after the excitation of the UV laser and that the main dissociation products involve the loss of the chromophore side chain.

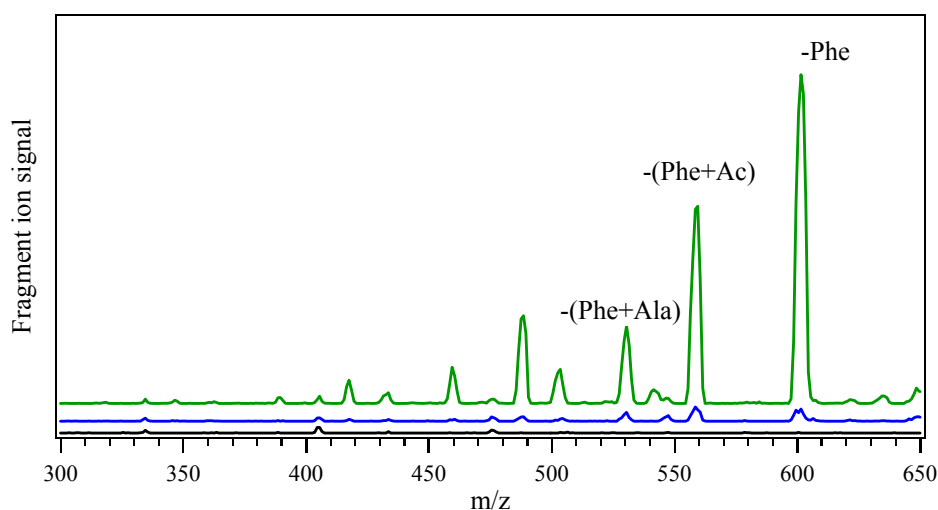


Figure 5.27: Photofragment mass spectra of Ac-Phe-(Ala)₅-LysH⁺ obtained by UV photofragmentation (blue trace), by UV excitation followed by VIS excitation (green trace) and by the visible laser alone set at 18130 cm⁻¹ (black trace). The UV laser is tuned at 37560.5 cm⁻¹.

Figure 5.28 shows the electronic spectrum in the visible region of the Ac-Phe-(Ala)₅-LysH⁺ intermediate species formed promptly after the UV excitation, obtained monitoring the m/z 601 fragment, which is due to the cleavage of the C_α-C_β bond, as the wavelength of the visible laser is scanned.

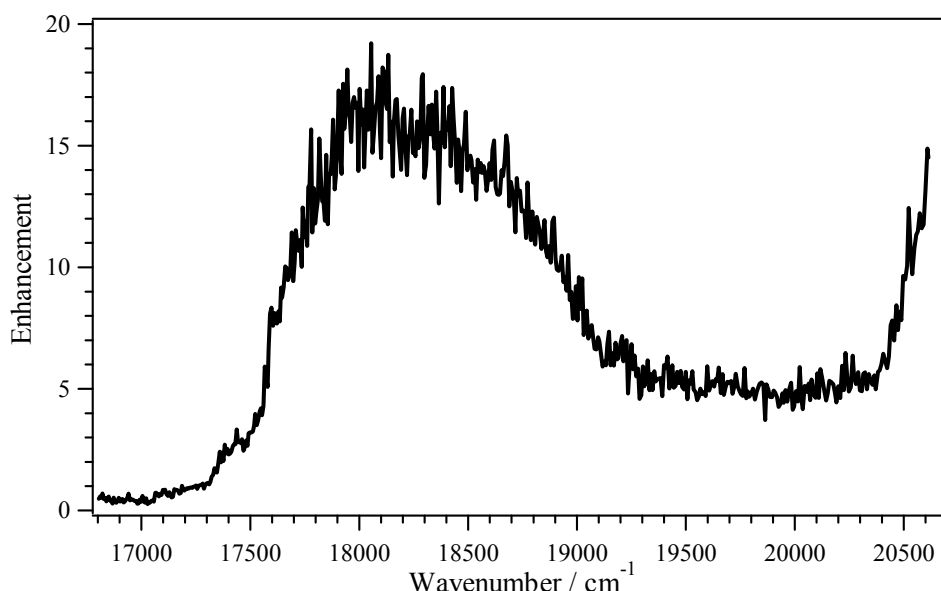


Figure 5.28: Electronic spectrum of the biradical cation formed promptly after the UV excitation of Ac-Phe-(Ala)₅-LysH⁺ measured monitoring the photofragment due to the cleavage of the C_α-C_β bond. The visible laser is fired 200 ns after the UV laser, as in the usual IRLAPS scheme (Figure 5.3).

In these measurements the delay between the UV and the visible lasers is 200 ns to maximize the photofragment signal due to the absorption of the two lasers and the dependence of the signal as a function of the timing between the lasers is the same observed in the usual IRLAPS experiment (cf. *Section 5.4.1*). These results indicate that it is possible to assist the dissociation of a UV pre-excited peptide with a visible laser instead of a CO₂ laser (*VISLAPS*), supporting the idea that the UV excitation of protonated molecules leads to the formation of biradical cations.

Excited-state ab initio calculations on Ac-Phe-(Ala)₃

As already mentioned, according to the studies of Sobolewski and Domcke on hydrogen-bonded molecular systems [33-39], the biradical species produced immediately after the electronic excitation is short-lived, which contradicts our observations (cf. *Section*

5.4.1) as well as those made in the Dugourd group [47]. This suggests that there may be a further minimum in the CT state of Figure 5.24 corresponding to a stable conformation of the intermediate species that lives several milliseconds. The additional absorption of the CO₂ or the visible laser by this species would then break its weakest bond, which is the C_α-C_β bond as discussed in Section 5.4.2.

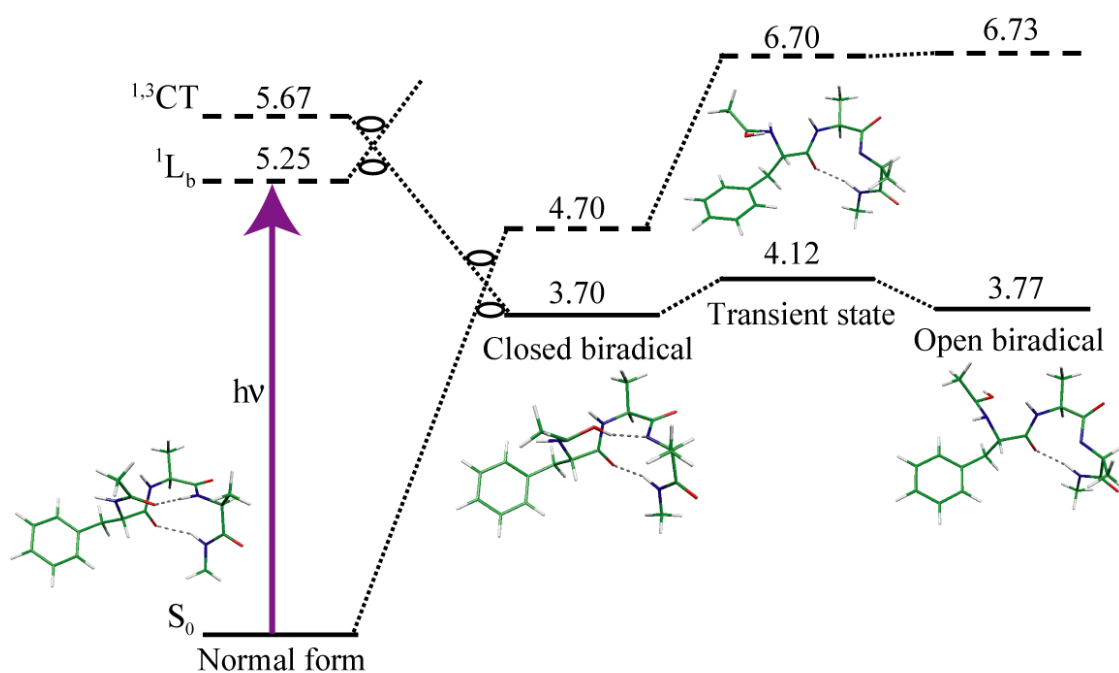


Figure 5.29: Photophysical scheme of Ac-Phe-(Ala)₃ determined by excited-state *ab initio* calculations. Solid lines denote optimized states while vertical energy levels calculated at a given geometry are denoted by dashed lines. Dotted lines denote adiabatic correlations between the states. Numbers denote energy in eV relative to the ground state. (Adapted from [49]).

Sobolewski has recently performed preliminary excited-state *ab initio* calculations on a truncated version of Ac-Phe-(Ala)₅-Lys-H⁺, the neutral protected peptide Ac-Phe-(Ala)₃ [49]. Figure 5.29 illustrates the lowest-energy electronic states involved in the photophysics of this small molecule. As in the tripeptide Gly-Phe-Ala [39], the spectroscopic $\pi\pi^*$ state, populated through the absorption of a UV photon, relaxes to a ¹LE state *via* a low-lying conical intersection. There exists a second crossing point between the latter state and the ^{1,3}CT, the population of which implies an electron transfer from the Ala³ NH group to the Phe¹ CO group along the intramolecular hydrogen-bond they form. The proton then follows the electron, stabilizing the charge transfer state by the formation of the COH \cdots N hydrogen-bond between Ala³ and Phe¹ which produces a closed biradical species. This is a short-lived

species because of the conical intersection existing between the ^1CT state and the ground electronic state, S_0 , as in the case of Gly-Phe-Ala [39]. However, another form of the biradical species is energetically accessible after the EDPT process, i.e. the open biradical, which results from the rotation of the acetyl group along the dihedral angle CCNC and can live long because of the lack of a direct access to the conical intersection with the ground state [49]. One could then imagine that after electronic excitation the two forms coexist and are both stable. As already mentioned, the formation of a hydrogen-bond, after the EDPT process, stabilizes the closed biradical species. On the other hand, intramolecular vibrational energy redistribution (IVR) might stabilize the open form, dissipating the excitation energy into other intramolecular degrees of freedom. Collisions between the UV pre-excited peptides with residual helium in the 22-pole ion trap might also contribute to the stabilization of the open biradical form. As discussed in *Section 5.4.1*, IRMPE subsequent to electronic excitation enhances the photofragment signal associated with the chromophore loss even for 200 ns delay between the two lasers. This indicates that the open biradical species is already formed and stabilized right after the absorption of the UV laser light prior to any collisions between the helium buffer gas and the pre-excited peptides, since the collisional rate in the 22-pole ion trap is on the order of $10^{-1} \mu\text{s}^{-1}$. We can thus conclude that the dissipation of the energy *via* IVR is the major stabilization factor for the open biradical species.

Figure 5.30 compares the experimental electronic spectrum of the intermediate species produced by the absorption of a UV photon by Ac-Phe-(Ala)₅-LysH⁺, measured employing the VISLAPS technique, with that of the open biradical form of Ac-Phe-(Ala)₃ simulated by preliminary TDDFT calculations of Sobolewski [49]. The generally good agreement between our experiment and Sobolewski's calculations suggests that the visible spectrum of the UV pre-excited Ac-Phe-(Ala)₅-LysH⁺ in Figure 5.30a (or Figure 5.28 in wavenumber) might derive from the absorption of the open biradical form due to the rotation of the acetyl group respect the CCNC dihedral angle.

According to the discussion above, the electronic excitation of Ac-Phe-(Ala)₅-LysH⁺ should produce two stable biradical configurations, i.e. the short-lived, closed and the long-lived, open forms. The formation of the latter would occur by rotating the acetyl group along the CCNC dihedral angle and it would be stabilized by energy dissipation into other intramolecular degrees of freedom *via* IVR. Thus, when performing the IRLAPS experiment on Ac-Phe-(Ala)₅-LysH⁺, the open biradical species would absorb the CO₂ laser, enhancing

the fragmentation signal associated to the cleavage of the weakest bond in the pre-excited cation, i.e. the C_α - C_β bond.

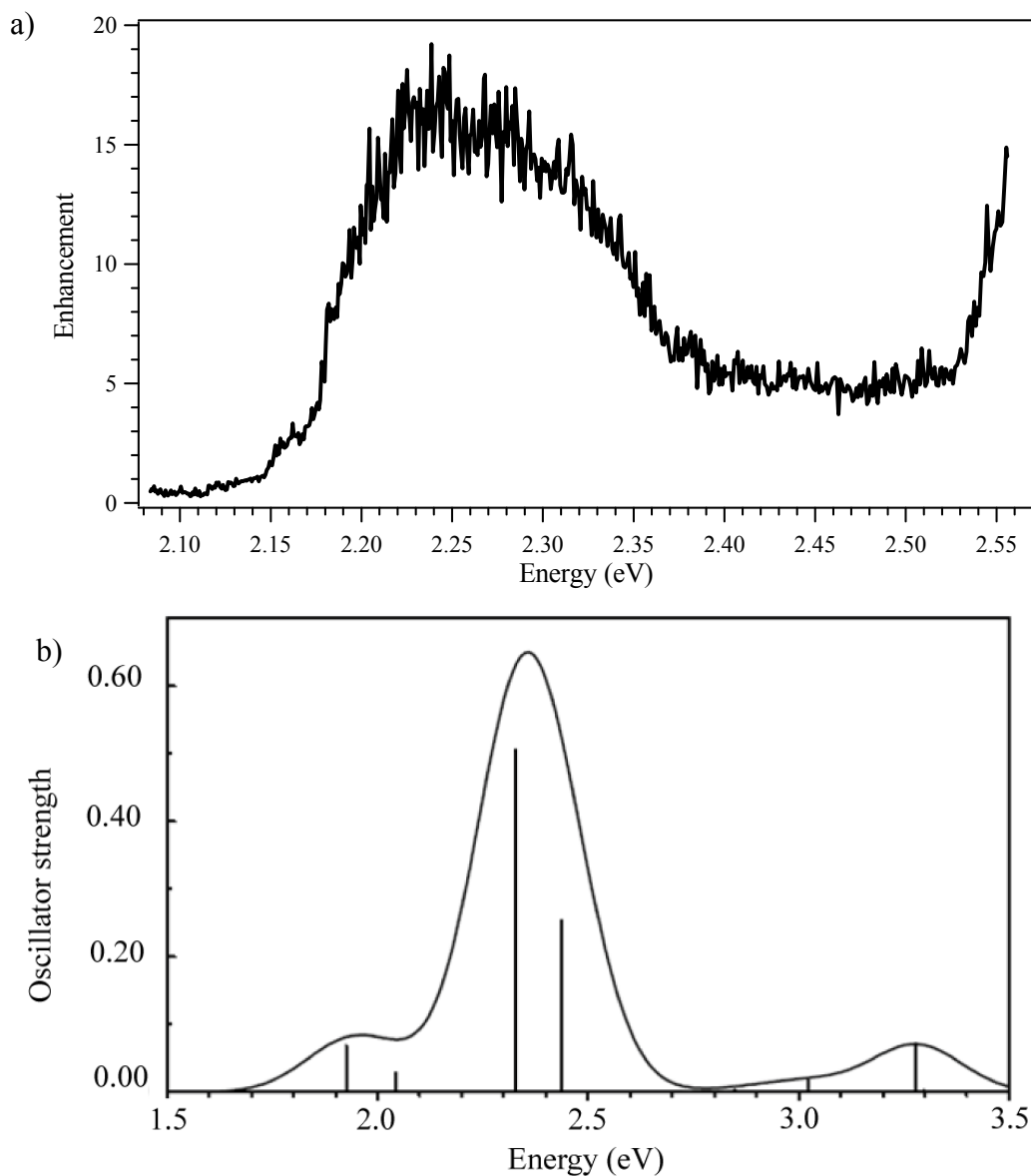


Figure 5.30: (a) Electronic spectrum of the biradical species formed after the absorption of a UV photon by $\text{Ac-Phe-(Ala)}_5\text{-LysH}^+$ measured employing the VISLAPS technique; (b) preliminary TDDFT calculations of the electronic absorption spectrum of the open biradical form of Ac-Phe-(Ala)_3 [49].

Generality of the model

The essential feature of the model just presented is that the energy released during the EDPT process is enough to break a specific hydrogen-bond in the molecule and to induce the

internal rotation of the molecule about the peptide backbone. The dissipation of the energy *via* IVR stabilizes this species, leading to the formation of an open biradical species.

In general, in multi hydrogen-bonded systems, the absorption of a UV photon by the probing chromophore could *a priori* induce the EDPT process to occur along any of these bonds. However, the energy released during this process is not enough to break definitely all the hydrogen-bonds, the reformation of which would then hinder the rotation of a particular group and the consequent formation of an open biradical species. In all the protected, protonated peptides studied with the IRLAPS method in this thesis work, the protecting acetyl group is covalently bound to the aromatic amino acid and, most probably, forms a hydrogen-bond with another amino acid in the chain in analogy with the tripeptide Ac-Phe-(Ala)₃ investigated by Sobolewski [49]. It is thus plausible to employ the aforementioned model to explain the observed enhancement of the fragment due to the C_α-C_β bond cleavage upon IRMPD subsequent to electronic excitation. Indeed, the acetyl group is connected to the rest of the molecule with a single hydrogen-bond and the energy released in the EDPT process is enough to break this specific bond and to induce the rotation of the acetyl group, as previously discussed.

These observations suggest that the IRLAPS method would work by this particular mechanism only on a specific class of peptides-those having a moiety whose rotation is only hindered by the existence of a single hydrogen-bond with the rest of the molecule. The cleavage of this bond, due to the EDPT process induced by electronic absorption, would leave the moiety free to rotate. However, this spectroscopic technique has been also employed to measure the electronic and the vibrational spectra of other small, natural-occurring, protonated peptides, namely bradykinin and the cyclic gramicidin S [50, 51]. Because of the two highly basic arginines, bradykinin can form a salt-bridge, thus assuming a compact structure [52]. On the other hand, the cyclic gramicidin S is expected to form β -sheets in solution [53]. These two biological molecules thus differ significantly from the protected peptides investigated with the IRLAPS technique in this thesis work (cf. Figure 5.31). Both proteins contain two phenylalanines and their main dissociation product upon IRMPD following UV excitation is that due to the loss of one of the two chromophores *via* the cleavage of the C_α-C_β bond, as in the protected charged peptides [50, 51]. These results indicate that the IRLAPS method works also in systems with multi hydrogen-bonds where it

is not trivial to identify a moiety free to rotate after the EDPT process occurs. One could then hypothesize that the absorption of a UV photon can populate the closed biradical form and a new biradical species, which should not be necessarily the open rotamer. It is thus possible that the molecules undergo a conformational change before reforming the hydrogen-bonds broken during the EDPT process. This new excited state conformation can be stabilized through IVR and would be able to absorb the CO₂ laser pulse, thus enhancing the fragment signal associated with the cleavage of the weakest bond, i.e. the C_α-C_β bond. The new conformation obtained after the absorption of a UV photon and the EDPT cannot be *a priori* established and it has to be calculated for every molecule. In the specific case of a protected peptide, the conformational change is easily identified in the rotation of the protecting group.

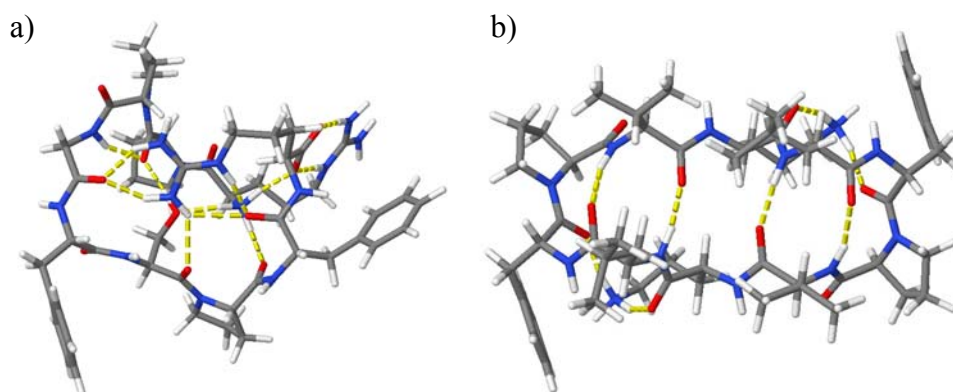


Figure 5.31: Model-structures of (a) the doubly protonated bradykinin ($\text{ArgH}^+(\text{Pro})_2\text{-Gly-Phe-Ser-Pro-Phe-ArgH}^+$) and (b) the doubly protonated cyclic gramicidin S ($\text{cyclo-Val-OrnH}^+\text{-Leu-Phe-Pro-Val-OrnH}^+\text{-Leu-Phe-Pro}$) as generated from Macromodel [54].

5.5 Conclusions

This chapter has discussed the recent experimental developments made in our group to measure the electronic and the vibrational spectra of large, protonated peptides of up to seventeen amino acids using a photofragment-based detection scheme. The break-through has been to assist the dissociation of the UV pre-excited molecules by a CO₂ laser, applying the IRLAPS method, which was originally developed to measure weak overtone transitions of small polyatomic molecules, to large peptide ions.

We have shown that IRMPE subsequent to the UV absorption does not distort the electronic and vibrational spectra of three different seven-amino-acid peptides, which differ only in the aromatic amino acid used as a chromophore. The same technique was also successfully applied to measure the ultraviolet and infrared spectra of larger peptides. The striking feature of these results is the increase of the photofragment signal of up to two orders of magnitude induced by the additional absorption of the CO₂ laser when phenylalanine is used as the unique chromophore in the peptide sequence. In the case of tyrosine-, tryptophan- or double-chromophore-containing peptides, the supplementary IRMPE enhances the dissociation yield by one order of magnitude. The unexpected result is that, independently of the chromophore used as a probe, the cleavage of the C_α-C_β bond is the preferred dissociation channel, even if it is not the weakest bond in the ground electronic state molecules. Moreover, the fragmentation through this channel occurs promptly after the electronic excitation and forms an intermediate with a lifetime on a millisecond timescale.

Two models are discussed in this chapter to explain our observations. The first one relies on the work of Jouvét and coworkers on the electronic excited dissociation of protonated aromatic amino acids [24-32]. The basis of the second model lies on the EDPT process occurring in multi hydrogen-bonded systems investigated by Sobolewski and Domcke [33-39]. Both models suggest the fast formation of a biradical intermediate species after the electronic excitation, which then leads to the loss of the chromophore side chain *via* the rupture of the C_α-C_β bond. The supplementary absorption of the CO₂ laser by the biradical species would finally enhance the photofragmentation signal due to the neutral chromophore side chain loss. However, both models predict a short-lived intermediate species, contradicting our experimental results. In addition the charge does not seem to play an essential role in the applicability of the IRLAPS method, as one might expect in the model proposed by Jouvét and coworkers in explaining the enhancement of the aromatic ring loss channel. Nevertheless, the work carried out in the Jouvét group helps elucidate the behavior of the single aromatic amino acids upon IRMPE after electronic excitation as well as the C_α-C_β bond cleavage channel after UV-only absorption. The model of Sobolewski and Domcke considers neutral molecules, which renders it suitable to explain the formation of a biradical intermediate independent of the peptide charge, but it predicts a fast deactivation of the pre-excited electronic state. Recent calculations on a protected, phenylalanine-containing, neutral tripeptide by Sobolewski show that in addition to a short-lived biradical, there may

exist a long-lived intermediate species, corresponding to an open biradical form. Indeed, the energy released during the EDPT process is enough to induce the rotation of the protective group, with the new conformation stabilized through IVR. The additional absorption of the CO₂ laser by the open biradical species would then lead to the increase of the photofragment signal due to the C_α-C_β bond cleavage. These calculations suggest that the IRLAPS technique would work on a specific class of peptides, those having a moiety free to rotate. However, the method was successfully employed to measure the electronic and vibrational spectra of protonated bradykinin and gramicidin S, whose structures differ significantly from that of the protected peptides investigated in this thesis work. One could then hypothesize that the energy released in the EDPT process is enough to induce a conformational change in the peptides and that this new species is stable. The new structure would then fragment upon IRMPD enhancing the chromophore side chain loss channel, since after the electronic excitation the C_α-C_β bond is the weakest in the peptide. It is generally difficult to predict the conformational change induced by the absorption of a UV photon and it should be calculated for each molecule. In the specific case of N-protected peptides, it is, however, easy to determine which moiety of the molecule causes the structural change. If the electronic excitation of a protonated peptide generates a stable biradical species independently of the structure, then the IRLAPS technique would always work. An additional confirmation of this idea would then be to hinder the rotation of any moieties of the peptide using, for example, prolines and determine whether the IRLAPS method will still enhance the signal due to the neutral chromophore side chain loss.

It should be finally pointed out that in cases in which the primary deactivation channel subsequent to UV absorption is direct internal conversion to the ground electronic state, the IRLAPS technique should work as originally proposed, by acceleration of the dissociation rate on the ground electronic surface.

References

1. Stearns, J.A., Seaiby, C., Boyarkin, O.V., and Rizzo, T.R., *Phys. Chem. Chem. Phys.*, **2009**, 11: p. 125-132.
2. Stearns, J.A., Boyarkin, O.V., and Rizzo, T.R., *J. Am. Chem. Soc.*, **2007**, 129: p. 13820-13821.

3. Stearns, J.A., Mercier, S., Seaiby, C., Guidi, M., Boyarkin, O.V., and Rizzo, T.R., *J. Am. Chem. Soc.*, **2007**, 129(38): p. 11814-11820.
4. Mercier, S., *Electronic and Vibrational Spectroscopy of cold protonated amino acids in the gas phase*, in *PhD Thesis, EPFL, Lausanne*. 2008.
5. Robinson, P.J. and Holbrook, K.A., *Unimolecular Reactions*. 1972, London New York Sydney Toront: Wiley-Interscience, a division of John Wiley & Sons Ltd.
6. Dunbar, R.C. and McMahon, T.B., *Science*, **1998**, 279(5348): p. 194-197.
7. Settle, R.D.F. and Rizzo, T.R., *J. Chem. Phys.*, **1992**, 97(4): p. 2823-2825.
8. Lubich, L., Boyarkin, O.V., Settle, R.D.S., Perry, D.S., and Rizzo, T.R., *Faraday Discuss.*, **1995**, 102: p. 167-178.
9. Boyarkin, O.V. and Rizzo, T.R., *J. Chem. Phys.*, **1996**, 105: p. 6285-6292.
10. Boyarkin, O.V., Lubich, L., Settle, R.D.S., Perry, D.S., and Rizzo, T.R., *J. Chem. Phys.*, **1997**, 107: p. 8409-8422.
11. Boyarkin, O.V., Rizzo, T.R., and Perry, D.S., *J. Chem. Phys.*, **1999**, 110(23): p. 11346-11358.
12. Yeh, L.I., Okumura, M., Myers, J.D., Price, J.M., and Lee, Y.T., *J. Chem. Phys.*, **1989**, 91(12): p. 7319-7330.
13. Mukherjee, P. and Kwok, H.S., *J. Chem. Phys.*, **1987**, 87: p. 128-138.
14. Boyarkin, O.V., Ionov, S.I., and Bagratashvili, V.N., *Chem. Phys. Lett.*, **1988**, 146(1-2): p. 106-112.
15. Boyarkin, O.V., Rizzo, T.R., Rueda, D., Quack, M., and Seyfang, G., *J. Chem. Phys.*, **2002**, 117(21): p. 9793-9805.
16. Guidi, M., Lorenz, U.J., Papadopoulos, G., Boyarkin, O.V., and Rizzo, T.R., *J. Phys. Chem. A*, **2009**, 113: p. 797-799.
17. Kaleta, D.T. and Jarrold, M.F., *J. Am. Chem. Soc.*, **2003**, 125(24): p. 7186-7187.
18. Zilch, L.W., Kaleta, D.T., Kohtani, M., Krishnan, R., and Jarrold, M.F., *J. Am. Soc. Mass Spectrom.*, **2007**, 18(7): p. 1239-1248.
19. Hopkins, J.B., Powers, D.E., and Smalley, R.E., *J. Chem. Phys.*, **1980**, 72(9): p. 5039-5048.
20. Stearns, J.A., Guidi, M., Boyarkin, O.V., and Rizzo, T.R., *J. Chem. Phys.*, **2007**, 127: p. 154322.
21. Stearns, J.A., Boyarkin, O.V., and Rizzo, T.R., *to be published*, **2009**.
22. Paizs, B. and Suhai, S., *J. Am. Soc. Mass Spectrom.*, **2004**, 15(1): p. 103-113.
23. Paizs, B. and Suhai, S., *Rapid Commun. Mass Spectrom.*, **2002**, 16(5): p. 375-389.
24. Kang, H., Dedonder-Lardeux, C., Jouvét, C., Martrenchard, S., Gregoire, G., Desfrancois, C., Schermann, J.P., Barat, M., and Fayeton, J.A., *Phys. Chem. Chem. Phys.*, **2004**, 6(10): p. 2628-2632.
25. Kang, H., Jouvét, C., Dedonder-Lardeux, C., Martrenchard, S., Grègoire, G., Desfrancoise, C., Schermann, J.P., Barat, M., and Fayeton, J.A., *Phys. Chem. Chem. Phys.*, **2005**, 7: p. 394-398.
26. Kang, H., Dedonder-Lardeux, C., Jouvét, C., Gregoire, G., Desfrancois, C., Schermann, J.P., Barat, M., and Fayeton, A., *J. Phys. Chem. A*, **2005**, 109(11): p. 2417-2420.
27. Grègoire, G., Jouvét, C., Dedonder, C., and Sobolewski, A.L., *Chem. Phys.*, **2006**, 324(2-3): p. 398-404.
28. Gregoire, G., Jouvét, C., Dedonder, C., and Sobolewski, A.L., *J. Am. Chem. Soc.*, **2007**, 129(19): p. 6223-6231.

29. Lepere, V., Lucas, B., Barat, M., Fayeton, J.A., Picard, V.J., Jouvét, C., Carcabal, P., Nielsen, I., Dedonder-Lardeux, C., Gregoire, G., and Fujii, A., *J. Chem. Phys.*, **2007**, 127(13): p. 134313.
30. Lucas, B., Barat, M., Fayeton, J.A., Perot, M., Jouvét, C., Gregoire, G., and Nielsen, S.B., *J. Chem. Phys.*, **2008**, 128(16): p. 7.
31. Lucas, B., Barat, M., Fayeton, J.A., Jouvét, C., Carcabal, P., and Gregoire, G., *Chem. Phys. Lett.*, **2008**, 347(1-3): p. 324-330.
32. Gregoire, G., Lucas, B., Barat, M., Fayeton, J.A., Dedonder-Lardeux, C., and Jouvét, C., *Eur. Phys. J. D*, **2009**, 51(1): p. 109-116.
33. Sobolewski, A.L., Domcke, W., and Hatting, C., *Proc. Natl. Acad. Sci. U. S. A.*, **2005**, 102: p. 17903-17906.
34. Sobolewski, A.L., Domcke, W., and Hattig, C., *J. Phys. Chem. A*, **2006**, 110(19): p. 6301-6306.
35. Sobolewski, A.L. and Domcke, W., *Phys. Chem. Chem. Phys.*, **2006**, 8(29): p. 3410-3417.
36. Sobolewski, A.L. and Domcke, W.G., *J. Phys. Chem. A*, **2007**, 111(46): p. 11725-11735.
37. Lan, Z.G., Frutos, L.M., Sobolewski, A.L., and Domcke, W., *Proc. Natl. Acad. Sci. U. S. A.*, **2008**, 105(35): p. 12707-12712.
38. Sobolewski, A.L., *Phys. Chem. Chem. Phys.*, **2008**, 10(9): p. 1243-1247.
39. Shemesh, D., Sobolewski, A.L., and Domcke, W., *J. Am. Chem. Soc.*, **2009**, 131(4): p. 1374-1375.
40. Svendsen, A. and Rizzo, T.R., *in preparation*, **2009**.
41. Talbot, F.O., Tabarin, T., Antoine, R., Broyer, M., and Dugourd, P., *J. Chem. Phys.*, **2005**, 122: p. 074310.
42. Kang, H., Jouvét, C., Dedonder-Lardeux, C., Martrenchard, S., Charrière, C., Grègoire, G., Desfrancoise, C., Schermann, J.P., Barat, M., and Fayeton, J.A., *J. Chem. Phys.*, **2005**, 122(8): p. 084307.
43. Raevsky, O.A., Solov'ev, V.P., Solotnov, A.F., Schneider, H.-J., and Rudiger, V., *J. Org. Chem.*, **1996**, 61(23): p. 8113-8116.
44. Julian, R.R. and Beauchamp, J.L., *Int. J. Mass Spectrom.*, **2001**, 210-211: p. 613-623.
45. Wilson, J.J., Kirkovits, G.J., Sessler, J.L., and Brodbelt, J.S., *J. Am. Soc. Mass Spectrom.*, **2008**, 19(2): p. 257-260.
46. Wyer, J.A., Ehlerding, A., Zettergren, H., Kirketerp, M.-B.S., and Brøndsted Nielsen, S., *J. Phys. Chem. A*, **2009**, 113: p. 9277-9285.
47. Joly, L., Antoine, R., Allouche, A.-R., and Dugourd, P., *J. Am. Chem. Soc.*, **2008**, 130(42): p. 13832-13833.
48. Crespo, A., Turjanski, A.G., and Estrin, D.A., *Chem. Phys. Lett.*, **2002**, 365(1-2): p. 15-21.
49. Sobolewski, A.L., *private communication*, **2009**.
50. Svendsen, A. and Rizzo, T.R., *to be published*, **2009**.
51. Nagornova, N., Boyarkin, O.V., and Rizzo, T.R., *in preparation*, **2009**.
52. Schnier, P.D., Price, W.D., Jockusch, R.A., and Williams, E.R., *J. Am. Chem. Soc.*, **1996**, 118(30): p. 7178-7189.
53. Krauss, E.M. and Chan, S.I., *J. Am. Chem. Soc.*, **2002**, 104(7): p. 1824-1830.
54. MACROMODEL, *version 9.1*. **2005**, Schrödinger, LLC: New York.

Chapter 6

Conclusions and Perspectives

This thesis has investigated the three-dimensional structures of closed-shell biomolecular ions in a cold ion trap measuring their conformer-specific vibrational spectra, recorded by applying photofragment spectroscopy techniques and interpreted by comparison with theoretical calculations.

In the study of the dipeptides H^+AlaTyr and H^+TyrAla , we analyzed the role of the charge in driving the conformational preferences of small peptides. The stronger interaction between the charge and the chromophore in H^+AlaTyr with respect to H^+TyrAla results in a reduction of the number of the stable conformers (one instead of four) as well as in a different photodissociation dynamics. In H^+TyrAla the number of bonds between the ammonium group and the aromatic ring is the same as in protonated tyrosine so that these two molecules produce both ground- and excited-state photofragments [1, 2], while the other dipeptide lacks the latter species because of the strong interaction.

The influence of the nature of the probe chromophore and its location in the peptide chain on its conformational preferences was investigated by comparing the electronic and conformer-specific vibrational spectra of $\text{Ac-Tyr-(Ala)}_5\text{-LysH}^+$ and $\text{Ac-(Ala)}_5\text{-Phe-LysH}^+$ with those of the helical peptide $\text{Ac-Phe-(Ala)}_5\text{-LysH}^+$ [3, 4]. Our results demonstrate that the nature of the chromophore influences only the number of stable conformers preserving their helical structures. On the other hand, the chromophore position in the peptide chain affects significantly the conformer structure. Two other important issues that we investigated in the process of moving toward large, natural peptides are the interaction between distinct chromophores and their ability to probe the same vibrational bands. The results on the double-chromophore, seven-amino-acid peptide, $\text{Ac-Tyr-(Ala)}_4\text{-Phe-LysH}^+$, show a weak

interaction between the two aromatic amino acids and demonstrate that they can be used to probe the same infrared spectra.

The question of the mechanism of IR-UV double-resonance methods was addressed in this thesis by analyzing the conformer-specific infrared spectra of all the seven-amino-acid peptide chains investigated. These results indicate that after the absorption of a resonant infrared photon, IVR occurs in the molecule before electronic excitation, broadening its electronic absorption. Consequently, the intensity of the UV absorption of the vibrationally-pre-excited molecules at the probe wavelength will be lower than that of the cold ions, leading to a dip in the photofragment signal.

Comparison between measured and calculated vibrational spectra ideally allows associating a structure to each conformer. However, we verified that this is not always the case because of a non-exhaustive exploration of the conformational space of a molecule as well as inaccuracies in the calculated energies and vibrational frequencies of the conformers. The highly-resolved vibrational spectra of the biomolecular ions of the dipeptides and the seven-amino-acid peptides shown in this thesis provide stringent benchmark for theory. Theoretical calculations must be able to reproduce the spectra obtained here in the well-defined and controlled environment of a cold ion trap in order to lend credence to their predictions on even larger molecules and/or those in more complex environments. It is our hope that such benchmark experiments can help provide the means to improve theoretical approaches.

The essential requirement for electronic photofragment spectroscopy to work is that the molecule has to dissociate upon electronic excitation. However, as the molecule gets larger, its dissociation yield decreases so that it becomes increasingly difficult to monitor the fragmentation on the time scale of our experiment and thus to measure electronic and conformer-specific vibrational spectra. This thesis demonstrates that such problem can be solved by implementing the IRLAPS technique to measure electronic and vibrational spectra of large biomolecular peptides containing up to seventeen amino acids. The unexpected result is that, instead of accelerating the dissociation of excited molecules on the ground electronic state, IRMPD subsequent to electronic excitation enhances the fragment due to the C_{α} - C_{β} bond cleavage, which is not the weakest in the molecule and which is associated with fragmentation on an excited state surface [5-12]. The mechanism we discussed to explain

such results involves the formation of a long-lived intermediate species (i.e., a biradical) subsequent to electronic excitation. This model suggests that the IRLAPS scheme would work only on a specific class of molecules, those having a moiety free to rotate such as the N-protected peptides investigated in this thesis work. However, the IRLAPS method is found to work by enhancing the signal due to the side-chain loss channel also in molecules with globular or cyclic structures, suggesting that the proposed model is not exhaustive. Developing a spectroscopic scheme to measure the infrared spectrum of the intermediate species and comparing it with high-level *ab initio* calculations would provide a means to investigate the nature of the intermediate state populated after the electronic excitation. Information on the conformational change of the intermediate species with respect to the ground-electronic state molecule could then be inferred by comparing their infrared spectra. For instance, one could think of a three laser spectroscopic scheme. The intermediate species produced after absorption of a UV photon would be excited by an infrared laser and then a visible or a CO₂ laser would probe the effect of the vibrational excitation. To achieve this goal, the IR laser should be at a half the repetition rate of the other two lasers.

The studies performed to interpret the experimental findings on the IRLAPS technique led us developing a variant of this technique, VISLAPS, where the photofragmentation is assisted by a visible laser. This has allowed us to measure a spectrum of the intermediate species mentioned above in the visible region of the spectrum, which is consistent with the view that it is some sort of radical species.

As the molecules we investigate get larger, even if efficient collisional cooling is achieved, spectral congestion can render the applicability of our photofragment spectroscopic schemes increasingly difficult, because of the large number of Franck-Condon active low-frequency vibrations as well as of conformational heterogeneity. A way to reduce the contribution of the latter would be to couple the ESI source with an ion mobility stage in our apparatus. The pre-selection of the conformers by ion mobility should lead to a simplification of the electronic spectrum of the species of interest, since only the vibronic transitions belonging to the selected conformer will appear in the spectrum. However, an important question must be addressed whether the conformer-selected ions undergo interconversion after being selected by their mobility. The coupling of ion mobility with laser spectroscopy would be an exciting new direction, but one that would easily form the basis of a completely separate PhD thesis.

References

1. Stearns, J.A., Mercier, S., Seaiby, C., Guidi, M., Boyarkin, O.V., and Rizzo, T.R., *J. Am. Chem. Soc.*, **2007**. *129*: p. 11814-11820.
2. Stearns, J.A., Guidi, M., Boyarkin, O.V., and Rizzo, T.R., *J. Chem. Phys.*, **2007**. *127*: p. 154322.
3. Stearns, J.A., Seaiby, C., Boyarkin, O.V., and Rizzo, T.R., *Phys. Chem. Chem. Phys.*, **2009**. *11*: p. 125-132.
4. Stearns, J.A., Boyarkin, O.V., and Rizzo, T.R., *J. Am. Chem. Soc.*, **2007**. *129*: p. 13820-13821.
5. Kang, H., Dedonder-Lardeux, C., Juvet, C., Martrenchard, S., Gregoire, G., Desfrancois, C., Schermann, J.P., Barat, M., and Fayeton, J.A., *Phys. Chem. Chem. Phys.*, **2004**. *6*: p. 2628-2632.
6. Kang, H., Juvet, C., Dedonder-Lardeux, C., Martrenchard, S., Grègoire, G., Desfrancoise, C., Schermann, J.P., Barat, M., and Fayeton, J.A., *Phys. Chem. Chem. Phys.*, **2005**. *7*: p. 394-398.
7. Kang, H., Juvet, C., Dedonder-Lardeux, C., Martrenchard, S., Charrière, C., Grègoire, G., Desfrancoise, C., Schermann, J.P., Barat, M., and Fayeton, J.A., *J. Chem. Phys.*, **2005**. *122*: p. 084307.
8. Kang, H., Dedonder-Lardeux, C., Juvet, C., Gregoire, G., Desfrancois, C., Schermann, J.P., Barat, M., and Fayeton, A., *J. Phys. Chem. A*, **2005**. *109*: p. 2417-2420.
9. Gregoire, G., Juvet, C., Dedonder, C., and Sobolewski, A.L., *J. Am. Chem. Soc.*, **2007**. *129*: p. 6223-6231.
10. Talbot, F.O., Tabarin, T., Antoine, R., Broyer, M., and Dugourd, P., *J. Chem. Phys.*, **2005**. *122*: p. 074310.
11. Lepere, V., Lucas, B., Barat, M., Fayeton, J.A., Picard, V.J., Juvet, C., Carcabal, P., Nielsen, I., Dedonder-Lardeux, C., Gregoire, G., and Fujii, A., *J. Chem. Phys.*, **2007**. *127*: p. 134313.
12. Lucas, B., Barat, M., Fayeton, J.A., Perot, M., Juvet, C., Gregoire, G., and Nielsen, S.B., *J. Chem. Phys.*, **2008**. *128*: p. 7.

List of Figures

Figure 2.1: Schematic overview of the techniques combined together	20
Figure 2.2: Electrospray ionization.....	22
Figure 2.3: The nano-electrospray source used in our apparatus.....	22
Figure 2.4: Ideal quadrupole mass filter	24
Figure 2.5: Stability diagram of a quadrupole mass filter	25
Figure 2.6: Relative effective potentials of a quadrupole, an octupole and a 22 pole.....	26
Figure 2.7: Calculated ion trajectories in several RF-only multipoles.....	27
Figure 2.8: Velocity distribution of the ions stored in traps with different multipolarity.....	29
Figure 2.9: Schematic section view and picture of the 22-pole ion trap.....	30
Figure 2.10: Section view of the tandem mass spectrometer	31
Figure 2.11: Schematic diagram of the UV generation	34
Figure 2.12: Schematic diagram of the IR generation	35
Figure 2.13: Layout of the OPO/OPA.....	35
Figure 3.1: Schematic diagram of the photophysical processes	42
Figure 3.2: Spectroscopic scheme of electronic photodissociation	44
Figure 3.3: Typical timing diagram for a photodissociation experiment	46
Figure 3.4: Spectroscopic schemes of IR-UV double resonance	54
Figure 3.5: Electronic spectra of a cold molecule with and without IR-pre-excitation.....	57
Figure 4.1: Electronic spectra of H^+TyrAla	73
Figure 4.2: Fragmentation mass spectra of H^+TyrAla	73
Figure 4.3: Calculated structures and zero point corrected energies of H^+TyrAla	74
Figure 4.4: Infrared spectra of H^+TyrAla in the NH stretch region	76
Figure 4.5: Measured and calculated infrared spectra of H^+TyrAla	77
Figure 4.6: Ultraviolet spectrum of H^+AlaTyr	79
Figure 4.7: Fragmentation mass spectrum of H^+AlaTyr	79
Figure 4.8: Calculated structures and zero point corrected energies of H^+AlaTyr	80
Figure 4.9: Measured and calculated infrared spectrum of H^+AlaTyr	81
Figure 4.10: Electronic spectrum of $\text{Ac-Tyr-(Ala)}_5\text{-LysH}^+$	85

Figure 4.11: Photofragment mass spectra of Ac-Tyr-(Ala) ₅ -LysH ⁺	86
Figure 4.12: Infrared spectra of Ac-Tyr-(Ala) ₅ -LysH ⁺	87
Figure 4.13: Gain and depletion infrared spectra of Ac-Tyr-(Ala) ₅ -LysH ⁺	88
Figure 4.14: Infrared spectra of Ac-Tyr-(Ala) ₅ -LysH ⁺ and Ac-Phe-(Ala) ₅ -LysH ⁺	89
Figure 4.15: Lowest-energy calculated conformers of Ac-Tyr-(Ala) ₅ -LysH ⁺	90
Figure 4.16: Measured and calculated spectra of Ac-Tyr-(Ala) ₅ -LysH ⁺ conformer A	93
Figure 4.17: Measured and calculated spectra of Ac-Tyr-(Ala) ₅ -LysH ⁺ conformer B	94
Figure 4.18: Electronic spectrum of Ac-(Ala) ₅ -Phe-LysH ⁺	96
Figure 4.19: Infrared spectra of Ac-(Ala) ₅ -Phe-LysH ⁺	97
Figure 4.20: Measured and calculated spectra of Ac-(Ala) ₅ -Phe-LysH ⁺ conformer A	99
Figure 4.21: Measured and calculated spectra of Ac-(Ala) ₅ -Phe-LysH ⁺ conformer B	100
Figure 4.22: Electronic spectrum of Ac-Tyr-(Ala) ₄ -Phe-LysH ⁺	101
Figure 4.23: Fragment mass spectrum of Ac-Tyr-(Ala) ₄ -Phe-LysH ⁺	102
Figure 4.24: Electronic spectra of Ac-Tyr-(Ala) ₄ -Phe-LysH ⁺ , Ac-Tyr-(Ala) ₅ -LysH ⁺ and Ac-(Ala) ₅ -Phe-LysH ⁺	103
Figure 4.25: Infrared spectra of Ac-Tyr-(Ala) ₄ -Phe-LysH ⁺	104
Figure 4.26: Measured and calculated spectra of Ac-Tyr-(Ala) ₄ -Phe-LysH ⁺ conformer A	106
Figure 4.27: Measured and calculated spectra of Ac-Tyr-(Ala) ₄ -Phe-LysH ⁺ conformer B	107
Figure 4.28: Infrared spectra of Ac-Tyr-(Ala) ₄ -Phe-LysH ⁺ in tyrosine and phenylalanine region	108
Figure 5.1: Ultraviolet spectra of three phenylalanine-containing peptides	118
Figure 5.2: IRLAPS scheme to measure the overtone transitions	121
Figure 5.3: IRLAPS scheme to measure electronic and vibrational spectra of large biomolecules	123
Figure 5.4: UV-only and IRLAPS electronic spectra of Ac-Phe-(Ala) ₅ -LysH ⁺	125
Figure 5.5: UV-only and IRLAPS electronic spectra Ac-Phe-(Ala) ₇ -LysH ⁺ -(Pro) ₂ -(Ala) ₅ - LysH ⁺	126
Figure 5.6: Electronic spectrum of Ac-Phe-(Ala) ₇ -LysH ⁺ -(Pro) ₂ -(Ala) ₅ -LysH ⁺	127
Figure 5.7: Infrared spectra of Ac-Phe-(Ala) ₅ -LysH ⁺ obtained with and without the assistance of the CO ₂ laser	127
Figure 5.8: IRLAPS infrared spectra of Ac-Phe-(Ala) ₇ -LysH ⁺ -(Pro) ₂ -(Ala) ₅ -LysH ⁺	128
Figure 5.9: UV-only and IRLAPS electronic spectra of Ac-Tyr-(Ala) ₅ -LysH ⁺	129

Figure 5.10: UV-only and IRLAPS electronic spectra Ac-Tyr-(Ala) ₇ -LysH ⁺ -(Pro) ₂ -(Ala) ₅ -LysH ⁺	130
Figure 5.11: IRLAPS infrared spectra of Ac-Tyr-(Ala) ₇ -LysH ⁺ -(Pro) ₂ -(Ala) ₅ -LysH ⁺	131
Figure 5.12: UV-only and IRLAPS electronic spectra of Ac-Trp-(Ala) ₅ -LysH ⁺	132
Figure 5.13: UV-only and IRLAPS electronic spectra of Ac-Tyr-(Ala) ₄ -Phe-LysH ⁺	133
Figure 5.14: Photofragment mass spectra of Ac-Phe-(Ala) ₅ -LysH ⁺ and Ac-Tyr-(Ala) ₅ -LysH ⁺	134
Figure 5.15: Photofragment mass spectra of Ac-Trp-(Ala) ₅ -LysH ⁺	135
Figure 5.16: Photofragment mass spectra of Ac-Tyr-(Ala) ₄ -Phe-LysH ⁺	136
Figure 5.17: IRLAPS percentage of fragmentation of Ac-Phe-(Ala) ₅ -LysH ⁺ as a function of the lasers delay	139
Figure 5.18: Depletion signal of Ac-Phe-(Ala) ₅ -LysH ⁺ as a function of the time delay between the IR and UV lasers	141
Figure 5.19: Schematic of the two mechanisms giving the C _α -C _β rupture in TrpH ⁺	143
Figure 5.20: Photofragment mass spectra of PheH ⁺	145
Figure 5.21: Photofragment mass spectra of protonated phenethylamine	146
Figure 5.22: Photofragment mass spectra of the complex Ac-Phe-(Ala) ₅ -LysH ⁺ with 18-crow- 6 ether	148
Figure 5.23: Ground state equilibrium geometry of Gly-Phe-Ala	150
Figure 5.24: EDPT process in intermolecular hydrogen bonded systems	151
Figure 5.25: Photofragment mass spectrum of the doubly deprotonated [M-2H] ²⁻ WVVVV and electronic spectrum of the radical species	152
Figure 5.26: VISLAPS scheme	153
Figure 5.27: Photofragment mass spectra of Ac-Phe-(Ala) ₅ -LysH ⁺	153
Figure 5.28: VISLAPS electronic spectrum of the biradical cation	154
Figure 5.29: Calculated photophysical scheme of Ac-Phe-(Ala) ₃	155
Figure 5.30: Calculated and measured electronic spectrum of the biradical species	157
Figure 5.31: Model structures of bradykinin and cyclic gramicidin S	159

List of Tables

Table 4.1: Calculated conformations of Ac-Tyr-(Ala) ₅ -LysH ⁺ and their assignments	92
Table 4.2: Calculated conformations of Ac-(Ala) ₅ -Phe-LysH ⁺ and their assignments	98
Table 4.3: Calculated conformations of Ac-Tyr-(Ala) ₄ -Phe-LysH ⁺ and their assignments...	105

List of Schemes

Scheme 4.1: C ₅ and C ₇ intramolecular NH...O=C interactions in peptides	72
Scheme 4.2: Nomenclature used for the fragmentation products in CID experiments	86

Acknowledgments

There are many people I would like to thank for their contributions to this thesis work, both for their scientific inputs and for their friendship:

First of all, Prof. Tom Rizzo, who accepted me in his bio-group and supported me in the hard moments of this thesis work;

Prof. John Simons, Prof. Christophe Jouvet, Prof. Anne-Clemence Corbinboeuf and Prof. Lothar Helm for agreeing to evaluate this thesis;

Dr. Oleg Boyarkine for the useful discussions on the IRLAPS results and for his constant help in the laboratory;

Prof. Andrzej Sobolewski for the calculations on the IRLAPS model.

Thinking of the early days in the lab, of course my mind goes to Dr. Anthi Kamariotis and Dr. Sebastien Mercier, my first officemates. I want to thank Dr. Jaime Stearns with whom I started to know and use the machine...and to fight with the needles! She also introduced me to the wonderful and mysterious world of the calculations...Dr. Annette Svendsen for her constant help during my writing, her important inputs and her contagious smile; Dr. Sandra Brunken for the wine that night; Natalia Nagornova for the measurements on the IR-UV experiments with the IRLAPS technique; Ulrich Lorenz and Yiorgos Papadopoulos because they manage to survive in a girl-world without showing any serious consequences...yet; Caroline Seaiby, simply because she was, depending on the circumstances, either my light or my “plafon”! It was a pleasure to work with all of you!

I want to thank the entire LCPM group, the actual and the former members, for the nice atmosphere during the coffee-breaks, for our scientific and “not” discussions, for your smiles, for your constant support, for the beers! Many of you became true friends during these five years!

A special thank to Marianne Dang because she always has a nice word to say and she never makes us feel alone.

When I look back to these last five years, I realize how many persons entered in my life, leaving an indelible mark...thanks to all my friends here in Lausanne and to the ever-green ones all around the world...a special thought to Sara.

Last and not least, thanks to my family because in the hard moments we can always count one on the other!

Curriculum vitae

PERSONAL

Date and place of birth: 14/08/1978, Frascati (Rome), Italy

Nationality: Italian

Marital status: single

EDUCATION

2005–2009: Ph.D. thesis in Physical Chemistry at the Ecole Polytechnique Fédérale de Lausanne (EPFL), Switzerland in the group of Prof. Thomas Rizzo
Spectroscopy and Dissociation Dynamics of Cold, Biomolecular Ions

1997-2004: Master's degree in Physics at the University "La Sapienza" of Rome, Italy.
Specialization in Biophysics with Prof. Adalberto Bonincontro and Prof. Camillo La Mesa

1992-1997: Diploma in "Liceo" specializing in scientific studies at the Liceo B.Touschek, Grottaferrata (Rome), Italy.

PUBLICATIONS

Conformation-Specific Spectroscopy and Photodissociation of Cold, Protonated Tyrosine and Phenylalanine, J. A. Stearns, S. Mercier, C. Seaiby, M. Guidi, O. V. Boyarkin, and T. R. Rizzo, **2007**, *J. Am. Chem. Soc.* 129 (38), 11814-11820.

Conformation-specific infrared and ultraviolet spectroscopy of tyrosine-based protonated dipeptides, J. A. Stearns, M. Guidi, O. V. Boyarkin, and T. R. Rizzo, **2007**, *J. Chem. Phys.* 127, 154322.

Spectroscopy of Protonated Peptides Assisted by Infrared Multiple Photon Excitation, M. Guidi, U. J. Lorenz, G. Papadopoulos, O. V. Boyarkin, and T. R. Rizzo, **2009**, *J. Phys. Chem. A* 113: p. 797-799.

LANGUAGES

Italian (mother tongue), English (fluent), French (Fluent)